Functional Characterization of CutA:

A Conserved Protein Involved in Bacterial Stress Adaptation

Dissertation

der Mathematisch-Naturwissenschaftlichen Fakultät

der Eberhard Karls Universität Tübingen

zur Erlangung des Grades eines

Doktors der Naturwissenschaften

(Dr. rer. nat.)

vorgelegt von

Berenike C. Wagner

aus Stuttgart

Tübingen

2025

Gedruckt mit Genehmigung der Mathematisch-Naturwissenschaftlichen Fakultät der Eberhard Karls Universität Tübingen.

Tag der mündlichen Qualifikation:	03.03.2026
Dekan:	Prof. Dr. Thilo Stehle
1. Berichterstatter/-in:	Prof. Dr. Karl Forchhammer
2. Berichterstatter/-in:	apl. Prof. Dr. Christiane Wolz

Erklärung

Ich erkläre hiermit, dass ich die zur Promotion eingereichte Arbeit selbständig verfasst, nur die angegebenen Quellen und Hilfsmittel benutzt und wörtlich oder inhaltlich übernommene Stellen als solche gekennzeichnet habe. Ich erkläre, dass die Leitlinien zur Sicherung guter wissenschaftlicher Praxis der Universität Tübingen (Beschluss des Senats vom 11.2.2021) beachtet wurden. Ich versichere an Eides statt, dass diese Angaben wahr sind und dass ich nichts verschwiegen habe. Mir ist bekannt, dass die falsche Abgabe einer Versicherung an Eides statt mit Freiheitsstrafe bis zu drei Jahren oder mit Geldstrafe bestraft wird.

Tübingen, den _____

Berenike Wagner

Sometimes, growth takes time.

- ***S. elongatus***

Table of Contents

I. List of Abbreviations

The abbreviations included in this list are those used consistently throughout the thesis. Less frequent abbreviations are defined when first introduced.

ACN	Acetonitrile
AHT	Anhydrotetracycline
Amp	Ampicillin
BH2	7,8-Dihydrobiopterin
BH4	5,6,7,8-Tetrahydrobiopterin
bp	Base pairs
Cm	Chloramphenicol
Cb	Carbenicillin
cut genes	*copper uptake and transport* genes
DMSO	Dimethyl Sulfoxide
Dxan-B2	2'-Deoxyxanthopterin B2
E. coli / Ec	*Escherichia coli*
ESI	Electrospray Ionization
FBMN	Feature Based Molecular Networking
H_2NTP	7,8-Dihydroneopterin triphosphate
HEPES	4-(2-Hydroxyethyl)-1-piperazinethanesulfonic acid
HPLC	High-Performance Liquid Chromatography
Kan	Kanamycin
kb	Kilobases
Kd	Dissociation Constant
LC-MS	Liquid Chromatography-Mass Spectrometry
LFQ	Label-free quantification
m/z	Mass to charge ratio
MeOH	Methanol
MES	2-(N-morpholino)ethanesulfonic acid
MH4	5,6,7,8-Tetrahydromonapterin
MS/MS	Tandem Mass Spectrometry
Nostoc sp.	*Nostoc* sp. PCC 7120
PCC	Pasteur Culture Collection
PCoA	Principal Coordinate Analysis
PCR	Polymerase Chain Reaction
ROS	Reactive Oxygen Species
rpm	Revolutions per Minute
RT-PCR	Reverse Transcriptase PCR
RT	Retention Time
S. elongatus/ Se	*Synechococcus elongatus* PCC 7942
SI	Supplementary Information
SPE	Solid Phase Extraction
TIC	Total Ion Chromatogram
Tm	Melting Temperature
WT	Wild Type

II. Abstract

A substantial fraction of proteins remains functionally uncharacterized. This “dark matter” of the proteome includes conserved proteins whose roles are incompletely understood but are likely fundamental to cellular physiology. Among these proteins is CutA, a small homotrimeric and evolutionarily widespread protein, conserved across all domains of life: from cyanobacteria to humans. Although early studies suggested a possible role in copper tolerance, this hypothesis has been debated. Motivated by its broad conservation, this study aimed to investigate the possible cellular function of CutA.

To explore the potential role of CutA, wild-type and *ΔcutA* mutant strains of *Escherichia coli (E. coli)* and *Synechococcus elongatus* PCC 7942 (*S. elongatus*) were exposed to various stress conditions. *ΔcutA* mutants exhibited increased heat sensitivity in both species, along with enhanced copper and pH sensitivity in *E. coli* and increased susceptibility to β-lactam antibiotics in *S. elongatus*, indicating that CutA contributes to the stress response. To identify possible interactors, a native mass spectrometry workflow was applied to screen potential binding partners from cell extracts. This revealed a putative ligand from *S. elongatus* cell extract that interacts with CutA from both species. The compound was subsequently purified and structurally characterized by nuclear magnetic resonance spectroscopy as a previously unknown pteridine, which was named 2'-deoxyxanthopterin B2. Pteridines are ubiquitous metabolites that act as redox cofactors through stepwise electron transfer. Microscale thermophoresis and nano differential scanning fluorimetry confirmed binding of 2'-deoxyxanthopterin B2 and other purchased pteridines to CutA. Microscale thermophoresis experiments also revealed binding of $CuSO_4$ to CutA, with binding observed to increase in the presence of tetrahydrobiopterin.

In *E. coli*, the fatty acid biosynthesis proteins FabZ and AcpP were enriched in pulldown proteomics experiments with CutA under both standard and heat stress conditions.

Together, these results identify pteridines as CutA-binding metabolites and reveal interactions with copper, suggesting that CutA supports stress resilience via modulation of copper binding, redox homeostasis, and membrane-associated processes. These findings align with the roles of other *cut* genes, which often function not only in copper homeostasis but also in the cell envelope stress response.

The following monographic dissertation integrates a peer-reviewed research article that forms the core of the CutA investigation.

III. Zusammenfassung

Ein erheblicher Anteil aller Proteine ist bislang funktionell nicht charakterisiert. Diese „dunkle Materie“ des Proteoms umfasst konservierte Proteine, deren Funktion bislang nur unzureichend verstanden sind, für die jedoch grundlegende Rollen in der zellulären Physiologie angenommen werden. Zu diesen Proteinen zählt CutA, ein kleines, homotrimeres und evolutionär weit verbreitetes Protein, das in allen Domänen des Lebens konserviert ist, von Cyanobakterien bis hin zum Menschen. Obwohl vorangegangene Studien eine mögliche Rolle in der Kupfertoleranz vermuten, ist diese Funktion bislang umstritten. Die weite Verbreitung von CutA über viele Spezies hinweg veranlasste die Untersuchung einer möglichen zellulären Funktion des Proteins in dieser Arbeit.

Zur Charakterisierung von CutA wurden Wildtyp- und *ΔcutA*-Mutanten von *Escherichia coli* (*E. coli*) und *Synechococcus elongatus* PCC 7942 (*S. elongatus*) verschiedenen Stressbedingungen ausgesetzt. *ΔcutA*-Mutanten von beiden Spezies zeigten eine erhöhte Hitzesensitivität. In *E. coli* zeigte die *ΔcutA*-Mutante eine erhöhte Kupfer- und pH-Empfindlichkeit und in *S. elongatus* eine verstärkte Anfälligkeit gegenüber β-Lactam Antibiotika. Dies weist darauf hin, dass CutA zur Stressantwort beitragen könnte.

Zur Identifizierung potenzieller Interaktionspartner wurde native Massenspektroskopie angewandt, um mögliche Bindungspartner aus Zellextrakten zu finden. Dabei wurde ein Metabolit in *S. elongatus* Zellextrakten gefunden, der mit CutA beider Spezies interagiert. Diese Verbindung wurde anschließend aufgereinigt und mittels NMR-Spektroskopie als bislang unbekanntes Pteridin charakterisiert, das 2'-Deoxyxanthopterin B2 genannt wurde. Pteridine sind weit verbreitete Metabolite, die als Kofaktoren für Redox-Reaktionen über stufenweise Elektronenübertragung wirken.

Microscale Thermophoresis und Nano Differential Scanning Fluorimetry bestätigten die Bindung von 2'-Deoxyxanthopterin B2 sowie weiterer kommerziell verfügbarer Pteridine an CutA. Zusätzlich zeigte die Microscale Thermophoresis eine Bindung von $CuSO_4$ an CutA, wobei die Bindungsaffinität in Anwesenheit von Tetrahydrobiopterin erhöht war. In *E. coli* zeigten Pulldown-Proteomik-Experimente unter Standard- und Hitzebedingungen eine Anreicherung der Fettsäurebiosyntheseproteine FabZ und AcpP zusammen mit CutA.

Die Ergebnisse identifizieren Pteridine als Metabolite, die an CutA binden und belegen Interaktionen mit Kupfer, was darauf hindeutet, dass CutA zur Stressresilienz durch Modulation der Kupferbindung, Redox-Homöostase und membranassoziierter Prozesse beiträgt. Diese Ergebnisse decken sich mit den Funktionen anderer *cut*-Gene, die sowohl an der Kupferhomöostase als auch an der Stressantwort der Zellhülle beteiligt sind.

Die vorliegende monographische Dissertation bezieht einen peer-reviewten Forschungsartikel mit ein, welcher den zentralen Kern dieser Arbeit zur Untersuchung der Funktion von CutA darstellt.

IV. Contributions to Scientific Publications

This dissertation is structured as a monograph and integrates two publications: (1) a peer-reviewed research article that forms the basis of Chapter 4, and (2) a manuscript in preparation derived from the work presented in the Appendix. In addition to the two chapters included in this thesis, I contributed to several other projects and publications during my PhD, which are listed below.

1. Peer-reviewed research article, based on the results presented in Chapter 4 of this thesis

Wagner, Berenike C.; Steuer-Lodd, Karoline; Geibel, Christian; Stadelmann, Amelie; Rapp, Johanna; Link, Hannes; Schramm, Tilman; Boodaghian, Nouneh; Hsiao, Ansel; Nussbaum, Eva; Grenzendorfer, Heinz-Paul; Albrecht, Reinhard; Hartmann, Marcus D.; Forchhammer, Karl; Selim, Khaled A.; Hughes, Chambers C. & Petras, Daniel (2025). **Native metabolomics identifies pteridines as CutA ligands and modulators of copper binding.** *Proceeding of the National Academy of Sciences*, *122*(48), e2509468122. https://doi.org/10.1073/pnas.2509468122

Personal Contribution: Together with Karl Forchhammer (main supervisor for this project and thesis, physiological experiments), Daniel Petras (untargeted and native LC/MS, main corresponding author), Khaled A. Selim (project idea together with Karl Forchhammer, corresponding author), and Chambers C. Hughes (compound purification and NMR analysis, corresponding author) I conceptualized and planned the experiments. I coordinated communication among all collaborators throughout the project. I designed the cloning and phenotyping experiments and performed them together with Amelie Stadelmann and Eva Nussbaum, also in cooperation with Karoline Steuer-Lodd, who performed phenotyping experiments for the revision process. I carried out heterologous protein expression and purification by FPLC using an ÄKTA Purifier, with support from Heinz-Paul Grenzendorfer when additional protein was required. Together with Daniel Petras and Christian Geibel, I conceptualized, planned, and performed the untargeted LC-MS/MS and native MS experiments. In cooperation with Johanna Rapp and Hannes Link, we designed and performed targeted metabolomics experiments. I purified four pteridines together with, and under the supervision of, Chambers C. Hughes, who also analyzed their NMR spectra. I performed NanoDSF and MST experiments with support from Reinhard Albrecht and under the supervision of Marcus D. Hartmann. For the revision process, I designed additional experiments together with Daniel Petras, Karoline Steuer-Lodd, Tilman Schramm, Nouneh Boodaghian, and Ansel Hsiao, and I prepared the responses to the reviewers' comments with input from all authors. In addition, I analyzed all data except the NMR measurements and prepared all figures. I wrote the manuscript with support from Chambers C. Hughes and Daniel Petras.

2. Manuscript in preparation based on the results presented in the Appendix of this thesis

Wagner, Berenike C.; Vitale, Giovanni A.; Hughes, Chambers C.; Forchhammer, Karl; Petras, Daniel (2025): **Native metabolomics-based profiling of serine protease inhibitors across 20 cyanobacterial strains**. *Unpublished manuscript*.

Personal Contribution: I cultivated cyanobacterial strains to screen for protease inhibitors, with guidance from Karl Forchhammer. I performed solid-phase extraction (SPE) of supernatants and cell pellet extracts, followed by LC-MS/MS and native MS analysis under the supervision of Daniel Petras. I optimized cultivation conditions and upscaling for *Mastigocladus laminosus* cultures and purified a putative protease inhibitor together with Giovanni Andrea Vitale with advice from Chambers C. Hughes. I also conducted the data analysis and authored the manuscript. The work was in part funded by a CMFI Young Investigator Grant I acquired, alongside additional contributions from other collaborators.

3. Peer-reviewed research article

Reher, Raphael; Aron, Allegra T.; Fajtová, Pavla; Stincone, Paolo; **Wagner, B.**; …; Gerwick, William H. & Petras, Daniel. **Native metabolomics identifies the rivulariapeptolide family of protease inhibitors.** *Nature Communications* **13**, 4619 (2022). https://doi.org/10.1038/s41467-022-32016-6

Personal Contribution: I purified the CutA protein as a multimeric model to validate the functionality of the native metabolomics method and performed native MS measurements of CutA and other proteins together with and under the supervision of Daniel Petras.

4. Peer-reviewed research article

Zuffa, Simone; Schmid, Robin; Bauermeister, Annelise;…; **Wagner, Berenike C**.; Forchhammer, Karl; Petras, Daniel; …, Wang, Mingxun & Dorrestein, Pieter C. (2024). **microbeMASST: A taxonomically informed mass spectrometry search tool for microbial metabolomics data**. *Nature Microbiology*, *9*(2), 336–345. https://doi.org/10.1038/s41564-023-01575-9

Personal Contribution: I cultivated 20 different cyanobacterial strains under the supervision of Karl Forchhammer and extracted metabolites from cell pellets and supernatants using solid-phase extraction. Under the supervision of Daniel Petras, I analyzed the extracts via LC-MS/MS, processed the data, and uploaded it to the MASSIVE and GNPS platforms. Additionally, I tested whether the MicrobeMASST search tool functions as intended.

5. Peer-reviewed research article

Mantovani, Oliver; Haffner, Michael; Walke, Peter; Elshereef, Abdalla A.; **Wagner, Berenike**; Petras, Daniel; Forchhammer, Karl; Selim, Khaled A.; Hagemann, Martin (2024). **The redox-sensitive R-loop of the carbon control protein SbtB contributes to the regulation of the cyanobacterial CCM.** *Scientific Reports*, *14*(1), 7885. https://doi.org/10.1038/s41598-024-58354-7.

Personal Contribution: I planned the Top-down proteomics experiment with Michael Haffner and Daniel Petras to perform MS analysis of the intact P_{II}-like SbtB protein. Under the supervision of Daniel Petras, I conducted intact protein MS analysis and acquired MS1 and MS/MS spectra in Top3 data-dependent acquisition mode, processed the data using Xcalibur 4.1, performed spectral deconvolution with Xtract in FreeStyle™, and matched protein spectra using ProSight Lite. Additionally, I visualized the data for the manuscript with advice from Karl Forchhammer.

6. Peer-reviewed research article

Huergo, Luciano F.; Selim, Khaled A.; Conzentino, Marcelo S.; Gerhardt, Edileusa C. M.; Santos, Adrian R. S.; **Wagner, Berenike**, Alford, Janette T.; Deobald, Nelli; …; Rodrigo A. Reis & Forchhammer, Karl (2021). **Magnetic Bead-Based Immunoassay Allows Rapid, Inexpensive, and Quantitative Detection of Human SARS-CoV-2 Antibodies**. *ACS Sensors*, *6*(3), 703–708. https://doi.org/10.1021/acssensors.0c02544

Personal Contribution: In collaboration with Nelli Deobald and Janette Alford, I purified the SARS-CoV-2 N-Protein by FPLC using an ÄKTA purifier. Under the guidance of Edileusa C. M. Gerhardt and Luciano F. Huergo, and in partnership with the NMI Reutlingen, we performed magnetic bead-based immunoassays using human blood samples.

7. Peer-reviewed research article

Conzentino, Marcelo S.; Santos, Tatielle P. C.; Selim, Khaled A.; **Wagner, Berenike**; Alford, Janette T.; Deobald, Nelli; Paula, Nigela M.; Rego, Fabiano G. M.; Zanette, Dalila L.; Aoki, Mateus N.; Nardin, Jeanine M.; Huergo, Maria C. C.; Reis, Rodrigo A.; Huergo, Luciano F. (2021). **Ultra-fast, high throughput and inexpensive detection of SARS-CoV-2 seroconversion using Ni^{2+} magnetic beads.** *Analytical Biochemistry*, *631*, 114360. https://doi.org/10.1016/j.ab.2021.114360

Personal Contribution: same as in the article above: In collaboration with Nelli Deobald and Janette Alford, I purified the SARS-CoV-2 N-Protein by Fast Protein Liquid Chromatography using an ÄKTA purifier. Under the guidance of Edileusa C. M. Gerhardt and Luciano F. Huergo, and in partnership with the NMI Reutlingen, we performed magnetic bead-based immunoassays using human blood samples.

8. Peer-reviewed research article

Pakkir Shah, Abzer. K.; Walter, Axel; …; **Wagner, Berenike C**.;….; Ernst, Madeleine & Petras, Daniel (2025). **Statistical analysis of feature-based molecular networking results from non-targeted metabolomics data.** Nature Protocols, 20(1), 92–162. https://doi.org/10.1038/s41596-024-01046-3

Personal Contribution: I tested and validated the statistical analysis protocol on my untargeted metabolomics datasets, including an assessment of both the computational code and the app interface.

9. Peer-reviewed research article

Shahneh, Mohammad Reza. Z.; Strobel, Michael; Vitale, Giovanni A.; Geibel, Christian; Abiead, Yasin El; Garg, Neha; **Wagner, Berenike**; Forchhammer, Karl; Aron, Allegra; Phelan, Vanessa V.; Petras, Daniel & Wang, Mingxun (2024**). ModiFinder: Tandem Mass Spectral Alignment Enables Structural Modification Site Localization.** *Journal of the American Society for Mass Spectrometry*, *35*(11), 2564–2578. https://doi.org/10.1021/jasms.4c00061

Personal Contribution: I performed cultivation of *S. elongatus,* HPLC extraction and acquired LC-MS/MS data of the extracts.

10. Peer-reviewed research article

Rapp, Johanna; **Wagner, Berenike;** Brilisauer, Klaus; Forchhammer, Karl. (2021). ***In vivo* Inhibition of the 3-Dehydroquinate Synthase by 7-Deoxysedoheptulose Depends on Promiscuous Uptake by Sugar Transporters in Cyanobacteria.** *Frontiers in Microbiology*, *12*, 692986. https://doi.org/10.3389/fmicb.2021.692986

Personal Contribution: I supported the study by performing bioactivity assays, PCR of selected genes, and constructing *Anabaena* sp. PCC7120+frtRABC for the analysis of spontaneous 7dSh-resistant mutants with input and guidance from Johanna Rapp. Additionally, I interpreted and discussed the experimental results with the other authors.

11. Manuscript in preparation

Bader, Marius; Högner, Mona; …; **Wagner, Berenike C.;…;** Grond, Stephanie; Kayser, Leonard (2025): **Echinosporin biosynthesis is frequent in the bacterial kingdom and is the founding member of a plant herbicide diversity.** *Unpublished manuscript*.

Personal Contribution: I designed, executed, and analyzed bioactivity assays with *Synechococcus elongatus* PCC 7042, *Synechocystis* PCC 6804, and *Anabaena variabilis* ATCC 29413, and determined the minimum inhibitory concentrations (MICs) of echinosporin and other compounds on these three cyanobacterial strains.

1 Introduction

1.1 CutA: Name Origin and Background

The discovery of *cutA* genes in *Escherichia coli* traces back to an unexpected source - a piggery wastewater sample. In this environment, a plasmid conferring copper resistance was identified in copper resistant *E. coli*[1,2]. This finding revealed a bacterial strategy to survive toxic metal stress caused by copper sulfate-supplemented diets used to promote growth in pig farming[1]. Copper is an essential trace element involved in redox reactions and enzymatic activity, but becomes toxic at elevated concentrations, where it can disrupt enzyme function and damage cellular membranes. To manage this duality, bacteria must tightly regulate copper homeostasis and coordinate detoxification mechanisms with essential copper-dependent processes[3]. Following the initial discovery of the resistant strain, a series of genetic investigations led to the characterization of the large conjugative plasmid, which conferred copper tolerance to laboratory *E. coli* strains[1,2]. Through mutagenesis and complementation studies, a cluster of genes presumed to be involved in copper uptake and transport ("*cut*-genes")[4–7] were found. Mutants of these genes responded differently to increased copper concentration in comparison to the wild type (WT) strain and were categorized into seven complementation groups: *cutA* - *cutF*, along with a regulator named *cutR*[8]. An overview of the *cut*-genes is shown in Table 1.1.

Table 1.1: The *cut*-genes of *E. coli.*

Gene	Protein	Function	Location in *E. coli*	Location in the cell
cutA1	CutA1	In mammals: involved in protein processing and trafficking and may be linked to neurodegenerative pathways such as Alzheimers`s disease[9,10] Overexpression of human CutA isoform 2 sensitized cells to copper toxicity, suggesting a modulatory role[11]. In bacteria: Conserved trimeric cytoplasmic protein with a ferredoxin-like fold. Initially linked to copper tolerance[5,12], but later studies questioned this role and suggested a function in small-molecule binding or signaling[13].	b4137	Cytoplasm
cutA2 (dsbD)	Thiol:disulfide interchange protein DsbD	Inner membrane redox protein acting as a "redox hub" that transfers electrons to periplasmic partners for disulfide bond formation and isomerization[14], and in c-type cytochrome biogenesis in the periplasm[15].	b4136	Cell inner membrane, Multi-pass membrane protein
cutA3 (yjdC)	Predicted, HTH-type transcriptional regulator YjdC	Putative transcription factor[16].	b4135	
cutB		Function unknown; possibly involved in copper tolerance, presumed copper uptake[8].	Not specified	
cutC (micL)		Possibly involved in copper tolerance[7] but copper sensitivity was later traced to MicL sRNA loss, which raises Lpp (major outer membrane lipoprotein Lpp) levels. MicL is transcribed from the 3' UTR of *cutC*, so mutations in *cutC* can disrupt its expression and indirectly affect copper tolerance[17]. Silent mutations disrupting the *micL* promoter cause copper sensitivity[17]. In *Xylella fastidiosa*, CutC binds copper and contributes to copper tolerance[18].	b1874	Cytoplasm
cutD		Function unknown; possibly involved in copper tolerance via copper efflux[4].	Not specified	

cutE (lnt)	Apo-lipoprotein N-acyltransferase	Copper transport[6].	b0657	Cell inner membrane, Multi-pass membrane protein
cutF (nlpE)	Lipoprotein NlpE	Copper homeostasis[7]. Involved in envelope stress responses. Its overproduction triggers the CpxA/CpxR two-component system, leading to periplasmic serine endoprotease DegP (HtrA) induction[19]	b0192	Cell outer membrane

Subsequent investigations have shown that several genes initially identified as copper tolerance genes, such as *cutF* (*nlpE*), *cutE* (*lnt*), *cutC* (*micL*), and *cutA2* (*dsbD*) play roles in the bacterial cell envelope stress response rather than being directly involved in copper homeostasis[20]. These findings illustrate that the physiological functions of *cut* genes are more diverse and complex than originally thought, which is an important consideration when assessing the role of CutA.

In the early 1990s, the *E. coli* chromosomal locus labelled *cutA* was presumed to mediate Cu(I) uptake and to be part of a zinc uptake system[8]. A few years later, the *cutA* locus was characterized to be comprised of two operons[5]: One operon encodes the cytoplasmic protein CutA1 while a second operon encodes two inner membrane proteins: CutA2 (also referred to as DsbD), which maintains periplasmic redox balance by transferring electrons from the cytoplasm, and CutA3 (also referred to as YjdC), a putative HTH-type transcriptional regulator. A knockout of the whole chromosomal locus *cutA* led to sensitivity to divalent cations including zinc, nickel, cadmium, cobalt and copper and also increased uptake of the radioactive isotope copper-64[5]. Based on fusion of *cutA* with the *lux* reporter operon, it was observed that *cutA* expression is induced by several stress-causing transition metals, including copper, zinc, nickel and cobalt with weaker induction by cadmium, manganese and silver[5].

Concurrently, another research group investigating the biogenesis of heme-containing cytochromes c, sequenced the same gene locus and identified *cutA2/dsbD* as the c-type cytochrome biogenesis protein DipZ[15]. Since *cutA1* and *cutA2/dsbD* share a 25-base pair overlapping region, it has been debated whether the copper sensitivity observed in *cutA* mutants arises from pleiotropic effects related to *cutA2*[21].

Arnesano et al.[12] demonstrated that *Escherichia coli* CutA1 binds Cu^{2+} ions *in vitro* at a solvent-accessible type II copper site via a His_2Cys coordination motif, which they characterized using X-ray absorption spectroscopy and electron paramagnetic resonance spectroscopy. They proposed that CutA1's lack of strict metal specificity suggests a role upstream in copper homeostasis, potentially cooperating with disulfide oxidoreductases such as CutA2/DsbD to regulate the redox state of thiol groups within metal-binding CXXC motifs, which are found, for example, in Cu(I)- and Zn(II)/Cd(II)-ATPases[12,22].

However, a recent study by Selim et al. 2020 using physiological experiments found that the *cutA1* gene does not appear to be involved in copper tolerance in either *E. coli* or *Synechococcus elongatus* PCC 7942[13,23]. Although the *E. coli cutA1* knockout strain exhibited increased sensitivity to Cu^{2+} compared to the wild-type strain, further analysis suggested that this was likely due to polar effects on the neighboring *cutA2/dsbD* gene. Complementation experiments indicated that CutA2, but not CutA1, restored copper resistance, implying that CutA1 does not contribute to copper tolerance. Therefore, the precise cellular function of CutA1 (hereafter referred to as CutA) remains to be investigated.

1.2 CutA - A P_{II}-like Protein

CutA is a homo-trimeric protein found across a plethora of bacteria, archaea but also eukaryotes, including plants and mammals, with each monomer weighing approximately 12 kDa. The protein typically assembles into a very stable, barrel-like trimeric complex exhibiting near C_3 symmetry, characterized by a threefold rotational axis[13,24] (Figure 1.1A and F). Its trimeric structure is stabilized by formation of inter-subunit β-sheets surrounded by α- helices on the surface of the protein, a feature typical of the P_{II} superfamily of signal transduction proteins, which are broadly distributed across bacteria, archaea, and plastids in plants[25]. An overlay of both proteins in *E. coli* and *S. elongatus* is shown in Figure 1.1B and G, respectively.

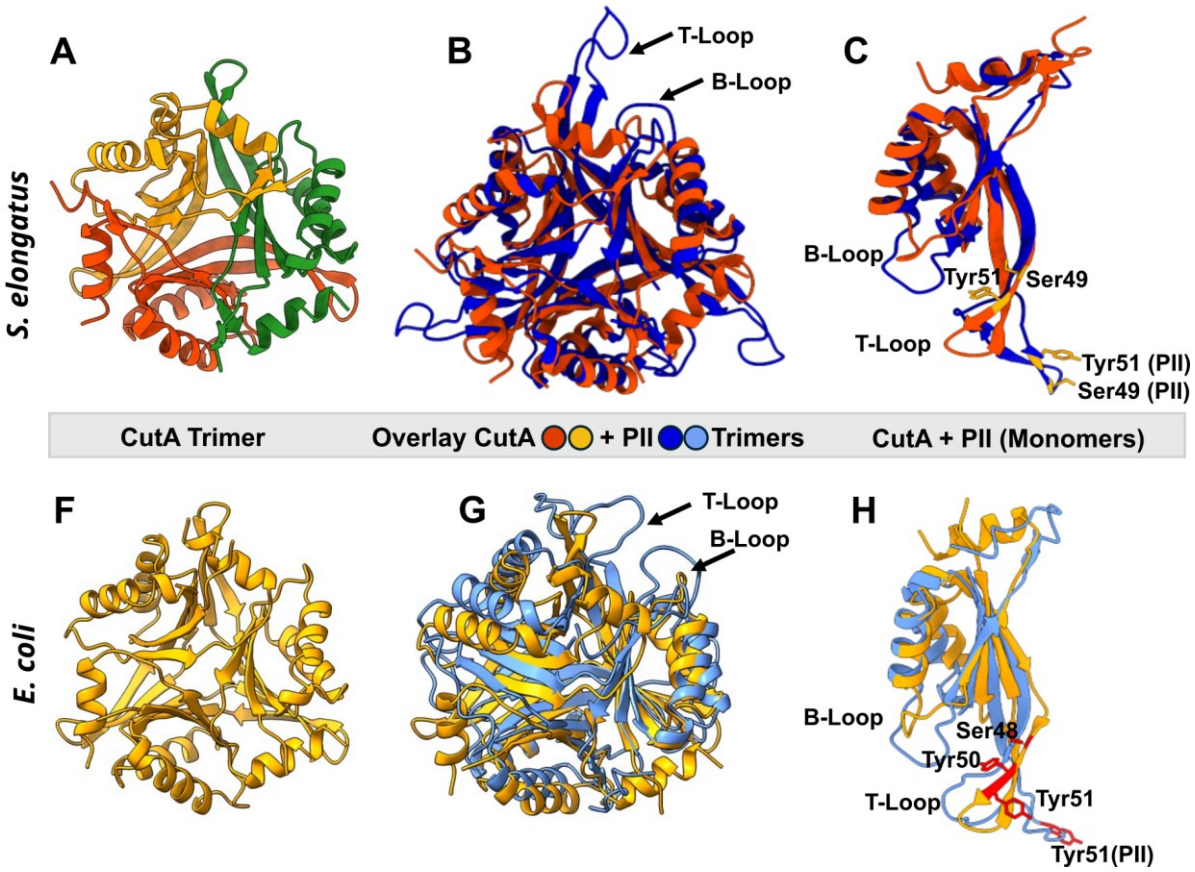

Figure 1.1: Structural comparison of *E. coli* and *S. elongatus* CutA and P_{II} (GlnB) proteins.
(A-C) *S. elongatus* **(A)** Quaternary structure of the CutA trimer. **(B)** Structural overlay of CutA (red) and P_{II} (blue) trimers. **(C)** Overlay of individual monomers of CutA and PII. Structures based on PDB IDs: CutA:6GDU, P_{II}:1QY7. P_{II} monomer: AF-P0A3F4-F1.
(F-H) *E. coli*: **(F)** Quaternary structure of the CutA trimer. **(G)** Overlay of *E. coli* CutA(yellow) and GlnB (cornflower blue) trimers. **(H)** Overlay of CutA and P_{II} (GlnB) monomers with conserved tyrosines (Tyr50 in CutA, Tyr51 in GlnB) in red. Structures based on PDB IDs: CutA:1NAQ, GlnB:2P_{II}. All structures were visualized and aligned using ChimeraX.

P_{II} proteins are indispensable for survival under nitrogen limitation and for re-establishing metabolic homeostasis by orchestrating the traffic of metabolites through central pathways[26]. They do so by integrating signals of the cell's carbon, nitrogen, and energy status, specifically by sensing metabolites such as 2-oxoglutarate (α-ketoglutaric acid**,** carbon status), glutamine (nitrogen status), and the ATP/ADP ratio (energy status), to modulate key enzymatic and transport activities and of the cell[27,28]. These signals induce post-translational modifications and conformational changes in P_{II} proteins, thereby regulating their interactions with diverse target proteins. Through these interactions, P_{II} proteins control critical enzymatic steps in nitrogen assimilation (e.g., glutamine synthetase activity), nitrogen uptake (e.g., ammonium transport via AmtB), and arginine biosynthesis (e.g., N-acetylglutamate kinase, NAGK), as well as other essential metabolic pathways[25,26]. Although CutA forms trimers structurally

resembling P_{II} proteins, it lacks sequence homology with the P_{II} family, and is therefore classified as a P_{II}-like protein (described in more detail in section 1.3)[24,26,29–31]. This divergence hints at the potential for distinct, yet functionally analogous, regulatory roles in cellular metabolism.

Each subunit of the P_{II} trimer comprises three conserved loops (designated T-, B-, and C-loop) that coordinate effector binding and protein-protein interactions. Under nitrogen starvation, decreased intracellular glutamine concentrations activate the uridylyl-transferase activity of GlnD[32], resulting in the covalent modification of Tyr-51 located at the apex of the solvent-exposed T-loop (see Figure 1.1 C and H)[33]. Conversely, under nitrogen-replete conditions, GlnD catalyzes the removal of this uridylyl modification, restoring P_{II} to its unmodified state[25,34,35]. This uridylylation mechanism is predominantly observed in proteobacteria while in other bacterial taxa, P_{II} regulation is commonly achieved through alternative post-translational modifications. For instance, in *Streptomyces coelicolor*, the P_{II} homolog GlnK undergoes adenylylation at Tyr-51 by the adenylyltransferase GlnE[36], whereas in unicellular cyanobacteria like *Synechococcus*, the P_{II} protein undergoes phosphorylation at Ser-49 in response to cellular nitrogen availability[37] .

An overview of the amino acid sequences of P_{II} and CutA proteins from the strains of this study, *E. coli*, *S. elongatus* and *Nostoc* sp. PCC 7120, is presented in Figure 1.2. While the overall structures of these proteins are notably similar, their sequences vary considerably, as illustrated by the consensus alignment. Nonetheless, both proteins are of comparable length and share conserved serine and tyrosine residues at analogous positions.

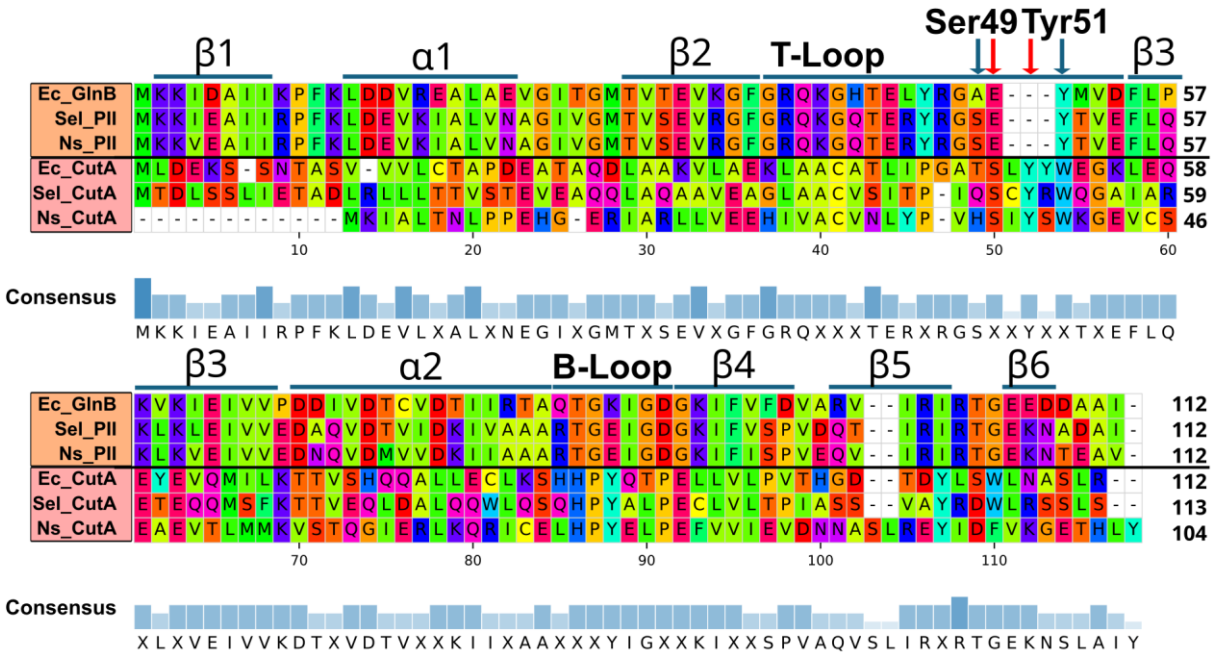

Figure 1.2: Multiple sequence alignment of P_{II} (GlnB in *E. coli*) and CutA homologues from *Escherichia coli* (Ec), *Synechococcus elongatus* (Se), and *Nostoc* sp. PCC 7120 (Ns).
Residues are colored according to the Taylor scheme. The consensus line denotes the degree of conservation across all six sequences. Sequences were retrieved from UniProt and aligned using ClustalW in MEGA X. Secondary structure elements of P_{II} (α-helices and β-strands) are shown above the alignment. Arrows indicate conserved serine and tyrosine residues of P_{II} (in black) or CutA (red).

While CutA proteins and P_{II} share a common ferredoxin-like core fold and possess a B-loop (as shown in Figure 1.1), their T-loop architectures diverge markedly in structure and function. In canonical P_{II} proteins, the T-loop is a flexible element that undergoes large, ligand-induced conformational changes to gate effector binding and mediate protein-protein interactions[26,38,39]. By contrast, in CutA the analogous region is truncated to a short β2-β3 connector ("vestigial T-loop") that contributes to the lining of a deep, negatively charged pocket rather than performing gating motions[13]. The extended β2-β3 hairpin that projects from the CutA scaffold is therefore not homologous to the P_{II} T-loop. Instead, it represents a structural adaptation for the stabilization of the trimer[12]. In CutA, this long hairpin drives assembly of intersubunits (visible in Figure 1.1, Figure 1.4), whereas the vestigial T-loop remains fixed, defining pocket geometry without undergoing the pronounced swings characteristic of P_{II}'s regulatory T-loop.

Although CutA proteins lack the prominent, protruding T-loop structure characteristic of canonical P_{II} proteins, they retain the two conserved residues, Tyr-51 and Ser-48/Ser-49 (amino acid numbering based on *E. coli* and *S. elongatus*), which occupy a structurally analogous position on β2 (visualized with a red arrow in CutA and a black arrow in GlnB/P_{II}

in Figure 1.2**).** These residues align spatially with the T-loop region of P_{II} proteins (see Figure 1.1 and 1.2), suggesting a possible functional analogy. They may serve as sites for post-translational modifications such as uridylylation, adenylylation, or phosphorylation, akin to the regulatory mechanisms observed in P_{II} proteins[26,32]. Both residues are conserved across a wide range of CutA homologs, including those from *Homo sapiens*. Figure 1.3 provides an overview of CutA sequences from diverse domains of life, including Archaea (*Pyrococcus horikoshii,)*, Bacteria (e.g. *E. coli*, *Salmonella typhi)*, and Eukaryota (plants and mammals) and shows amino acid residues that are conserved across all species examined.

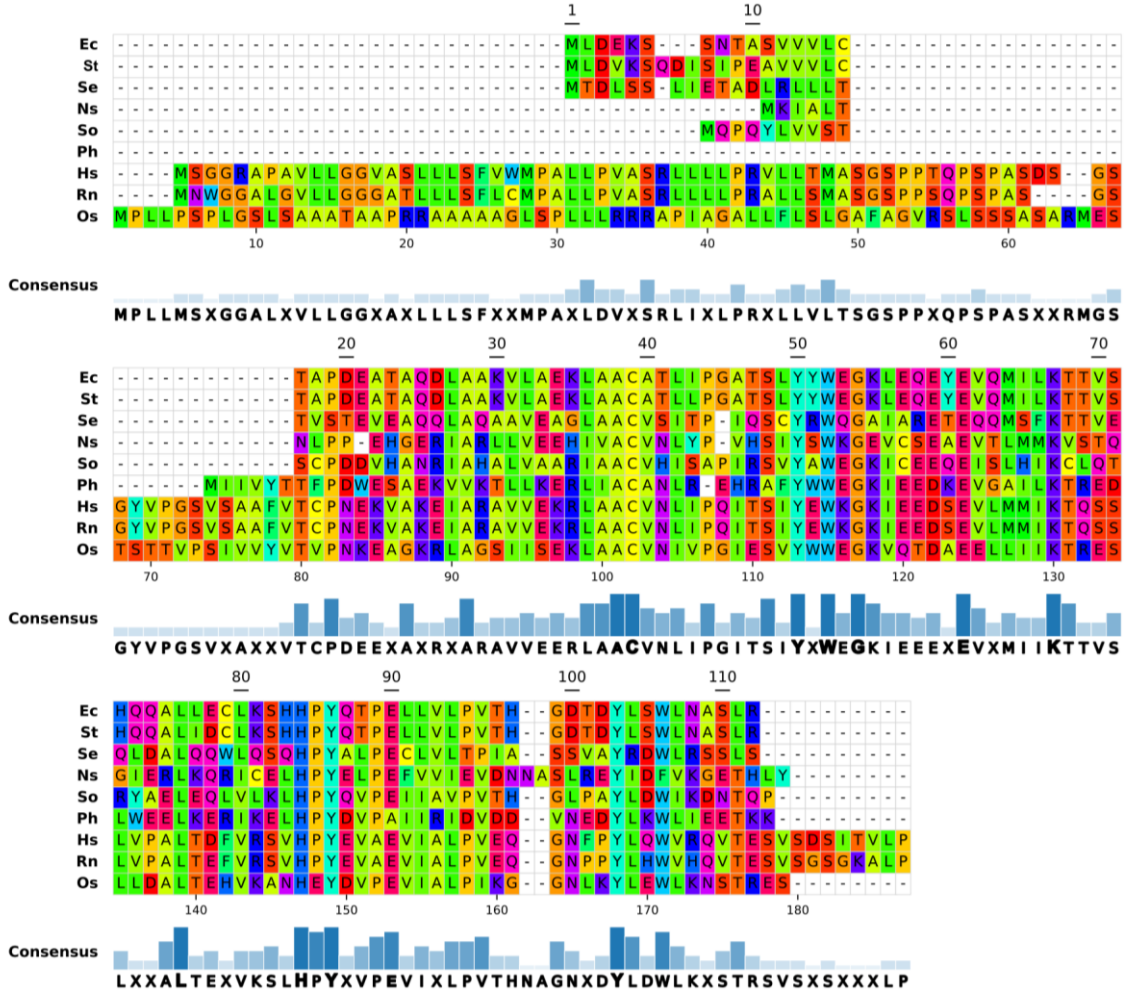

Figure 1.3: Multiple sequence alignment of CutA homologues from different domains of life:
Bacteria: *E. coli* (Ec), *Salmonelly typhimurium* (St), *Synechococcus elongatus* (Se), *Nostoc* sp. PCC 7120 (Ns), *Shewanella oneidensis* (So), **Archaea**: *Pyrococcus horikoshii*(Ph), **Eukaryota**: *Homo sapiens* (Hs), *Rattus norvegicus* (Rn), *Oryza sativa* (Os) Residues are colors according to the Taylor color scheme. The consensus line indicates the degree of conservation across all sequences. Sequence positions corresponding to the *E. coli* CutA numbering are shown above the alignment (emphasized). Sequences were retrieved from UniProt and aligned using ClustalW in MEGA X.

1.3 CutA Structure and Binding Pocket

In the CutA trimer, each subunit adopts a ferredoxin-like fold[12]. This fold follows a β-α-β-β-α-β motif, forming a central β-sheet flanked by α-helices, which is a common feature in ferredoxins (Figure 1.4A and D). Ferredoxins are iron-sulfur proteins[40] essential for electron transfer and metabolic reactions, including photosynthesis[41] and nitrogen fixation[42]. Variations of the ferredoxin fold can be found in certain metallochaperones, such as Atx1, a cytosolic copper chaperone that maintains copper homeostasis and protects cells from copper-catalyzed oxidative damage[43,44] as well as in the soluble domains of metal-transporting ATPases (like the copper-exporting P-type ATPase, CopA)[12,22,44]. Due to its structural versatility, the ferredoxin-like fold is highly conserved across diverse life forms, and is also characteristic of P_{II} and P_{II}-like proteins, suggesting an ancient evolutionary origin[45]. In CutA, this fold follows the sequence β1α1β2β3α2β4 and includes an additional β-strand (β5), a C-terminal helix (α3), and an extended β-hairpin between β2 and β3, which contribute to its stability and function[12].

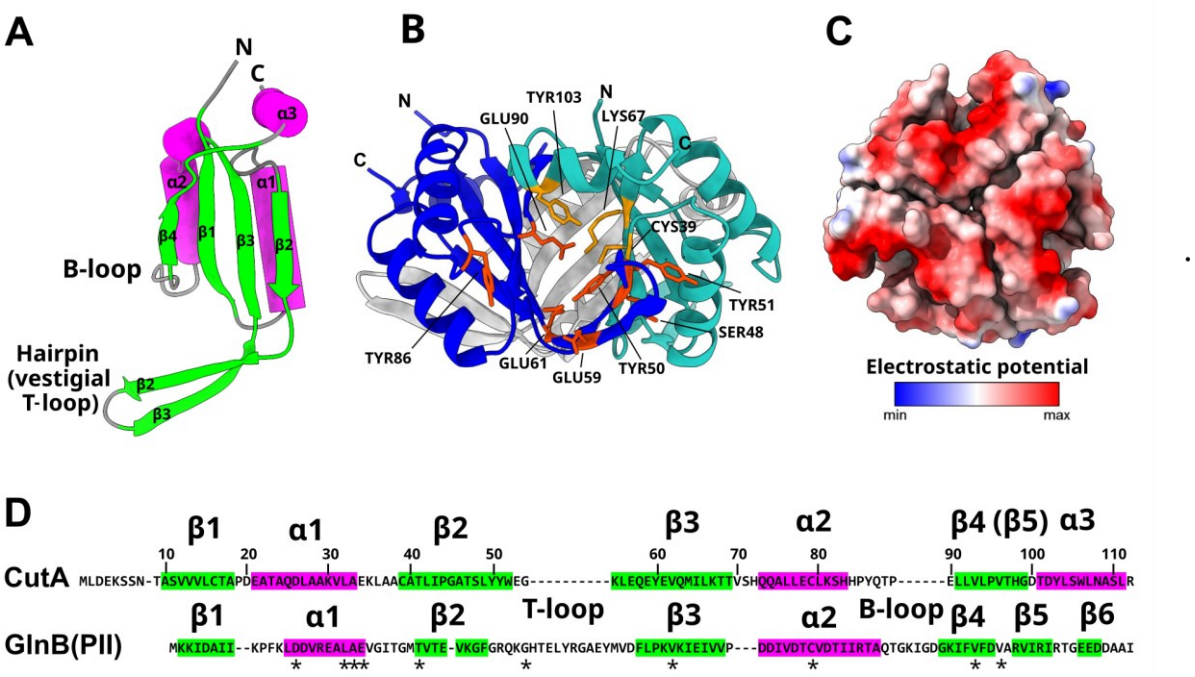

Figure 1.4: Overview of *E. coli* CutA binding pockets.
(A) Secondary structures of *E. coli* CutA showing the hairpin structure and B-loop. β-strands are shown in green and α-helices in pink. **(B)** Side view of *E. coli* CutA showing the putative binding pocket and conserved residues. Residues on one monomer are shown in red (monomer in blue) and residues on the other monomer are shown in yellow (monomer in turquoise). Panel B of this figure appears also in modified form in Wagner et al., 2025[46] **(C)** Electrostatic potential of *E. coli* CutA protein was calculated and visualized in ChimeraX using Coulombic surface coloring. The protein surface is shown with negatively charged regions in blue, positively charged regions in red, and neutral regions in white. **(D)** Structure-based sequence alignment of *E. coli* CutA and GlnB, adapted from Arnesano et al. (2003). Secondary structure elements are indicated above the alignment, with β-strands in green and α-helices in pink, matching the color coding in panel **(A).** Conserved residues are marked with asterisks (*). Amino acid numbering corresponds to the CutA sequence.

CutA trimers contain three intersubunit pockets at the subunit interfaces, reminiscent of the nucleotide-binding clefts found in P_{II} proteins[12,13]. Each pocket is primarily formed by the β2-β3 hairpin of one subunit and the C-terminal α3 helix of an adjacent subunit, with additional contributions from the vestigial T-loop (connecting β2 and β3), the B-loop (linking α2 and β4), and the β1-α1 linker[12,13]. Electrostatic surface analysis of multiple CutA proteins have revealed that these pockets are highly polar and strongly negatively charged[12,13,47] (also in Figure 1.4B and C). Key residues contributing to this environment include Tyr-50, Glu-59, Glu-61, Tyr-86, Glu-90, and Tyr-103 (numbering according to *E. coli*), which collectively define a surface-accessible opening leading to the trimer's internal aqueous cavity. The conserved residues Cys-39 and Lys-67 also are positioned in this opening, while Tyr-50, Tyr-51 and Ser-48 are located on the outer surface (Figure 1.4B)[13].

Structure-based sequence alignment of *E. coli* CutA with GlnB (Figure 1.4D) shows that both share a ferredoxin-like fold (Figure 1.4A and D), but differ in sequence, also in those residues forming the CutA binding pockets, suggesting a functional divergence despite structural similarity. A distinctive feature of CutA is the presence of Cys-39 (absent in P_{II}), which is located near Tyr-50 and Tyr-51 from an adjacent monomer and Tyr-103 from the same monomer, placing it in a position suitable for potential interactions at the trimer interface[12]. The presence of conserved cysteine and different conserved tyrosine residues in close spatial proximity within CutA suggests the potential formation of a covalent Cys-Tyr thioether crosslink, similar to that characterized in the copper-dependent enzyme galactose oxidase, where copper facilitates electron transfer through this crosslink[48].

In addition, Lys-67 lies only ~3.8 Å from Cys-39 (measured in ChimeraX), which places these residues in a position suitable for forming a redox-sensitive nitrogen-oxygen-sulfur (N-O-S) bridge, a reversible covalent modification recently identified between cysteine and lysine residues under oxidative conditions[49]. In this mechanism, the cysteine thiol is first oxidized to sulfenic acid, which then reacts with the lysine amino group to form the N-O-S linkage. The oxygen atom is derived from molecular oxygen or reactive oxygen species (ROS), making the modification reversible. This modification could also act as a redox switch to regulate CutAs function under oxidative stress.

The high conservation of residues within and surrounding the CutA intersubunit pockets underscores their likely functional importance. Supporting this, X-ray structures have captured buffer-derived ligands (Bis-Tris, MES, HEPES)[13,47] bound within these clefts, indicating the potential to accommodate small-molecule ligands or cofactors[13]. Furthermore,

structural studies indicate that CutA1 proteins can bind metal ions at positions analogous to ATP-binding sites in P_{II} proteins, implicating a role in metal ion homeostasis[12,13].

1.4 P_{II}-like Proteins and Their Function

P_{II} proteins were first characterized in 1969 as regulatory components of the glutamine synthase system. The designation "P_{II}" originated from their appearance as the second protein peak fraction eluting during gel filtration chromatography[50,51]. Subsequent studies established that the P_{II} family represents a widely distributed group of signal transduction proteins occurring in nearly all bacteria, as well as in archaea and in the chloroplasts of algae and plants[25]. Within this superfamily, P_{II}-like proteins constitute a distinct subgroup. Although they share the conserved trimeric architecture and ferredoxin-like fold characteristic of canonical P_{II} proteins (see Figure 1.5**)**, P_{II}-like proteins exhibit low sequence similarity and lack the canonical PROSITE signature motifs (short, conserved sequence patterns used to identify protein families and predict function) typical of classical P_{II} proteins[24,52,53].

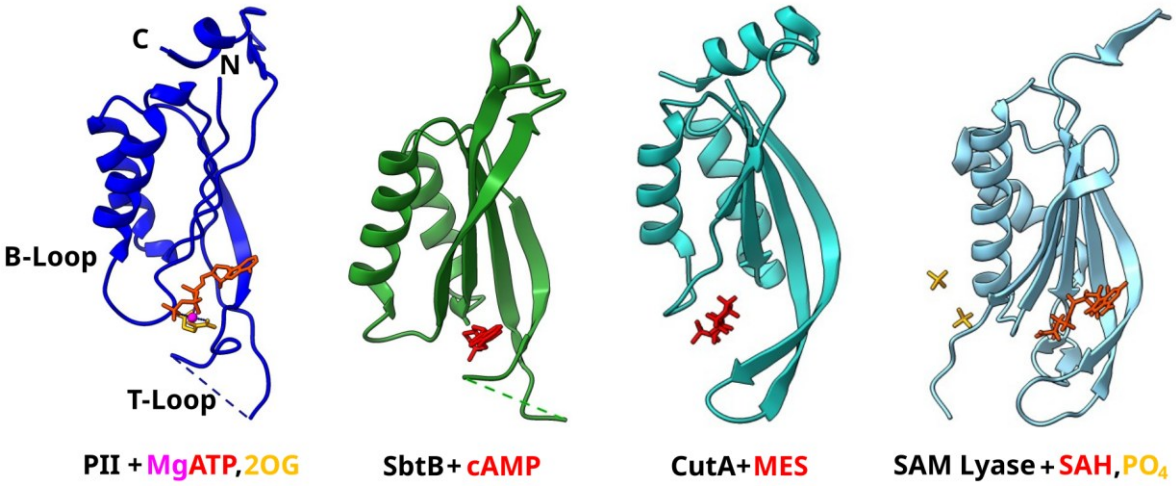

Figure 1.5: Crystal structures of proteins from the P_{II}-like superfamily bound to different ligands. From left to right: *S. elongatus* P_{II} bound to MgATP and 2-oxoglutarate (2OG, Protein Data Base (PDB): 2XUL); *Synechocystis* sp. PCC 6803 SbtB bound to cAMP (PDB: 5O3Q); *Nostoc* sp. 7120 CutA bound to MES (2-(N-morpholino)ethanesulfonic acid, PDB: 6T7E); and a phage SAM lyase bound to SAH (S-adenosyl-L-homocysteine, PDB: 6ZMG). The B-loop and T-loop are indicated in the P_{II} structure (left) to provide orientation for comparison with the related folds.

While P_{II} proteins primarily bind adenine nucleotides and serve as key metabolic regulators, P_{II}-like proteins exhibit distinct functional roles. Nevertheless, many P_{II}-like proteins also interact with nucleotides and contribute to important regulatory processes. The high sequence conservation and relatively short length (~112 amino acids) of P_{II} proteins renders their

phylogenetic reconstruction particularly challenging[24]. Nevertheless, protein structure determination revealed that many of these P_{II}-paralogues maintain strong structural homology to canonical P_{II} proteins despite limited amino acid sequence conservation[26,30].

These structural homologues often occur in unique genetic contexts, often associated with metal transporter operons[24], suggesting specialized regulatory functions distinct from the classical roles in carbon and nitrogen sensing roles. Importantly, the hallmark flexible surface-exposed loops of P_{II} proteins are largely conserved in P_{II}-like variants. This conservation allows for example binding of adenine nucleotides (ATP, ADP, AMP) or second messengers (cAMP, c-di-AMP) and permits regulation through multiple posttranslational modifications, enabling to sense cellular energy, carbon, nitrogen and redox states[26,54]. An overview of different P_{II}-like proteins and their known ligands is shown in Table 2.

A prominent example is the cyanobacterial P_{II}-like protein SbtB, which regulates carbon metabolism through interactions with bicarbonate transporters and glycogen-branching enzymes[26,54]. SbtB controls carbon concentrating mechanisms through a redox-sensitive C-terminal loop-structure that can form a disulfide bond in response to the cell`s diurnal redox state, which depends on photosynthetic electron transport[55]. The architectural conservation, combined with functional diversification, reflects the evolutionary plasticity of the P_{II} superfamily[54]. Recent studies have highlighted P_{II}-like proteins as versatile metabolic sensors that contribute to complex regulatory networks by integrating multiple signals, thus expanding the cellular roles of P_{II}-related proteins across prokaryotic and eukaryotic organisms[30,54].

Table 1.2: Overview of different P_{II} like proteins, their ligands and function (information compiled from Forchhammer (2022)[26], unless stated otherwise).

Protein Name	Ligands	Function
P_{II} (GlnB/GlnK)	2-oxoglutarate, Mg^{2+}-ATP, ADP	• Global regulator of nitrogen metabolism • Interacts with: - **NAGK** (arginine synthesis)[26,56] - **GlnE/NtrB-NtrC** (glutamine synthetase regulation)[25,26,57,58] - **AmtB** (ammonium channel)[26,59] - **ACC** (fatty acid biosynthesis)[26,60]
CP_{II} (Carboxylation P_{II}-like protein)	ADP, AMP, bicarbonate	• Senses bicarbonate availability • Regulates carbon metabolism and acetyl-CoA carboxylase (ACC)
SbtB	ATP, ADP, AMP, cAMP, c-di-AMP	• Regulates SbtA bicarbonate transporter and glycogen branching enzyme • GlgB involved in carbon storage and stress adaptation • Regulates SbtA bicarbonate transporter and glycogen branching enzyme GlgB; senses energy and redox state via a redox-sensitive R-loop
PstA	c-di-AMP	• Putative c-di-AMP receptor • Involved in osmoregulation and potassium transport in bacteria
DarA	c-di-AMP	• Predicted c-di-AMP binding protein
SAMase (phage protein)		• Phage-encoded SAM hydrolase • Depletes host S-adenosylmethionine (SAM) to induce lysis

1.5 CutA in Mammals

CutA proteins are evolutionarily conserved across all domains of life, including eukaryotes such as mammals[13]. In humans, *cutA* is expressed in various tissues, also prominently in the brain, where it has been proposed to contribute to the processing of the β-amyloid precursor protein (APP).The accumulation of β-amyloid (Aβ) peptides, which arise from sequential cleavage of APP by β- and γ-secretases, is a hallmark of Alzheimer`s disease, and the generation of Aβ is influenced by the cellular distribution of these enzymes[10]. In this context, CutA has been reported to regulate the β-cleavage of APP by interacting with the β-site APP cleaving enzyme 1 (BACE1)[10,61], thereby connecting it to pathways associated with neurodegenerative processes. In addition, CutA has been associated with the anchoring of acetylcholinesterase (AChE) in neuronal cell membranes. Although a direct interaction between CutA1 and AChE has not been observed, the *cutA1* gene is broadly expressed across various brain regions, where its expression pattern closely mirrors that of AChE[23]. Furthermore, CutA1 co-purifies with AChE from the human caudate nucleus[62], a region of the basal ganglia, indicating a potential role in supporting the structural maturation, assembly, trafficking, and membrane targeting of AChE[9,63].

1.6 CutA and Copper

1.6.1 Copper in Cells: A Double-Edged Sword

Copper has a distinctive geochemical history. Due to its soft nature and strong affinity for sulfur ligands, copper became sequestered in sulfide precipitates in primordial environments[64,65]. This limited bioavailability prevented ancient microorganisms from using copper as a cofactor. By contrast, copper in present-day organisms is predominantly associated with catalytic metal centers in enzymes that emerged after atmospheric oxygen became abundant, approximately 2 billion years ago[66].

Today, copper is a widely distributed environmental element, primarily found in sulfide ores such as chalcopyrite ($CuFeS_2$) and chalcocite (Cu_2S). Under oxidative weathering, these primary sulfide phases undergo redox transformation and hydrolysis, yielding more bioavailable secondary copper species in the form of soluble cuprous (Cu^+) and cupric (Cu^{2+}) salts, including carbonates (e.g., malachite) and chlorides (e.g., atacamite)[8].

The biological utility of copper stems from its ability to switch reversibly between the monovalent (Cu^+) and divalent (Cu^{2+}) states. Copper(II) (Cu^{2+}) acts as an oxidizing agent, undergoing one-electron reduction to form Copper(I) (Cu^+), while Cu^+ can be re-oxidized to Cu^{2+}. This reversible redox cycling between the monovalent and divalent states of copper is fundamental to its function in biological electron transfer processes[67,68].

Yet, copper is a double-edged sword in cellular systems. The same redox activity that makes it essential can also drive toxicity. Copper catalyzes Fenton-like reactions ($Cu^+ + H_2O_2 \rightarrow Cu^{2+} + OH^- + {}^{\bullet}OH$), which result in the formation of highly reactive hydroxyl radicals (${}^{\bullet}OH$). These ROS induce lipid peroxidation[69], compromising membrane integrity, and oxidize proteins, leading to loss of function and aggregation[70], or damage other cellular components like nucleic acids[67]. In addition, Cu^+ can reduce O_2 to superoxide (O_2^-), which subsequently dismutates to hydrogen peroxide (H_2O_2), further fueling Fenton-like reactions and amplifying oxidative stress[67,71].

Copper toxicity is not limited to ROS generation. Due to its strong affinity for metalloproteins, particularly those containing iron-sulfur (Fe-S) clusters, copper can displace iron in these clusters, causing mis-metalation, cluster disassembly[72], and release of free iron, which in turn propagates further oxidative damage through Fenton chemistry. Thus, copper overload destabilizes core cellular processes at multiple levels.

Despite their damaging potential, ROS are not solely harmful. At controlled concentrations and defined locations, they act as essential signaling molecules that regulate diverse physiological processes, including immune responses, cell proliferation or stress adaptation[73,74]. Hence, the biological impact of copper-derived ROS depends critically on their localization, concentration and duration of exposure.

To manage these risks, organisms rely on tightly regulated copper homeostasis. Both prokaryotic and eukaryotic cells employ sophisticated mechanisms to buffer, sequester, and safely distribute copper ions. Low-molecular-weight ligands such as glutathione, as well as copper chaperones (e.g. the *cop* operon or Atx1), chelate Cu(I) and Cu(II), limiting uncontrolled redox cycling while ensuring biological availability[12,75,76]. In *E. coli*, copper resistance genes may also be plasmid encoded. For example, the plasmid-borne *pco* operon enhances copper efflux in an energy-dependent manner, though the mechanisms remain incompletely understood[2,8].

While copper dysregulation can be lethal to bacteria, a property exploited in hospital disinfectants to prevent biofilm formation[77,78], it also plays a complex role in mammals. It is used as a growth promoter in pig farming[79] but can also cause severe damage, leading to fatal neurological disorders. Examples include Menkes disease (caused by copper deficiency)[80], Wilson disease (caused by copper accumulation)[81], and its potential involvement in Alzheimer's pathology. Current research focuses on biologically essential metals like iron, zinc, and copper, as their regulation appears to be altered in Alzheimer's disease. Among these, copper has garnered the most interest due to its putative interactions with the amyloid precursor protein (APP) and amyloid β (Aβ) peptides, both of which play key roles in disease progression[82–84].

1.6.2 CutA and Copper Binding

CutA proteins adopt a ferredoxin like fold similar to copper chaperones like Atx1, which initially suggested a role in copper tolerance[12]. However, unlike canonical metallochaperones, CutA lacks the canonical CXXC motif required for Cu(I) coordination. Instead, there are three cysteine residues in *E. coli* CutA per monomer (Cys16, Cys39, and Cys79), which are neither sequentially nor spatially positioned to support classical metal binding, either within a single subunit or across the trimer. This suggests that CutA1 engages in copper homeostasis via a mechanism distinct from known metallochaperones[12,22].

Extended X-ray Absorption Fine Structure (EXAFS) spectroscopy studies revealed that *E. coli* CutA can bind Cu(II) in vitro through His_2Cys coordination at a type II site that is accessible to solvent molecules[12]. The absence of metal specificity in this coordination environment led Arnesano et. al. (2003) to propose that CutA may act upstream of metallochaperones, potentially in cooperation with disulfide oxidoreductase such as CutA2/DsbD, by modulating the redox state of thiol groups in CXXC motifs present in Cu(I)-ATPases and Zn(II)/Cd(II)-ATPases[12,22].

In archaeal CutA homologs, similar but distinct copper-binding behaviors have been observed. In *Pyrococcus horikoshii* CutA (PhoCutA), the crystal structure of a Cu(II)-bound complex revealed that the metal ion is coordinated by Asp-48 residues located at the trimer-trimer interface[47,85]. Binding of various heavy metals in vitro induced reversible protein-protein aggregation, which could be completely dissolved by chelation with EDTA or dialysis against metal-free buffer. Substitution of Asp-48 with alanine diminished this aggregation, demonstrating that Asp-48 plays a central role in metal-dependent aggregation[85]. Interestingly, CutA proteins from *E. coli*, *S. elongatus*, and the filamentous cyanobacterium *Nostoc* 7120 do not harbor the Asp-48 residue identified as a Cu^{2+} ligand in PhoCutA. However, amino acid sequence alignments (Figure 1.3) show that at the equivalent position, other CutA proteins (e.g. *E. coli, S. elongatus*, and *Nostoc* 7120, used in this work) carry a chemically similar glutamic acid (E), and in some other species an aspartic acid (D), suggesting a degree of conservation of an acidic side chain at this site. A conserved acidic residue at this position may underline metal-binding in CutA proteins.

In plants, the *Arabidopsis thaliana* CutA homolog forms a tetramer and has been shown (in recombinant form) to selectively bind Cu(II) ions, supporting a role for CutA in copper homeostasis across different domains of life[86].

However, attempts to crystallize *E. coli* CutA with Cu(II) salts, including copper sulfate ($CuSO_4$), have so far been unsuccessful (Arnesano et. al., 2003; Selim et al., 2020 also in this study) with precipitation of the protein likely preventing crystal formation.

1.7 The Bacterial Strains Used for This Study

The role of CutA was mainly investigated in two distinct bacterial taxa, *S. elongatus* and *E. coli*, to identify potential conserved functions of the CutA protein. Both taxa were subjected to various stress conditions in order to elucidate the functional roles of CutA across different environmental contexts.

1.7.1 *Synechococcus elongatus* PCC 7942

Synechococcus elongatus PCC 7942 (*S. elongatus*), also historically referred to as *Anacystis nidulans*, is a well-established photosynthetic model organism with a small, streamlined genome with a size of approximately 2.7 Mb[87]. Members of the genus *Synechococcus* form a diverse, polyphyletic group of unicellular cyanobacteria inhabiting a wide range of ecological niches from marine, freshwater, and brackish water habitats[88] to terrestrial environments, where they can be found in microbial hot-spring mats[89] or biofilms[90] on rocks[91] or humid stone walls[92]. *Synechococcus* species, along with *Prochlorococcus*, are among the most abundant members of the picophytoplankton and are essential contributors to global marine primary production and carbon fixation, accounting for at least 25% of global primary productivity[93,94]. *S. elongatus* was first isolated from the San Francisco Bay area and deposited in the Pasteur Culture Collection (PCC) in 1979, where it became the 42nd strain in the collection[95]. Previous studies already used *S. elongatus* strains for CutA research[13,23].

1.7.2 *Escherichia coli* K-12 BW25113

Escherichia coli (hereafter referred to as *E. coli*) is a facultative anaerobic, Gram-negative gammaproteobacterium that paradoxically functions both as a predominant commensal organism in the vertebrate gastrointestinal tract and as a versatile pathogen causing a wide range of intestinal and extraintestinal infections[96]. This dual role is reflected in its biological diversity and importance in health and disease. *E. coli* was chosen for this study due to its well-characterized genetics, ease of laboratory manipulation, and the presence of conserved CutA protein homologs. Additionally, previous studies on CutA were carried out using *E. coli*, providing a foundation for further investigation.

2 Motivation and Research Objectives

The motivation of this thesis is to elucidate the cellular function of the highly conserved protein CutA, which is present across all domains of life, from cyanobacteria to eukaryotes, including humans. CutA was originally identified in *Escherichia coli* within a gene locus associated with Cu^{2+} tolerance. However, this connection has been questioned in recent studies. Its deep evolutionary conservation strongly suggests an essential, possibly primordial, regulatory function that has been maintained throughout evolution. Understanding such universally conserved proteins is central to deciphering the core molecular principles that sustain life and enable diverse organisms to sense and adapt to environmental change.

Although CutA shares structural similarities with P_{II}-signaling proteins, it lacks the flexible T-loop structure required for canonical P_{II}-mediated interactions. This structural divergence, together with the presence of a conserved binding pocket, indicates that CutA may be involved in distinct regulatory mechanisms, potentially involving small-molecule binding.

To address this knowledge gap, CutA is examined in two phylogenetically distant organisms: *E. coli,* a facultative anaerobe central to microbiome-associated metabolism, and *Synechococcus elongatus* PCC 7942, a photosynthetic cyanobacterium with different metabolic and environmental dynamics. This comparative approach enables assessment of whether CutA fulfills analogous functions across diverse bacteria. Insights into CutA biology may extend beyond bacterial systems and ultimately contribute to a broader understanding of conserved mechanisms of metabolic regulation across lifeforms.

The experimental strategy includes phenotypic stress assays of wild-type and knockout strains, mass spectrometry-based pulldown analyses to identify interaction partners, and ligand-binding studies to assess the capacity of CutA to bind small effector molecules. These methods are complemented by metabolomic profiling of the strains.

Research Objectives

The overarching aim of this thesis is to better understand the physiological function of CutA. Specifically, this work seeks to:

1. Characterize the phenotypic and metabolic consequences of CutA deletion in *E. coli* and *S. elongatus* under standard and different stress conditions.
2. Identify CutA-associated protein partners using mass spectrometry–based pulldown assays
3. Determine whether CutA binds small effector molecules via native mass spectrometry and ligand-binding assays.
4. Investigate metabolic alterations in the absence of CutA to gain insights into cellular functions that may be connected to CutA.

3 CutA and Cell Envelope Stress

CutA proteins are known to be very heat stable due to a compact, symmetric structure and a highly hydrophobic core. The CutA protein from the hyperthermophile *Pyrococcus horikoshii* exhibits exceptional heat stability, with a denaturation temperature of approximately 150 °C at pH 7.0[97], one of the highest melting temperatures known for proteins[98]. Table 3.1 gives an overview of different CutAs and their melting temperatures.

Table 3.1: Melting temperatures of different CutAs.

Species	Melting temperature (°C)	Literature
Pyrococcus horikoshii **(hyperthermophile)**	148.5	Tanaka et al., 2006[99]
Thermus thermophilus **(extreme thermophile)**	113 112.8	Tanaka et al., 2006[99] Sawano et al., 2008[100]
Oryza sativa	97.3	Sawano et al., 2008[100]
Homo sapiens	96.4	Bagautdinov et al., 2015[101]
E. coli **K-12 W3110**	89.9	Matsuura et al., 2010[102]
Shewanella **sp. SIB1**	~89.85	Sato et. al., 2011[103]

All melting points are above the usual growth temperatures of the organisms. In the present study, melting temperatures for *Nostoc* sp. PCC 7120, *S. elongatus* and *E. coli* (Figure 3.1) were determined using Nano Differential Scanning Fluorimetry (NanoDSF).

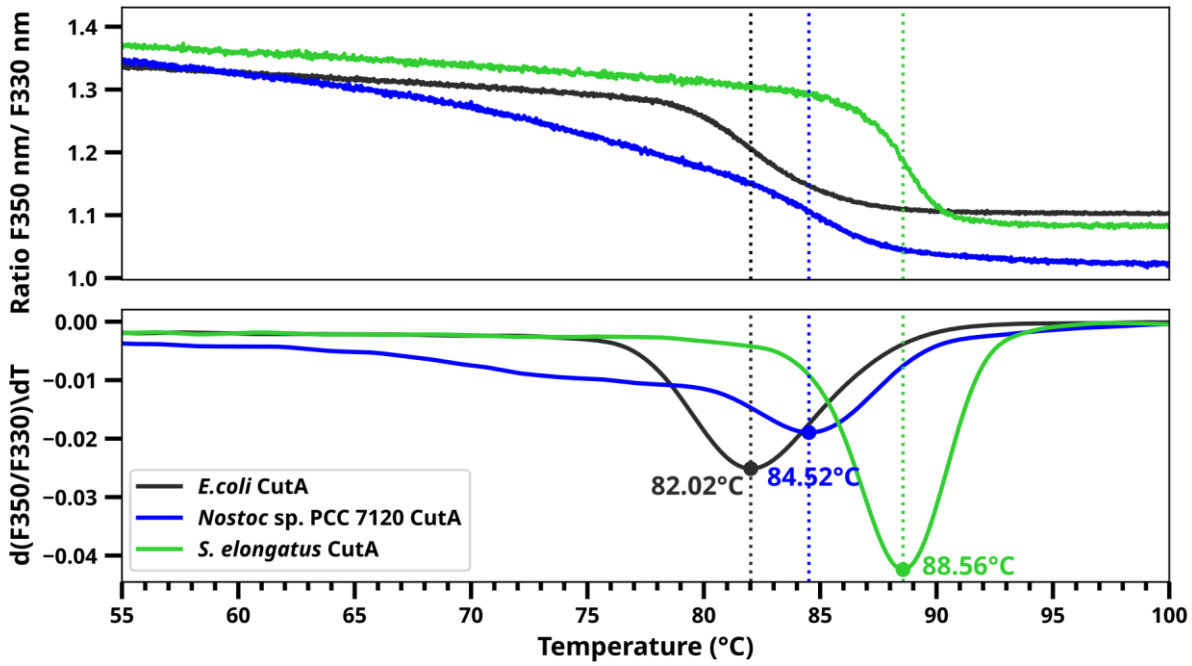

Figure 3.1: Melting of CutA proteins.
Melting of CutA from *E. coli* (black), *S. elongatus* (green), and *Nostoc* sp. PCC 7120 (blue) performed using NanoDSF with a temperature slope of 0.5 °C/min. The fluorescence emission ratio (F350/F330) is shown as a function of temperature (top), and the first derivative of the ratio (bottom) is used to determine the melting temperature (Tm). Tm values were 82.0 °C for *E. coli* CutA, 84.3 °C for *Nostoc* CutA, and 88.6°C for S. *elongatus* CutA (n=1).

The melting temperatures of CutA proteins from *S. elongatus*, *Nostoc* sp. PCC 7120, and *E. coli* were measured using nano-differential scanning fluorimetry (NanoDSF), which monitors changes in the fluorescence of intrinsic tryptophan residues to assess protein unfolding. Proteins were heated in 0.5 °C increments to determine the melting temperature (Tm). The fluorescence ratio at 350 nm to 330 nm (F350/F330) was plotted against a thermal denaturant concentration gradient. The Tm was identified at the inflection point of the plot and further confirmed by the minimal turning point in the first derivative analysis. CutA proteins from *E. coli, S. elongatus*, and *Nostoc* 7120 exhibited main melting points above 80°C (see Figure 3.1), far beyond the normal growth temperatures of the organisms (Tm *S. elongatus:* 88.56 °C, *Nostoc* 7120: 84.52 °C, *E. coli:* 82.02 °C). Literature reports for *E. coli* CutA include a melting temperature of 89.9 °C (pH9, Matsuura et al.[102]). The slight variation likely results from differences in experimental methods, strain, buffers, and pH.

The unusually high melting temperatures of CutA indicate a potential involvement in cellular stress adaptation rather than in standard physiological processes. Proteins with elevated thermal stability can maintain their structural integrity and functional activity under

conditions in which less stable proteins denature. Thus, they may contribute to cellular stress responses. To examine this hypothesis, *E. coli* WT and *ΔcutA::kan* (Keio collection) were exposed to different growth conditions alongside a seamless *cutA* deletion mutant generated in this study (described in methods part 7.5). Similar experiments were performed using *S. elongatus* WT and the *S. elongatus ΔcutA::kan,* described characterized in Selim et al. (2021)[13].

3.1 The *ΔcutA* mutant exhibits no significant growth defects under standard growth conditions

To determine whether *cutA* deletion influences bacterial growth under standard conditions, the growth of *E. coli* and *S. elongatus* WT and *ΔcutA* strains was monitored over time. The results are summarized in Figure 3.2.

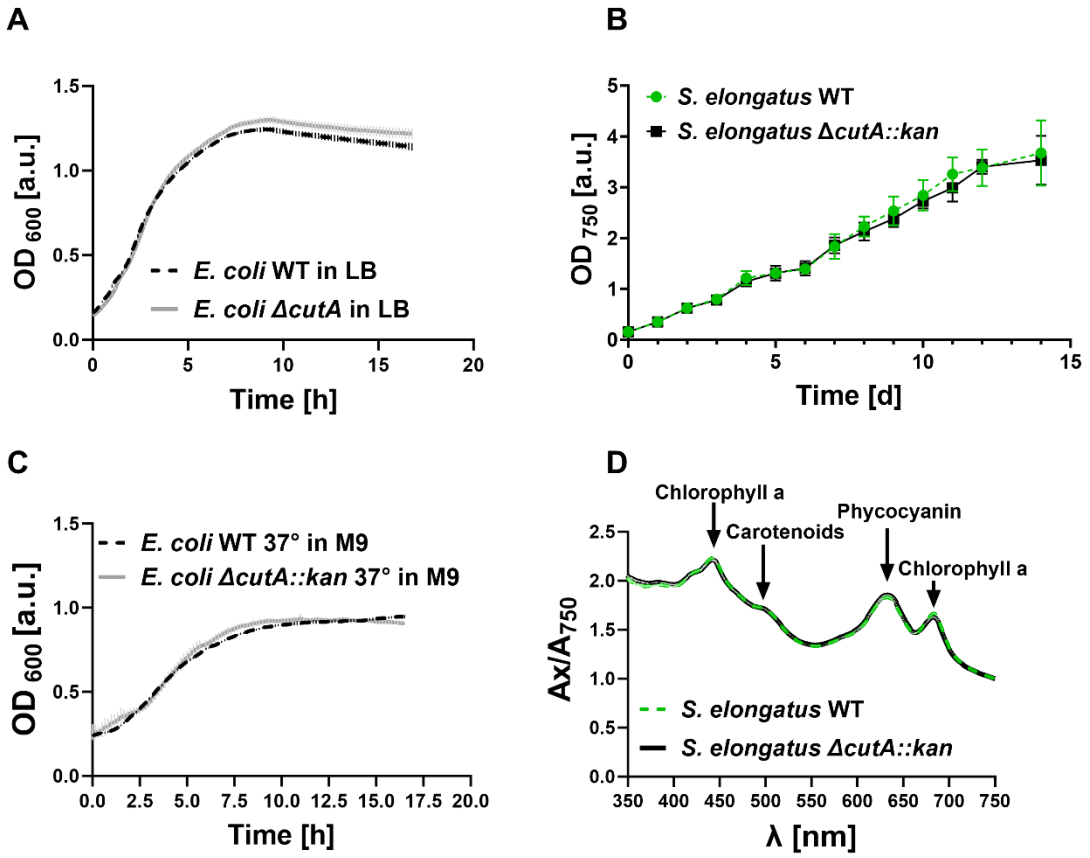

Figure 3.2: Growth and spectral analysis of *E. coli* and *S. elongatus* WT and *ΔcutA* strains under standard conditions.
(A) Growth of *E. coli* WT and *ΔcutA* in LB medium at 37 °C, inoculated at an initial OD_{600} of 0.2. **(B)** Growth of *S. elongatus* WT and *ΔcutA::kan* in BG11 medium under continuous light (30-60 µmol photons m^{-2} s^{-1}) at 28 °C, inoculated at an initial OD_{750} of 0.15. Panel B of this figure appears also in modified form in the SI of Wagner et al., 2025[46] **(C)** Whole-cell absorption spectra of *S. elongatus* WT and *ΔcutA* measured at OD_{750} = 0.7.

Under standard growth conditions (37 °C for *E. coli*, 28 °C for *S. elongatus*), no differences in growth behavior were observed between WT and *ΔcutA* strains. This was consistent across both rich (LB) and minimal (M9) media for *E. coli*, and in BG11 medium for *S. elongatus*, as determined by monitoring of cell growth via optical density (OD) (OD_{600} for *E. coli*, OD_{750} for *Synechococcus*). OD_{750} was chosen for *S. elongatus* to specifically monitor cell density while minimizing interference from photosynthetic pigments. Likewise, whole-cell absorbance spectra which reflect the relative abundance of light-absorbing pigments such as chlorophylls, carotenoids, and phycobiliproteins, showed no differences between *S. elongatus* WT and *ΔcutA* strains.

Therefore, additional experiments under stress conditions were performed to further elucidate the potential role of CutA in response to environmental challenges.

3.2 Impaired Recovery of *S. elongatus ΔcutA::kan* under Heat Stress Conditions

Firstly, *S. elongatus* was exposed to different high temperatures for varying times, and the recovery of WT and *ΔcutA* mutant was observed on solid and in liquid media (Figure 3.3). As *S. elongatus* is a mesophilic bacterium, heat stress was considered to occur at temperatures above 50 °C.

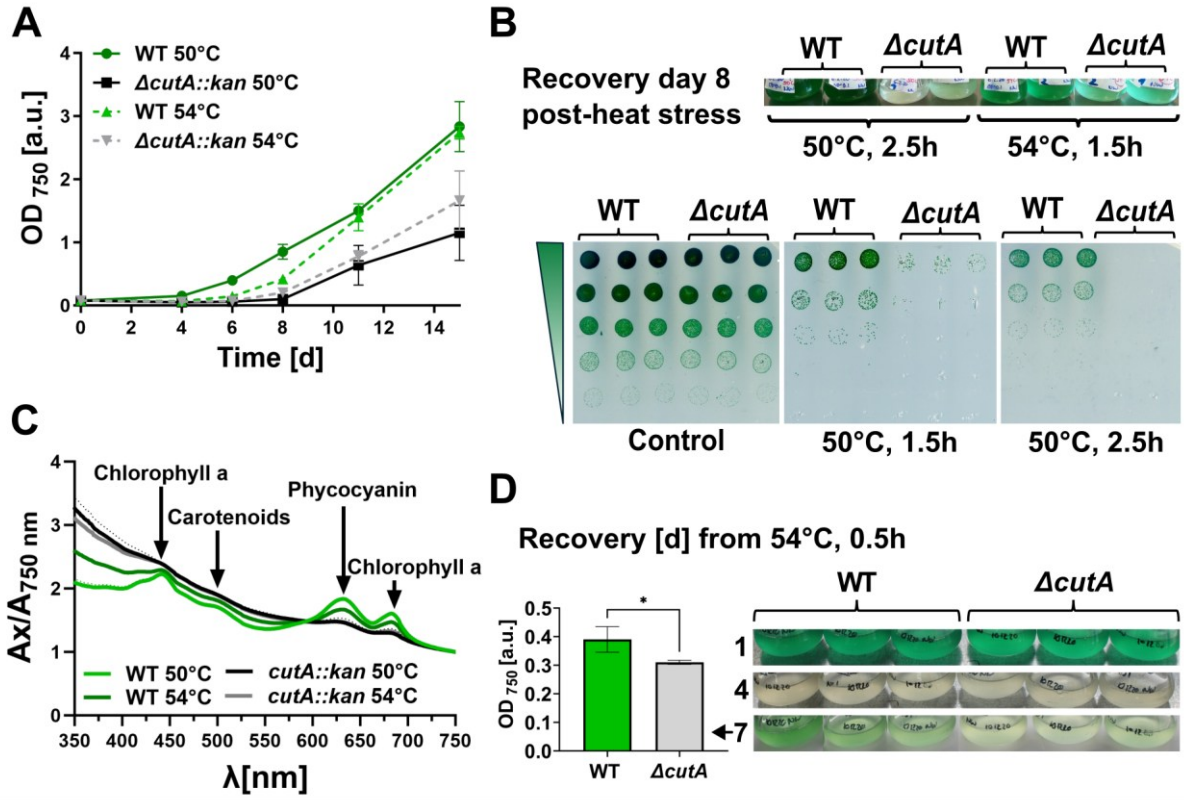

Figure 3.3: Recovery of *S. elongatus ΔcutA::kan* following heat stress.
(A) Recovery growth curves of *S. elongatus* WT and *ΔcutA::kan* following heat shock at 50 °C for 2.5 h or 54 °C for 1.5 h. Cultures (in duplicates) were inoculated at OD_{750} = 0.1 and monitored for 15 days in BG11 medium under continuous light (30-60 µmol photons $m^{-2}s^{-1}$), performed in duplicates. **(B)** Visual comparison of recovery after 8 days post-treatment. Top: culture flasks show reduced pigmentation in the mutant (duplicates from (A)). Bottom: drop dilution assays (1:10 series from OD_{750} = 1) plated on BG11 agar immediately after treatment, in triplicates (different experiment). Untreated cultures served as a control. Plates were incubated at 28°C under continuous light for 8 days. Panel B of this figure appears also in modified form in Wagner et al., 2025[46]. **(C)** Whole-cell absorption spectra (350-750 nm) recorded on day 6 post-treatment (50 °C or 54 °C for 2.5h) and normalized to OD_{750} = 1 (duplicates of A). **(D)** Recovery of liquid cultures following heat stress (54 °C for 30 min). Left: OD_{750} after 7 days (WT=0.39, *ΔcutA::kan*=0.31). Right: Time-course photographs of cultures over 7 days, showing delayed pigment recovery in the mutant.

Heat stress assays demonstrated decreased recovery of the *ΔcutA::kan* mutant strain compared to the WT. As shown in Figure 3.3A, the *ΔcutA::kan* mutant exhibited reduced regrowth (measured via OD_{750}) following heat stress (2.5 h at 50 °C or 1.5 h at 54 °C). This impaired

recovery was further confirmed by the culture appearance on day 8 post-treatment (Figure 3.3B top and bottom). Both strains initially exhibited a pronounced loss of pigmentation, likely attributable to degradation of chlorophyll and phycobiliproteins, as indicated by whole-cell absorbance spectra recorded on day 6 (Figure 3.3C). Drop-dilution assays (Figure 3.3B bottom) revealed that WT cells retained viability up to a 10^{-2} dilution, whereas *ΔcutA::kan* cells showed only minimal recovery in undiluted or 10^{-1} samples after 50 °C treatment for 1.5 hours. Following 2.5 h of heat stress, no visible colony formation was observed for the mutant on solid medium. In liquid culture recovery assays (Figure 3.3 A, B and D), the WT consistently regained pigmentation and growth more effectively than the mutant. After 7 days, WT cultures exhibited higher OD_{750} values and a greener appearance compared to the mutant.

3.3 Impaired Recovery of *E. coli ΔcutA* Under Heat Stress Conditions

To determine whether the *E. coli ΔcutA* mutant was also affected by heat treatment, experiments were conducted at temperatures significantly above the normal growth temperature of 37 °C. Initial experiments were conducted using an *E. coli ΔcutA::kan* mutant from the Keio collection[104] (JW4097), which contains a kanamycin resistance cassette inserted into the *cutA* gene. For subsequent studies, to avoid potential downstream effects and enable testing of antibiotic susceptibilities, a seamless *ΔcutA* mutant was generated (described in 7.5), which lacks any antibiotic resistance. In the following, the Keio strain is referred to as *E. coli ΔcutA::kan*, and the seamless mutant as *E. coli ΔcutA*.

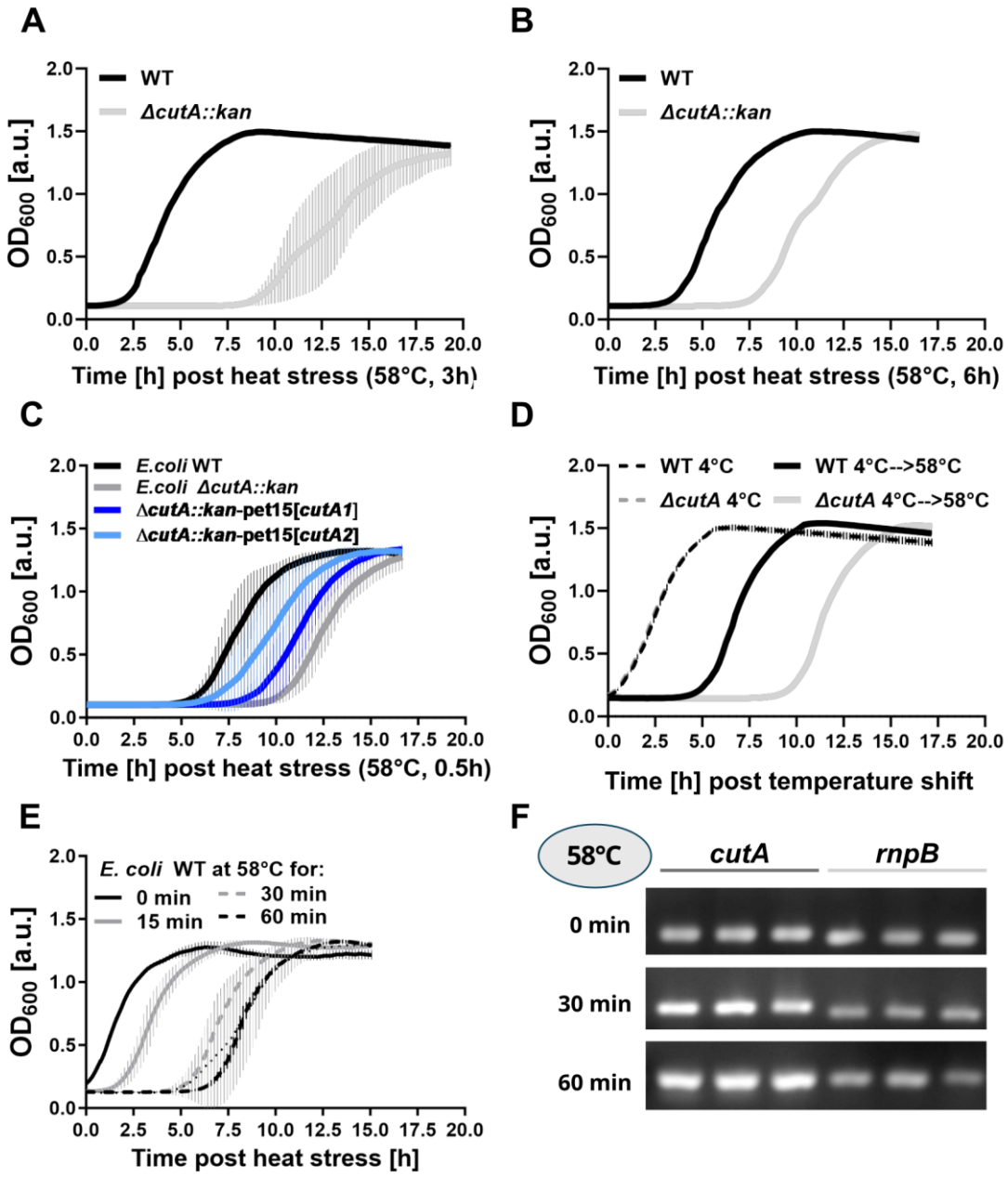

Figure 3.4: Recovery growth curves of *E. coli*.
(A) Recovery of *E. coli* wild type (WT, black) and *ΔcutA::kan* mutant (gray) strains after heat treatment. Cultures were normalized to OD_{600} = 0.6, heat-treated for 3 hours, diluted 1:10 in fresh LB medium, and growth was monitored using a Tecan plate reader. (**B)** Same as (A), but with a 6-hour heat treatment. Three biological replicates were used for each strain. **(C)** Growth of *E. coli* WT (black) and the *ΔcutA::kan* (gray) complemented with a plasmid carrying either CutA1 (*ΔcutA* pet15[CutA1), dark blue or Δ*cutA* pet15[CutA2], bright blue). Precultures were grown in 5 mL LB in glass tubes. Induction of pet15 strains with 0.1 mM IPTG for 1 hour was followed by dilution to OD_{600} = 0.2 in fresh LB without IPTG. Cultures were incubated in 2 mL Eppendorf tubes at 58 °C for 30 minutes on a heat block with shaking (600 rpm). Panel C of this figure appears also in modified form in the SI of Wagner et al., 2025[46]. **(D)** Cells were incubated overnight at 4°C, then diluted to OD_{600} = 0.2 in cooled LB and incubated at 58 °C for 15 minutes on a thermoshaker. Cultures were diluted 1:10 and growth was monitored using a plate reader. Triplicates were used for each condition, with measurements taken in technical duplicates on the plate reader. (**E)** Growth and retardation of *E. coli* WT in LB after 58°C heat treatment for 0, 15, 30 or 60-minutes (in triplicates) **(F)** Semi-quantitative RT-PCR was performed in biological triplicates to evaluate *cutA* expression levels under heat stress. Transcripts were amplified using gene-specific primers for *cutA* and the housekeeping gene *rnpB*. Approximately 50 ng/µL of cDNA was loaded onto a 1.5% agarose gel stained with Midori Green.

Figure 3.4 A-D shows that after different kinds of heat treatment, both the *E. coli ΔcutA::kan* mutant and the seamless *ΔcutA* strain exhibited prolonged lag phases (~5 hours) before resuming growth compared to the WT. This growth delay was alleviated by complementation with plasmids encoding *cutA1* or *cutA2* (Figure 3.4C). As shown in Figure 3.4D, long-term incubation at 4 °C alone had no noticeable effect on growth, however, a subsequent heat shock following cold incubation resulted in faster recovery of the WT compared to the *ΔcutA* mutant, again with a prolonged lag time of ~ 5 hours (Figure 3.4D).

To assess whether *cutA* expression is heat-responsive, semi-quantitative reverse transcriptase PCR (RT-PCR) was performed using *rnpB* as a constitutively expressed control gene. An upregulation of *cutA* under elevated temperatures would suggest a role of the protein in cellular stress adaptation. Wild-type and Δ*cutA* strains were exposed to 58 °C for 0, 30, and 60 minutes (Figure 3.4E). Growth retardation became apparent after 15-30 minutes of heat exposure, indicating that the treatment induced stress. Correspondingly, agarose gel analysis revealed increased *cutA* transcript levels in heat-treated samples compared to the control, suggesting that *cutA* expression is heat inducible.

3.4 Impaired Recovery of *E. coli ΔcutA* Under pH Stress Conditions

Since *E. coli* is a gastrointestinal bacterium, its response to other physiologically relevant stress conditions such as extreme acidity was also investigated. WT and Δ*cutA* strains were exposed to pH 2 for 1 hour, mimicking conditions in the empty stomach. This approach was inspired by previous findings of Small et al.[105], who demonstrated that *E. coli* K-12 and *Shigella flexneri* can survive at pH 2-3 in stationary phase, despite a growth limit near pH 4.5.

For the experiment, LB medium was adjusted to pH 2 using HCl, and cultures were incubated for 0.5 or 1 hour. After treatment, the cells were diluted into fresh medium, and recovery was monitored by measuring recovery growth curves.

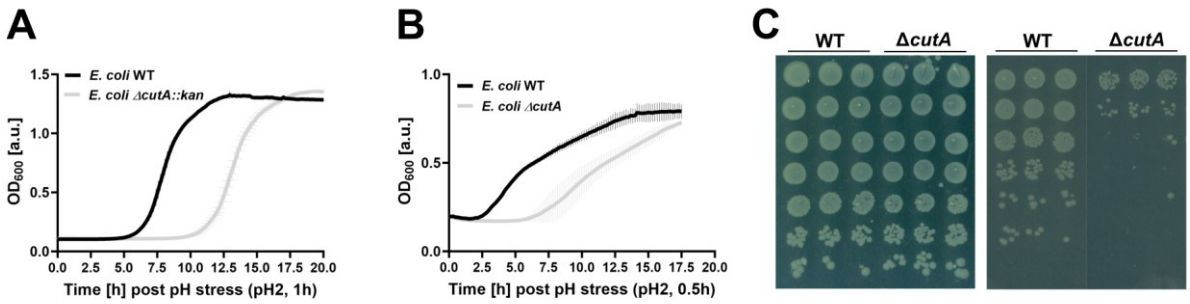

Figure 3.5: Recovery of *E. coli ΔcutA* strains after acid stress.
WT and *ΔcutA* strains were subjected to acid stress at pH 2, followed by recovery in fresh LB medium. **(A)** WT and *ΔcutA::kan* strains were exposed to pH 2 for 1 hour at an initial OD_{600} of 0.2. Recovery was monitored by OD_{600} measurements. Panel A of this figure appears also in modified form in the SI of Wagner et al., 2025[46]. **(B)** WT and seamless *ΔcutA* strains were exposed to pH 2 for 0.5 hours at an initial OD_{600} of 0.6. Recovery was assessed through OD_{600} measurements and via **(C)** drop dilution assays after treatment. For drop dilution assays, cultures were diluted 1:10 after treatment and dropped on LB agar plates. All experiments were performed in biological triplicates.

Similar to the heat stress experiments, both *E. coli* Δ*cutA*::*kan* (Figure 3.5A) and the seamless *ΔcutA* strain (Figure 3.5 B) exhibited prolonged lag phases (~5 hours) compared to the WT when exposed to acid stress. Recovery was monitored via growth curves and, for the seamless mutant, additionally by drop plate assays (Figure 3.5 C). In this assay, the WT formed colonies across all tested dilutions (10^0 to 10^{-5}), whereas the Δ*cutA* strain only grew up to the 10^{-2} dilution. The response of *S. elongatus* WT and Δ*cutA*::kan to pH stress was also examined (data not shown). However, no significant differences were observed between the WT and the *S. elongatus* Δ*cutA*::*kan*, which may be attributable to the capacity of *S. elongatus* to readjust the pH of the medium, thereby potentially masking strain-specific effects. Unlike most heterotrophic bacteria that acidify their environment through their proton gradient, the orientation of the proton gradient in the *S. elongatus* cell membrane is reversed, resulting in an alkalinization of the surrounding medium[106].

3.5 *S. elongatus ΔcutA::kan* Exhibits Impaired Recovery Following β-Lactam Antibiotic Exposure

Given that both, low pH and heat stress, might influence cell wall integrity and could thereby contribute to the prolonged lag phase observed in the *ΔcutA* strains compared to the WT, the structural integrity of the cell envelope was further investigated. To this aim, WT and *ΔcutA* strains were exposed to the β-lactam antibiotics ampicillin and carbenicillin which target penicillin-binding proteins (PBPs), essential for peptidoglycan crosslinking and cell wall stability.

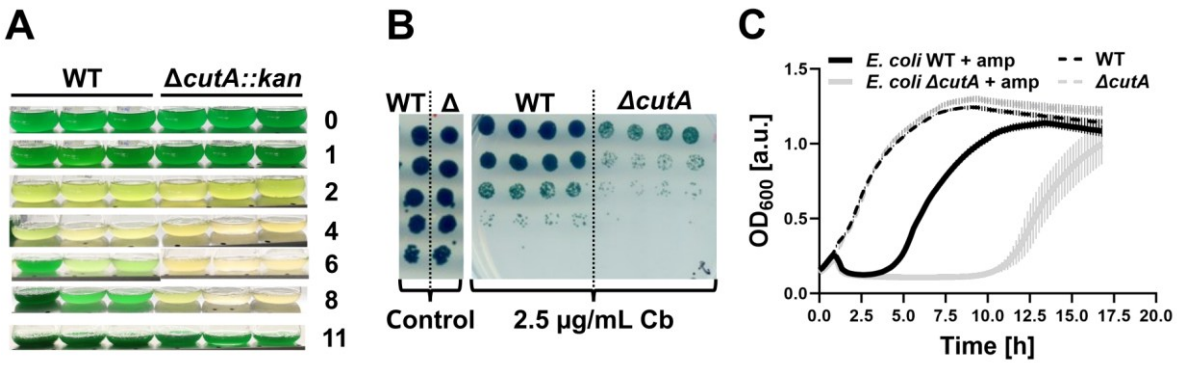

Figure 3.6: β-lactam sensitivity of *S. elongatus* Δ*cutA::kan* and *E. coli* WT and *ΔcutA*.
(A) Growth of liquid *S. elongatus* WT and Δ*cutA::kan* cultures treated with 10 µg/mL ampicillin, inoculated at $OD_{750} = 0.4$ and monitored over 14 days (n=3). **(B)** Drop dilution assay on BG11 agar containing 2.5 µg/mL carbenicillin. Serial 1:10 dilutions were spotted from cultures at $OD_{750} = 1$. **(D)** Growth curve of *E. coli* in the presence of ampicillin. Panel A and B of this figure appears also in modified form in the SI of Wagner et al., 2025[46]. **(C)** *E. coli* cultures were adjusted to an optical density at 600 nm (OD_{600}) of 0.2 and incubated in 24-well plates containing 20 µg/mL ampicillin. Growth was monitored at regular time intervals using a plate reader. This result was just observed one time and could not be reproduced. Panel A and B are also shown in the Supplementary part of Chapter 4 and the repetition of A is shown in Fig. 4.2. All assays were conducted at 28 °C under continuous light (30-60 µmol photons m^{-2} s^{-1}) for *S. elongatus* and at 37°C for *E. coli.*

Both the *S. elongatus* WT and *ΔcutA*::*kan* strains lost pigmentation after two days of exposure to ampicillin treatment (Figure 3.6 A). The WT strain was able to recover pigmentation after six days, while the *ΔcutA* mutant exhibited a delayed recovery. In a repeated experiment conducted with Amelie Stadelmann (Supplementary Figure 1), both strains showed loss of pigmentation already after one day of treatment, but the WT strain recovered much earlier, within two days, compared to the previous observation.

For the carbenicillin sensitivity assay (Figure 3.6C, performed together with Amelie Stadelmann), the drop plate method was used on BG11 agar plates supplemented with 2.5 µg/mL carbenicillin. The WT strain was able to grow up to a dilution of 10^{-3}, whereas the

ΔcutA mutant showed limited growth up to dilution 10^{-2}, indicating an increased sensitivity of the mutant strain to carbenicillin.

In panel D, *E. coli* growth in the presence of ampicillin is shown. After one hour of exposure, the OD_{600} of both strains decreased. This effect could not be repeated, as in repetition experiments either both strains died or recovered. However, comparable to other stress conditions, the WT strain recovered faster than the *ΔcutA* mutant, which displayed a significantly longer lag phase, more than five hours longer than the WT, before entering the exponential growth phase.

In conclusion, the observed phenotypes in *S. elongatus* and *E. coli ΔcutA* mutants do not appear to result from a specific stressor, but rather from a general sensitivity to stress. The prolonged lag phases suggest that recovery is delayed in the mutants, potentially due to increased demand for cellular repair mechanisms in the absence of *cutA*.

3.6 CutA Pulldown with Cell Extracts from *S. elongatus* and *Nostoc* sp. PCC 7120

Since P_{II} and many P_{II}-like proteins are known to play pivotal roles by interacting with other proteins, it was investigated whether CutA (despite lacking the T-loop typically essential for such interactions) might also have other proteins as binding partners. To examine this, a proteomics pulldown experiment was performed. Strep-tagged CutA was immobilized on magnetic beads and incubated with cell extracts to capture potential interaction partners.

To reduce nonspecific interactions, the experiment was conducted under three different conditions (see Figure 3.7): two under standard cultivation conditions but differing in the time point at which magnetic beads were added, and one following heat treatment. The latter was included based on the hypothesis that CutA may be involved in heat tolerance and could exhibit enhanced binding activity under stress conditions. The pulldown assay was conducted using *Nostoc* 7120 and *S. elongatus,* under the assumption that CutA interacts with conserved partners across species. The experimental setup is illustrated in Figure 3.7. Treatments A and B were both performed at 28 °C, with the order of addition differing between them: in Treatment A, the whole-cell extract was added before the beads, whereas in Treatment B, the beads were added first. Treatment C followed the same procedure as Treatment A but was carried out at 58 °C. To further control for unspecific interactions, such as those resulting from the affinity tag or magnetic beads, three different negative controls were included:

1. SbtB treated under condition A and 2. SbtB treated under condition B (SbtB is another P_{II}-like protein, depicted in Figure 1.5, which is absent in *S. elongatus*) and 3. whole cell extract that was added to the beads without any protein.

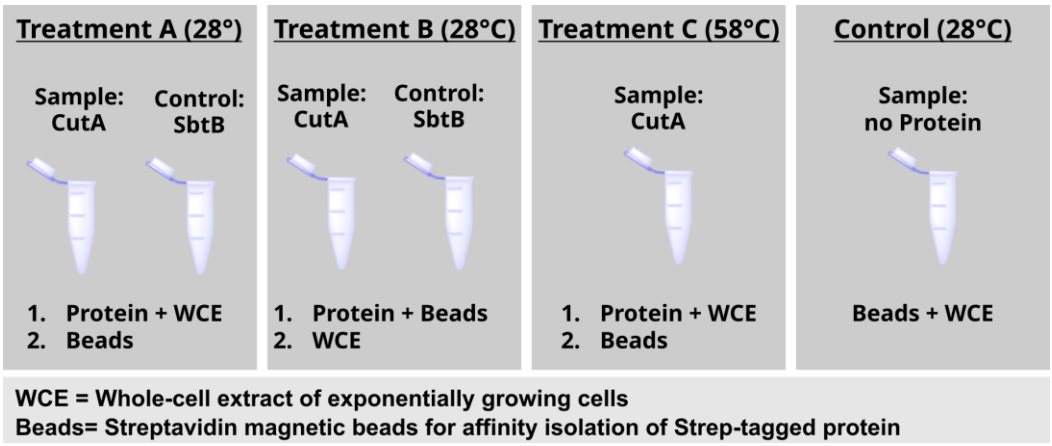

Figure 3.7: Pulldown assay with purified CutA_strep from *Nostoc* or *S. elongatus* as bait protein.
In treatment A and C, 50 µg of purified protein was incubated with 3 mg/mL of crude cell extract from exponentially growing cultures for 15 minutes, followed by the addition of magnetic beads coated with a streptavidin variant for another 15 minutes. In Treatment B, the order was reversed: beads were incubated with purified protein for 15 minutes, followed by the addition of crude cell extract for 15 minutes. After incubation, beads were washed and eluted with a biotin-containing buffer. Crude extracts were prepared by lysing exponentially growing cultures (OD600 = 0.6-0.7) and determining total protein concentration using a BCA assay.

For data analysis, the three experimental conditions involving CutA were grouped together to represent the CutA pulldown. Likewise, the three control conditions were combined to represent the pulldown without CutA. Proteins specifically interacting with CutA were expected to be more abundant in the CutA-containing samples compared to the controls.

To visualize differential enrichment, a volcano plot was generated (Figure 3.8 and Figure 3.9). Proteins enriched in the presence of CutA appear on the right side of the plot, while proteins predominantly or exclusively found in the control samples are shown on the left. Non-significant proteins are depicted in gray. In addition to the volcano plot, the two flanking plots display proteins detected exclusively in either the control samples (“Only in the Control”, left) or exclusively detected in the CutA samples (“Only with CutA”, right). Proteins detected exclusively in either the CutA pulldown or the control but not in the other condition could not be assigned a finite fold change, as division by zero results in infinite values on the $\log_2$ scale. Therefore, the fold change appears as +inf or -inf.

To assess statistical significance within the right and left plot, proteins had to be consistently detected across all three replicates of one condition and entirely absent from the other. Under

these criteria, proteins present in all three CutA pulldown samples and absent in all control samples were considered significantly enriched, if the variation between replicates was low enough to support statistical testing. In contrast, proteins detected in only one or two replicates of the CutA pulldown (plus completely absent in the control) were not considered statistically significant due to high variability and insufficient data for reliable p-value estimation. However, such proteins were still included in the supplementary plots, as they may represent biologically relevant but less confidently identified candidates.

In this proteomics pulldown experiment, iBAQ (intensity-based absolute quantification) values were used to compare the relative abundance of proteins across samples. iBAQ is a mass spectrometry-based method that quantifies protein abundance by normalizing the peptide intensities to the number of observable peptides for each protein, providing a more accurate estimation of protein levels in complex samples like the used cell extracts.

Figure 3.8 shows the results for putative protein-protein interactions of CutA in *Nostoc* 7120 and Figure 3.9 depicts the results for *S. elongatus*.

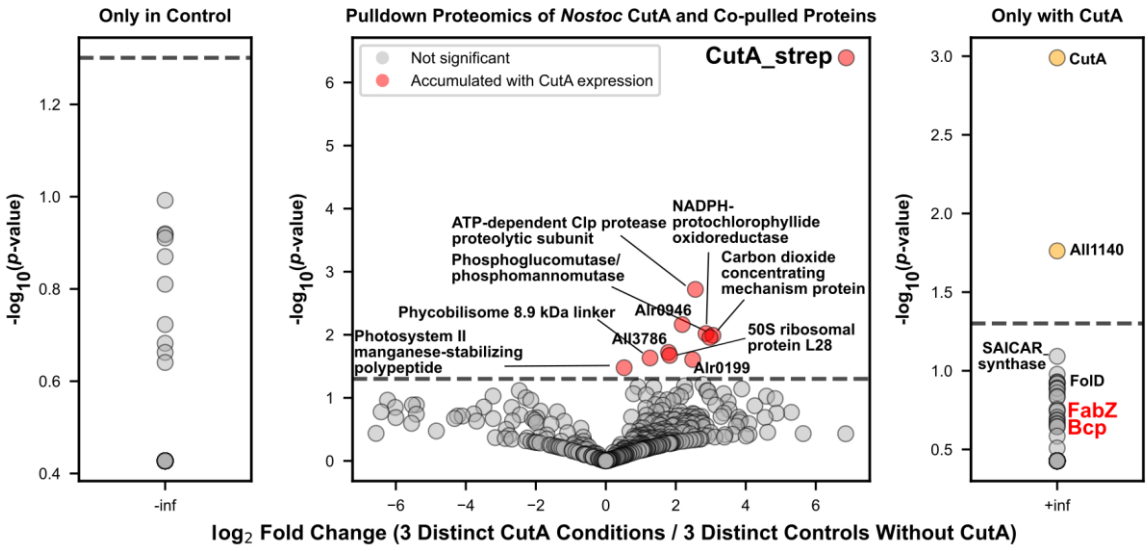

Figure 3.8: Volcano plot of proteins identified via proteomics in pulldown with CutA from *Nostoc* sp. PCC 7120.
$\log_2$ fold changes ($\log_2$FC) of proteins identified in "Pulldown containing CutA" versus "Pulldown without CutA" are plotted against $-\log_{10}$(p-values). Proteins significantly enriched in CutA pulldowns appear to the right of the vertical axis and are depicted in red. The flanking panels show proteins that were exclusively detected in one condition: Only in Control (left) or Only with CutA (right), representing proteins assigned infinite fold changes due to absence in the other condition. Dashed horizontal lines indicate the significance threshold of unpaired, two-tailed t-tests ($p < 0.05$ which corresponds to $-\log_{10}(p) > 1.3$). Proteins annotated in orange were exclusively detected in all three CutA pulldowns, not in the control. Red font: proteins also present in pulldown of *S. elongatus* or *E. coli.*

Both Strep-tagged and untagged versions of CutA were detected in the pull-down experiment of *Nostoc* 7120 (shown in the volcano and "Only with CutA" plot on the right). This is likely because CutA forms oligomers with native CutA from the *Nostoc* WT cell extract, leading to co-purification of the untagged protein. Alternatively, tryptic digestion may have produced fragments without the strep-tag, which were then identified as untagged CutA in the analysis.

The only protein consistently detected in all three CutA samples with significantly high iBAQ intensities (and absent in all three controls) was All1140. This is an amidase that hydrolyzes peptidoglycan, facilitating the formation of channels that connect neighboring cells within the filament. These channels are essential for the exchange of metabolites and signals between adjacent cells, particularly during heterocyst differentiation under nitrogen-deprived conditions[107]. FolD, an enzyme of the folate pathway (pathway is shown in Figure 5.2), was also exclusively present in the pulldowns with CutA and absent in the controls.

In the pulldown experiment with *S. elongatus* CutA, multiple proteins accumulated in samples containing CutA compared to controls without CutA (Figure 3.9).

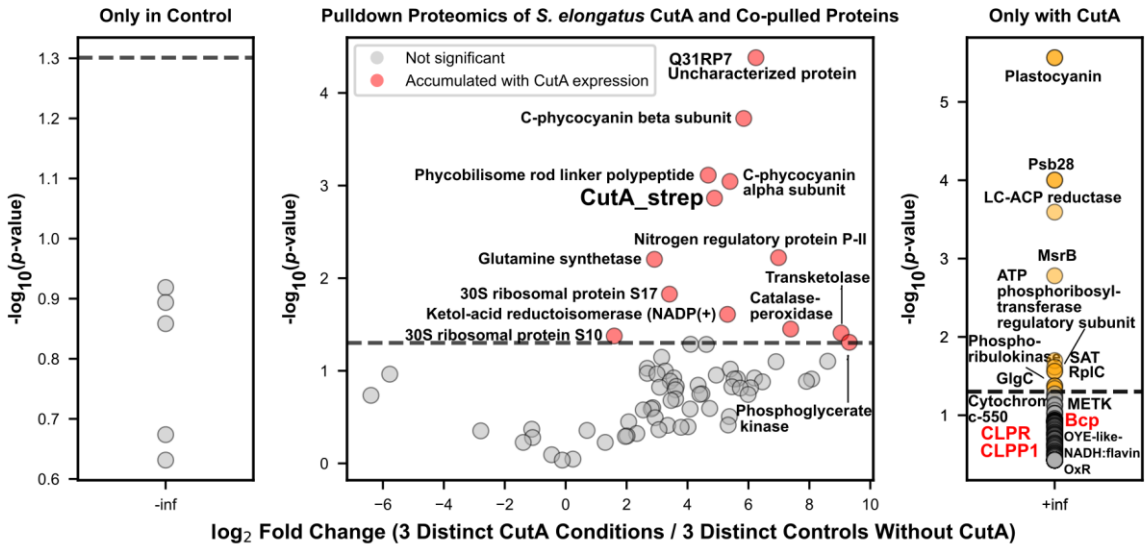

Figure 3.9: Volcano plot of proteins identified via proteomics in pulldown with CutA from *S. elongatus*. $\log_2$ fold changes ($\log_2$FC) of proteins identified in the pulldown containing CutA versus the pulldown without CutA are plotted against $-\log_{10}$(p-values). Proteins significantly enriched in CutA pulldowns appear to the right of the vertical axis and are depicted in red. The flanking panels show proteins that were exclusively detected in one condition: Only in Control (left) or Only with CutA (right), representing proteins assigned infinite fold changes due to absence in the other condition. Dashed horizontal lines indicate the significance threshold of unpaired, two-tailed t-tests ($p < 0.05$ which corresponds to $-\log_{10}(p) > 1.3$). Proteins annotated in orange were exclusively detected in all three CutA pulldowns, not in the Control. Red font: proteins also present in pulldown of *Nostoc* 7120 CutA.

The most significant protein detected was plastocyanin, a copper-binding electron carrier involved in electron transfer between P700 and the cytochrome b_6f complex in photosystem I. Plastocyanin was present in all three CutA pulldown samples but absent from the controls.

In addition, the proteins ClpR, ClPP1 and Bcp were also found exclusively in the *S. elongatus* CutA containing samples. ClpP proteolytic subunit and Bcp (Bacterioferritrin comigratory protein) were also enriched in the pulldown with *Nostoc* 7120 CutA.

Since multiple putatively interacting proteins were enriched in the CutA pulldown samples, the focus was placed on those identified in both strains. Their detection across species suggests a conserved and functionally relevant interaction and makes unspecific binding less likely. Additionally, proteins found exclusively in one species, but with higher iBAQ values in the heat-treated samples, are shown. This selection was based on the expectation that CutA's involvement and its potential interactions would be stronger under stress conditions, such as heat treatment.

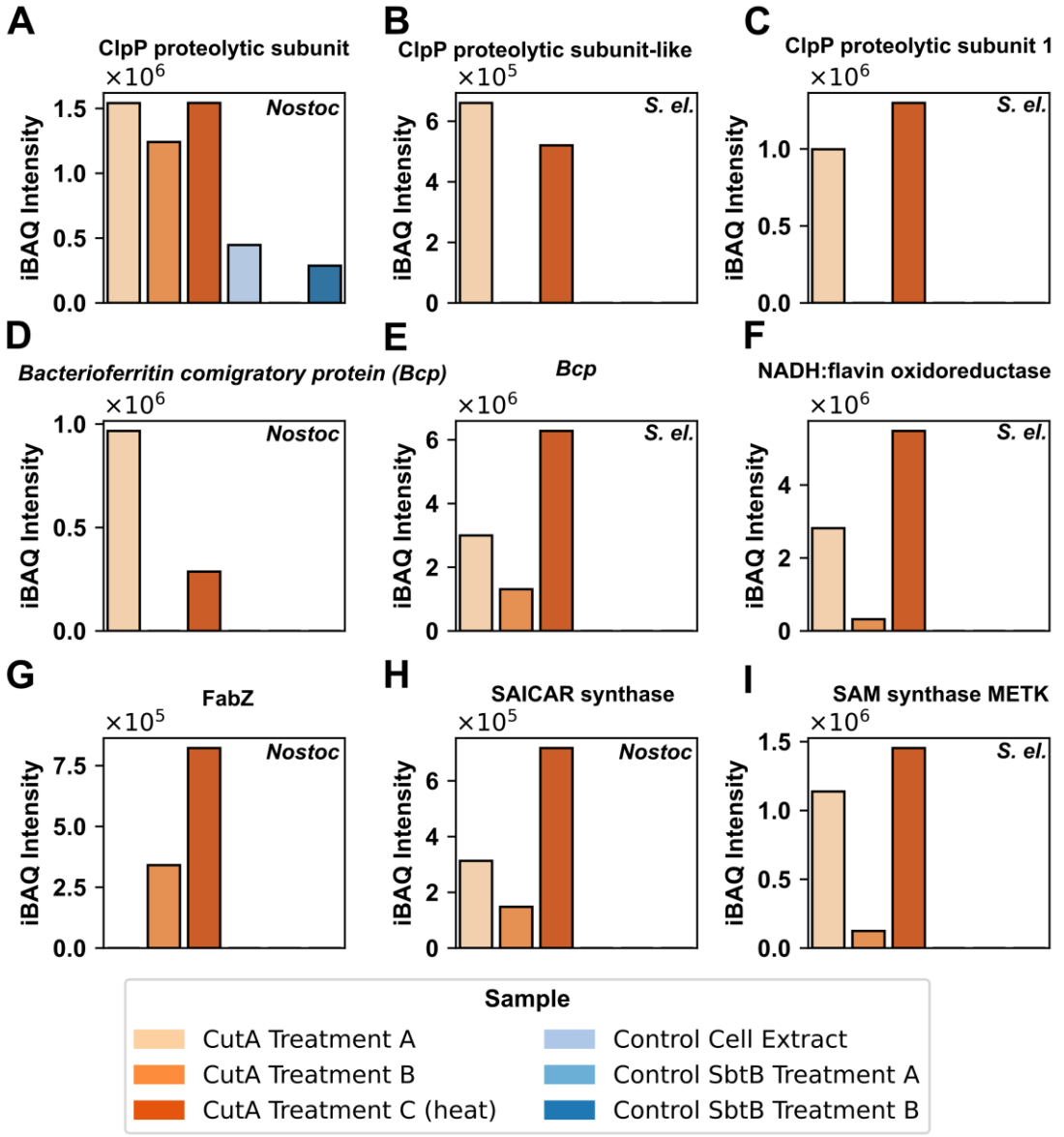

Figure 3.10: Proteins accumulated in the pulldown with CutA as bait protein that were present in two different organisms and/or enriched under heat treatment.
(A) ATP-dependent Clp protease proteolytic subunit (Nostoc, Q8YP42), **(B)** putative ATP-dependent Clp protease proteolytic subunit-like (*S. elongatus*, Q9L4P4), **(C)** ATP-dependent Clp protease proteolytic subunit 1 (*S. elongatus*, P54415), **(D)** bacterioferritin comigratory protein (*Nostoc*, Q8YSA6), **(E)**: bacterioferritin comigratory protein, (*S. elongatus*, Q31L59) **(F)** NADH:flavin oxidoreductases Old Yellow Enzyme family-like (*S. elongatus,* Q31R14), **(G)** 3-hydroxyacyl-[acyl-carrier-protein] dehydratase FabZ (*Nostoc*, Q8YUR4), **(H)** phosphoribosylaminoimidazole-succinocarboxamide synthase (*Nostoc*, PurC, SAICAR synthase, Q8YUR7), **(I)** S-adenosylmethionine synthase(*S. elongatus* metK, Q31KC6).

As shown in Figure 3.10, several proteins associated with stress response were enriched in the CutA pulldown samples from both *Nostoc* and *S. elongatus*. In both strains, proteolytic subunits of the ATP-dependent Clp protease were identified, which are involved in stress adaptation. In *S. elongatus* PCC 7942, these proteins are specifically known to contribute to acclimatization under high light irradiance[108]. Furthermore, bacterioferritin comigratory

protein (Bcp), also known as thioredoxin-dependent peroxiredoxin, was enriched. This protein detoxifies peroxides and functions in hydrogen peroxide-mediated signaling, thereby protecting the cell from oxidative stress[109]. Also, NADH:flavin oxidoreductases of the Old Yellow Enzyme (OYE)-like family were present in the CutA pulldown samples but absent in the controls and showed a marked accumulation in the heat-treated CutA pulldown (treatment C). These are enzymes involved in redox reactions and electron transfer[110]. Additionally, two key enzymes from central metabolic pathways were also found: SAICAR synthase, which catalyzes the seventh step of de novo purine biosynthesis[111], and S- adenosylmethionine synthase (MetK), which produces S-adenosylmethionine (SAM) from methionine and ATP and is essential for methylation reactions.

3.7 *In vivo* pulldown in *E. coli*

To optimize the experimental setup and investigate the function of CutA in a gut microbiome-relevant model organism, the pulldown experiment was repeated in *Escherichia coli* using a refined design and biological triplicates. In this setup, label-free quantification (LFQ) values were measured instead of iBAQ, as LFQ provides improved accuracy for comparing protein abundances across samples due to enhanced normalization and handling of replicate variability. The approach aimed to identify potential *in vivo* interaction partners by comparing CutA-overexpressing cells to a genetically identical control lacking CutA expression. For this, *E. coli ΔcutA* was transformed with the plasmid pASK[CutA], harboring *cutA* under the control of the anhydrotetracycline (AHT)-inducible *tet*-promoter.

In parallel cultures, CutA expression was either induced or left uninduced, which enabled comparison under otherwise identical conditions. To investigate the function of CutA during heat treatment and detect putative interaction partners, the experiment was performed under standard growth conditions (37°C) and under heat treatment (58°C for 30 min). The experimental setup is shown in Figure 3.11.

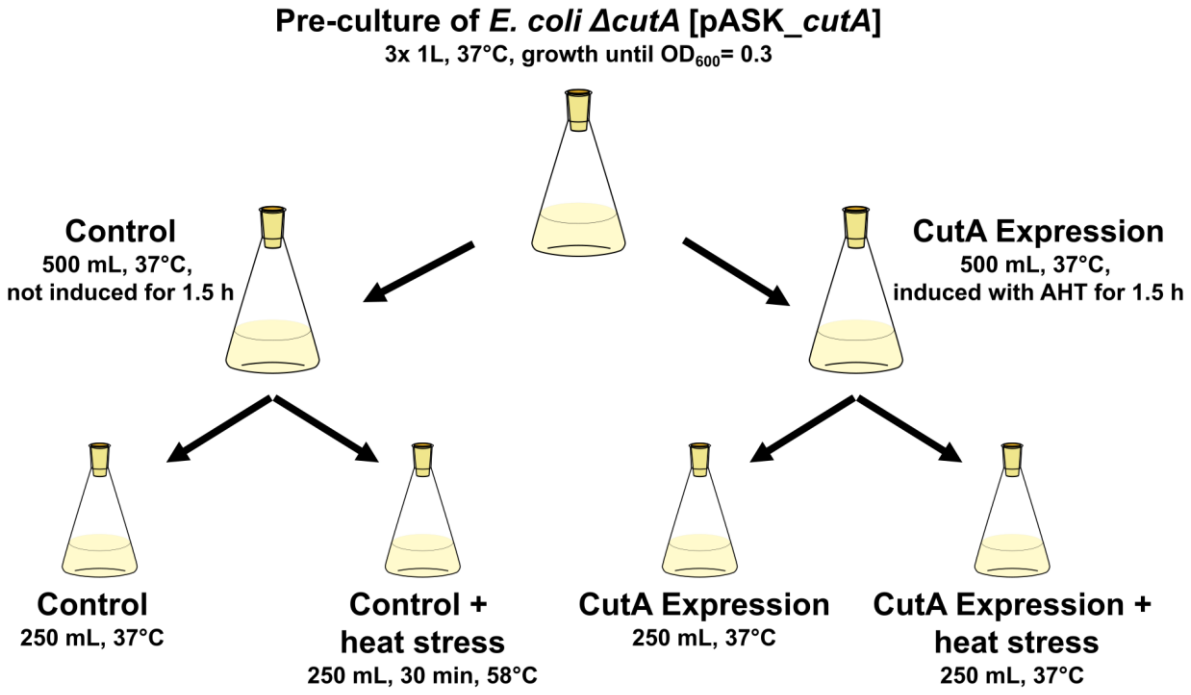

Figure 3.11: Experimental setup for *in vivo* pulldown assays to investigate CutA-mediated protein interactions and heat stress responses in *E. coli* BW25113 Δ*cutA* strains carrying *cutA* under the AHT inducible tet-promoter on the pASK[*cutA*_strep] plasmid.
Cultures were grown to OD_{600} 0.3 and split into induced (AHT-treated for CutA expression) and non-induced groups. Each group was subjected to either standard growth at 37°C or a 30-minute heat shock at 58°C following induction. Biological triplicates were prepared for all conditions. Cells were harvested by centrifugation, lysed, and crude extracts were incubated with Strep-Tactin magnetic beads to capture CutA_strep and associated proteins. Pulldown samples were analyzed by comparing LFQ intensities. The setup was designed to enable the *in vivo* identification of CutA-interacting proteins under standard and heat-stress conditions.

The results of the *in vivo* pulldown were analyzed and visualized in the same manner as in the pulldown experiment described in section 3.6. The results of the pulldown experiments are illustrated as volcano plots in Figure 3.12 (standard growth, 37°C) and Figure 3.13 (heat stress, 58°C, 30 min).

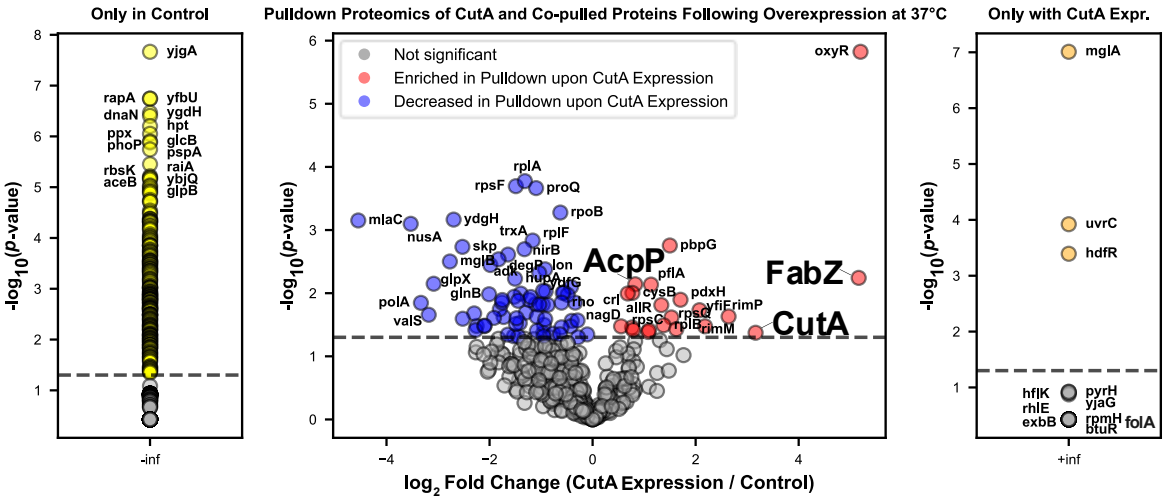

Figure 3.12: Proteomics analysis of pulldowned lysates using *Ec*CutA as a bait following overexpression at 37 °C.
The central volcano plot displays $\log_2$ fold changes (CutA expression vs. control) of proteins co-purified with Strep-tagged CutA, plotted against $-\log_{10}$(p-values). Significantly enriched proteins upon CutA overexpression are shown in red, while those significantly decreased are shown in blue. Gray dots represent proteins without significant changes; CutA is labeled for reference. Left panel: proteins exclusively detected in control samples. Right panel: proteins exclusively detected upon CutA expression. Orange dots represent proteins that were detected in all three CutA-overexpressing samples.

The most abundant proteins under standard growth conditions were OxyR (DNA-binding transcriptional dual regulator OxyR, a peroxide-sensor[112]), PdxH (Pyridoxine/pyridoxamine 5'-phosphate oxidase, that catalyzes the oxidation of pyridoxine 5`phosphate or pyridoxamine 5`phosphate into the biologically active form pyridoxal 5`phosphate (vitamin B6).[113]), PbpG (penicillin binding protein G/D-alanyl-D-alanine endopeptidase), FabZ and AcpP. Only present in all three replicates with AHT induction and not in the controls were MglA (a galactose/methyl galactoside import ATP-binding protein MglA), UvrC (component of the UvrABC system, part of the nucleotide excision repair system[114]) and HdfR (HTH-type transcriptional regulator, involved in flagellar regulation and motility[115]).

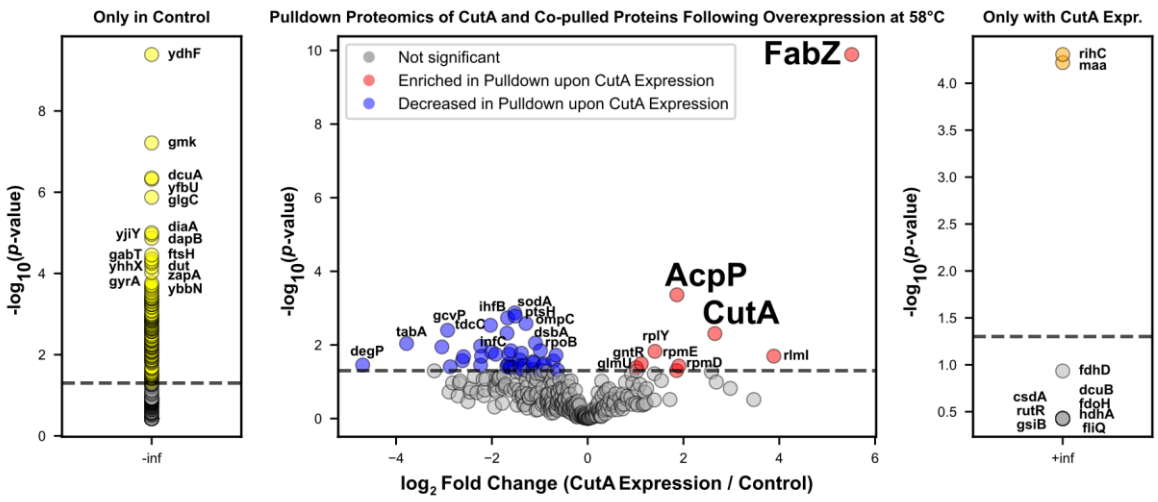

Figure 3.13: Proteomics analysis of pulldowned lysates using *Ec*CutA as a bait following overexpression at 37 °C and 30 min at 58 °C.
The central volcano plot shows $\log_2$ fold changes (CutA expression vs. control) of proteins co-purified with Strep-tagged CutA immobilized on magnetic beads, plotted against $-\log_{10}$(p-values). Proteins significantly enriched upon CutA overexpression are shown in red, while those significantly decreased are shown in blue. Gray dots represent proteins without significant changes; CutA is labeled for reference. Left panel: Proteins exclusively detected in control samples. Right panel: Proteins exclusively detected upon CutA expression. Dashed lines indicate significance thresholds ($p < 0.05$).

Under heat treatment, the protein most enriched with CutA were FabZ and AcpP. Only present in all three replicates with AHT induction and not in the controls was RihC, a non-specific ribonucleoside hydrolase, that hydrolyses both purines (e.g. guanosine or inosine) and pyrimidine (e.g. uridine, cytidine) ribonucleotides[116]. Also found was Maa, a Maltose O-acetyltransferase, that transfers an acetyl group from acetyl-CoA to maltose or other sugars[117].

Since multiple proteins were significantly enriched in both datasets, focus was placed on those present in both conditions. CutA was significantly present in the anhydrotetracycline (AHT) induced samples. It was also detected at low levels in the non-induced control samples, indicating leaky expression from the pASK plasmid in the absence of AHT. Nevertheless, CutA levels were significantly higher in the induced samples (Figure 3.14) confirming that AHT effectively enhanced expression despite the low-level leaky expression observed in the controls.

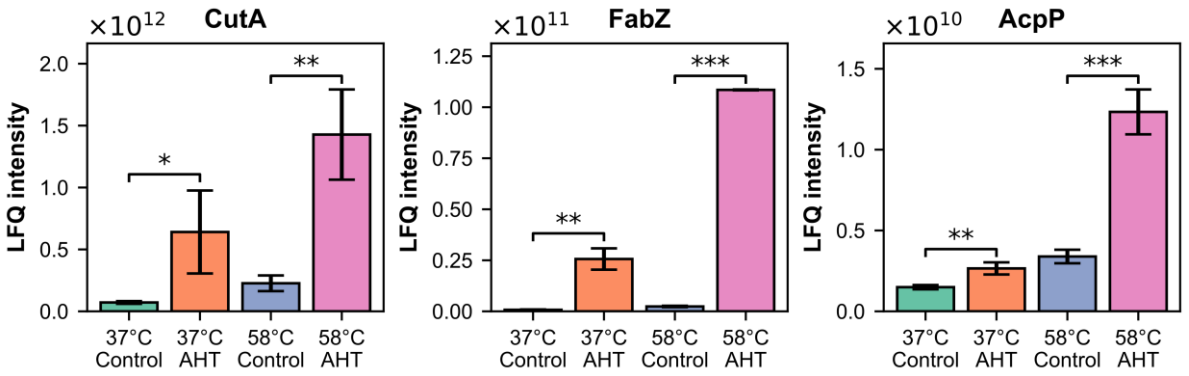

Figure 3.14: Protein accumulation in pulldown experiments under 37°C and 58°C treatment conditions. Bar plots display the mean LFQ intensities ± standard deviation for three proteins identified in the pulldown experiment, under both 37°C and 58°C treatment conditions, with and without AHT induction. Each bar represents the mean of triplicates. Statistical significance between AHT-treated and untreated samples was determined using an unpaired t-test for each temperature. Significance levels are indicated as follows: $p < 0.05$ (*), $p < 0.01$ (**), $p < 0.001$ (***), and n.s. = not significant.

In addition to CutA, the 3-hydroxyacyl-[acyl-carrier-protein] dehydratase FabZ (Uniprot ID: P0A6Q6) was significantly enriched in pulldown experiments with expressed CutA and was more abundant in heat-treated samples. A similar observation was made in *Nostoc* 7120, where FabZ also co-purified with CutA and showed greater enrichment under heat stress conditions (Figure 3.8 and Figure 3.10G) The acyl carrier protein AcpP (Uniprot ID: P0A6A8) was likewise significantly enriched in the CutA pulldown and more abundant following heat treatment. Given that FabZ and AcpP are both key components of the fatty acid biosynthesis pathway, their co-enrichment with CutA may indicate a functional link between CutA and lipid metabolism, particularly under stress conditions. A similar protein, the long-chain acyl-[acyl-carrier-protein] reductase (AAR, Uniprot_id: Q54765), was also found significantly enriched in all samples with CutA and not in the control without CutA of the *S. elongatus* pulldown, Figure 3.9, FabZ, AcpP, and AAR are key proteins in fatty acid biosynthesis[118]. Since membrane and lipid composition critically determine cellular tolerance to different environmental stress conditions, such as heat or pH stress, these results raise the possibility that CutA contributes to stress resilience by modulating lipid metabolism or membrane-associated processes. Taken together, the findings suggest that CutA may act as a factor linking fatty acid biosynthesis to cellular stress adaptation.

3.8 Untargeted Metabolomics of *S. elongatus* WT and *ΔcutA::kan*

To investigate metabolomic differences between *S. elongatus* WT and Δ*cutA*::*kan* strains, untargeted metabolomics were performed in parallel with the native metabolomics

experiment and compound purifications described in Chapter 4. Samples were collected during the exponential and stationary growth phases in five biological replicates, normalized to OD_{750} 0.6, extracted with 20% MeOH, and analyzed by LC-MS. Experimental setup and sampling time points during growth phases are indicated in Figure 3.15.

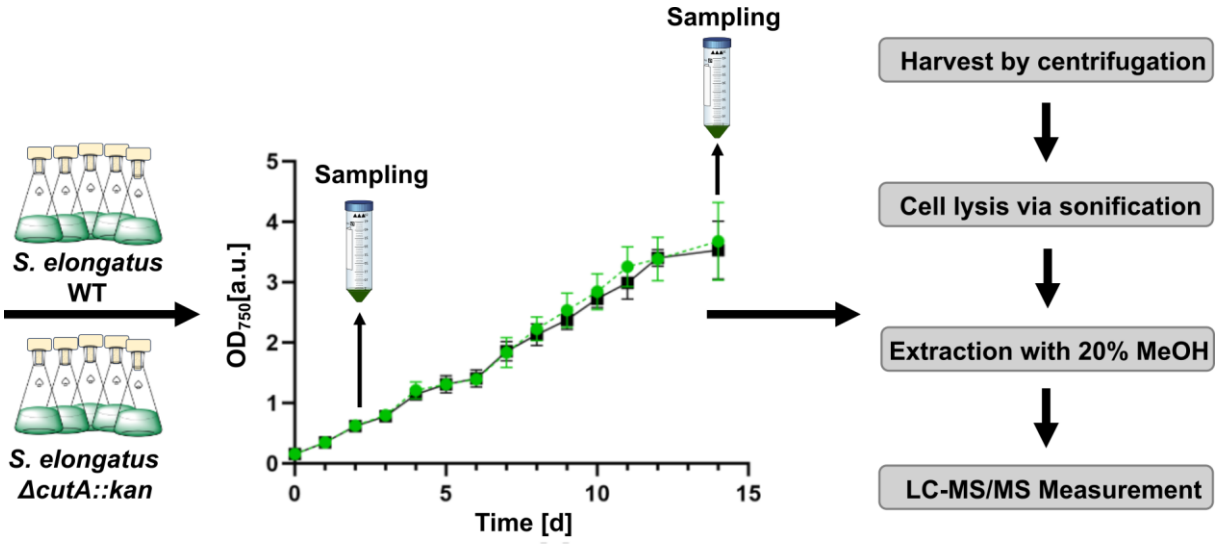

Figure 3.15: Experimental setup for untargeted metabolomics of *S. elongatus* WT and *ΔcutA::kan*. Cultures were grown in BG11 medium under continuous light (30-60 µmol photons $m^{-2}s^{-1}$) at 28 °C with shaking at 120 rpm, starting from an initial OD_{750} of 0.15. Samples were collected during exponential and stationary growth phases in five biological replicates. Cell densities were normalized to OD_{750}=0.6 for the exponential growth phase and 2.2 for stationary growth phase, extracted with 20% MeOH and analyzed by LC-MS.

The acquired data was processed using a workflow combining several open-source tools that are shown in Figure 3.16. After data acquisition, the raw files were inspected for proper measurement quality and subsequently converted into centroided mzML format using MSConvert (ProteoWizard)[119]. Feature detection, chromatographic alignment, and peak integration were carried out in MZmine 3[119]. In this context, a feature refers to a detected ion signal group, typically corresponding to a single metabolite, defined by its RT and mass-to-charge ratio (*m/z*). Each feature represents a measurable property of a detected ion, such as a peak in an XIC, and is characterized by attributes including abundance, peak shape, isotopic pattern or charge state. The goal of the feature detection process is to identify and extract all relevant ion signals from raw LC-MS data and compile them in a list. This list serves as the foundation for downstream analysis.

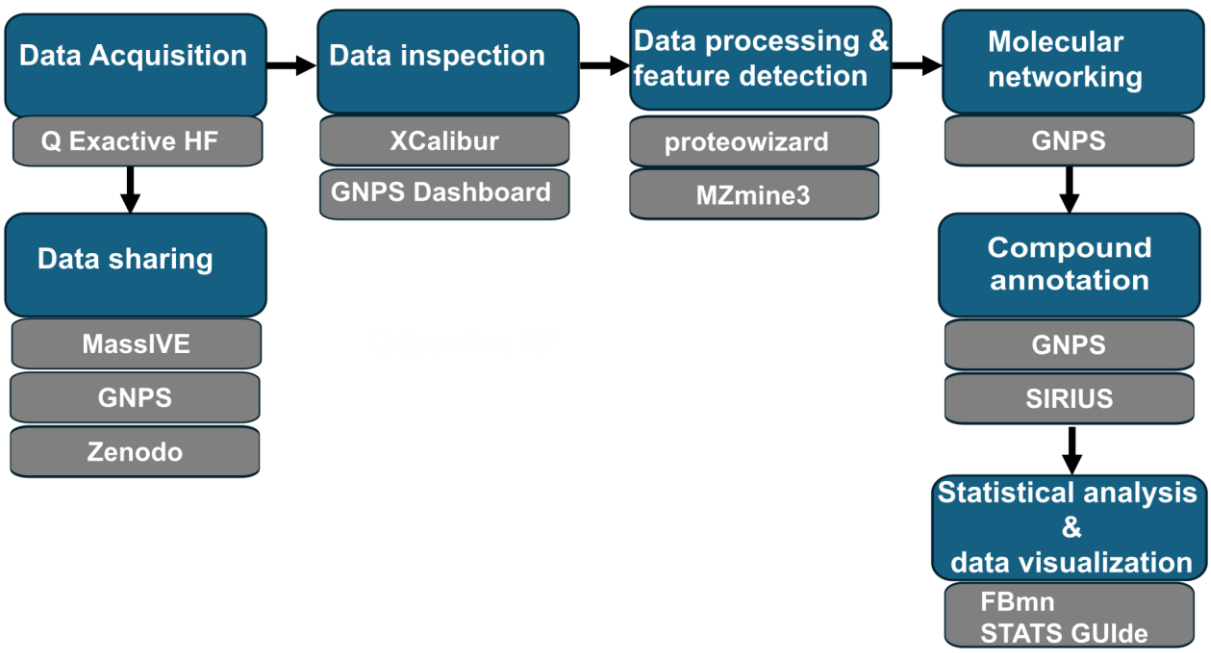

Figure 3.16: Workflow for untargeted metabolomics data processing and analysis.
The overall data workflow is shown in blue, and the software tools used for each step are depicted in gray boxes. Raw LC-MS/MS data were acquired using a Q Exactive HF mass spectrometer and inspected with XCalibur and the GNPS Dashboard. Data processing and feature detection were performed using ProteoWizard and MZmine3. Molecular networking and compound annotation were conducted via the GNPS platform and SIRIUS. Data were shared through MassIVE, GNPS, and Zenodo. Statistical analysis and visualization were carried out using FBMN STATs GUIde.

Chromatographic alignment ensures that features corresponding to the same metabolite across different samples are correctly matched, compensating for small variations in retention time. It should be noted that due to measurement properties, such as overlapping elution profiles or adduct formation, a single compound can generate multiple features during the LC-MS run.

Molecular networking using GNPS provided an overview of connected features and enabled compound annotation by comparing experimental MS/MS spectra to reference spectral libraries. However, many features remained unannotated, as spectral information for cyanobacterial metabolites is still limited in public databases. Therefore, SIRIUS[120] was used to predict molecular formulas and putative compound structures based on fragmentation patterns. Subsequent data clean-up and statistical processing, including blank removal, randomized imputation and Total Ion Chromatogram (TIC) normalization, were performed using the FBMN (Feature based molecular networking) STATS GUIde[121]. The resulting cleaned dataset was then used for principal coordinate analysis (PCoA, Figure 3.17) and volcano plot visualization to show the differential abundance of detected features across WT and mutant and growth phases (Figure 3.18).

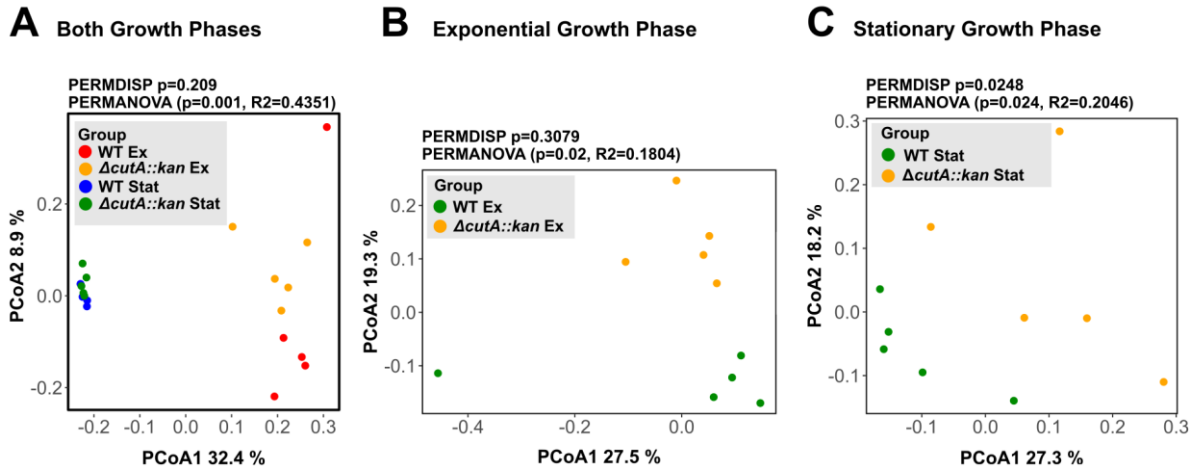

Figure 3.17: Principal coordinates analysis (PCoA) of untargeted *S. elongatus* data.
(A) Comparison of *S. elongatus* WT and *ΔcutA::kan* in exponential (Ex, depicted in red and yellow) and stationary (Stat, depicted in blue and green) growth phases. **(B)** PCoA of exponential growth phase samples. **(C)** PCoA of stationary growth phase samples. Five biological replicates were analyzed using the Canberra distance matrix.

PCoA analysis using the Canberra distance matrix showed that samples clustered primarily according to growth phase rather than genotype (Figure 3.17A), suggesting that metabolic changes are largely driven by growth stage. Growth phases separated clearly along PCoA1 (PERMANOVA: $p = 0.001$, $R^2 = 0.4351$; PERMDISP: $p = 0.209$). When each growth phase was examined separately, moderate but statistically significant differences between WT and *ΔcutA::kan* were observed, indicating that the *cutA* deletion subtly affects the metabolic profile within each phase. In the exponential phase, WT and *ΔcutA* differed moderately (PERMANOVA: $p = 0.02$, $R^2 = 0.1804$; PERMDISP: $p = 0.308$), and a similar trend was observed in the stationary phase (PERMANOVA: $p = 0.024$, R2= 0.2046; PERMDISP: $p = 0.0248$).

Following an overview of the growth phases using PCoA plots, the data were further analyzed to identify putative significant features distinguishing WT and *ΔcutA::kan* in both growth phases. A total of 5154 features were detected (after blank removal), of which 424 were significantly different ($p < 0.05$) between WT and mutant in the exponential growth phase and 575 in the stationary growth phase.

To visualize the distribution of these features, the data were plotted as volcano plots. Features exhibiting both significant differences and GNPS annotations were depicted in darker colors and labelled in a legend adjacent to the plots. The results are shown in Figure 3.18A and B.

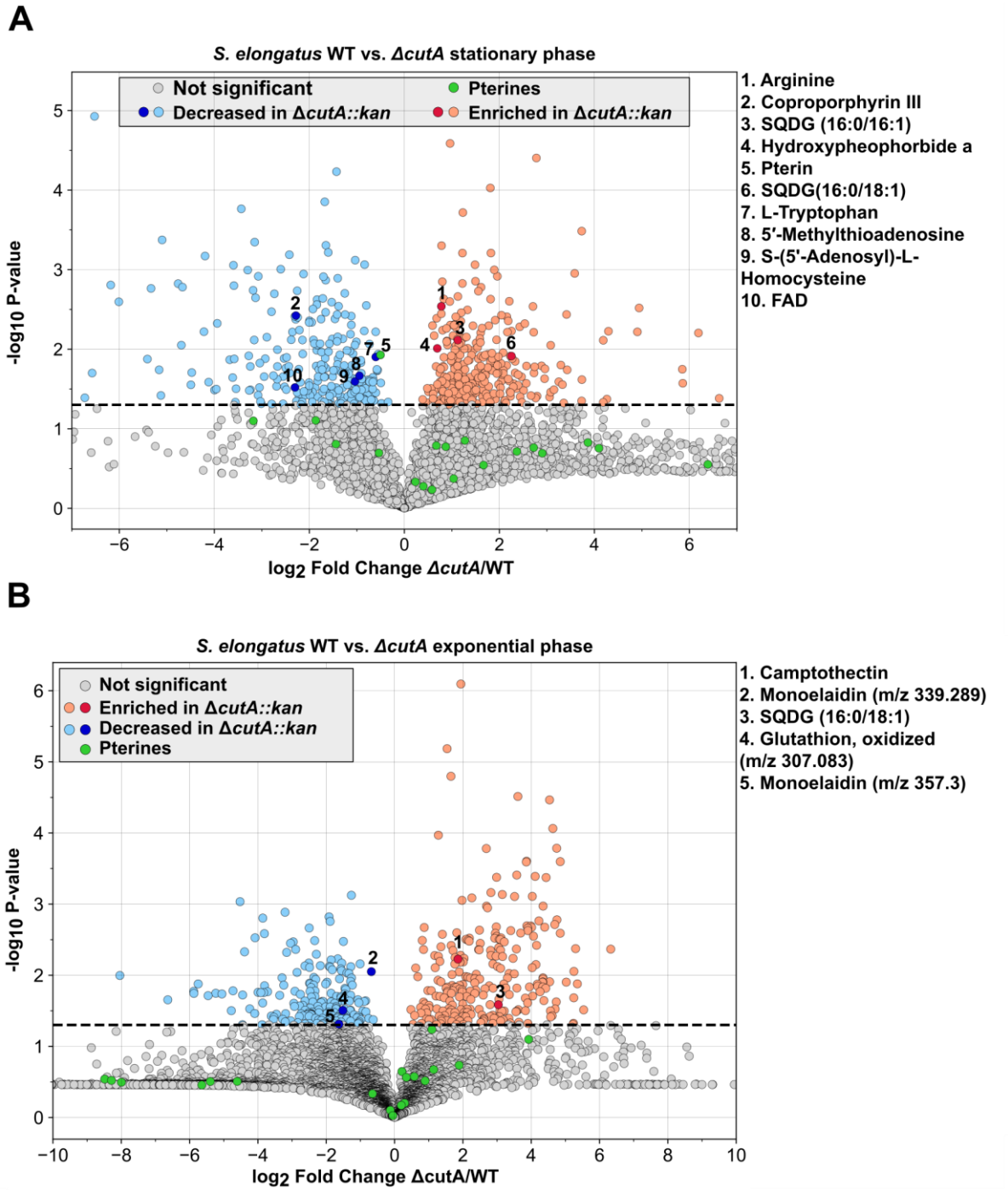

Figure 3.18: Volcano plot of features detected in untargeted metabolomic samples comparing *S. elongatus* WT and *ΔcutA::kan* in the (A) exponential and the (B) stationary growth phase.
log_2 fold changes (log_2 FC) are plotted against -log10 (p) values from unpaired, two-tailed *t*-tests. Features significantly enriched in *ΔcutA::kan* appear to the right of the vertical axis and are shown in red. Features significantly decreased in *ΔcutA::kan* appear to the left and are shown in blue. Non-significant features are shown in gray, while predicted pteridine derivatives identified via SIRIUS are shown in green. The most significant features (lowest P-values) are depicted in darker colors and labeled in the legend on the right. Dashed horizontal lines indicate the significance threshold ($p > 0.05$, $-\log10(p) > 1.3$). Features detected multiple times with the same mass, similar RT and identical GNPS annotation were averaged. These included monoelaidin, glutathione, coproporphyrin III, SQDG (16:0/16:1) SQDG(16:0/18:1), L-tryptophan, 5'-S-methyl-5'-thioadenosine (5`-Methylthioadenosine), 3^{10}S-Hydroxypheophorbide a. Five biological replicates are shown.

In the exponential growth phase, enriched features included SQDG (167:0/18:1) whereas decreased features included monoelaidin (*m/z* 339.289 and *m/z* 357.3) and oxidized glutathione. In the stationary phase, enriched features included arginine, SQDG (16:0/16:1), hydroxypheophorbide a and SQDG (16:0/18:1). Decreased features comprised L-tryptophan, coproporphyrin III, pterin, 5'-S-methyl-5'-thioadenosine (5`-methylthioadenosine), S-(5`- adenosyl)-L-homocysteine and FAD. In both growth phases, several pteridines (depicted in green) were predicted using SIRIUS. However, only "pterin" showed a significant decrease in the *ΔcutA::kan* strain in the stationary growth phase. This could also be observed in untargeted metabolomics samples where *E. coli* strains were investigated.

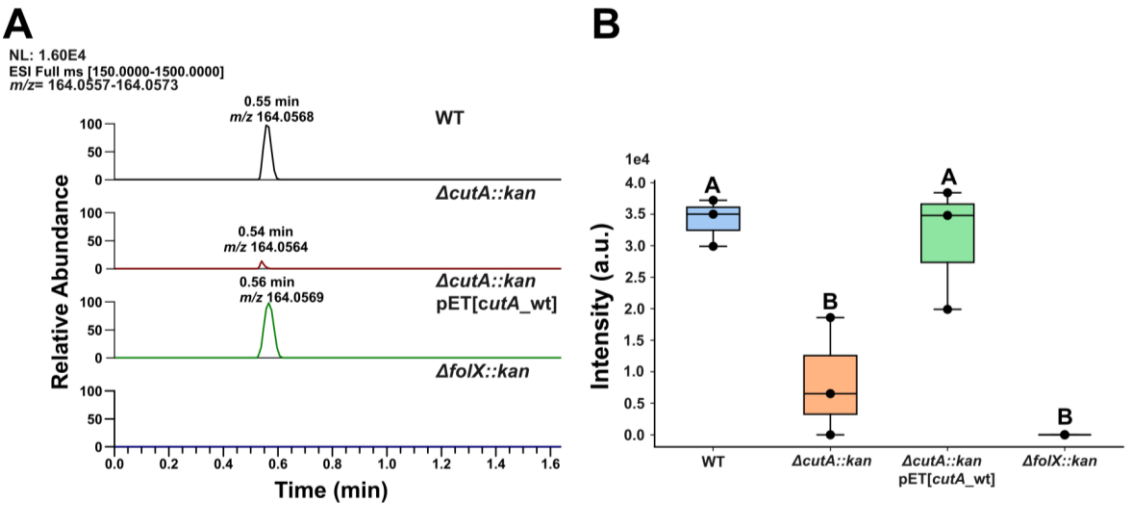

Figure 3.19: Pterin abundance in different *E. coli* cell extracts.
(A) Extracted ion chromatograms (XICs) of pterin (*m/z* 164.0568) in crude extracts from WT, *ΔcutA::kan*, *ΔcutA::kan* complemented with *cutA* under its native promoter, and *ΔfolX::kan*. The signal is strongly reduced in *ΔcutA*::kan and absent in *ΔfolX::kan*, while complementation restores it to WT levels. **(B)** Box plots of three biological replicates showing pterin intensity in each strain. Statistical analysis was conducted using one-way ANOVA, followed by Tukey's multiple comparison test as a post-hoc analysis. Significant differences between means ($p \leq 0.05$) are indicated by different letters. Data represents the mean ± standard deviation of three independent replicates. This figure is also appears in the SI of Wagner et al., 2025[46].

In *E. coli*, pterin was present in the WT strain, whereas its levels were markedly decreased in the *ΔcutA::kan* mutant and undetectable in the *ΔfolX* strain, in which monapterin biosynthesis is blocked. Complementation of *ΔcutA::kan* with *cutA* under its native promoter restored pterin levels to those observed in the WT.

4 CutA and Pteridines

Building on initial findings from physiological and proteomic analyses that suggested a putative role for CutA proteins in cellular stress responses and homeostasis, we sought to investigate their function more deeply through metabolomic approaches. To this end, we performed further targeted, untargeted, and native mass spectrometry experiments. The resulting data are presented and discussed in the following chapter. The chapter is based on the article "Native metabolomics identifies pteridines as CutA ligands and modulators of copper binding" which was published in 2025 in Proceedings of the National Academy of Sciences of the United States of America (PNAS), Volume 122, Issue 48 (DOI: 10.1073/pnas.2509468122). The references originally cited in the article have been incorporated into the main reference list of this thesis and adjusted to follow the sequential numbering of the thesis-wide bibliography (section 8, p.131 ff).

Native Metabolomics Identifies Pteridines as CutA Ligands and Modulators of Copper Binding

Advances in next-generation sequencing and the application of mass spectrometry to high-throughput biological studies have revolutionized our understanding of biology. Yet, a substantial fraction of genes and proteins remain functionally uncharacterized. One of those enigmatic proteins is CutA, first identified in *Escherichia coli* as part of a gene cluster consisting of copper uptake and transport (*cut*) genes[4,5]. CutA's conservation across all domains of life[12,13], implies a crucial biological function. It is part of a widespread signal transduction superfamily of the homo-trimeric P_{II}-like proteins[24,13,31], with each monomer weighing approximately 12 kDa. Despite similar core structures and trimeric assembly, CutA does not share any sequence homology with the nitrogen (N)- and carbon (C)-sensing P_{II} proteins[13,24] - key regulators of C/N homeostasis[26,30,122,123]- it lacks amino acid sequence homology, defining CutA as a P_{II}-like protein[13,26]. In mammals, CutA is implicated in β-amyloid precursor processing via its interaction with β-site APP cleaving enzyme 1 (BACE1)[124,125]. CutA also co-purifies with acetylcholinesterase (AChE)[126] and exhibits a similar expression pattern in the brain[127], where it is described to facilitate AChE folding,

oligomerization, secretion[9] and surface localization[127]. Due to its conservation across diverse organisms, from ancient cyanobacteria to eukaryotes including humans, CutA proteins are proposed to fulfill a fundamental role analogous to P_{II} proteins in sensing and regulating cellular homeostasis.

E. coli mutants in the *cut* cluster, categorized as *cutA-cutF*, display altered copper responses. The *cutA* locus encodes three proteins, including the cytoplasmic trimeric CutA1 (CutA in the following), the membrane-associated CutA2/DsbD (which transfers electrons from the cytoplasm to the periplasm of *E. coli*, preserving cysteine thiols in their reduced state[128]) and CutA3. Deletion mutants of the *cutA* locus exhibit hypersensitivity to metals and increased copper uptake[5], although the contribution of *cutA1* to copper tolerance remains debated[13], with putative pleiotropic effects of the neighboring *dsbd* complicating interpretations[12]. Structurally, *E. coli* CutA is described to bind Cu(II) via a His_2Cys coordination[12], potentially mediating redox regulation of thiol groups in copper and zinc transport ATPases[12,22]. The binding site in CutA shares structural similarity with the ATP-binding site of P_{II} proteins[12,129,130]. Arnesano et al. (2003) proposed that CutA may function as a sensor or regulator in copper homeostasis, potentially mitigating excess copper levels through direct binding or by modulating copper import or export via interactions with membrane transporters[22]. However, recent phenotyping studies indicated that CutA is not essential for copper tolerance in either *E. coli* or the cyanobacterium *Synechococcus elongatus*[13,23]. These findings, along with CutA's conserved structure resembling signal-transducing P_{II} proteins, its broad distribution, and potential copper interactions, motivated us to explore its biological function in greater depth.

Our research focused on two distinct bacterial taxa to identify a potential common function: *Escherichia coli* BW25113 (*E. coli*) and *Synechococcus elongatus* PCC 7942 (*S. elongatus*). By exposing both taxa to various stress conditions, we aimed to shed light on the functional roles of the CutA protein in different environmental contexts. Building on the known extreme heat stability of many CutA proteins[97,131,132], we explored their response to this stress condition. Next, we used a range of metabolomics approaches to investigate potential changes in intracellular metabolomes and search for CutA binding molecules. Using native metabolomics[133,134], we could identify a set of putative CutA ligands, which we verified using orthogonal biophysical characterization methods. Using nuclear magnetic resonance (NMR) spectroscopy and high-resolution tandem mass spectrometry (MS/MS), we solved the structure of a novel pteridine derivative, which ultimately identified pteridines as CutA ligands and putative regulators of copper affinity and cellular redox homeostasis.

Results and Discussion

4.1 CutA Deletion Alters Tolerance and Metabolite Homeostasis during Heat Stress

Given CutA's exceptional thermal stability[131,135], we investigated its role under environmental stress conditions. Exposure to 50 °C revealed that recovery of the *S. elongatus* Δ*cutA::kan* mutant was severely impaired compared to the WT (Figure 4.1A).

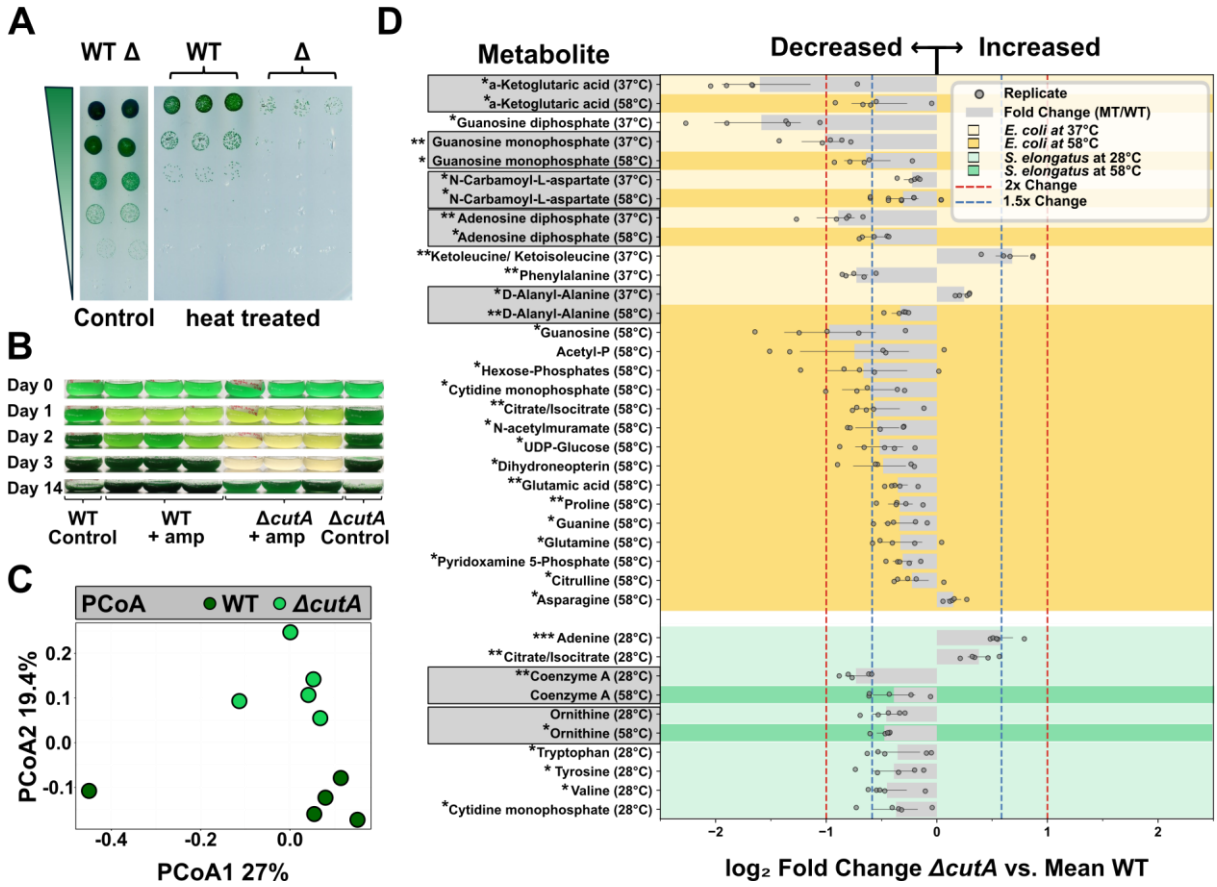

Figure 4.1: Role of CutA in heat and cell envelope stress tolerance.
(A) Viability drop dilution assay shows impaired recovery of the *S. elongatus* Δ*cutA::kan* mutant after heat stress. *S. elongatus* WT and Δ*cutA::kan* cultures were exposed to 50 °C for 1.5 h, serially diluted (1:10, *Top* to *Bottom*), and incubated at 28 °C for 7 d under constant light (30 to 60 µmol photons $m^{-2}s^{-1}$), n = 3. **(B)** Ampicillin sensitivity of the *S. elongatus* Δ*cutA::kan* mutant. The growth of cultures treated with 10 µg/mL ampicillin was monitored over 14 d. Controls without treatment are shown for comparison, n = 3. **(C)** PCoA reveals significant divergence in the global metabolome (30) of *S. elongatus* Δ*cutA::kan* compared to the WT (PERMANOVA, *P* = 0.017, permutations = 999, R2 = 0.1806, PERMDISP *P* = 0.3067). Blanks (medium controls) were subtracted before analysis, n = 5. **(D)**Targeted metabolomic analysis of *E. coli* (yellow) and *S. elongatus* (green) under standard (bright colors) and heat-stress (dark colors) conditions. Significantly different concentrations (*P*-values below 0.05) of metabolites in the Δ*cutA* mutants normalized to the WT are shown for *S. elongatus* (28 °C, 58 °C) and *E. coli* (37 °C, 58 °C). Mean value and SD of five biological replicates are shown. Each replicate was divided by the mean of the WT and shown additionally as a single dot. Gray metabolite name labels indicate significant effects observed in both treatments. Blue and red dotted lines denote thresholds for 1.5-fold and twofold changes, respectively. Data are presented as mean ± SD for five biological replicates. Statistical analysis was performed using unpaired, two-tailed *t* tests. Differences between means with *P*-values < 0.05, < 0.01, and < 0.001 are indicated by one, two, or three stars, respectively

Similarly, the *S. elongatus* Δ*cutA::kan* mutant exhibited increased susceptibility to ampicillin-induced cell wall stress, with pronounced effects observed after 2 d of treatment (Figure 4.1B). Repetition of the experiments and full plates are shown in Supplementary Fig. 1-2.

A similar sensitivity was observed on carbenicillin plates (Supplementary Fig. 3). In *E. coli*, the *ΔcutA* mutant showed increased sensitivity when exposed to heat or acidic conditions (Supplementary Fig. 4). This heightened sensitivity in the *ΔcutA* mutants may be attributed to dysbalanced levels of reactive oxygen species (ROS) generated in response to β-lactam exposure[136–138], potentially exacerbating cellular damage in the absence of CutA-mediated protective mechanisms. Global metabolomic profiling of *S. elongatus* revealed significant metabolic differences between the WT and Δ*cutA* strains. A principal coordinate analysis (PCoA) revealed significant differences in the observed metabolomes between the two groups (PERMANOVA, $P = 0.017$, Figure 4.1C).

Targeted metabolomics of *ΔcutA* and WT strains of *E. coli* and *S. elongatus* under control and heat stress (58 °C) revealed mutation-specific alterations in central metabolism. In *E. coli*, α-ketoglutarate, N-carbamoyl-L-aspartate, ADP, and GMP were decreased in the *ΔcutA* mutant under both conditions, suggesting a consistent stress-associated metabolic state. Under heat stress, citrate/isocitrate levels were further diminished, suggesting impaired replenishment of α-ketoglutarate from the tricarboxylic acid cycle. Because α-ketoglutarate fuels glutamate and proline biosynthesis and also supports amino group transfer for purine and pyrimidine biosynthesis, its depletion could coincide with observed diminished levels of glutamic acid, proline, purines, and pyrimidines (Figure 4.1D). Diminished guanine nucleotide pools could also explain the loss of pterin metabolites like dihydroneopterin, which derives from GTP.

In *S. elongatus,* coenzyme A and ornithine were decreased compared to WT under both control and heat stress. CoA, a central acyl-group carrier and protective thiol in redox regulations (protein CoAlation), undergoes copper-catalyzed air oxidation and can function as a cellular antioxidant[139] while ornithine, a precursor of polyamines, contributes to additional ROS scavenging and stress protection[140].

Together, these data suggest impaired cofactor biosynthesis, which could compromise the cell's ability to mitigate oxidative stress that usually is generated under thermal stress[141–143].

4.2 Native Metabolomics uncovers CutA Binders in Cyanobacterial Cell Extracts

To further investigate the mechanisms underlying the physiological and metabolomic changes in the Δ*cutA* mutants, we utilized a native metabolomics approach that enables rapid screening of potential binding molecules from crude cell extracts (Figure 4.2A)[133].

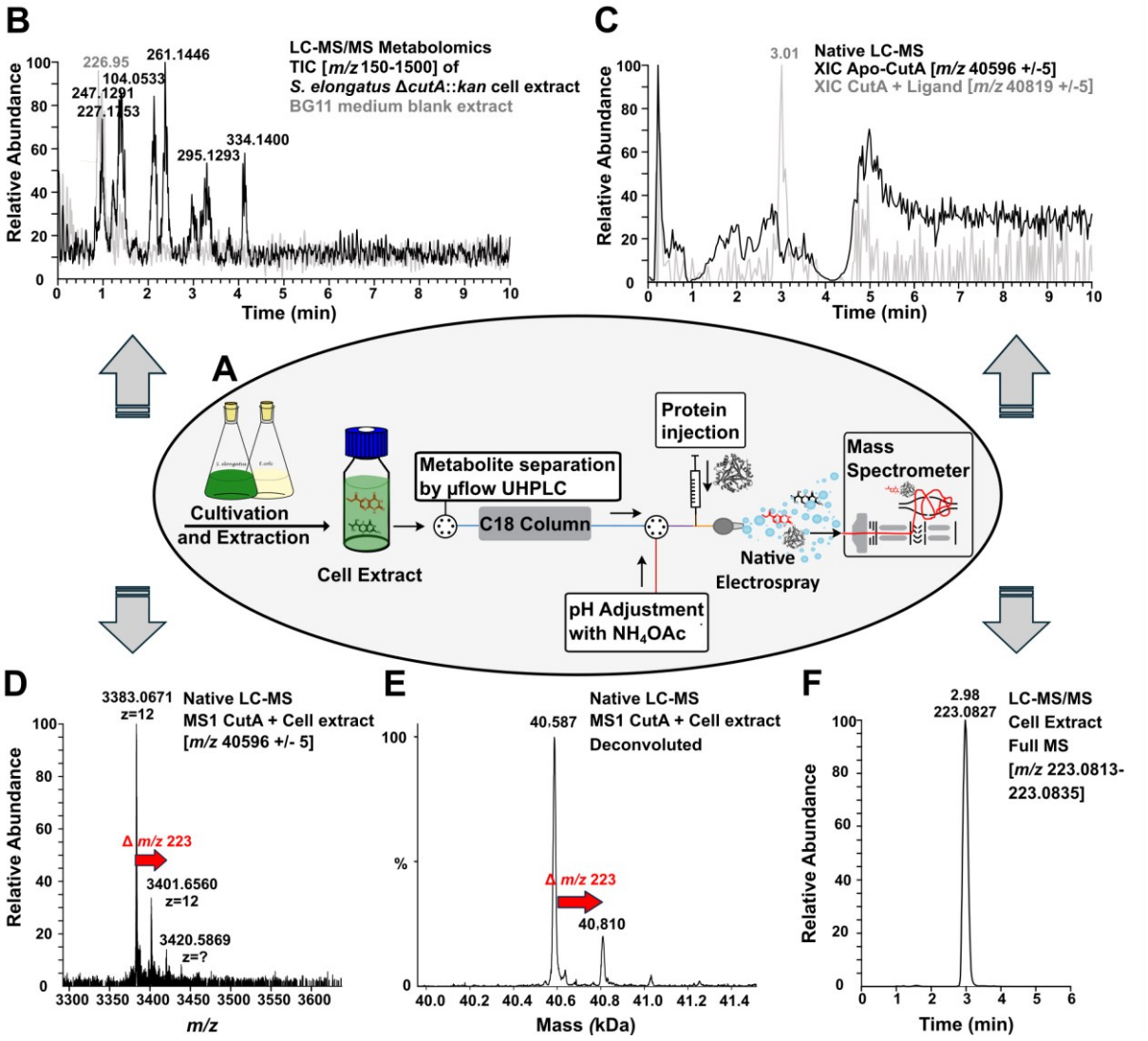

Figure 4.2: Native MS setup and identification of a putative CutA ligand using native metabolomics. **(A)** *E. coli* CutA protein was analyzed under native conditions and screened against crude cell extracts of *S. elongatus* and *E. coli* WT or *ΔcutA*. Native MS Setup (24). Cellular extracts were separated using µ-flow UHPLC. After column separation, the eluate was adjusted to near-physiological pH with ammonium acetate to preserve the protein's native state. As metabolites eluted from the column, they could interact with the infused protein, enabling detection of protein–ligand complexes as mass increases of the apo-protein by MS. A separate metabolomics run (high-resolution UHPLC-MS/MS) without protein infusion was performed to identify metabolites by comparing their RTs and masses with the mass shifts observed in the protein during binding events. **(B)** TIC of *S. elongatus* cell extract (black) and BG11 medium (control, gray), revealing the metabolomic profile. **(C)** Extracted Ion Chromatogram (XIC) of apo-CutA (black) and CutA bound to ligand (gray). The decrease in the XIC of apo-CutA at RT = 3.01 min (depicted in black) corresponds to an increase in the peak for the protein–ligand complex at the same RT (depicted in gray). **(D)** Mass spectrum of the *E. coli* CutA trimer infused to *S. elongatus* metabolites. In addition to the CutA trimer (3,383.0671 × 12 Da, including the Strep tag), a new peak appears at 3,401.6560 × 12 Da. The mass shift between the protein–ligand complex

(*m/z* 40,819.9 ± 5) and the unbound protein (*m/z* 40,596.8 ± 5) suggested a molecular weight of 223 ± 2 Da for the putative binder. **(E)** Deconvoluted spectrum showing the shift from apo-CutA to the protein-ligand complex. **(F)** Metabolomics run of cell extract without protein infusion showing the RT and mass corresponding to the protein-ligand binding event observed in panel D.

For these experiments, cell extracts from *E. coli* or *S. elongatus* were first separated by reversed-phase chromatography, which fractionates compounds according to polarity and simultaneously provides mass data for each eluting compound. Following elution from the chromatography column, the pH of the mobile phase was adjusted to near-physiological conditions (~pH 6.1) with an ammonium acetate buffer to maintain the protein's native trimeric structure. The purified protein was then infused post-column, enabling it to interact directly with the eluting metabolites. Protein- metabolite complex formation was subsequently monitored by native MS, which was detected as a mass increase of the apo-protein corresponding to the bound metabolite. Binding events were assigned to specific retention times (RTs), as complexes formed when compounds eluted within defined time frames. To verify the identity of putative binders, a parallel run of the extract without protein was performed, enabling RT and metabolite mass to be matched to the observed complexes.

Figure 4.2B presents the Total Ion Chromatogram (TIC) of *S. elongatus* cell extracts compared to BG11 medium extracts. The cell extracts exhibited a greater number of peaks, reflecting a higher diversity of compounds, particularly polar metabolites, eluting in the early stages of the chromatographic gradient. Over 1,000 molecular features were detected in *S. elongatus* extracts and more than 1,500 in *E. coli* extracts (Supplementary Fig. 5). Figure 4.2C overlays the signal of *E. coli* apo-CutA (black), measured without metabolites, and the *Ec*CutA-ligand complex (gray), observed during the analysis of *Ec*CutA with metabolites from *S. elongatus* cell extracts. A marked reduction in the apo-*Ec*CutA signal (black) coincides with the appearance of a prominent peak corresponding to the *Ec*CutA-ligand complex (gray), indicating ligand binding. Specifically, a mass shift from 40,596.8 ± 5 Da (apo-*Ec*CutA) to 40,819.9 ± 5 Da (ligand-bound *Ec*CutA) was observed at a RT of 2.98 min in the measurement of *Ec*CutA protein with *S. elongatus* cell extract (Figure 4.2D). The deconvoluted spectrum is shown in Figure 4.2E. Ligand binding was also observed with *S. elongatus* CutA (*Se*CutA) (Supplementary Fig. 6), which showed multiple species, likely corresponding to isoforms with or without the N-terminal methionine. Therefore, subsequent experiments were performed with *E. coli* CutA, which produced a single peak.

The *m/z* difference was used to calculate the ligand's exact mass. The additional LC-MS/MS run without protein, but identical LC gradient facilitated the identification of putative ligands

by comparing retention time, molecular weight, and MS/MS fragmentation patterns. In this case, a metabolite corresponding to the observed mass shift (plus a proton from ionization) was detected at 2.98 minutes in the chromatogram of the extract analyzed without protein (Figure 4.2F). The MS/MS spectrum of this compound is shown in Figure 4.3B. Based on its mass and RT, the putative binder was identified as a small polar compound. MS/MS analysis of the ion (monoisotopic mass, MR = 222.0753 Da, *m/z* = 223.0824 $[M+H]^+$) revealed a molecular formula of $C_9H_{10}N_4O_3$. Subsequent database searches yielded over ten potential structures; however, the idea that this binder represented a chemical structure was also a distinct possibility.

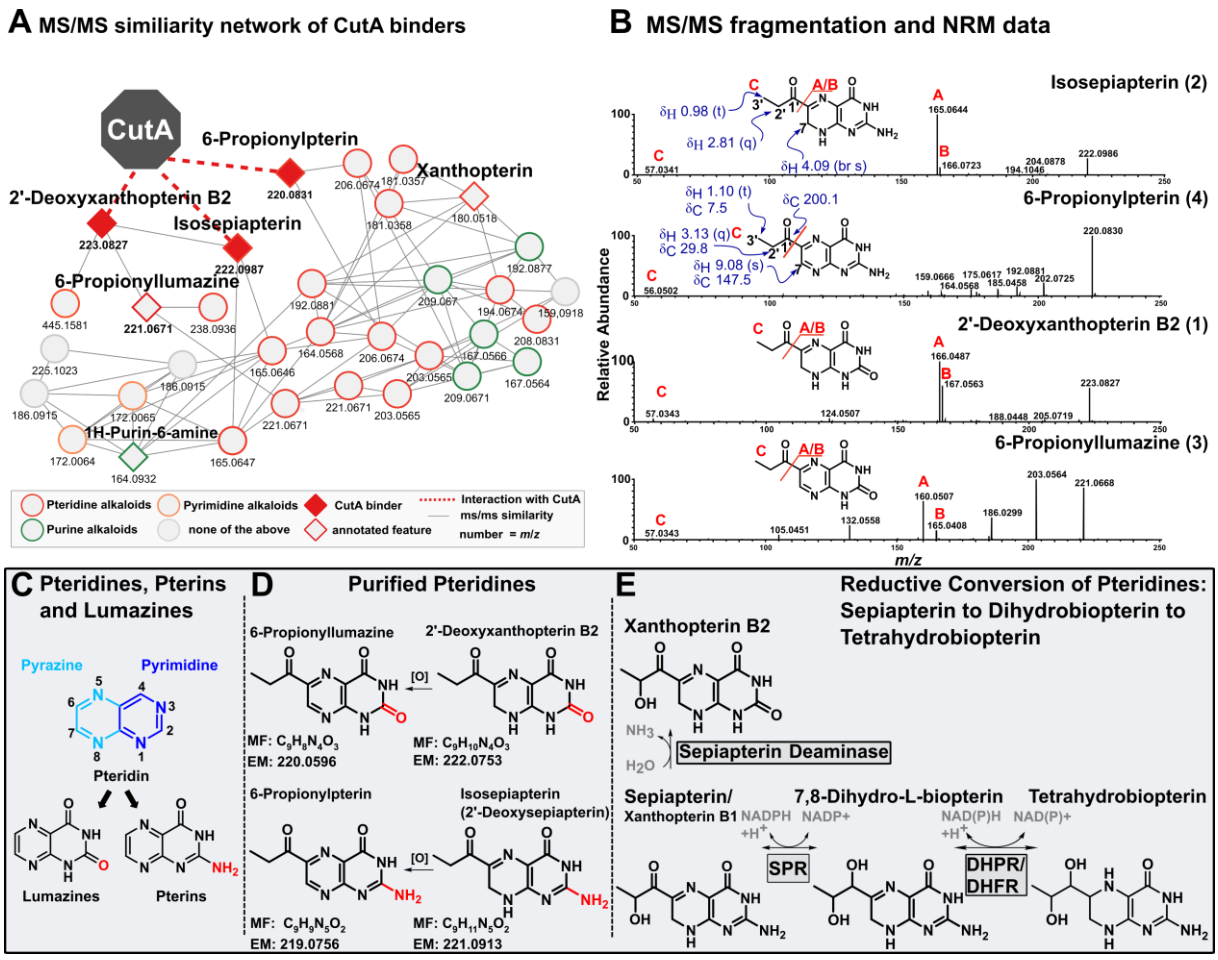

Figure 4.3: Characterization and Structural Analysis of Putative CutA ligand and Co-purified Pteridines. **(A)** Molecular correlation network based on MS/MS similarity for HPLC fractions of 2'-deoxyxanthopterin B2 and copurified compounds of *S. elongatus* cell extracts. **(B)** Comparison of MS/MS fragmentation patterns for 2'- deoxyxanthopterin B2 and copurified pteridines, with structures determined via HMBC and MS/MS. **(C)** Structural overview of pteridines: a pyrazinering (light blue) fused to a pyrimidine ring (dark blue). Pteridines are classified into lumazines (with a carbonyl group at C-2, red) and pterins (with an aminogroup at C-2, red). **(D)** Summary of purified and identified lumazines (above) and pterins (below). MF = molecular formula, EM = exact mass. **(E)** Conversion ofdifferent pteridines to tetrahydrobiopterin, relevant enzymes are depicted in gray boxes: SPR = sepiapterin reductase, DHPR = dihydropteridine reductase, DHFR = dihydrofolate reductase.

4.3 Purification and Structure Elucidation of the CutA Binder 2'- deoxyxanthopterin B2

To determine the structure of the *Ec*CutA and *Se*CutA ligand (compound 1, *m/z* 223.0824 $[M+H]^+$), we scaled up the cultivation of *S. elongatus* WT and purified this compound via solid-phase extraction and HPLC. Growth of the culture and abundance of the putative CutA ligand are presented in Supplementary Fig. 7. In addition to compound 1, three nitrogen-containing heterocyclic compounds with similar MS/MS fragmentation patterns were also purified (Figure 4.3b). Compounds 1 (*m/z* 223.0824 $[M+H]^+$) and 3 (*m/z* 221.0675 $[M+H]^+$) were detected at lower levels, while compounds 2 (*m/z* 222.0991 $[M+H]^+$) and 4 (*m/z* 220.0831 $[M+H]^+$) were produced at higher titers. Based on their similar masses and predicted molecular formulas, we hypothesized that elucidating the structure of any of these metabolites would reveal the architecture of this metabolite family. Targeting compound 4, we were able to purify enough material for NMR analysis (Supplementary Fig. 8-12). The ^{1}H NMR and HSQC NMR spectra of compound 4 in DMSO- d_6 showed one aromatic proton (δ_H 9.08), two aliphatic protons (δ_H 3.13 (2H)), and one methyl group (δ_H 1.10 (3H)). The presence of three exchangeable protons was confirmed with HPLC-MS analysis using MeCN and D_2O as eluents, wherein compound 4 became $[M+D]^+$ at *m/z* 224.1078 (Δ -0.9 ppm). The HSQC data further revealed the carbon chemical shifts of the protonated carbons (δ_H 9.08/δ_C 147.5; δ_H 3.13/δ_C 29.8; δ_H 1.10/δ_C 7.5). A COSY correlation connected H_3-3' (δ_H 1.10) and H_2-2' (δ_H 3.13); shared HMBC correlations from H_2-2' and H_3-3’ to C-1' (δ_C 200.1) then outlined a propionyl moiety. Based on the propionyl substructure, molecular formula, and natural product database searches, 6-propionylpterin (exact mass: 219.0756; molecular formula: $C_9H_9N_5O_2$) was proposed as the structure of compound 4. The UV/Vis data of compound 4 (λ_{max} 216, 304, 346 nm) was also consistent with that reported for 6-propionylpterin[144]. This pterin, found in different bacteria, is described as blue-fluorescent[145] and is supposedly a cofactor for cyanide monooxygenase and involved in the degradation of cyanide[146]. ^{1}H NMR data pertaining of compound 2 could be deciphered from ^{1}H NMR data of compound 4/compound 2 mixtures (compound 2 slowly oxidized to compound 4), showing two heteroatom-substituted protons (δ_H 4.09), two aliphatic protons (δ_H 2.81 (^{2}H)), and one methyl group (δ_H 0.98 (3H)). Four exchangeable protons could be observed (Supplementary Fig. 12). Again, using the putative propionyl substructure, molecular formula, and natural product databases, isosepiapterin was proposed as the structure of compound 2 (exact mass 221.0913, molecular formula: $C_9H_{11}N_5O_2$). The UV/Vis data of compound 2 (λ_{max} 214, 264, 286 (sh), 410 nm) was also consistent with that

reported for isosepiapterin, corroborating previous reports in *S. elongatus*, where absorption peaks at 270 nm and 410 nm were also observed for isosepiapterin[147].

At this stage, the structures of compound 1 and compound 3 were identified as lumazines, corresponding to the pterin compounds 2 and compound 4, respectively. Specifically, compound 1 was determined to be a previously undescribed lumazine, which we named 2'-deoxyxanthopterin B2 due to its structural similarity to xanthopterin B2 (PubChem CID 439706, KEGG ID C02333), a metabolite previously identified in silkworms (*Bombyx mori*)[148] and mouse cerebellum extracts[149]. 2'-deoxyxanthopterin B2 has an exact mass of 222.0753 and a molecular formula of $C_9H_{10}N_4O_3$. The UV/Vis data of 2'-deoxyxanthopterin B2 (λ_{max} 216, 282, 398 nm) is consistent with its structure. Compound 3 was identified as 6 - propionyllumazine, with an exact mass of 220.0596 and a molecular formula of $C_9H_8N_4O_3$. Its UV/Vis data (λ_{max} 214, 272, 326 nm) agreed with a previous study, which reported the presence of 6-propionyllumazine in the extract of a bioluminescent polychaete[150] without describing its function. All identified compounds belong to the pteridine class of metabolites which are characterized by a heterocyclic pteridine ring structure ($C_6H_4N_4$), consisting of a fused pyrimidine and pyrazine ring (Figure 4.3C**)**. These metabolites are further divided into pterins and lumazines. Pterins are distinguished by an amino group at the C-2 position, while lumazines possess a carbonyl group at C-2 (Figure 4.3C). Pterins are well-documented as pigments, cofactors and redox mediators[151] across biological systems, while lumazines remain understudied.

To confirm the interaction of pteridines with *Ec*CutA, we performed a series of additional native MS measurements using a pre-purified HPLC fraction enriched in 2'-deoxyxanthopterin B2 (compound 1) along with co-purified compounds of similar mass, retention time, and polarity. This fraction was expected to have a higher overall pteridine concentration compared to the crude cell extract that was previously analyzed. With this data, and the obtained information about the spectral relationship of the compounds in the HPLC fraction, a network was generated showing the predicted compound classes (Figure 4.3A). The network predominantly contained unannotated pteridines and their derivatives. We observed binding between *Ec*CutA and masses corresponding to isosepiapterin, 6-propionylpterin, and 2'-deoxyxanthopterin B2.

Pterins exhibit multielectron redox reactivity, mirroring the redox capabilities of transition metals[152]. They exist in multiple oxidation states - oxidized, semi-reduced (dihydro), and fully

reduced (tetrahydro) - interconverting via two-electron, two-proton redox reactions. Many pterins, such as biopterin, show biological activity predominantly in their reduced tetrahydro form, such as tetrahydrobiopterin (BH4), a crucial cofactor in various biological processes[153,154]. Figure 4.3E illustrates the stepwise reduction of sepiapterin to dihydrobiopterin, followed by its further conversion to tetrahydrobiopterin (BH4) through two-electron, two-proton redox reactions. Based on this knowledge, we hypothesized that our purified compounds 1-4 may be redox equivalents of each other (Figure 4.3D)**.** Due to its central role in cellular processes, we focused on tetrahydrobiopterin and its oxidized form, 7,8-dihydrobiopterin (BH2) to elucidate the potential functions of CutA. To investigate this, we obtained both compounds and tested their binding to *Ec*CutA.

4.4 Verification of CutA interactions with pteridines and copper binding

To investigate the interaction of *Ec*CutA with purified pteridine derivatives, we conducted further native mass spectrometry, microscale thermophoresis (MST), and nano differential scanning fluorimetry (NanoDSF). Native mass spectrometry experiments revealed that CutA forms complexes with purified pteridines, observed by mass shifts between apo and ligand-bound peaks (Figure 4.4A*,* left). For some pteridines, especially for 2'-deoxyxanthopterin B2 (DXan B2), we saw more than one shift, indicating multiple binding events (Supplementary Fig. 13). NanoDSF assays demonstrated that BH4 and BH2 significantly destabilize *Ec*CutA, decreasing the melting temperature (Tm) of the protein by 11.5 °C and 8.2 °C, respectively. A decrease in Tm was also observed for DXan B2, however, it could not be quantified due to limitations in the concentration range available for testing (Figure 4.4A, right). Titration experiments further confirmed concentration-dependent binding of BH2, isosepiapterin, and DXan B2, while folic acid, which contains a pteridine moiety, showed no significant interaction (Figure 4.4B).

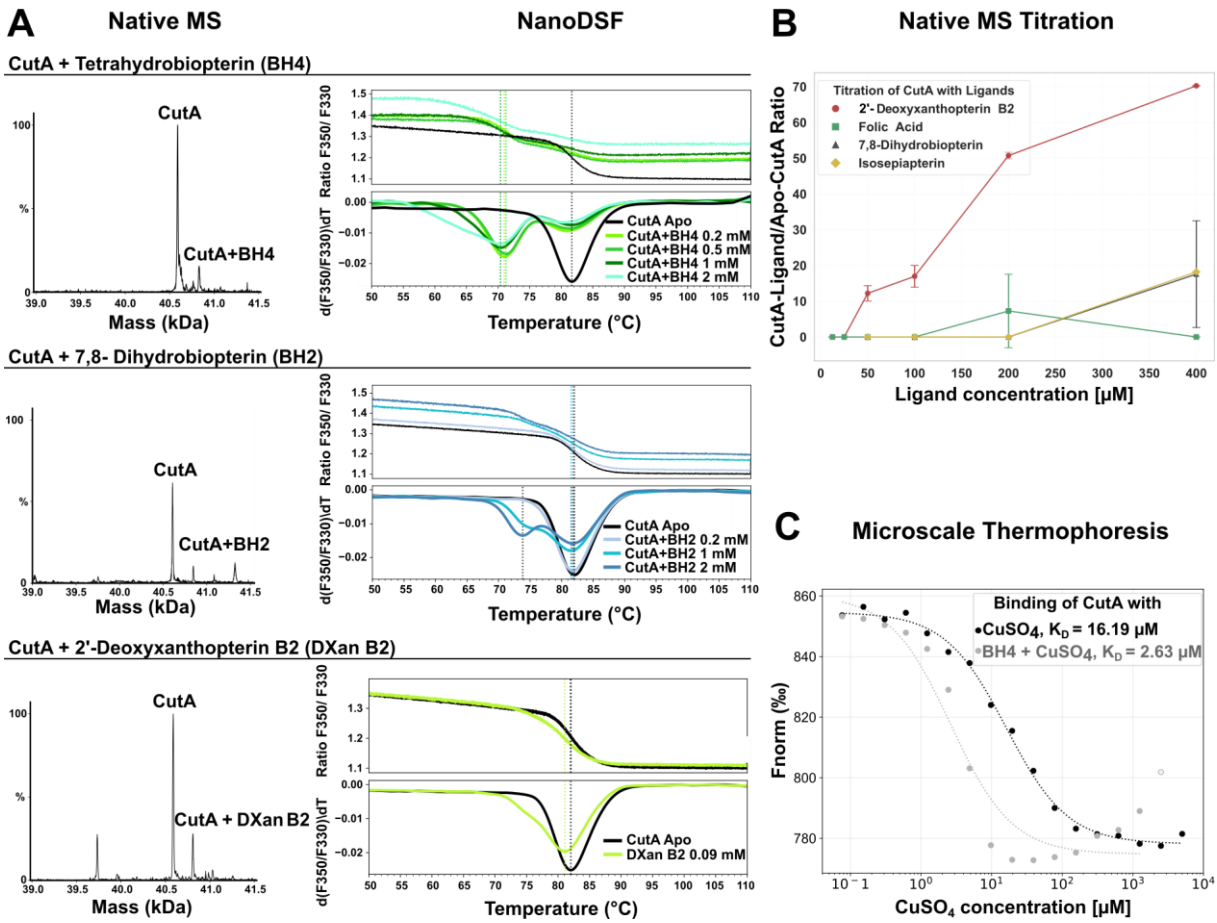

Figure 4.4: Orthogonal Binding Studies of Pteridines and $CuSO_4$ to EcCutA Using Native MS, NanoDSF, and MST.
(A) Binding of BH4, BH2, and DXan B2 Left: NativeMS spectra show mass shifts corresponding to the formation of EcCutA–pteridine complexes with BH4, BH2, and DXan B2. The corresponding NanoDSF measurements are depicted on the Right, showing changes in EcCutA thermal stability (Tm) upon ligand binding. **(B)** Native MS titration curves indicate concentration-dependent interactions of EcCutA with various pteridines (duplicates; isosepiapterin: single measurement). **(C)** MST measurements reveal binding affinities of $CuSO_4$ to EcCutA. Black curve: without BH4; gray: with constant 0.5 mM BH4 with dissociation constants (K_d) of 16.19 µM or 2.63 µM, respectively.

Given conflicting reports about the ability of *Ec*CutA to bind copper ions[12,13,85,155], we aimed to further explore this interaction. We performed MST experiments to confirm binding of copper ions to *Ec*CutA and also to evaluate whether pteridines can influence the binding of copper sulfate ($CuSO_4$). Binding curves (Figure 4.4C) demonstrated $CuSO_4$ binding to *Ec*CutA with a K_d of about 16.19 µM. In a second experiment, CutA was incubated with 0.5 mM BH4, and $CuSO_4$ binding was measured by MST. The data suggested a reduced K_d value of 2.63 µM in the presence of BH4, indicating a potential role for pterin as a cofactor of *Ec*CutA in copper binding. Many enzymes rely on both a metal ion and a pterin derivative as cofactors for essential biochemical reactions, including redox processes. Molybdopterin-dependent enzymes like nitrate reductase (EC1.7.1.2), xanthine oxidase (EC1.17.3.2)[156,157],

and sulfite oxidase (EC1.8.3.1)[158] require molybdenum, while tetrahydrobiopterin-dependent hydroxylases, such as phenylalanine hydroxylase (EC1.14.16.1)[159], tyrosine 3-monooxygenase[160] (EC1.14.16.2) or tryptophan hydroxylase (EC1.14.16.4) utilize iron. Tetrahydrobiopterin has been shown to reduce the Mn(III) center of a porphyrin to Mn(II)[161] and is also known to form complexes with cupric ions, facilitating the reduction of Cu(II)[152] (see also Supplementary Fig. 14). This dual reliance on metal ions and pterin derivatives raises intriguing questions about the potential role of CutA in mediating such interactions. Additionally, pteridine biosynthesis appears to be influenced by metal availability. The *pts* gene, which encodes 6-pyruvoyl tetrahydrobiopterin synthase, a zinc-dependent enzyme[162] that structurally resembles CutA and catalyzes the conversion of 7,8-dihydroneopterin triphosphate to 6-pyruvoyl-tetrahydropterin, the second reaction in de novo biosynthesis of BH4, was upregulated in cyanobacteria under both iron and copper perturbations[56]. Given the high levels of pteridine glycosides produced by cyanobacteria and the role of pterins in stress responses to UV and blue light[163], it is plausible that CutA's interaction with pterins extends beyond copper binding, potentially contributing to broader metal stress adaptation mechanisms. While further experiments are required to confirm and assess the mechanisms of pterin-mediated copper binding, our results provide new functional insights into CutA and the role of pterins in cellular copper homeostasis.

4.5 CutA Deficiency Increases Copper Sensitivity in *E. coli*

CutA proteins from diverse organisms contain conserved intersubunit clefts that have been observed to accommodate small buffer-derived molecules, such as Bis-Tris, MES, and HEPES, in crystallography structures[13,47]. These clefts are lined by highly conserved polar and negatively charged amino acids (Figure 4.5A), suggesting that they may provide a chemically suitable environment for accommodating small polar ligands, such as pteridines. Molecular docking predictions using Boltz-2 (NVIDIA) further support the potential for pteridines to occupy this conserved intersubunit pocket (SI Appendix, Fig. S15). To assess the functional relevance of CutA in copper stress, we examined *E. coli* wild type, a *ΔcutA::kan* mutant, and the *ΔcutA::kan* strain complemented with wild type *cutA* under its native promoter. To investigate the functional role of the predicted pteridine-binding pocket, we further analyzed a *ΔcutA::kan* strain complemented with a *cutA* allele in which three conserved glutamate residues were substituted with alanine (*cutA*::E59A,E61A,E90A). These residues (highlighted yellow in Fig. 5A), together with other conserved residues form a negatively charged surface that has been proposed to coordinate pteridine ligands.

Additionally, a Δ*folX::kan* mutant was included, as FolX is an essential enzyme in pterin biosynthesis in *E. coli*[164] (also SI Appendix, Fig. S16). Under copper stress, the *ΔcutA::kan* mutant exhibited markedly increased sensitivity relative to the WT (Figure 4.5B, control and repetition of the experiment in SI Appendix, Fig. S17). Complementation with wild type *cutA* partially rescued the phenotype. The complemented strain was able to maintain growth during the initial stress; however, it did not fully reach WT growth levels, suggesting that CutA is required for an effective response to copper stress. By contrast, complementation with *cutA*:E59A,E61A,E90A provided even weaker rescue, indicating a functional requirement for the conserved binding pocket. The *ΔfolX* mutant displayed only modest sensitivity to copper stress, indicating that CutA exerts a more critical role than FolX during copper induced stress.

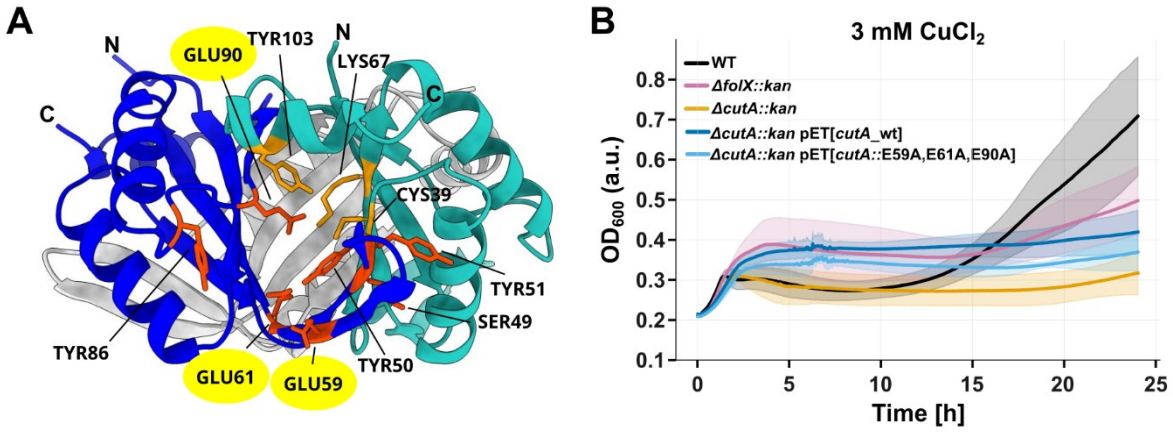

Figure 4.5: *E. coli* CutA harbors a conserved binding pocket that may accommodate small molecules such as pteridines and contributes to copper stress tolerance.
(A) Ribbon representation for the CutA trimer (crystal structure from PDB ID: 1NAQ) with one monomer in blue and the neighboring monomer in turquoise. Conserved residues are depicted in red, with three glutamates (E59, R61, E90) emphasized in yellow. **(B)** Growth curves of *E. coli* strains under copper stress (3 mM $CuCl_2$), comparing WT, *ΔfolX::kan, ΔcutA::kan*, *ΔcutA::kan* complemented with either wild-type cutA or a mutant in which the three yellow-highlighted glutamates were replaced by alanine *cutA*:E59A, E61A, E90A. All complemented constructs were expressed under the control of the native promoter.

4.6 Conclusion

Our study uncovered the interaction between the conserved trimeric protein CutA and pteridine metabolites, including tetrahydrobiopterin. Using a combination of native MS and NanoDSF, we show that these interactions destabilize *Ec*CutA, suggesting a functional link between this protein and pterin redox chemistry. Given the critical roles of pterins in redox regulation, enzymatic catalysis, and oxidative stress responses, these findings provide insights into CutA's physiological role. While *Ec*CutA has been primarily associated with copper tolerance, our data points to a more nuanced role for this protein, potentially bridging copper homeostasis and cellular redox regulation via pteridine metabolism. This function could be particularly relevant in mitigating oxidative stress caused by copper dysregulation, a process that threatens critical pathways such as respiration and photosynthesis. 2'-deoxyxanthopterin B2, a pteridine from *S. elongatus* extract that binds both *Se*CutA and *Ec*CutA, further underscores the evolutionary conservation and functional versatility of pteridine metabolites across biological systems. Our results suggest that CutA plays a key role in cellular stress responses, particularly in mitigating ROS generated by heat and ampicillin-induced stress. Under these conditions, we observed metabolic imbalances, suggesting that CutA may help to maintain cellular integrity by regulating copper and redox homeostasis. While further research is required to uncover the broader implications of CutA-pteridine interactions, our study advances the understanding of CutA beyond its structural resemblance to P_{II} proteins. In summary, our data identified pteridines as CutA binding metabolites that may enhance its copper affinity, positioning CutA as a mediator of redox regulation and stress response, especially during copper-associated oxidative stress.

4.7 Materials and Methods

Growth Conditions

S. elongatus precultures were cultivated in shaking flasks containing BG11 medium according to Rippka et al.[165] with additional 5 mM $NaHCO_3$ under photoautotrophic conditions with continuous light (30 to 60 µmol photons $m^{-2}s^{-1}$) at 28 °C and constant shaking (120 rpm), if not described differently. *E. coli* precultures were cultivated in LB broth at 37 °C with constant shaking (250 rpm).

Drop Dilution Assay

S. elongatus culture (OD_{750} = 1) was serially diluted (10^0 to 10^{-6}) in BG11 medium. Subsequently, 5 µL of the dilutions were dropped in biological replicates on BG11 agar plates, which were incubated at 28 °C with continuous illumination (30 to 60 µmol photons $m^{-2}s^{-1}$).

Ampicillin Treatment of *S. elongatus*

50 mL early exponential culture (OD_{750} of 0.4 in BG11) were treated with 10 µg/mL ampicillin and incubated with shaking at 28 °C with constant illumination (30 to 60 µmol photons $m^{-2}s^{-1}$) for two weeks.

Bacterial Strains and Molecular Cloning of Seamless *E. coli ΔcutA* Mutant

S. elongatus PCC 7942 wildtype (WT) and *S. elongatus ΔcutA::kan* strain, as reported in Selim (2021)[13], were used in this study. *E. coli* strains included the *E. coli* BW25113 WT and a *ΔcutA* mutant was cloned for this project. The *cutA* deletion mutant without an antibiotic resistance cassette was created using scarless genome editing based on the method described by Kim et al. (63). The deletion mutant was verified through PCR and sequencing to confirm the deletion of the *cutA* gene. Fragments were sequenced through the "GATC LIGHTRUN" service by Eurofins Scientific (Luxembourg), and the results were analyzed using Clone Manager 9 (Scientific & Educational Software, Denver, CO). Sequence alignment is shown in Supplementary Figure 21.

Strains and Plasmids for $CuCl_2$ Assay

E. coli wild type (WT, BW25113), *ΔcutA::kan (JW4097),* and *ΔfolX::kan*(JW2300) strains were obtained from the Keio collection. For complementation, the *ΔcutA::kan* strain was transformed with pETblank derivatives (synthesized by TWIST Bioscience) carrying either the WT *cutA* gene or an engineered variant, in which three conserved glutamine residues in the predicted binding pocket were replaced by alanines. To ensure physiologically relevant expression, both constructs include 250 bp upstream of the *cutA1* gene, covering the σ-factor binding site, Shine–Dalgarno sequence within the 5′ UTR, the -35 (CTCAACA), and -10 (TATAGT) promoter elements, as well as additional bases to ensure that the transcription start site is fully encompassed.

Growth Curve Analysis under Copper Stress

All bacterial strains and mutants were cultivated overnight at 37 °C, 250 rpm in LB-broth using 3 biological replicates respectively. Precultures were inoculated 1:100 from ON-culture and grown for 2 h using the same incubation conditions. This was followed by diluting those cultures to an OD value of 0.1 and mixing the cells with 6 mM Copper(II)chloride ($Cu(II)Cl_2$) supplemented LB-broth, using equal ratios (1:1). Analysis was carried out with 3 biological and 3 technical replicates, respectively. Growth curve measurements at 600 nm were taken at an interval of 2 min. for 29 h at 37 °C using linear, continuous shaking at 493 rpm on the BioTek Synergy HTX Multimode Reader (Agilent, Santa Clara, CA).

Protein Expression and Purification

Proteins were expressed using the pASK-IBA vector (IBA Lifesciences) and purified on an AEKTA FPLC purifier system using StrepTrap HP 5 mL columns (Cytiva), following the respective manufacturers' protocols. For the induction of CutA expression, *E. coli* Lemo (64) strains harboring pASK [*E. coli_cutA1*] or pASK[*S. elongatus_cutA*] were grown in double-concentrated lysogeny broth (LB) supplemented with ampicillin (100 µg/mL) and chloramphenicol (34 µg/mL). Cultures were incubated at 37 °C with shaking (120 rpm) until reaching an OD_{600} of 0.5. CutA expression was induced by adding anhydrotetracycline to a final concentration of 200 µg/L, followed by incubation at 20 °C with shaking (120 rpm) for 12 to 14 h. Cells were harvested by centrifugation (4,000 × g, 12 min, 4 °C), and the resulting pellets were resuspended in lysis buffer (100 mM Tris-HCl, pH 8.0, 150 mM NaCl, 1 mM

EDTA) containing DNase I, RNase A, lysozyme, and protease inhibitors. Cell disruption was achieved by sonication, and debris was removed by centrifugation (39,000 × g, 60 min, 4 °C) followed by sterile filtration (0.22 µm filters). Proteins were eluted with an elution buffer (100 mM Tris-HCl, pH 8.0, 150 mM NaCl, 1 mM EDTA, 5 mM d-desthiobiotin). Protein quality was assessed by SDS-PAGE, and collected fractions were concentrated using Amicon Ultra Centrifugal Filters (3 kDa cutoff, Merck-Millipore). The buffer was exchanged to a dialysis buffer (20 mM Tris-HCl, pH 7.8, 150 mM KCl, 50% glycerol), and the concentration of CutA was determined using bicinchoninic acid or Bradford assay. SDS pages and chromatogram of purification are shown in Supplementary Figure 22 and Supplementary Figure 23.

Targeted Metabolomics

Cells were cultivated in minimal medium (*S. elongatus* PCC 7942 in BG11, *E. coli* in M9 medium) to an OD_{750} of ~0.45. A sample volume of 2 mL (*E. coli*) or 10 mL (*S. elongatus*) was collected and filtered through 1.2 µM pore-size filters (WHA1822025, Cytiva, Marlborough, MA). Filters were transferred into 500 µL of acetonitrile: methanol: H_2O (40:40:20) at -20 °C and incubated overnight in the extraction solvent at the same temperature. After cell lysis, the extract was transferred to a new tube and centrifuged. To ensure proper lysis of cyanobacterial cells, the *S. elongatus* extract was transferred into tubes containing glass beads and subjected to ribolysis at 6.5 m/s for 30 s in 2 cycles, with a 5-min break between cycles, then centrifuged at >13,000 × g for 15 min at -9 °C. The supernatant was transferred to a new tube and stored at -80 °C until analysis. LC-MS/MS analysis was performed using a 6495A triple quadrupole LC/MS system (Agilent, Santa Clara, CA), with relative quantification achieved using a ^{13}C internal standard. Detailed measurement and analysis parameters are described in Guder et al.[166]. For data analysis, the ratios of the ^{12}C sample to the ^{13}C internal standard were calculated and normalized to cell density. Next, foldchange of each sample relative to the means of the controls (WT) was determined and log_2-transformed for improved visualization (log_2 FC = 0: no change; log_2 FC = 1: 100% increase; log_2 FC = -1: 50% decrease).

Nontargeted Metabolomics

Five WT and five *ΔcutA::kan* strains were cultivated in pentaplicates in 200 mL BG11 medium in 500 mL shaking flasks under continuous light (~50 µE) at 28 °C. Half of the cultures were harvested during exponential growth (OD_{750} ~ 0.6) and the other half after 14 d in stationary phase. Cultures were centrifuged (4,200 rpm, 60 min, 4 °C), and 75 mL per culture were harvested. Cell pellets were frozen in liquid nitrogen and stored at -20 °C. The growth medium (BG11) was treated similarly as a control. Metabolites were extracted by adding 10 mL of 20% MeOH per gram of wet cell mass, vortexed, and subjected to ultrasonic bath treatment for 10 min. Cell extracts were dried, normalized to 2.5 mg/mL, and prepared for LC-MS measurement. LC-MS/MS data were collected using a Vanquish ultrahigh-performance liquid chromatography (UHPLC) system coupled to a Q Exactive HF mass spectrometer (Thermo Fisher Scientific, Bremen, Germany) with heated electrospray ionization. Chromatographic separation was performed at a constant flow rate of 0.5 mL/min with a mobile phase consisting of A (H_2O + 0.1% formic acid) and B (MeCN + 0.1% formic acid), using a gradient from 5 to 99% mobile phase B. 0.0 min: 5% B, 8.0 min: 50% B, 10.0 min: 99% B, 13.0 min: 99% B, 13.1 min: 5% B. The separation was achieved using a Kinetex 1.7 µm C18 reversed-phase UHPLC column (100 Å pore size, 50 × 2.1 mm L × i.d.) by Phenomenex (Torrance, CA). Data were acquired in data-dependent acquisition (DDA) mode, selecting the five most abundant ions for fragmentation following each MS survey scan (Top5).

Native MS and Microflow LC-MS/MS Data Acquisition

Native MS of CutA with ligands or cell extracts was performed using a Q Exactive HF Orbitrap instrument (Thermo Fisher Scientific). Purified proteins (2 mg/mL) were rebuffered into 10 mM ammonium acetate (pH 8) through five cycles of ultrafiltration (12,000 × g, 12 min, 4 °C) using centrifugal filters. Data acquisition for native MS and microflow LC-MS/MS followed the protocol by Reher et al. (24). To stabilize pH, 100 mM ammonium acetate buffer (150 µL/min) was delivered postcolumn via a make-up pump. Proteins were injected at 2 µL/min using an integrated syringe pump, while 5 µL of cell extracts were introduced at 100 µL/min. The MS scan range was set to 2,500 to 4,000 *m/z* at a resolution of 240,000 (*m/z* 200). Chromatographic separation was performed on a Phenomenex Kinetex EVO C18 column (1.7 µm, 100 Å, 150 × 1.0 mm l. × i.d.). All-Ion Fragmentation (AIF) was performed with a collision energy (CE) of 10 eV to fragment ions across the full *m/z* range.

Native MS measurements of cell extract of *S. elongatus* and *E. coli* (WT and *ΔcutA* strains) were carried out after the cells were extracted with 20% or 80% MeOH to obtain a broad range of polar or nonpolar compounds. The cell extracts were dissolved in 50% MeOH and separated using reversed-phase Ultra High-Performance Liquid Chromatography (UHPLC). Metabolomics runs were conducted under identical chromatographic conditions, excluding protein infusion. Sample volumes of 5µL were injected at a flow rate of 100 µL/min, using DDA (Top 5) with a scan range of 80 to 1,500 *m/z*. Pteridine titrations were performed using a 5 to 99% gradient over 5 min. Native MS was carried out in the 2,000 to 5,000 *m/z* range, with a resolution of 240,000 at *m/z* 200 and positive polarity and CE of 10 eV. A 33% ammonium acetate solution was infused via a make-up pump. Ligands dissolved in 50% MeOH were injected as 2 µL aliquots. For the binding curve, pteridines were prepared at 800 µM stock concentrations and diluted 1:2 for binding assays. Native MS spectra were deconvoluted using UniDec[167] (Charge range 6 to 20, mass range 10,000 to 50,000, mass sampling every 1.0 Da, peak detection range 5.0 ppm, peak detection threshold 0.1), and shifted mass peak intensities were expressed as percentages relative to the apo protein.

LC-MS/MS Data Analytics Workflow

Feature tables (.csv) and MS/MS spectra files (.mgf) were deposited in the MassIVE repository. LC-MS/MS raw files were converted to centroided mzML format using MSConvert from the ProteoWizard software package[168]. The files were then processed using MZmine3[169] for feature detection and alignment. The LC-MS/MS data were further submitted to GNPS[170] and GNPS2[171] (gnps2.org) for feature-based molecular networking analysis and metabolite annotation. The obtained metabolomics data were further processed and analyzed using SIRIUS[120] to predict molecular formulas and annotate fragmentation patterns from the high-resolution MS data, which provided further insights about the metabolites in the HPLC fraction. Feature-based molecular networking results were screened and visualized in Cytoscape[172], and statistical analyses were carried out using the Statistical Analysis of Feature-Based Molecular Networking script[121] or the associated web application (https://fbmn-statsguide.gnps2.org). Background noise was eliminated by removing blanks with a cutoff of 0.3 to improve data accuracy. To examine relationships between samples, Principal Coordinates Analysis (PCoA) was performed using the Canberra distance matrix to visualize dissimilarities among the samples.

Growth Conditions for Compound Purification

S. elongatus PCC 7942 was grown under continuous light conditions in a 10 L flask containing BG11 medium and, in parallel, for the purpose of higher cell mass in a CellDEG® (CellDEG GmbH, Germany) system with freshwater medium.

Pteridine Purification

Cells were harvested by centrifugation (4,200 rpm, 4 °C). The cell pellets were extracted with 20% MeOH. The cell extract was dry-loaded onto 5× Celite and fractionated using silica gel (100% hexane, 30% EtOAc in hexane, 100% EtOAc, 1% MeOH in DCM, 10% MeOH in DCM, 100% MeOH, each fraction ~5 column volumes). The 10% and 100% MeOH fractions were combined and concentrated. The product was first purified via HPLC [Kinetex C18, 250 × 21.2 mm, 5 µm, 100 Å pore size, 5% MeCN in water (0.1% TFA) for 5 min, 5 to 30% MeCN (0.1% TFA) in water over 15 min, 13 mL/min, 254 nm, tR = 14 to 20 min]. The product was further purified via two rounds of isocratic HPLC [Luna C18(2), 250 × 10 mm, 5 µm, 100 Å pore size, 10% MeCN in water (0.1% TFA), 3 mL/min, 254 nm, tR = 14 to 16 min; then PFP C18(2)column 250 × 10 mm, 5 µm, 100 Å pore size, 10% MeCN in water (0.1% TFA), 3 mL/min, 254 nm, tR = 16 to 18 min] to yield <1 mg of compound 4 and <1 mg of a mixture of compound 2 and 4.

Structure Elucidation of Compounds 1-4

^{1}H and 2D (COSY, HSQC, HMBC, NOESY) NMR spectra were recorded on a Bruker Avance III HDX 700 MHz spectrometer fitted with a 5 mm Prodigy (^{1}H,^{19}F/^{13}C/^{15}N) TCI Cryoprobe. ^{1}H NMR data were recorded at 700 MHz in DMSO-d_6 (2.50 ppm), and ^{13}C NMR data were recorded at 175 MHz in DMSO-d_6 (39.5 ppm). NMR spectra were processed using MestReNova (Mnova 14.3.0, Mestrelab Research) software. The following abbreviations are used to indicate the multiplicity in ^{1}H NMR spectra: s = singlet, d = doublet, t = triplet, q = quartet.

1: λ max (MeCN/H_2O/0.1% FA): 216, 282, 398 nm; HRESIMS *m/z* $[M+H]^+$ 223.0831 calcd for $C_9H_{10}N_4O_3$, 2'-deoxyxanthopterin B2.

2: λ max (MeCN/H_2O/0.1% FA): 214, 264, 286 (sh), 410 nm; HRESIMS *m/z* $[M+H]^+$ 222.09910, calcd for $C_9H_{11}N_5O_2$, Isosepiapterin

1H NMR: δ 4.09 (s, 2H), 2.81 (q, *J* = 7.5 Hz, 2H), 0.98 (t, *J* = 7.5 Hz, 3H)

3: λ max (MeCN/H_2O/0.1% FA): 214, 272, 326 nm; HRESIMS *m/z* $[M+H]^+$ 221.0674, calcd for $C_9H_8N_4O_3$, 6-Propionyllumazine

4: λ max (MeCN/H_2O/0.1% FA): 216, 304, 346 nm; HRESIMS *m/z* $[M+H]^+$ 220.08345, calcd for $C_9H_9N_5O_2$, 6-Propionylpterin ^1H NMR: δ 9.08 (s, ^1H), 3.13 (q, *J* = 7.3 Hz, 2H), 1.10 (t, *J* = 7.3 Hz, 3H); HSQC/HMBC: δ_H 9.08/δ_C 147.5; δ_H 3.13/δ_C 29.8; δ_H 1.10/δ_C 7.5; δ_C 200.1.

NanoDSF.

NanoDSF was performed using a Prometheus NT.48 instrument (Nanotemper Technologies, Munich, Germany) with standard Prometheus capillaries (PR-C002). Protein samples and ligands, both dissolved in HEPES buffer, were analyzed with a temperature ramp of 0.5 °C/min from 30 °C to 110 °C. Thermal stability was assessed by monitoring the fluorescence ratio (F_{350}/F_{330}) of tryptophan residues, with the melting temperature (Tm) determined from the inflection point of the fluorescence ratio curve and confirmed by first derivative analysis. ~300 µM of *E. coli* CutA trimer was used for the measurements.

MST

To investigate protein interactions via MST, *E. coli* CutA was labeled with a fluorescent dye using the Protein Labeling Kit RED-NHS® 2nd Generation (NanoTemper Technologies). NHS labeling attaches fluorescent dyes to proteins by reacting with primary amines to form stable amide bonds. This was necessary due to the fluorescence properties of pteridines. MST measurements were conducted with 10 nM protein concentration. The protein and ligands were dissolved in HEPES or MST buffer (50 mM Tris, 150 mM NaCl, 0.05% Tween-20, 10 mM $MgCl_2$, pH 7.4) for analysis. Ligands were prepared in a titration series with 1:2 dilutions, starting at 2.5 or 5 mM, and loaded into Monolith NT.115 capillaries. MST was performed using the Monolith NT.115 with settings of 25 °C TempControl, 80% LED Power, and 20% MST Power. Dose–response data were analyzed with MO.Affinity Analysis Software v2.3 (NanoTemper) and further fitted using a custom Python script applying nonlinear regression with a one_site_binding model.

Structural Visualization and Docking

CutA trimer structure (PDB ID: 1NAQ) was visualized and prepared using ChimeraX[173]. Molecular docking of tetrahydrobiopterin (BH_4) to the conserved intersubunit binding pocket of CutA was performed using Boltz-2 (NVIDIA)[174]. Predicted interactions, including hydrogen bonds and cation-π interactions, were analyzed and visualized within ChimeraX.

Data, Materials, and Software Availability

Native MS with crude cell extracts: (MassIVE MSV000088919), Zenodo: https://doi.org/10.5281/zenodo.10171306. Native MS with HPLC extract of pteridine purification: MassIVE MSV000092597. Native MS of *S. elongatus* CutA + Cell extract or HPLC extract: MassIVE MSV000092597. Nontargeted Metabolomics of *S. elongatus* WT vs. *ΔcutA::kan* exponential and stationary growth phase (for PCoA): MassIVE MSV000092427 or Zenodo DOI: https://doi.org/10.5281/zenodo.10041900. Native MS CutA and different pteridines: Zenodo: https://doi.org/10.5281/zenodo.14749948. Zenodo. https://doi.org/10.5281/zenodo.14750590. Nontargeted Metabolomics of crude *E. coli* cell extracts (WT, *ΔcutA::kan*, *ΔcutA::folX*, complemented strains): https://doi.org/10.5281/zenodo.17178004 and https://doi.org/10.5281/zenodo.17114483.

ACKNOWLEDGMENTS.

We thank Paolo Stincone, Michael Haffner, Nelli Deobald, and Andreas Kulik for technical support, Thomas Hamm for advice on protein modeling and molecular docking, as well as Klaus Hantke and Gulliver Black for insightful discussions. We are grateful to Dr. Libera Lo Presti for their critical review of the article. We acknowledge funding through the German Research Foundation through the Cluster of Excellence (EXC2124–390838134) Controlling Microbes to Fight Infections at the University Tuebingen (projects: 1-06.009 and 1-06.010). K.S.-L. was supported through an ExFab fellowship through the NSF under Cooperative Agreement DBI-2400327. This work was supported in part by the National Institute of General Medical Sciences, GM160154 to D.P. and GM158026 and AI181382 to A.H., and by the Simons Foundation International through award SFI-LS-ECIAMEE-00013858 to D.P.

4.8 SUPPLEMENTARY INFORMATION

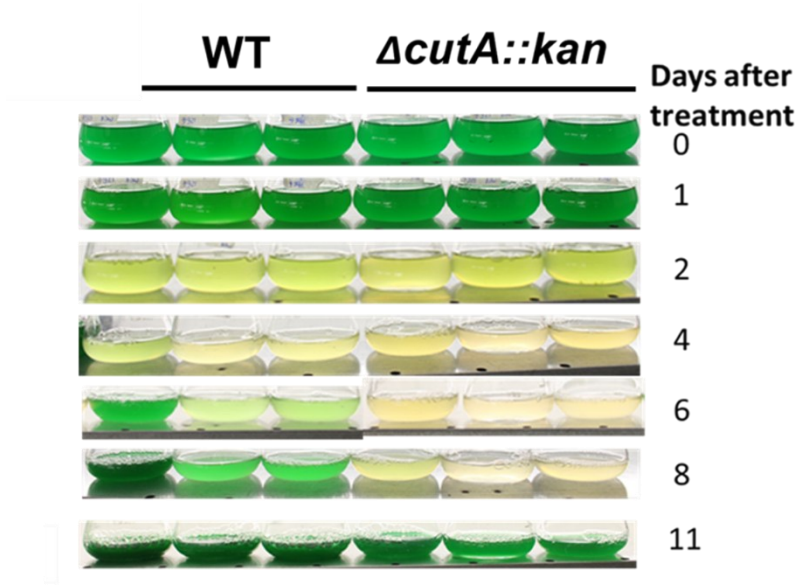

Supplementary Figure 1: Repetition of viability assay in liquid cultures of *S. elongatus*.
Cultures were treated with 10 µg/mL ampicillin and inoculated at a starting OD_{750} of 0.4. Incubation was carried out under continuous light (30-60 µmol photons $m^{-2}s^{-1}$) at 28°C in biological triplicates.

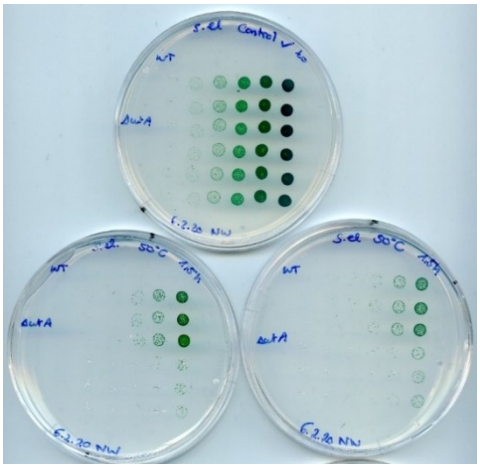

Supplementary Figure 2: Full plates and repetition of the viability assay presented in Figure 4.1.
The viability drop dilution assay demonstrates impaired recovery of the *ΔcutA::kan* mutant following heat stress. *Synechococcus elongatus* WT and *ΔcutA::kan* cultures were exposed to 50°C for 1.5 hours, serially diluted (1:10, right to left), and incubated at 28°C under constant light (30-60 µmol photons $m^{-2}s^{-1}$) for 7 days.

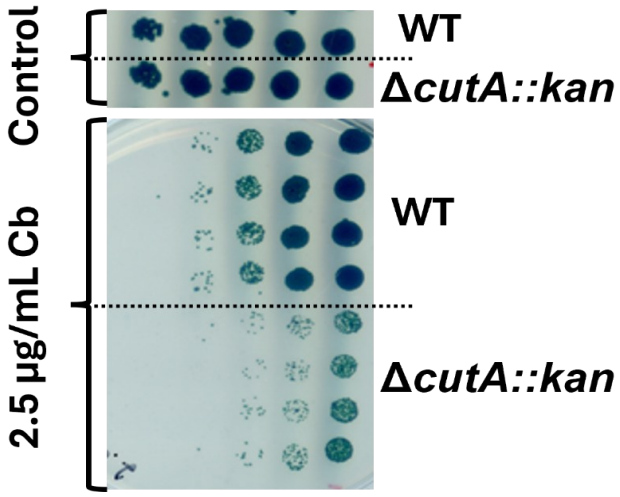

Supplementary Figure 3: Viability assay of *Synechococcus elongatus* WT and *ΔcutA::kan* on BG11 agar supplemented with 2.5 µg/mL carbenicillin (Cb).
A drop dilution assay was performed with 1:10 serial dilutions, starting at an OD_{750} of 1. Plates were incubated at 28°C under continuous light (30-60 µmol photons $m^{-2}s^{-1}$) for 14 days.

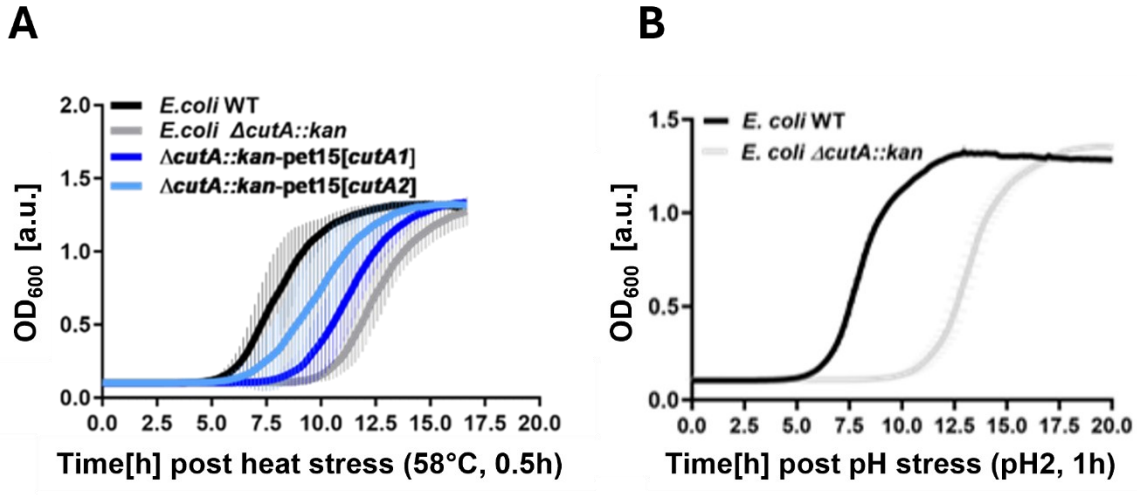

Supplementary Figure 4: Recovery of *E. coli* WT and ΔcutA::kan strains after heat and acid stress.
(A) Growth under heat stress. *E. coli* WT (black), *ΔcutA::kan* (gray), *ΔcutA* pET15[*cutA1*] (bright blue), and *ΔcutA::kan* pET15[*cutA2*] (dark blue) were pre-cultured in 5 mL LB in glass tubes. Expression of CutA in the pET15 construct was induced with 0.1 mM IPTG for 1 hour, followed by dilution to OD_{600} = 0.2 in fresh LB without IPTG. Cultures were incubated in 2 mL Eppendorf tubes at 58°C for 30 minutes on a heat block with shaking (500 rpm). Growth was monitored after heat treatment. (**B) Recovery after acid stress. Wt and** *ΔcutA::kan* strain were subjected to acidic stress at pH 2 for 1 hour at an initial OD_{600} of 0.2. Recovery was monitored in fresh LB medium by OD_{600} measurements.

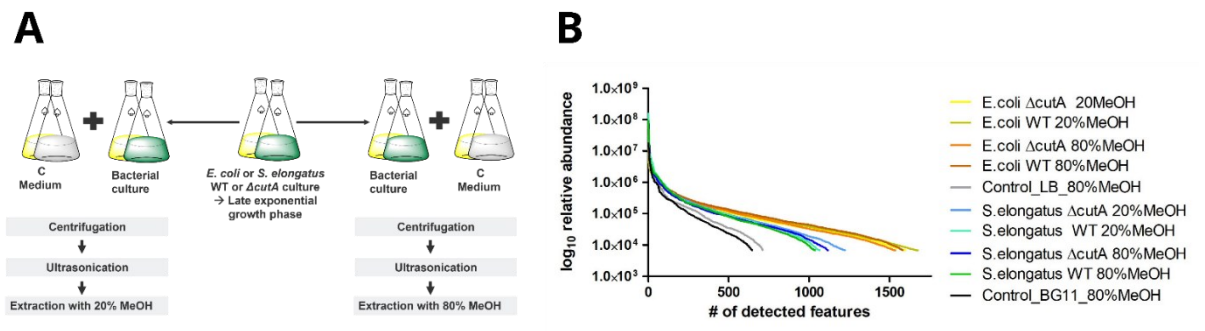

Supplementary Figure 5: (A) Extraction of *S. elongatus* and *E. coli* cells and (B) metabolite abundance. Extraction from late exponential phase cultures using 20% or 80% MeOH to capture a broad range of polar and non-polar compounds. **(B)** Feature abundance in media (gray) compared to *E. coli* (yellow) and *S. elongatus* extracts (blue and green).

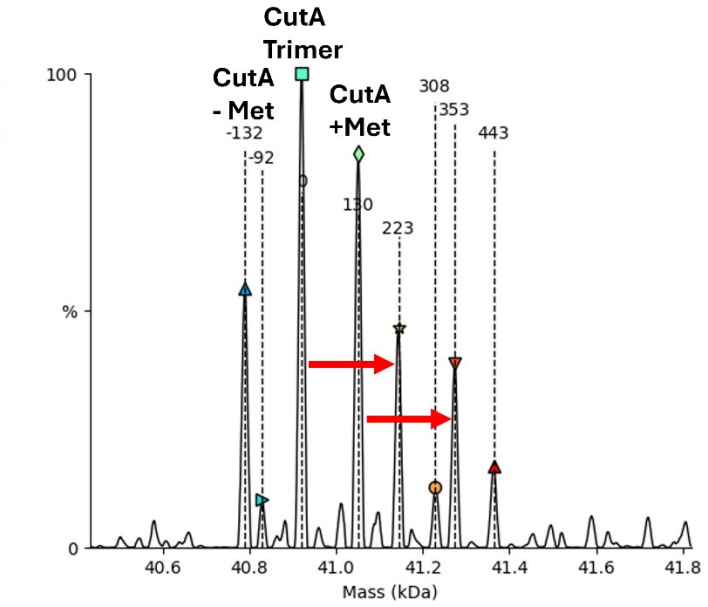

Supplementary Figure 6: Native mass spectrometry analysis of *S. elongatus* CutA.
Testing of HPLC extract containing various pteridines, including 2'-deoxyxanthopterin B2 (DXan-B2). Native MS revealed three distinct CutA trimers, likely resulting from methionine aminopeptidase activity, as the peaks were spaced by the mass of one methionine. Data was deconvoluted using UniDec, revealing mass shifts corresponding to *S. elongatus* CutA in complex with 2'-deoxyxanthopterin B2 (shift indicated by red arrow). Met= Methionine.

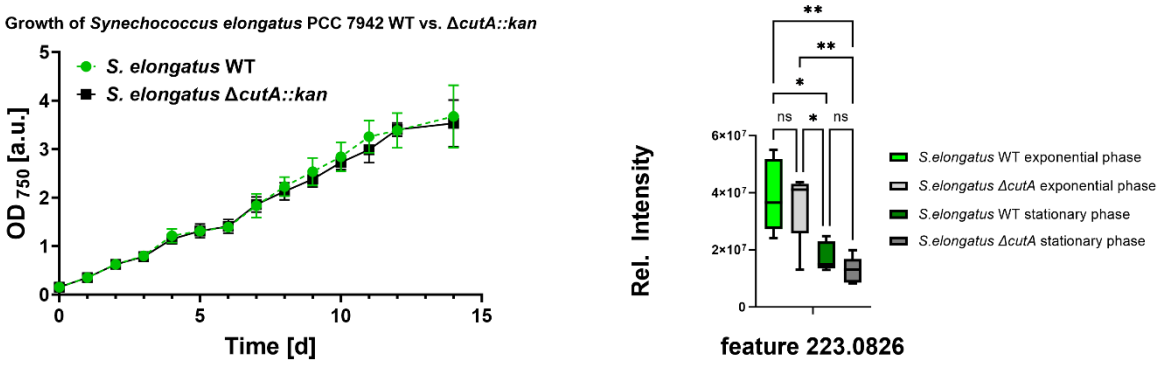

Supplementary Figure 7: Growth and abundance of DXan-B2.
Left: Growth of *S. elongatus* WT and *ΔcutA::kan* and right: abundance of 2'-deoxyxanthopterin B2. Statistical analysis was conducted using one-way ANOVA, followed by Tukey's multiple comparison test for post-hoc analysis. Analyses were performed in GraphPad Prism version 10.1.2 (334).

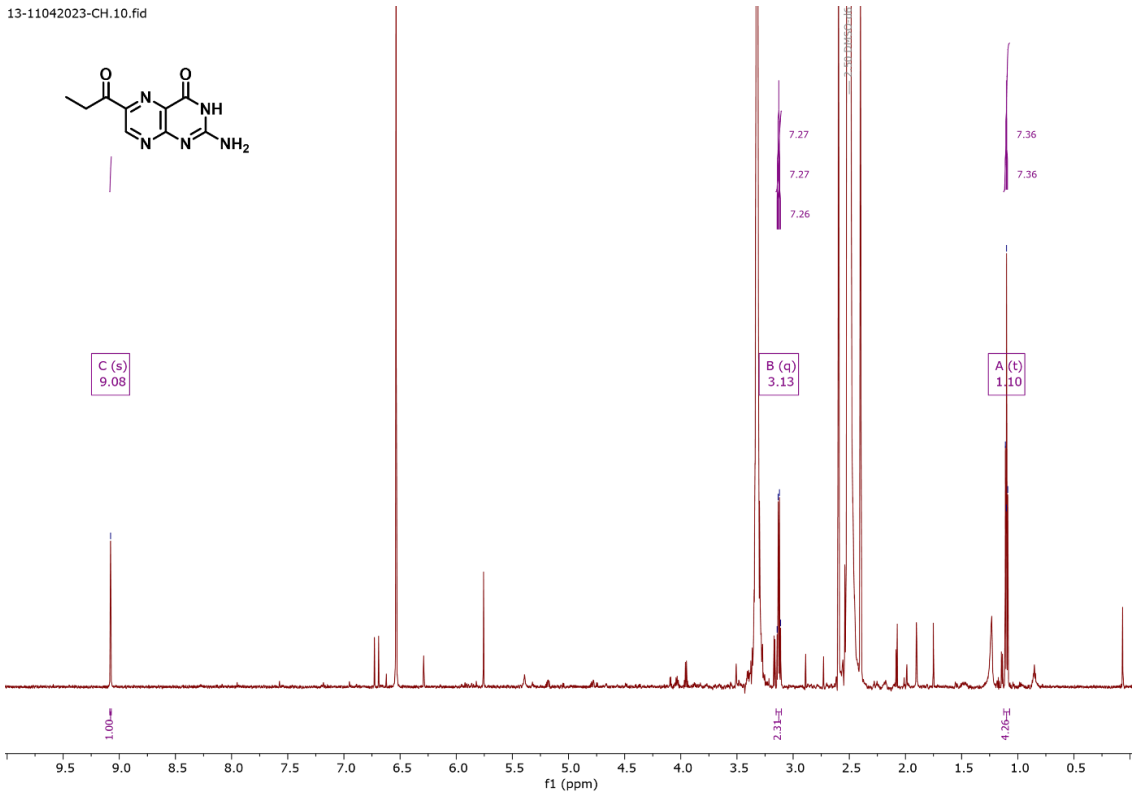

Supplementary Figure 8: ^{1}H NMR (DMSO-d_6, 700 MHz) of compound 4.

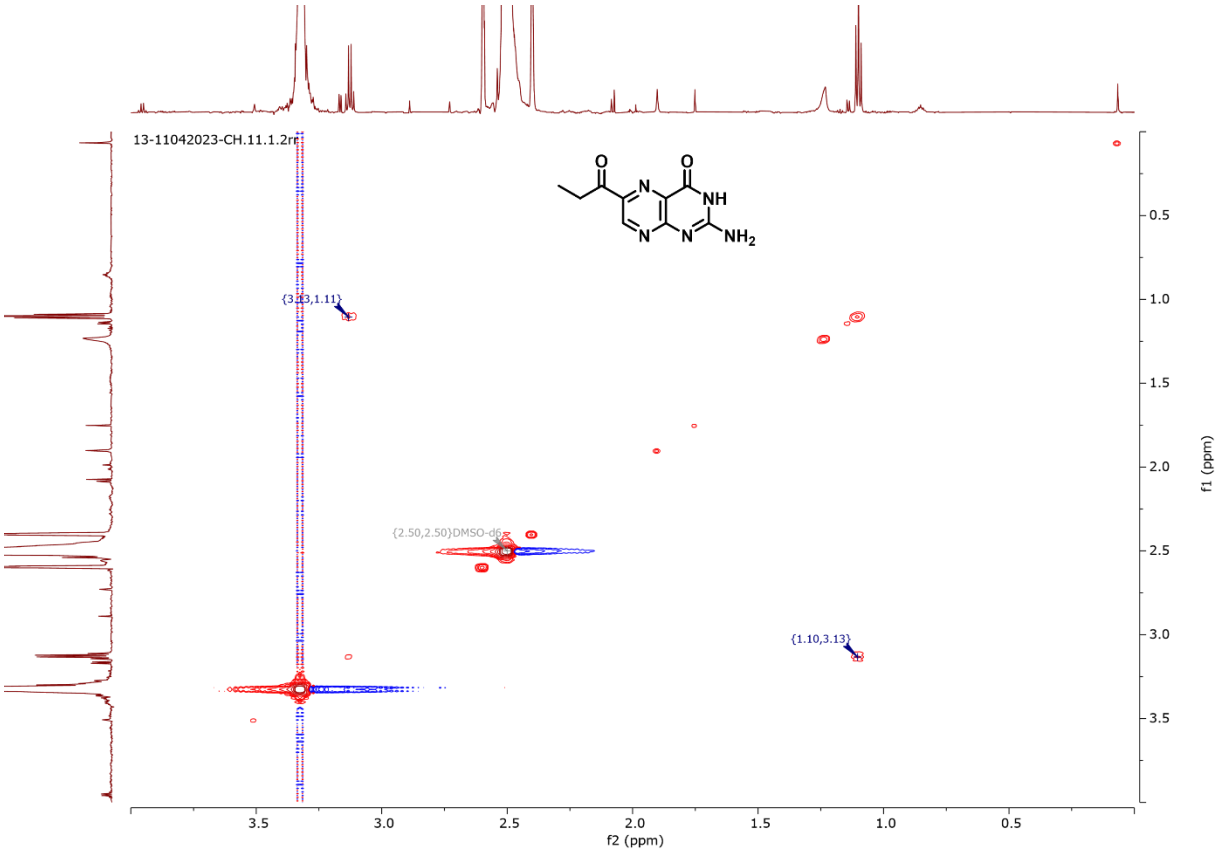

Supplementary Figure 9: COSY (DMSO-d6, 700 MHz) of compound 4

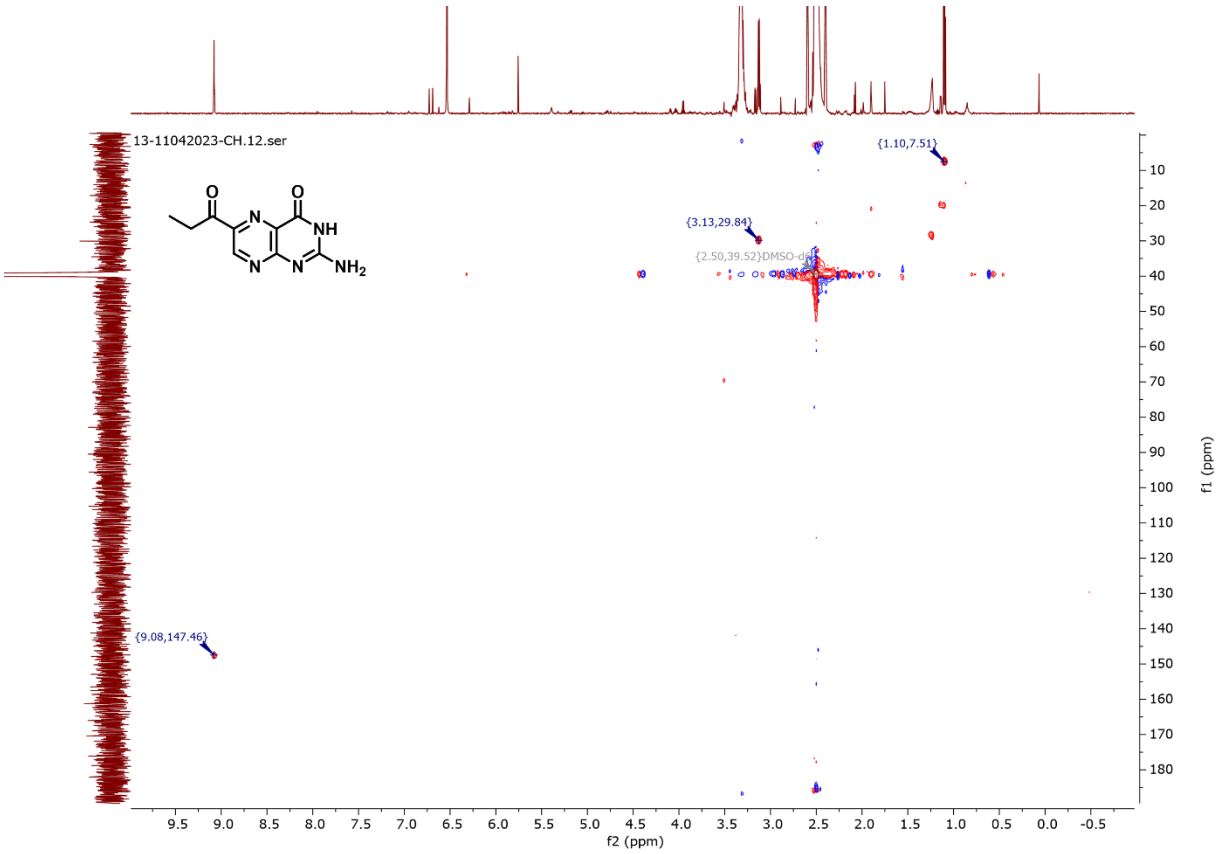

Supplementary Figure 10: HSQC (DMSO-d6, 700 MHz) of compound 4.

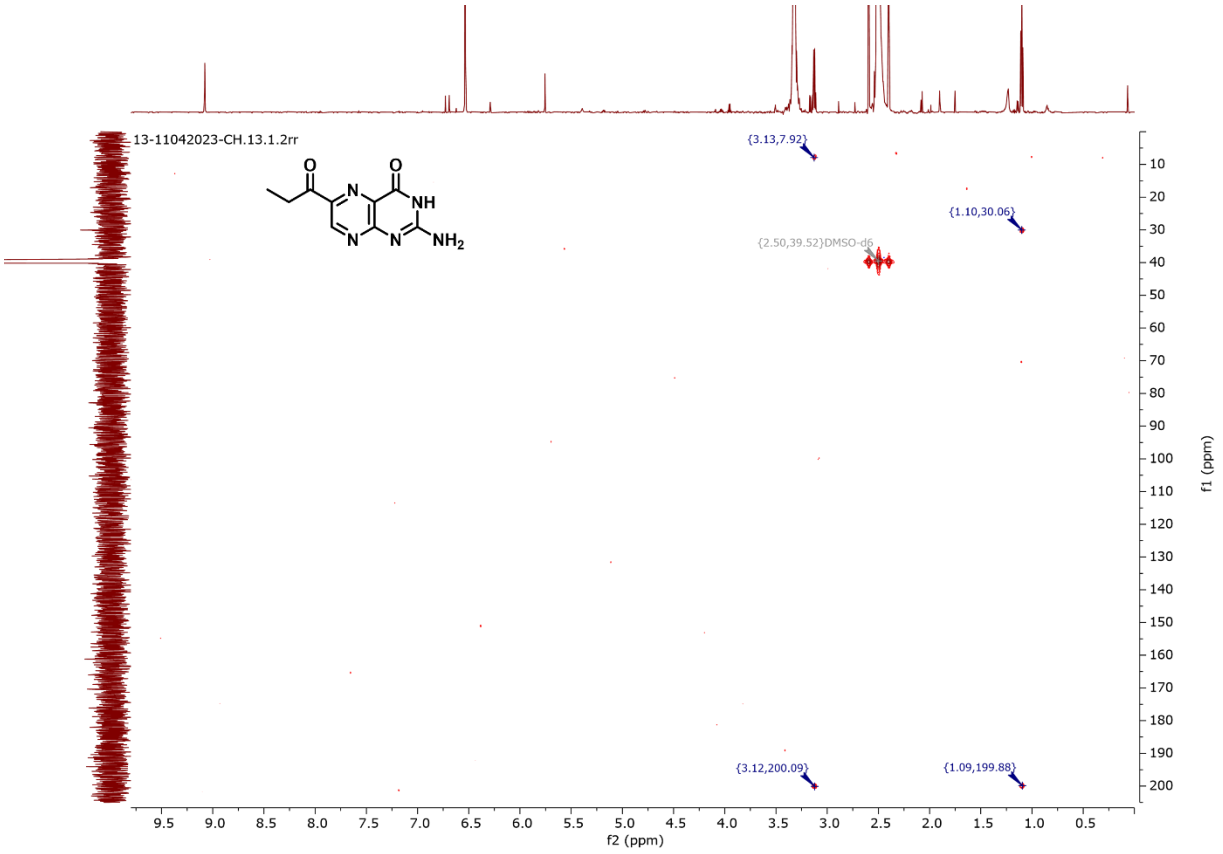

Supplementary Figure 11:HMBC (DMSO-d6, 700 MHz) of compound 4.

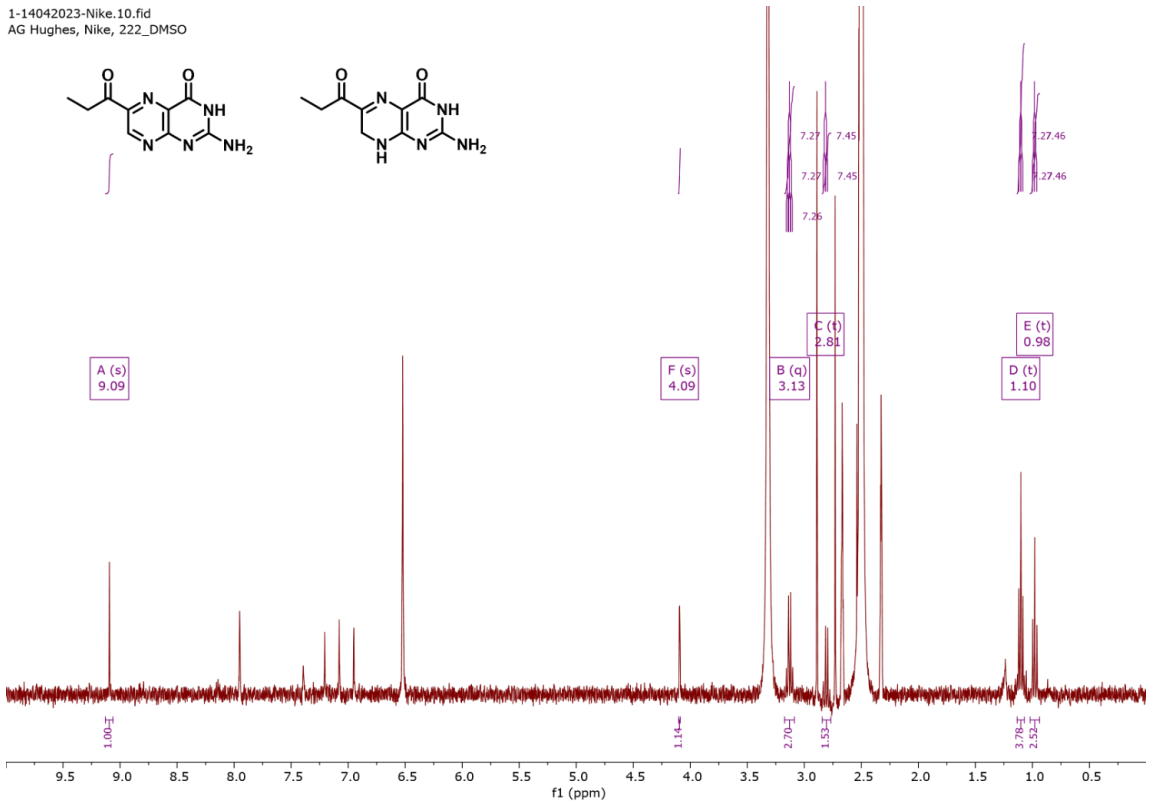

Supplementary Figure 12:1H NMR (DMSO-d6, 700 MHz) of 2 and 4.

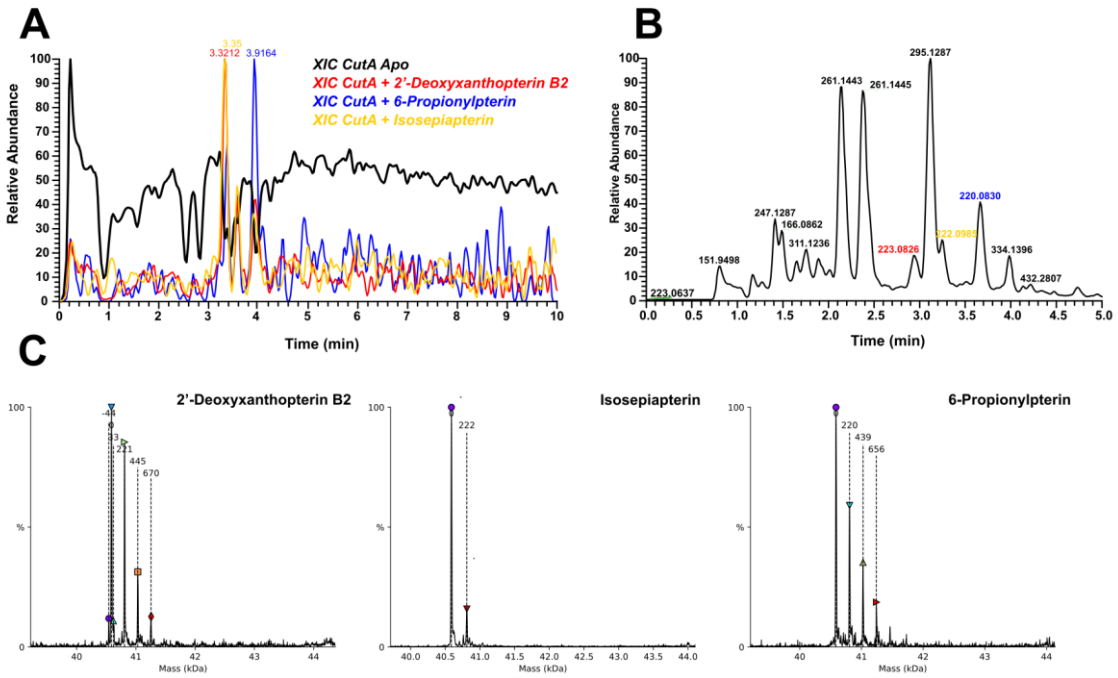

Supplementary Figure 13: Different pteridines binding to CutA.
(A) XIC of Apo *E. coli* CutA (black), XIC of *Ec*CutA+ different identified pteridines in HPLC fraction of *S. elongatus* cell extracts **(B)** TIC of HPLC fraction containing 2'-deoxyxanthopterin B2 **C)** Native MS of *Ec*CutA with various pteridines, indicating potential multiple binding events.

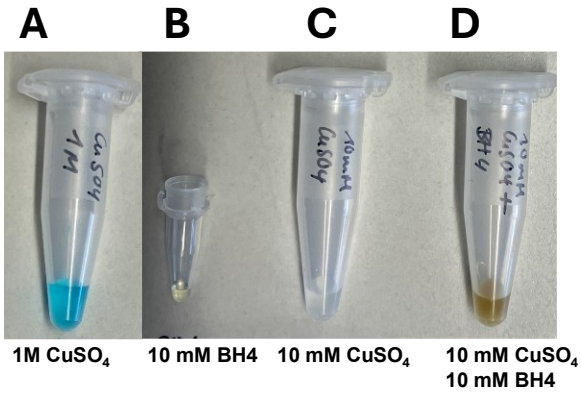

Supplementary Figure 14: Reaction of $CuSO_4$ with tetrahydrobiopterin.
(A) 1M $CuSO_4$ displays characteristic blue color. **(B)** 10 mM BH4 is colorless. **(C)** 10 mM $CuSO_4$ appears nearly colorless. **(D)** A 1:1 mixture of 10 mM $CuSO_4$ and 10 mM BH4 rapidly develops a brown color, indicating a redox reaction and formation of a Cu^{2+}-BH4 complex.

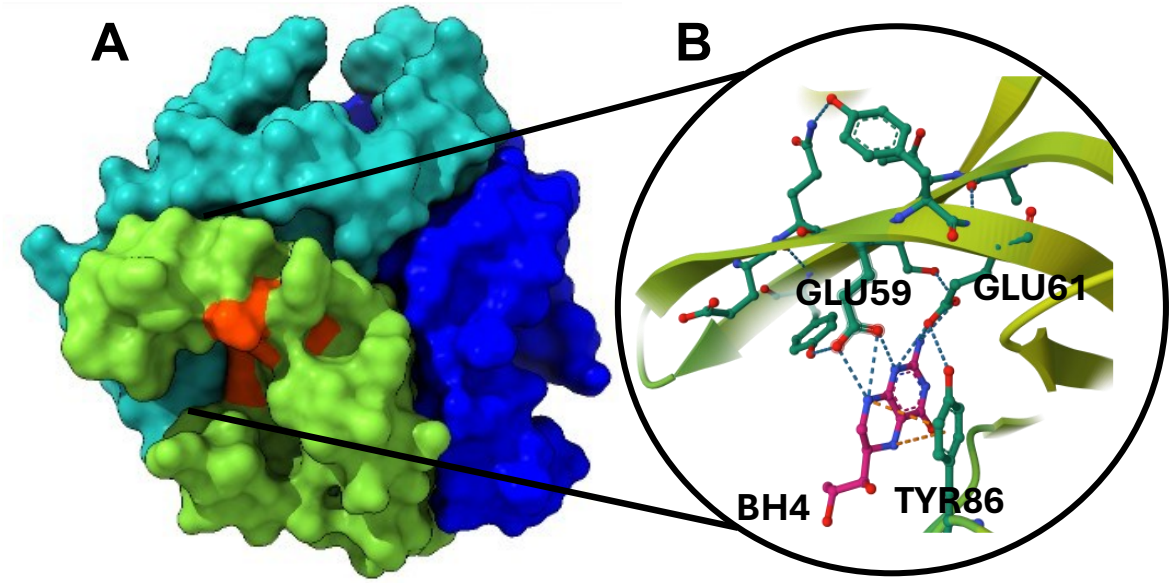

Supplementary Figure 15: Docking of BH4 to CutA.
(A) Surface representation of the CutA trimer, with each monomer shown in a different color. Conserved glutamate residues are highlighted in red. Structures are based on PDB ID:1NAQ and were visualized and aligned using ChimeraX.
(B) Molecular docking prediction of tetrahydrobiopterin (BH4, pink) binding to the conserved intersubunit pocket of CutA. Docking was performed using Boltz-2 (NVIDIA). Orange dotted lines indicate cation-π interactions, and blue dotted lines indicate hydrogen bonds.

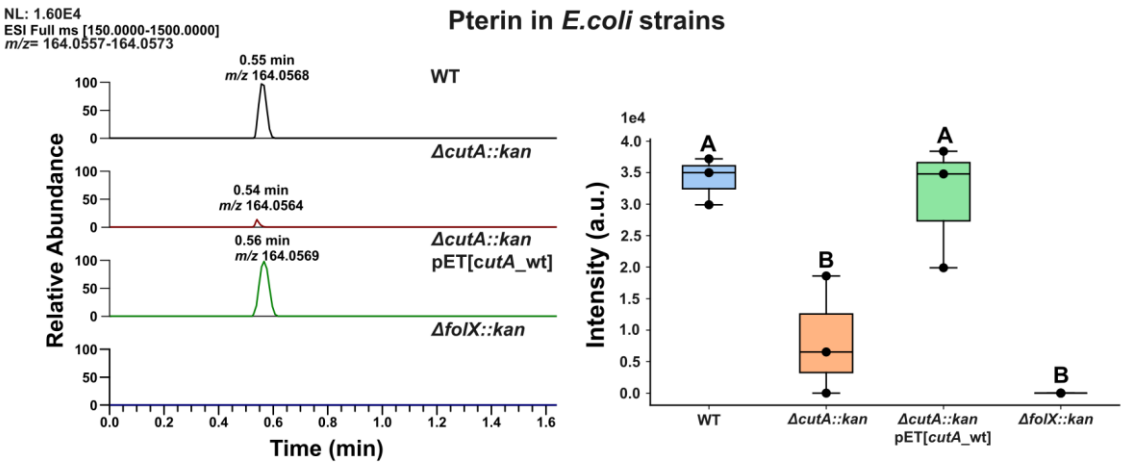

Supplementary Figure 16: Pterin abundance in different *E. coli* cell extracts.
(A) Extracted ion chromatograms (XICs) of pterin (*m/z* 164.0568) in crude extracts from WT, *ΔcutA::kan*, *ΔcutA::kan* complemented with *cutA* under its native promoter, and *ΔfolX::kan*. The signal is strongly reduced in *ΔcutA*::kan and absent in *ΔfolX::kan*, while complementation restores it to WT levels. **(B)** Box plots of three biological replicates showing pterin intensity in each strain. Statistical analysis was conducted using one-way ANOVA, followed by Tukey's multiple comparison test as a post-hoc analysis. Significant differences between means ($p \leq 0.05$) are indicated by different letters. Data represents the mean ± standard deviation of three independent replicates.

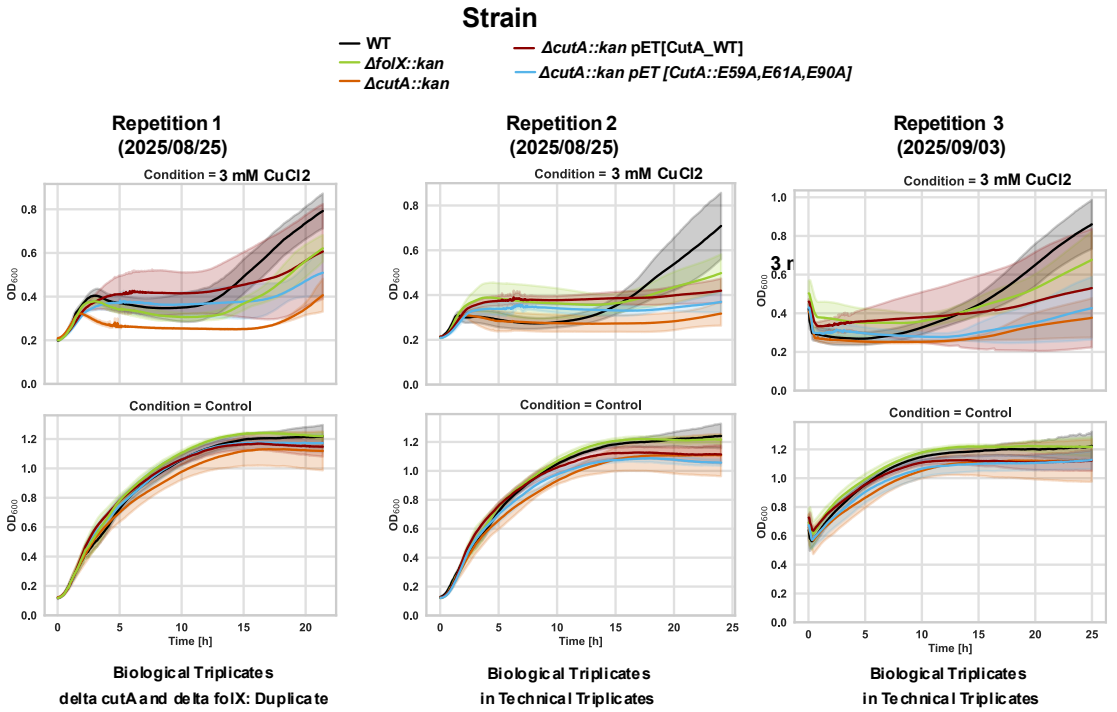

Supplementary Figure 17: Growth of *E. coli* WT, *ΔcutA::kan*, and *ΔfolX::kan* under copper stress. Wild-type (WT, BW25113), *ΔcutA::kan* (JW4097), and Δ*folX::kan* (JW2300) strains were obtained from the Keio collection. The *ΔcutA::kan* strain was complemented with pETblank-derived plasmids carrying either the wild-type cutA gene (*ΔcutA::kan pETblank* [*cutA*_WT] + amp resistance) or a triple-mutant variant (pETblank[*cutA*::E59A,E61A,E90A]+ amp resistance) in which three conserved glutamate residues in the predicted binding pocket were replaced with alanine. Both constructs include the native promoter and upstream regulatory region to ensure physiologically relevant expression. All bacterial strains were cultivated overnight at 37 °C and 250 rpm in LB broth using three biological replicates each. Pre-cultures were inoculated 1:100 from the overnight cultures and grown for 2 h under the same conditions. Bacteria were then diluted to a starting OD_{600} of 0.05 (measured in cuvettes) and grown in LB medium supplemented with 3 mM $Cu(II)Cl_2$. Growth was monitored at 37 °C with continuous shaking for approximately 25 h. OD_{600} measurements were taken every 2 min using a BioTek Synergy HTX Multimode Reader. Growth curves represent the mean ± SD of independent biological replicates. For Experiments 2 and 3, each biological replicate (n = 3) of the mutants was measured in technical triplicates. The control was always measured in biological triplicates, without technical replicates. For Experiment 1, *ΔcutA::kan and ΔfolX::kan* were measured in duplicates. For each biological replicate, the mean of the technical replicates was calculated. The plotted values correspond to the mean across biological replicates, with error bars indicating the standard deviation (SD).

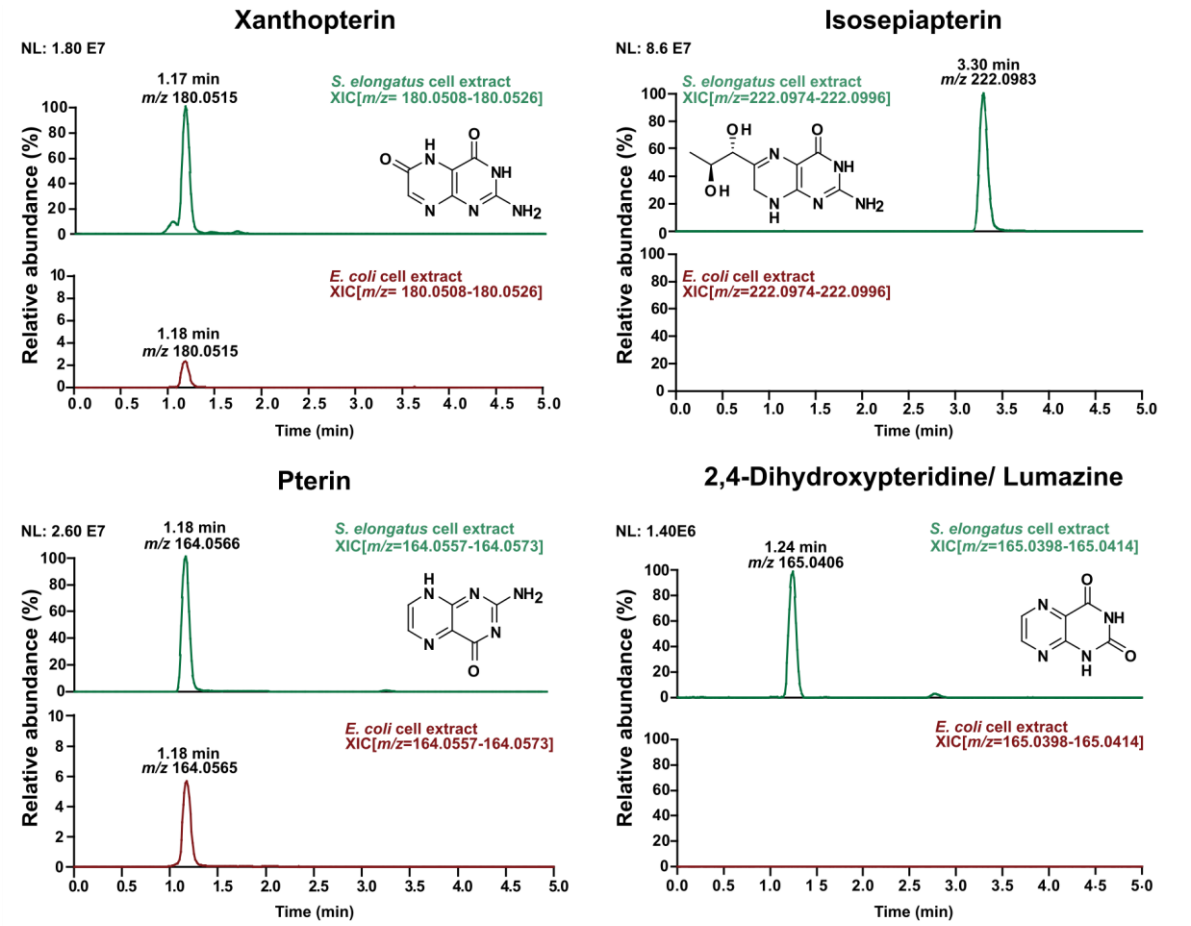

Supplementary Figure 18: Extracted ion chromatograms of pteridines detected in *E. coli* WT and *S. elongatus* WT cell extracts. Tandem mass spectrometry (MS/MS) data were acquired and analyzed using the Global Natural Products Social Molecular Networking (GNPS) platform, which assigns compound names to MS/MS spectra by spectral library matching. Masses, fragmentation patterns, and compound annotations corresponding to xanthopterin and pterin were detected in both species. Massive Dataset ID: MSV000088919.

Copper starvation of *S. elongatus* Wt and *ΔcutA::kan*

Given our finding that CutA binds copper, we hypothesized that CutA may function as a copper storage protein. To test this hypothesis, we initially grew cultures in BG11 medium, both with and without the addition of $CuSO_4$. Observing no significant differences in growth under these conditions, we introduced triethylenetetramine, a copper chelator that binds free copper ions with high affinity, to ensure the complete removal of any residual copper from the medium. Experiments were conducted by Eva Nußbaum.

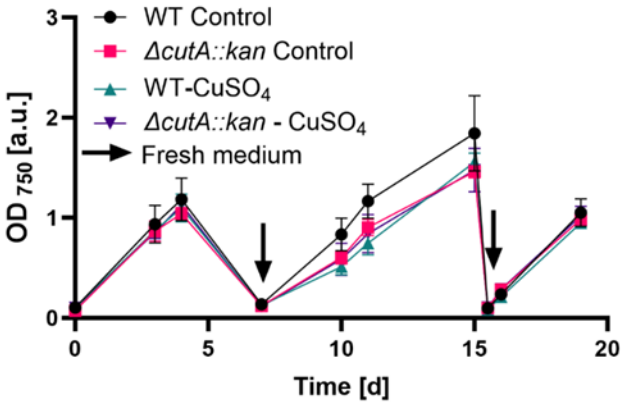

Supplementary Figure 19: Effect of copper starvation on growth of *S. elongatus* WT and *ΔcutA::kan*. *Synechococcus elongatus* WT and *ΔcutA::kan* strains were grown in copper-free BG11 medium (BG11 and BG11 without $CuSO_4$) in 50 mL plastic flasks. Cultures were inoculated at an initial OD_{750} of 0.1, illuminated at 30-60 µmol photons $m^{-2}s^{-1}$, and shaken at 120 rpm. All experiments were performed in biological triplicates.

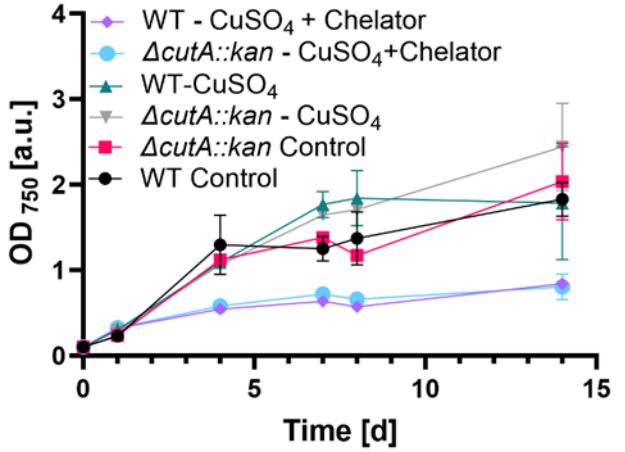

Supplementary Figure 20: Effect of copper starvation with the chelating agent triethylenetetramine on growth. Cultures were inoculated at an initial OD_{750} of 0.1 and grown under the following conditions: 2 replicates with copper (+Cu), 3 replicates without copper (-Cu), and 2 replicates without copper but with chelating agent triethylenetetramine 70 nM (-Cu + Che). The experiment was conducted in 50 mL cultures using plastic flasks, illuminated at 30-60 µmol photons $m^{-2}s^{-1}$, and shaken at 120 rpm.

No significant differences were observed in the growth of *Synechococcus elongatus* WT and *ΔcutA::kan* strains in BG11 medium, regardless of the addition of $CuSO_4$. Both strains also grew in the presence of the copper chelator triethylenetetramine, indicating that copper depletion did not significantly impact their viability. These results suggest that *S. elongatus* PCC 7942 compensates for copper limitation by switching from copper-dependent enzymes, such as plastocyanin (involved in photosynthetic electron transport), to iron-dependent alternatives like cytochrome c_6. This adaptive mechanism enables the cells to maintain efficient photosynthesis and electron transport under copper-starved conditions, supporting continued growth. Remarkably, the cells fully recovered after the experiment, even while remaining in copper-depleted medium.

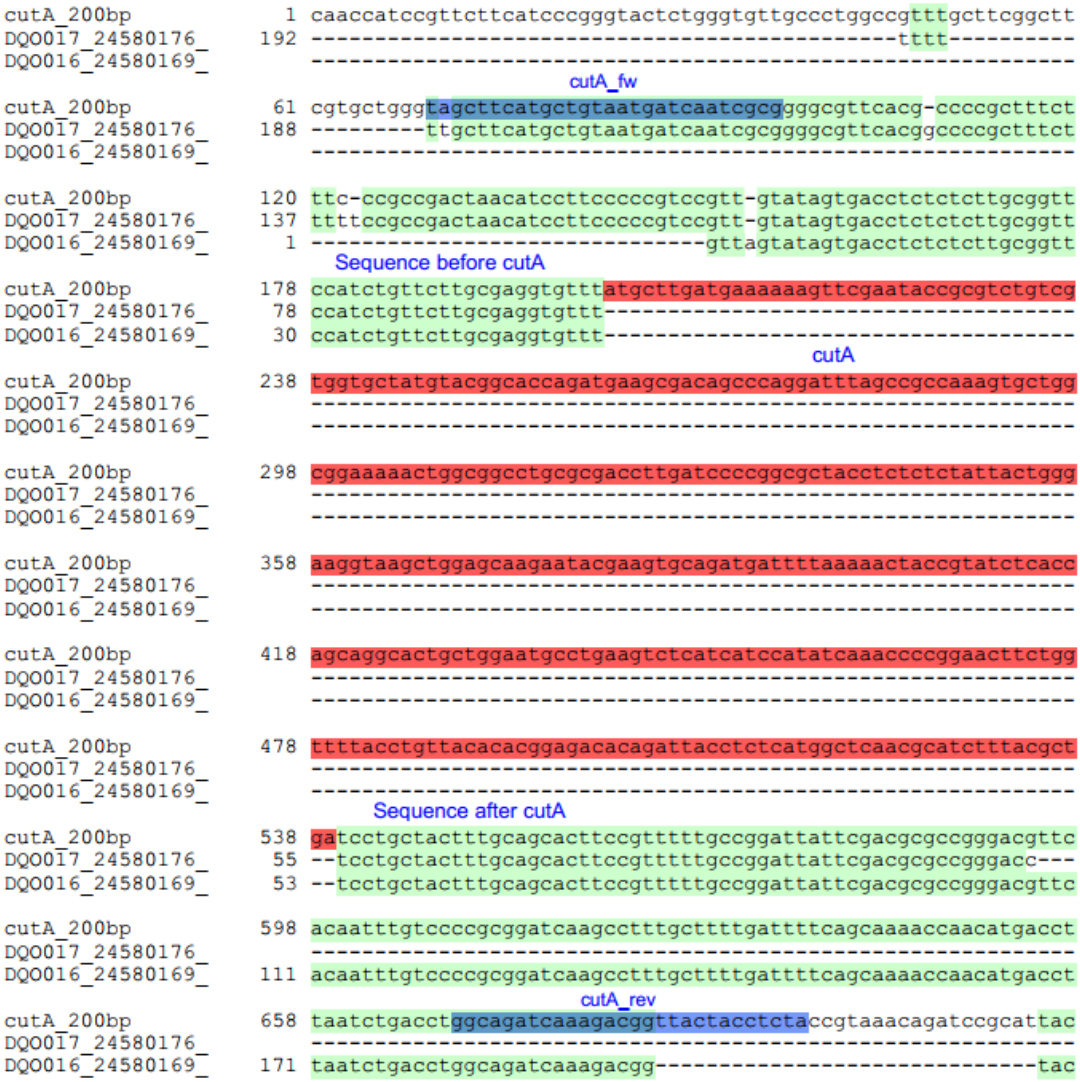

Supplementary Figure 21: Sequence alignment of *E. coli ΔcutA* after cloning.
Primers flanking the *cutA* sequence were used for sequencing. Alignment of the regions upstream and downstream of cutA, but the absence of alignment within the *cutA* sequence, confirms successful seamless cloning of *E. coli ΔcutA*. Forward primer cutA_fw (tagcttcatgctgtaatgatcaatcgc) and reverse primer cutA_rev (tagaggtagtaaccgtctttgatctgcc) were used for sequencing. The cutA sequence along with 200 bp upstream and/or downstream was included for comparison.

Purification of Proteins

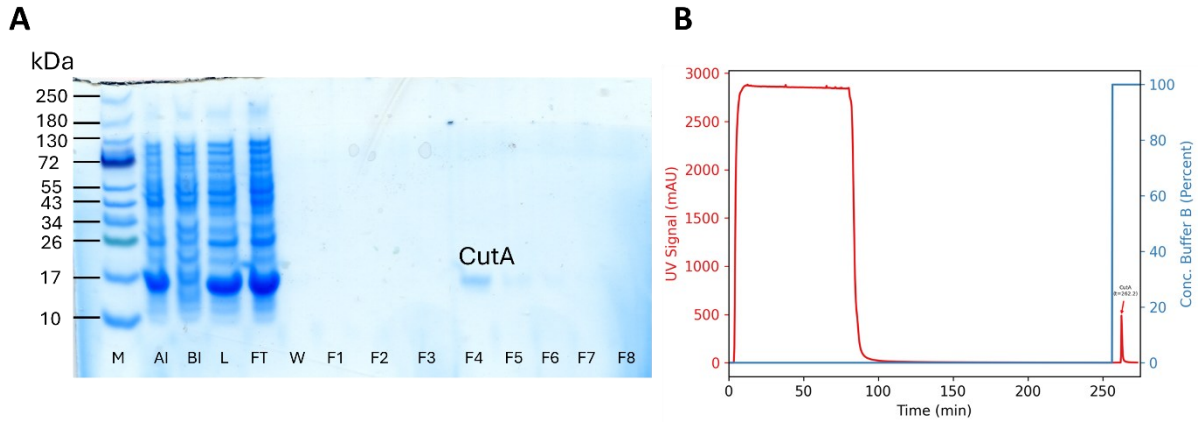

Supplementary Figure 22: Purification of *E. coli* CutA
(A) SDS-PAGE analysis of protein samples collected during the purification of E. coli CutA with a Strep-tag. The theoretical molecular weight of the CutA protein, including the Strep-tag, is 13.53 kDa. The samples include: protein marker (M; Color Prestained Protein Standard, Broad Range, 10-250 kDa; NEB P7719S), lysates before induction (BI), after induction (AI), total lysate (L), flow-through (FT), wash fractions (W), and elution fractions (F1-F8). Proteins were resolved on a 14% SDS-PAGE gel. **(B)** Elution profile from the ÄKTA purifier system showing the UV absorbance at 280 nm and the gradient of Buffer B used for protein elution.

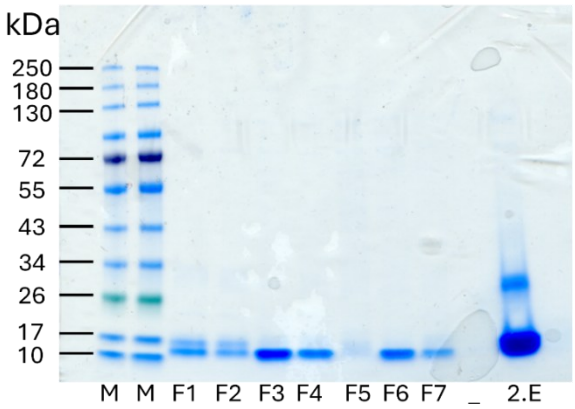

Supplementary Figure 23: Purification *S. elongatus* CutA
SDS-PAGE of different collected fractions after purification of *E. coli* CutA with a Strep-tag. The theoretical mass of the CutA protein, including the Strep-tag, is 13.69 kDa. Samples include protein marker (M; Color Prestained Protein Standard, Broad Range, 10-250 kDa; NEB P7719S), lysates before (BI) and after induction (AI), total lysate (L), flow-through (FT), wash fractions (W), and collected fractions (F1-F7), 2.E = second loading and elution of the column. Proteins were separated using a Q-PAGE™ TGN Precast Gel (Midi, 12 wells, 4-15%).

Supplementary Methods

Growth Curve Analysis under Copper Stress

All bacterial strains and mutants were cultivated over night at 37°C, 250 rpm in LB-broth using 3 biological replicates respectively. Pre-cultures were inoculated 1:100 from ON-culture and grown for 2 h using the same incubation conditions. This was followed by diluting those cultures to an OD value of 0.1 and mixing the cells with 6 mM Copper(II)chloride ($Cu(II)Cl_2$) supplemented LB-broth, using equal ratios (1:1). Analysis was carried out with 3 biological and 3 technical replicates, respectively. Growth curve measurements at 600 nm were taken at an interval of 2 min. for 29 h at 37°C using linear, continuous shaking at 493 cpm on the BioTek Synergy HTX Multimode Reader (Agilent, Santa Clara, CA, United States).

Bacterial Cultivation and metabolite extraction

The six bacterial strains and mutants were cultivated over night at 37°C at 250 rpm in LB-broth using 3 biological replicates, respectively. The supernatant was separated from the pellet by centrifugation (4000 x rpm, 20 minutes, 4°C),and washed 3 times with 1x sterile PBS. The was followed by resuspending the dry pellet with 50% ice-cold Methanol (10 mL per g of dry pellet) and sonicating the samples for 10 minutes. The metabolite extracts were concentrated using the Vacuum Concentrator (Eppendorf, Fisher Scientific GmbH, Schwerte, Germany) and resolubilized in 50% Methanol at a concentration of 2 mg/ml.

LC-MS/MS analysis of *E. coli* mutants

The untargeted metabolomics analysis was carried out with ultra-high pressure liquid chromatography (Vanquish UHPLC) (Thermo Fisher Scientific, Bremen, Germany) coupled to tandem mass spectrometry (MS) on a Orbitrap Exploris 480 (Thermo Fisher Scientific, Bremen, Germany) instrument. The samples were injected with 5 µl and the chromatographic separation was carried out by using a C18 reversed phase core-shell column (Kinetex, 50 x 2.1 mm, 1.7 µM particle size, EVO C18, 100 Å pore size, Phenomenex, Torrance, USA) with a flow-rate of 0.5 ml/min. The mobile phase was composed of Mobile Phase A (water and 0.1% of formic acid (FA)) and Mobile Phase B (Acetonitrile (ACN) + 0.1% FA). The elution gradient was linear and was set as follows; 0-2 min: 95% A / 5% B, 2-8 min: 60% A / 40% B, 8-13 min: 1% A / 99% B, and a subsequent re-equilibration phase; 13-16 min: 95% A / 5% B, for an overall 16-minute elution process. The separated metabolites were ionized using heated electron spray ionization (H-ESI), as the parameters were set to 45 Arb for sheath gas flow rate, 5 Arb auxiliary gas flow rate and 1 Arb sweep gas flow rate. Further settings were adjusted to a static spray voltage of 3.0 kV and 75 % for the RF-lens level. The ion transfer tube temperature was set to 325°C and the vaporizer temperature to 300°C. The MS measurement occurred in positive mode by setting the scan range to 150 to 1,500 *m/z* with a resolution of 120,000 *m/z* using one microscan. The maximum ion injection time was adjusted to 100 ms with an automated gain control (AGC) target of 100%.

The MS2 (MS/MS) scans were acquired with an Intensity Threshold of 1.0e5, in data dependent acquisition (DDA) mode. Per duty cycle 5 of the most abundant ions were measured with a resolution of 15,000 *m/z* with the acquisition of one micro-scan. The maximum injection time was set to 50 ms with an unchanged AGC target. Stepwise Collision-induced dissociation was done at 25, 35, and 45 eV, with an isolation window of 1 *m/z*, and the isolation offset disabled. Dynamic exclusion was set to 10.0 s and ions with an unassigned charge state were excluded after the first time using a mass tolerance of 10 ppm, with Isotope Exclusion set to a 3 *m/z* exclusion window. The processing of the raw datasets occurred by converting them to .mzXML files using MSConvert[119].

Bacterial strains, Plasmids and Primer

Table 4.1: Bacterial Strains Used in This Study.

Strain	Genotype	Purpose
Synechococcus elongatus PCC 7942	WT	Characterization, Pteridine Purification
Synechococcus elongatus PCC 7942 Δ*cutA::kan*[13]	Δ*cutA::kan*	Characterization
E. coli BW25113	WT	Characterization
E. coli BW25113 Δ*cutA (seamless)*	*E. coli* ΔcutA	Characterization
E. coli Lemo21(DE3)	*fhuA2 [lon] ompT gal (λ DE3) [dcm]* Δ*hsdS/* pLemo(Cam^R) *λ DE3 = λ sBamHIo* Δ*EcoRI-B int::(lacI::PlacUV5::T7 gene1) i21* Δ*nin5* pLemo = pACYC184-*PrhaBAD-lysY*	Protein purification (purchased)
E. coli Lemo21(DE3) pASK[EcCutA]		Protein purification of *E. coli* CutA
E. coli Lemo21(DE3) pASK[SeCutA]		Protein purification of *S. elongatus* CutA
NEB 10-beta Competent E. coli	*Δ(ara-leu) 7697 araD139 fhuAΔlacX74 galK16 galE15 e14-Φ80dlacZΔM15 recA1 relA1 endA1 nupGrpsL(StrR) rphspoT1 Δ(mrr-hsdRMS-mcrBC)*	Plasmid propagation for molecular cloning of larger plasmids or difficult constructs (purchased)
E. coli TOP10 *Competent Cells*	F$^-$ *mcrA Δ(mrr-hsdRMS-mcrBC) φ80lacZΔM15 lacX74 recA1 araD139 Δ(ara-leu)7697 galU galK rpsL (Str^r) endA1 nupG*	Plasmid propagation for molecular cloning of smaller plasmids (purchased)
E. coli Δ*cutA::kan*	F-, Δ(araD-araB)567, ΔlacZ4787(::rrnB-3), λ-, rph-1, Δ(rhaD-rhaB)568, ΔcutA763::kan, hsdR514	Characterization

E. coli Δ*cutA::folX*	F-, Δ(araD-araB)567, ΔlacZ4787(::rrnB-3), λ-, ΔfolX785::kan, rph-1, Δ(rhaD-rhaB)568, hsdR514	Characterization
E. coli Δ*cutA::kan pETblank-cutA*	pETblank carrying *cutA* including native promoter and RBS	Characterization
pETblank-cutA-E59A/E61A/E90A	pETblank carrying *cutA* allele with substitutions E59A, E61A, E90A, including native promoter and RBS	Characterization

Table 4.2: Plasmids Used in This Study.

Plasmid	Resistance	Purpose
pSLTS [175]	Amp (100)	Molecular cloning *ΔcutA, carries a selection marker, I-SceI cut site, and a transcription terminator (TT)*
pT2SK[175]	Ampicillin (100) and Kanamycin (50)	Molecular cloning *ΔcutA,* carries lambda-red recombinase + I-SceI for homologous recombination
pASK[*E. coli_cutA*]	Ampicillin (100 µg/mL)	Protein purification
pASK[*S. elongatus_cutA*]	Ampicillin (100 µg/mL)	Protein purification
pETblank[*E.c.cutA*]	Ampicillin (100 µg/mL)	Complementation
pETblank[*E.c.cutA1 E59A, E61A, E90A*]	Ampicillin (100 µg/mL)	Complementation

Table 4.3: Primers Used in This Study.

Primer	Sequence (5`→3´)	Purpose
P1_*cutA*_fw[13]	TAGCTTCATGCTGTAATGATCAATCGCG	Sequencing of *E. coli cutA*
P2_*cutA*_rev[13]	TAGAGGTAGTAACCGTCTTTGATCTGCC	Sequencing of *E. coli cutA*
pHA.seq.F	TATCAGGGTTATTGTCTCATGAGCG	Molecular cloning *ΔcutA**
pHA.seq.R	ACTTGAGCGTCGATTTTTGTGATGC	Molecular cloning *ΔcutA*
pKDTS-F	TAGGCGCAATCACTTTCGTCTACTC	Molecular cloning *ΔcutA*
pKDTS-R	TTGAGTGACATGCAAAGTAAGTATGATC TC	Molecular cloning *ΔcutA*
pHAFor	CGCAGGAAAGAACATGTG	Molecular cloning *ΔcutA*
pHARev	AAGGGCCTCGTGATACG	Molecular cloning *ΔcutA*
MF	ATCTCAAGAGTGGCAGC	Molecular cloning *ΔcutA*
MR	TTACGCCCCGCCCTGC	Molecular cloning *ΔcutA*

5`- mut cassette _fw	AGGCGTATCACGAGGCCCTTATGATCAA TCGCGGGGCGTTCAC	Molecular cloning *ΔcutA 5'mutation fragment*
5`- mut. Cassette rev	ACCGCTGCCACTCTTGAGATTGCAAAGT AGCAGGAAAACACCTCGCAAGAACAGAT GGAACCG	Molecular cloning *ΔcutA 5'mutation fragment*
3´mut. Cassette fw	GCAGGGCGGGGCGTAATCTTGCGAGGTG TTTTCCTGCTACTTTGCAGCACTTCCGTTT TTG	Molecular cloning *ΔcutA 3'mutation fragment*
3`mut. Cassette rev	CTCACATGTTCTTTCCTGCGCATGTTGGT TTTGCTGAAAATC	Molecular cloning *ΔcutA 3'mutation fragment*
*E. coli*_cutA_Gibson_fw	GTGAAATGAATAGTTCGACAAAAATCTA GATAACGAGGGCAAAAAA**ATGCTTGATG AAAAAAG**	Molecular cloning pASK [*E. coli_cutA1*] for protein purification
*E. coli*_pASK_cutA_Gibson_rev	CTTATTATTTTTCGAACTGCGGGTGGCTC CAAGCGCT**GCGTAAAGATGCGTTGAGC CATG**	Molecular cloning pASK [*E. coli_cutA1*] for protein purification
pASK_IBA3_Fw	GAGTTATTTTACCACTCCCT	Sequencing of pASK plasmids
pASK_IBA3_Rv	ACGCAGTAGCGGTAAAC	Sequencing of pASK plasmids

5 Overall Discussion CutA

CutA is a highly conserved protein found in all domains of life, with structural information available. Yet, its physiological role remains largely elusive. Earlier studies have proposed a link to copper tolerance; however, more recent evidence indicates a broader physiological significance that extends beyond copper detoxification.

In the present thesis, the function of CutA was examined in a broader physiological and biochemical context, combining results from phenotypic analysis, metabolomics, proteomics and protein-ligand interactions studies in *E. coli* and *S. elongatus*. While the main results have been discussed in Chapter 4, the following section seeks to integrate earlier findings, including additional physiological and proteomics experiments. In light of the insights gained from the results presented in the manuscript, these earlier observations can now be placed in a clearer physiological context.

5.1 Pteridine and Copper Binding to CutA

Native metabolomics experiments using purified CutA and *S. elongatus* cell extracts revealed that a previously uncharacterized pteridine compound could bind to both *Ec*CutA and *Se*CutA (Figure 4.2, Supplementary Figure 6). This metabolite was subsequently purified and identified as the lumazine derivative 2'-deoxyxanthopterin B2 (Figure 4.3). Based on this finding, additional experiments were performed to test other pteridine compounds for their interaction with CutA. These assays revealed that several pterins, including the redox-active cofactor tetrahydrobiopterin (although not endogenously present in *E. coli*), can also bind to *Ec*CutA (Figure 4.4), indicating an affinity of CutA for redox-active pteridines. *E. coli* naturally produces tetrahydromonapterin, a pterin structurally related to tetrahydrobiopterin (see section Figure 5.4, also section 5.4.5.2)

In addition to the interaction with pteridines, binding of $CuSO_4$ to *Ec*CutA was also observed (Figure 4.4). Moreover, deletion of *cutA* in *E. coli* displayed an increased sensitivity to copper exposure, while complementation with *cutA* under the native promoter alleviated this effect, indicating a functional role of CutA in cellular copper homeostasis (Figure 4.5, Supplementary Figure 17). Furthermore, in the presence of tetrahydrobiopterin, the affinity

of CutA for copper ions was enhanced (Figure 4.4). Although this observation requires further investigation, it suggests a possible interplay between pterin binding and copper coordination.

Considering the observed sensitivity of *cutA* mutants to copper and other stress conditions, these findings support a role of CutA in coordinating copper and redox homeostasis and suggest links to copper-mediated cellular stress.

5.2 Copper Homeostasis, Envelope Stress and Lipid Metabolism

5.2.1 Functional Reclassification of the *cut* Genes

As summarized by Giachino and Waldron (2020)[20] and outlined in the introduction of this thesis (Table 1.1 "*The* cut-genes *of E. coli"*), several genes originally classified as *cut* genes, including *cutF* (now identified as *nlpE*), *cutE* (*lnt*), *cutC* (*micL*), and *cutA2* (*dsbD*), play a role in the bacterial cell envelope stress response rather than in direct copper detoxification. Copper toxicity arises in part from its disruption of lipoprotein maturation, resulting in the accumulation of immature precursors within the inner membrane[20,176]. The process of outer membrane lipoprotein maturation involves stepwise acylation of the polypeptide, cleavage of the signal peptide and transport to the outer membrane. Copper ions target the N-terminal cysteine that accepts the acyl group, blocking access to the maturation enzymes[177,178]. The resulting stress triggers the envelope stress response, which in *E. coli* is coordinated by the CpxAR two-component system (reviewed in Raivio, 2014[179]*).* In *E. coli*, the sensor kinase CpxA responds to the accumulation of the outer membrane lipoprotein NlpE[177](CutF). Activated CpxR upregulates the lipoprotein-acylating enzymes Lgt and Lnt (CutE), as well as the small regulatory RNA MicL (CutC), which represses lipoprotein synthesis[17,20].

A further mechanism of copper toxicity in the bacterial envelope concerns the folding of periplasmic proteins. Copper can oxidize free thiols under aerobic conditions, and thereby catalyze the formation of aberrant disulfide bonds[20]. Under normal conditions, the oxidoreductases DsbA and DsbB introduce correct disulfide bonds into maturing proteins[20,180]. However, when copper introduces incorrect disulfide bonds, the additional oxidoreductase pair DsbC and DsbD (also known as CutA2) is required to correct these misfolded proteins[20,181]. DsbD (CutA2) mediates the transfer of electrons across the membrane, conveying reducing equivalents from the cytoplasmic thioredoxin (Trx) system and NADPH to DsbC through stepwise thiol-disulfide exchange (reviewed in Collet, 2020[182]).

Another possible consequence of disturbed copper homeostasis is the weakening of the peptidoglycan layer, which represents an envelope-specific effect of copper toxicity[20]. In enterobacteria like *E. coli*, peptidoglycan is cross-linked by two classes of transpeptidases (TPases): LD- TPases (linking the L- and D-forms of amino acids) and DD- (linking two D-forms) TPases. Binding of Cu(I) to catalytic cysteines of LD-TPases impairs proper cross-linking and attachment to outer membrane lipoproteins, thereby weakening the cell envelope and increasing sensitivity to detergents and other membrane-destabilizing compounds[20,183,184].

This partial reclassification of the *cut*-genes underscores that copper toxicity affects envelope integrity and that the *cut* genes act to counter these effects. Although these functions have been described mainly in *E. coli*, CutA is conserved across diverse phyla, which suggests a more fundamental role in maintaining envelope-associated redox balance and metal homeostasis.

5.2.2 CutA Phenotypes under Copper and Heat Stress

CutA from *Nostoc sp.* PCC 7120, *S. elongatus*, and *E. coli* exhibited unusually high thermal stability, with melting temperatures exceeding the organism's optimal growth temperatures (Figure 3.1). This stability likely enables CutA to remain functional during environmental stress. Δ*cutA* mutants of *E. coli* and *S. elongatus* consistently showed a more pronounced stress phenotype than the WT strains. In *E. coli*, this was reflected in prolonged lag phases after heat, copper ($CuCl_2$) or pH stress (Figure 3.4 and Figure 3.5), while in *S. elongatus* also photosynthetic proteins seemed severely affected after heat treatment (Figure 3.3). The delayed recovery of the mutant strains may point to impaired cell envelope repair mechanisms in the absence of CutA. Consistent with a role in stress response, results of reverse-transcriptase PCR in *E. coli* suggested that *cutA* transcript levels were elevated under heat treatment compared to the housekeeping gene *rnpB (*Figure 3.4), indicating that expression of CutA is stress-inducible.

5.2.3 Copper Sensitivity and Envelope Integrity

In *S. elongatus*, an increased sensitivity of the *ΔcutA* mutant to β-lactam antibiotics ampicillin and carbenicillin was observed (Figure 3.6), which supports a role in the cell envelope stress response, potentially also reflecting impaired copper regulation. Although *S. elongatus* is not an enterobacterium, similar principles of copper-mediated envelope stress as described for

E. coli could apply. In this context, the increased sensitivity of the *ΔcutA* mutant to ampicillin and carbenicillin in *S. elongatus* may reflect a role for CutA in maintaining copper homeostasis. Impaired copper regulation could compromise LD-TPase-like activity (as described in 5.2.1), weakening peptidoglycan cross-linking, while inhibition of DD-TPases by β- lactams would further exacerbate cell wall stress. Alternatively, the heightened sensitivity may be attributed to elevated levels of ROS generated in response to β-lactam exposure[138].

Another hint for a role of CutA in envelope integrity was obtained from targeted metabolite profiling of *ΔcutA* in *E. coli* (Figure 4.1d), which showed reduction in several precursors of cell wall biosynthesis. The dipeptide D-alanyl-D-alanine, a direct precursor for peptidoglycan crosslinking, was reduced, as was N-acetylmuramate, another peptidoglycan component. Furthermore, UDP-glucose, a key precursor for cell wall and lipopolysaccharide biosynthesis, also decreased in comparison to the WT.

5.2.4 CutA and Fatty Acid Metabolism

Protein interaction studies further supported a potential link between CutA and cell envelope-associated processes. In *E. coli*, the 3-hydroxyacyl-[acyl-carrier-protein] dehydratase FabZ (Uniprot ID: P0A6Q6) was significantly enriched in pulldown experiments with CutA, especially in heat-treated samples (Figure 3.12, Figure 3.13 and Figure 3.14). A similar observation was made in *Nostoc* 7120, where FabZ was also co-purified with CutA and showed greater enrichment under heat stress conditions (Figure 3.8, Figure 3.10G). The acyl carrier protein AcpP (Uniprot ID: P0A6A8) was likewise significantly enriched in the pulldown with expressed *Ec*CutA and more abundant following heat treatment. Given that FabZ and AcpP are both key components of the fatty acid biosynthesis pathway, their co-enrichment with CutA may indicate a functional link between CutA and lipid metabolism, particularly under stress conditions.

The levels of a similar protein, Long-chain acyl-[acyl-carrier-protein] reductase (LC-ACP reductase or AAR, Uniprot_id: Q54765, (Figure 3.9) was also significantly increased in all samples of the *S. elongatus* pulldown in presence of CutA. Like FabZ and AcpP, AAR is a protein of fatty acid biosynthesis[118]. Since membrane and lipid composition critically determine cellular tolerance to different environmental stress conditions, including copper imbalance, these results raise the possibility that CutA contributes to stress resilience by

modulating lipid metabolism or membrane-associated processes. Consistent with this, untargeted metabolomics (Figure 3.18) showed altered levels of lipid- and redox-associated metabolites in *S. elongatus ΔcutA::kan* compared to the WT. Here, sulfoquinovosyl diacylglycerols (SQDGs) were enriched in both exponential and stationary growth phases, whereas monoelaidin and oxidized glutathione were decreased. The accumulation of SQDGs, which are thylakoid membrane lipids[185], may indicate remodelling of the thylakoid or plasma membrane in response to cellular stress, as lipid adjustment. However, dedicated lipidomic analysis using optimized cell extraction and measurement would be required to confirm and quantify these changes.

5.2.5 CutA and its Putative Pteridine-Binding Pocket

CutA emerged from this work as a protein capable of binding both copper and pterin derivatives. These interactions link CutA to two key redox-active cofactors and suggests that it may function in balancing metal- and pterin-dependent redox processes, putatively within the cell envelope. CutA proteins from diverse organisms contain conserved intersubunit clefts that have been observed to accommodate small buffer-derived molecules such as Bis-Tris, MES, and HEPES in crystallography structures[13]. These clefts are lined by highly conserved polar and negatively charged amino acids (Figure 1.4), suggesting that they form a chemically suitable environment for accommodating small polar ligands, such as pteridines. Molecular docking predictions using Boltz-2 (NVIDIA) further support the potential for pteridines to occupy this conserved intersubunit pocket (Supplementary Figure 15). The functional importance of this predicted pocket is underscored by the observation that substitution of three conserved glutamate residues (E59A, E61A, E90A), which contribute to the negatively charged surface, resulted in reduced complementation efficiency of the *E. coli ΔcutA::kan* mutant under copper stress conditions. This suggests that the integrity of the binding pocket and the pocket itself is essential for CutA function during stress.

Tetrahydrobiopterin (BH4) dependent hydroxylases, such as phenylalanine hydroxylase (EC1.14.16.1)[159], tyrosine 3-monooxygenase(EC1.14.16.2)[160] or tryptophan hydroxylase (EC1.14.16.4) require iron as a cofactor to catalyze redox reactions. BH4 has also been shown to reduce the Mn(III) centers of porphyrins[161] and to from complexes with cupric ions[152], demonstrating the versatility of pterins in mediating metal-dependent redox chemistry. Against this background, it seems plausible that CutA may also interact with both Cu^{2+} and pteridin compounds.

Pteridine biosynthesis appears to be sensitive to metal availability. The *pts* gene encodes the zinc-dependent 6-pyruvoyl tetrahydrobiopterin synthase, an enzyme involved in pterin metabolism in cyanobacteria[186]. Its orthologs are PTPS in *Homo sapiens* and QueD in *E. coli* (also shown in Figure 5.3). The cyanobacterial enzyme catalyzes the second step of *de novo* BH4 biosynthesis and was upregulated in *Synechococcus* and *Prochlorococcus* species under iron and copper pertubations[187].

Given that both copper and pterins are redox-active molecules, the ability of CutA to bind both cofactors may allow it to modulate redox reactions. Such a dual binding capacity could enable CutA to buffer redox-fluctuations and prevent uncontrolled copper-induced oxidation of thiols or membrane lipids. This hypothesis aligns with the genetic proximity of *cutA* to *dsbD (cutA2)* in *E. coli,* which encodes the electron transfer protein required for maintaining periplasmic disulfide bond balance[182]. It is also consistent with the proposal by Arnesano et al. (2003)[12] that CutA may cooperate with oxidoreductases such as CutA2/DsbD to regulate the redox state of thiol groups within metal-binding CXXC motifs. CutA may thus operate in parallel or in coordination with the transmembrane DsbD to stabilize redox-sensitives protein folding or to prevent oxidative envelope damage under stress conditions. The impaired recovery of *ΔcutA* mutants under various stress conditions, combined with their sensitivity to copper and β-lactam antibiotics, further supports this view. Disturbed metal-pterin redox coupling may weaken envelope repair processes or compromise lipid and peptidoglycan synthesis.

5.3 CutA and Redox Homeostasis

The deletion of *cutA* in *E. coli* appears to perturb multiple aspects of redox homeostasis. As shown in the targeted metabolomics results (Figure 4.1d), α-ketoglutarate was significantly decreased in the mutant compared to the WT. α-ketoglutarate is a central hub metabolite that connects the TCA cycle, nitrogen assimilation via the GS-GOGAT pathway and nucleotide biosynthesis[188]. This could explain why other metabolites connected to these pathways, like proline, and guanine derivatives were also decreased. Beyond its biosynthetic role, α- ketoglutarate is also known to act as a redox buffer by directly scavenging ROS and maintaining NAD(P)H balance[189]. A similar role of TCA intermediates in oxidative stress defense has been described in *Pseudomonas fluorescence*, where modulation of α-ketoglutarate contributed to redox homeostasis[190].

The depletion of several redox-related metabolites that could scavenge ROS, including proline (which acts as ROS scavenger)[191], as well as pyridoxamine-5-phosphate (a vitamin B6 derivative with antioxidant activity)[192,193] and dihydrobiopterin (a precursor of redox-active pterins)[194] supports the idea that *ΔcutA* cells are under oxidative pressure, even under control conditions.

Proline has been shown to protect *E. coli* from oxidative stress by influencing the OxyR regulon[195]. Proline generates low levels of endogenous hydrogen peroxide, which is associated with activation of OxyR and the induction of antioxidant defense genes such as *grxA* (Glutaredoxin 1) and *trxC* (thioredoxin 2)[195]. The lower levels of proline in the *ΔcutA* mutant may therefore weaken OxyR mediated stress protection, further sensitizing cells to oxidative challenges. This interpretation is supported by the pulldown experiments of *E. coli*, where pyridoxamine/pyridoxamine 5`-phosphate oxidase (PdxH) and especially OxyR were enriched under standard conditions (Figure 3.12) in the *E. coli* pulldown with CutA while pyridoxamine/pyridoxamine 5`-phosphate was significantly decreased in the targeted metabolomics data in the *E. coli ΔcutA* strain (Figure 4.1). In *S. elongatus,* FAD, pterin (stationary growth phase) and oxidized Glutathione (exponential growth phase) were found to be decreased in the *ΔcutA::kan* strain in an untargeted metabolomics experiment (Figure 3.18). Together, this data suggests a potential functional link between CutA and the oxidative stress response.

5.4 Pteridines

The detection of pteridines as potential binding partners of CutA raises a series of compelling questions. To understand more about the putative role of CutA, it's important to understand the properties of its binders. What are the characteristic properties of this class of compounds? What functional role might CutA play in the cell, and how could its interaction with pteridines contribute to this role? The following section provides a brief overview of the pteridine class and places the findings of this study into a broader biological and biochemical context.

5.4.1 What are Pteridines? Pteridines in Biology: Pterins, Lumazines, and Their Natural Occurrence

Pteridines are an ubiquitous class of natural heterocyclic compounds of low molecular-weight, first observed by Gowland Hopkins in 1880s as wing pigments in the *Pieridae,* like the common English brimstone and cabbage white butterflies[196,197]. Later, Heinrich Otto Wieland further investigated these molecules and named them after the greek word *pteron* (πτερόν), meaning 'wing'[198]. Hopkins and further scientists first believed that pteridines are derivatives of uric acid[199]. But in contrast to the purines, to which uric acid belongs, the pterin structure features a condensed system of two six-membered rings[200]. This structure is derived from GTP (guanosine triphosphate) via specific biosynthetic pathways (visualized in Figure 5.2), which are biochemically separate from the catabolic pathway responsible for generating purine degradation products such as uric acid.

First identified in eukaryotes, where they serve diverse essential functions and contribute to vivid coloration, as exemplified by the yellow spots of fire salamanders[201], bacterial pteridines were found in cyanobacteria and other procaryotes soon after. Today, pteridines are recognized as derivatives of the heterocyclic core structure pteridine ($C_6H_4N_4$). As shown in Figure 5.1, pteridines consist of a pyrimidine ring fused with a pyrazine ring and are divided into pterins and lumazines. Pterins possess an amino group at the C-2 position and an oxy-group at C-4, while lumazines contain a carboxy group at C-2 (position depicted in red).

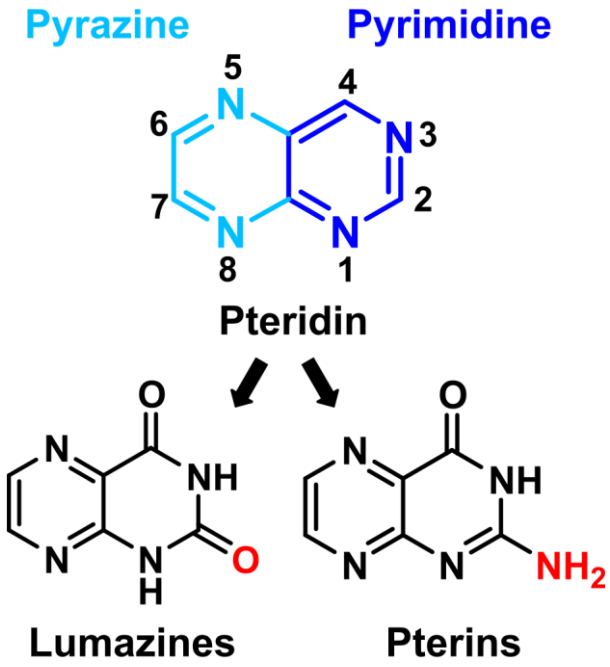

Figure 5.1: Core structure of pteridines and functional group differences between pterins and lumazines. Pteridines are composed of a fused heterocyclic ring system consisting of a pyrazine ring (cyan) and a pyrimide ring (blue). This core structure serves as the basis for the classification into pterins and lumazines. Pterins are defined by an amino group at the C-2 position and a keto group at C-4, while lumazines carry a carbonyl group (depicted in red). Th figure appears also in modified form in the SI of Wagner et al., 2025[46].

Pterins are widely distributed across all domains of life and are involved in various biological processes. They function as pigments[202], participate in single-carbon metabolism[203] and act as redox cofactors[204]. In addition, certain pterins, most notably neopterin, serve as established biomarkers of cellular immune activation and are routinely used in clinical diagnostics[205]. The pteridine ring system also serves as crucial biosynthetic precursor. It forms the structural backbone of essential compounds like folic acid, which consists of 2-amino-4-hydroxy-pteridine, *p*-amino-benzoic acid and a poly-γ-glutamate chain[206]. In contrast to pterins, lumazines have remained relatively understudied[207]. Lumazine is a key intermediate in the riboflavin pathway, where its ring structure contributes to the formation of flavins. Riboflavin (vitamin B_2) and its derivatives flavin mononucleotide (FMN), and flavin adenine dinucleotide (FAD) contain an isoalloxazine ring system, which is formed by the dismutation of two molecules of 6,7-dimethyl-8-ribityl-lumazine catalyzed by riboflavin synthase RibC[208] (Figure 5.2). This ring system is central to the redox activity of flavins and enables them to participate in electron transfer[209].

5.4.2 Pteridine Biosynthesis

Pteridine biosynthesis originates from guanosine triphosphate (GTP), which serves as a common precursor for a wide array of biologically active compounds. From this starting point, several distinct biosynthetic branches lead to various pteridine derivatives, including both essential cofactors and metabolic intermediates[210]. These routes are shown in Figure 5.2.

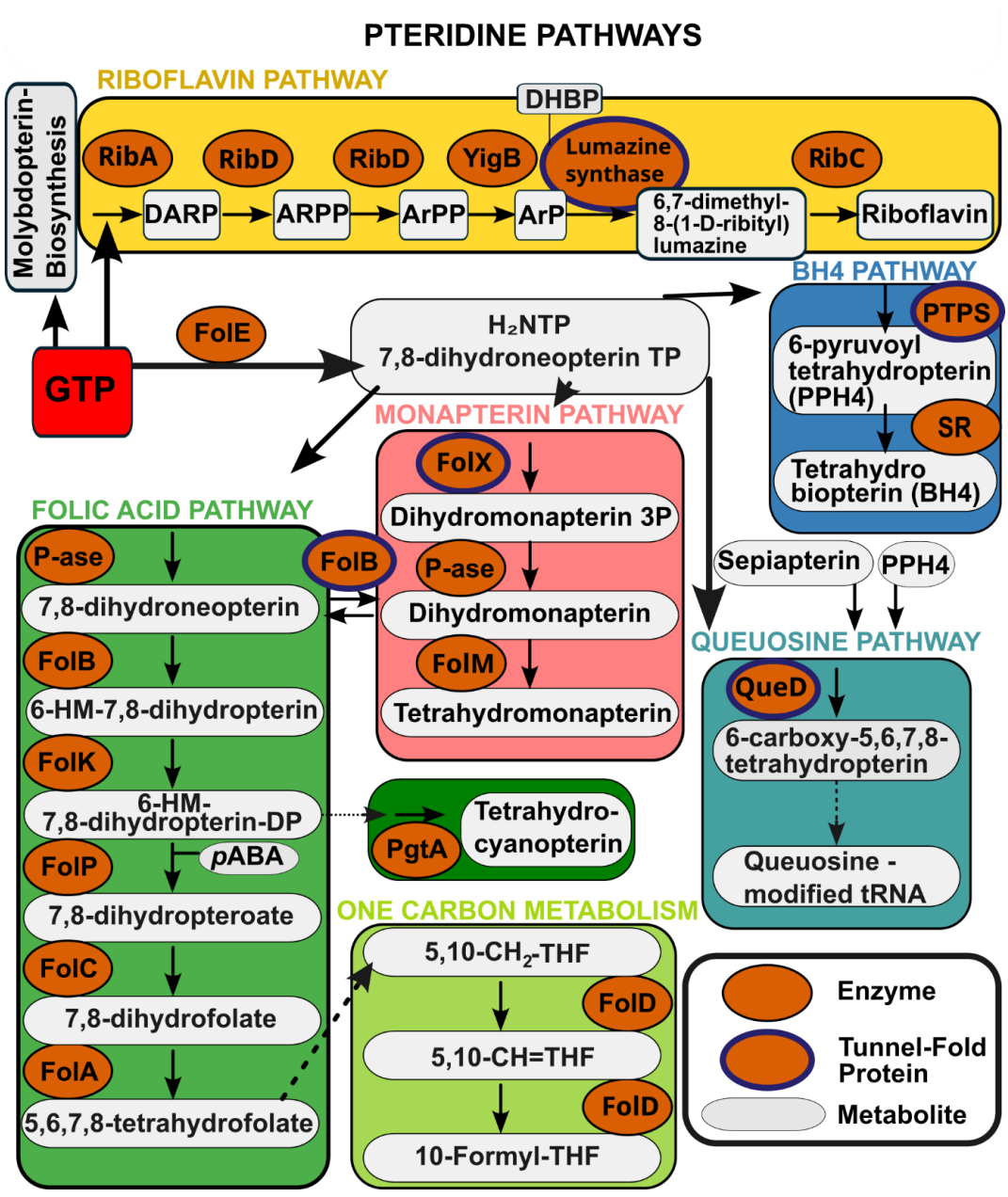

Figure 5.2: Generalized schematic overview of pterin-derived metabolic pathways in bacteria. Guanosine triphosphate (GTP) acts as the central precursor for all pteridine biosynthesis pathways in bacteria. From GTP, the riboflavin biosynthesis pathway (yellow), which leads to the formation of 6,7-dimethyl-8-(1-D-ribityl)lumazine and riboflavin, as well as the molybdopterin biosynthesis pathway are initiated. The conversion of GTP to 7,8-dihydroneopterin triphosphate (H_2NTP) by GTP cyclohydrolase I (FolE) gives rise to several downstream branches: the folic acid pathway (green), which connects to one-carbon metabolism (light green), the monapterin pathway (coral red), the tetrahydrobiopterin (BH_4) pathway (blue), the queuosine biosynthesis pathway (cyan), and organism-specific pathways, exemplified here by an additional branch (dark green) leading to tetrahydrocyanopterin, involving the protein PgtA. Enzymes are shown in orange, tunnel-fold proteins are

outlined in blue, and metabolic intermediates are depicted in gray. For clarity, the schematic focuses on major biosynthetic steps and omits cofactors and by-products. Pathway information was compiled from KEGG, UniProt, the BRENDA enzyme database, and the review "Pterin function in bacteria" by Feirer and Fuqua (2016). **Metabolites:** **GTP** (guanosine triphosphate), **H_2NTP** (7,8-dihydroneopterin triphosphate), **DARP** (2,5-diamino-6 ribosylamino-4(3H)-pyrimidinone 5′-phosphate), **DHBP** (3,4-dihydroxy-2-butanone 4-phosphate), **ARPP** (5 amino-6-ribitylamino-2,4(1H,3H)-pyrimidinedione 5′-phosphate), **ArPP** (phosphorylated form of ARPP), **ArP** (dephosphorylated form of ARPP), **6-HM-7,8-dihydropterin** (6-hydroxymethyl-7,8-dihydropterin), **6-HM-7,8 dihydropterin-DP** (diphosphate form), **pABA** (para-aminobenzoic acid), **PPH_4** (6-pyruvoyl-5,6,7,8 tetrahydropterin), **BH_4** (5,6,7,8-tetrahydrobiopterin), **THF** (tetrahydrofolate), **5,10-CH_2-THF** (5,10 methylenetetrahydrofolate), **5,10-CH=THF** (5,10-methenyltetrahydrofolate), **10-Formyl-THF** (10-formyltetrahydrofolate). **Enzymes**: **RibA** (GTP cyclohydrolase II), **RibD** (riboflavin biosynthesis protein), **YigB** (5-amino-6-(5-phospho-D-ribitylamino)uracil phosphatase), **RibH** (6,7-dimethyl-8-ribityllumazine synthase, **RibC** (riboflavin synthase), **FolE** (GTP cyclohydrolase I), FolB (dihydroneopterin aldolase), **FolK** (2-amino-4-hydroxy-6-hydroxymethyldihydropteridine pyrophosphokinase), FolP (dihydropteroate synthase), FolC (dihydrofolate synthase/folylpolyglutamate synthase), **FolA** (dihydrofolate reductase), **FolX** (dihydroneopterin triphosphate 2'epimerase), **FolM** (dihydromonapterin reductase), **QueD** (6-carboxy-5,6,7,8-tetrahydropterin synthase), **PTPS** (6 pyruvoyltetrahydropterin synthase), **SR** (sepiapterin reductase), **P-ase** (pyrophosphatase), **PgtA** (tetrahydrocyanopterin-associated protein).

One such branch is the riboflavin biosynthesis pathway, where 6,7-dimethyl-8-ribityllumazine is synthesized in the penultimate step by lumazine synthase (RibH, EC 2.5.1.78)[211]. Another major pathway leads to the formation of molybdopterin, a tricyclic pterin-based cofactor required for a variety of redox enzymes across all domains of life[212]. In parallel, GTP is also converted by GTP cyclohydrolase I (FolE, EC:3.5.4.16) into 7,8-dihydroneopterin triphosphate (H_2NTP), which acts as a central intermediate in multiple biosynthetic routes. In bacteria, H_2NTP is not only a precursor for folate biosynthesis, but also for the production of queuosine, a hypermodified nucleoside found in the anticodon loop of specific tRNAs[213]. The first step in queuosine biosynthesis is catalyzed by the 6-carboxy-5,6,7,8-tetrahydropterin synthase (QueD, EC:4.1.2.50), a homologue of 6-pyruvoyl-tetrahydropterin synthase (PTPS, EC:4.2.3.12), an enzyme typically associated with tetrahydrobiopterin (BH_4) biosynthesis[214]. While PTPS converts H_2NTP into 6-pyruvoyl-tetrahydropterin (PPH_4) as part of the biopterin biosynthetic pathway in many organisms, QueD in *E. coli* catalyzes the formation of 6-carboxy-5,6,7,8-tetrahydropterin (CPH_4)[215]. Interestingly, QueD exhibits catalytic promiscuity and can also convert alternative substrates, such as PPH_4 or sepiapterin, into CPH_4[215]. Besides direct production routes or pathways, pterins can also be converted into lumazine derivatives through the activity of pterin deaminases[207,216]. In addition to these main pathways, there are secondary or species-specific branches that involve additional enzymes, which further modify pteridine intermediates. In cyanobacteria, for instance, pterins can be glycosylated to form pterin glycosides, typically through the attachment of a sugar moiety to the C6-position of the pterin ring. One example is cyanopterin, a specialized pteridine derivative produced by the pteridine glycosyltransferase PgtA[217]. Another is tetrahydrobiopterin-glycoside, synthesized by the

enzyme UDP-glucose:tetrahydrobiopterin glucosyltransferase in *Synechococcus elongatus* PCC 7942[218].

The following paragraph compares key proteins involved in pteridine biosynthesis and examines potential structural and functional similarities with CutA.

5.4.3 Proteins of Pteridine Biosynthesis: Commonalities with CutA

The biosynthetic pathways of GTP-derived metabolites, including tetrahydrofolate, tetrahydrobiopterin and queuosine, a hypermodified nucleoside in tRNA, rely on several enzymes belonging to the tunnel-fold superfamily[219] depicted in Figure 5.3**.**

These enzymes catalyze the conversion of 7,8-dihydroneopterin triphosphate (H_2NTP) into diverse products. Structurally, the depicted tunnel-fold proteins involved in pteridine pathways are small subunits of 13-16 kDa (shown on the right) that assemble into trimers or tetramers (shown on the middle and left), which subsequently associate to form characteristic barrel-like hexamers or octamers[219,220]. Their classification as tunnel-fold proteins is based on a conserved oligomeric structure featuring a central cavity[221]. Although the CutA monomer resembles the tunnel-fold monomers and the CutA trimer adopts a similar flattened barrel-like shape with a central pore[47], it differs in its ferredoxin-like fold (β1α1β2-β3α2β4), whereas tunnel-fold proteins have a ββαααββ core topology[219,221]. Some members of the tunnel-fold proteins exhibit functional promiscuity toward different pteridines[219]. For instance, as shown in Figure 5.2, QueD/PTPS-I is capable to utilize both sepiapterin and H_2NTP (as well as their di- and monophosphates)[219]. This substrate flexibility is modulated in part by the identity of the coordinated metal ion, commonly Zn^{2+}, which is essential for catalysis and binds within the active site. Substrate recognition generally occurs at the interface between two subunits and often involves Glu or Gln residues that anchor planar molecules such as pterins[219,221] (illustrated for QueD and FolB in Figure 5.3). Moreover, it has been proposed that the activity of certain proteins is modulated by the identity of the coordinated metal ion[219]. Interestingly, the CutA protein (although not classified as a tunnel-fold enzyme but as P_{II}-like Protein[13]) shares some of these structural and functional features. It possesses a negatively charged pocket lined with conserved glutamate (Glu) residues[12], as visualized in Figure 1.3 and Figure 1.4, which has been crystallized with small buffer molecules such as MES and HEPES bound in this region. This pocket is thought to serve a conserved binding or signaling function in CutA[13].

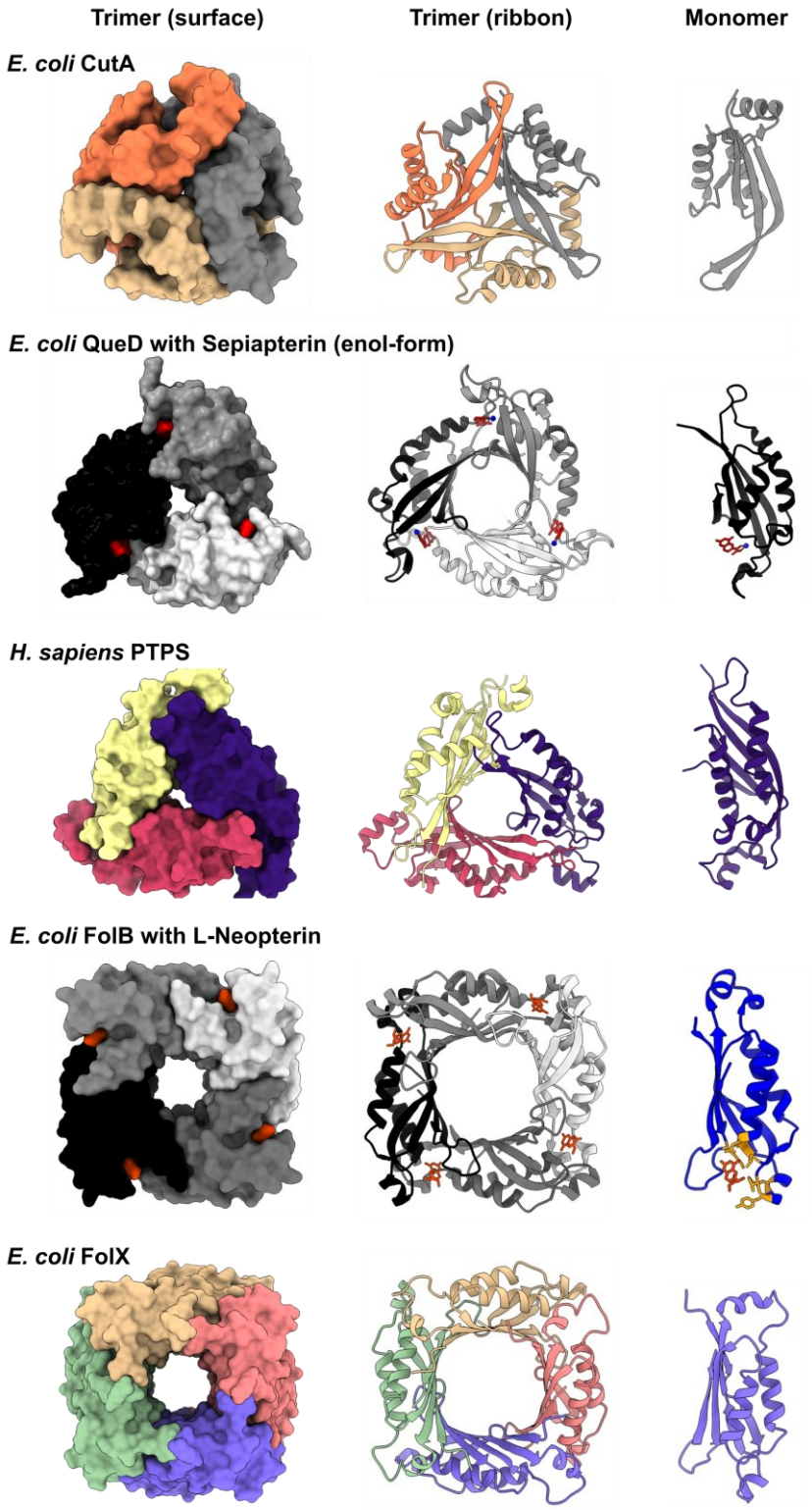

Figure 5.3: Comparison of CutA and tunnel-fold proteins QueD, PTPS, FolB and FolX.
From left to right: The outer molecular surfaces of the trimers/tetramers are shown, with each trimer/tetramer surface rendered in a distinct color. Next, ribbon representations of the trimers are displayed, with each monomer colored differently, followed by individual monomer structures. Protein names are labeled above their respective structures. In the QueD protein, sepiapterin and Zn^{2+} ions are shown in red and blue, respectively. Protein structures were obtained from the Protein Data Bank (PDB) using the following IDs: *E. coli* CutA (1NAQ), *E. coli* QueD (4NTK), *E. coli* FolB (2O90), *E. coli* FolX (1B9L), and *H. sapiens* PTPS (3I2B). Structures were visualized using ChimeraX.

These observations suggest that this binding pocket could also accommodate pterin ligands. Although CutA is not classified as a tunnel-fold protein, its ability to interact with different pteridine compounds suggests that it may possess a promiscuous ligand-binding site. This notion is supported by our protein-ligand docking results, which showed a possible placement of the pterin moiety within the binding cavity, as well as by native mass spectrometry, where higher pterin concentrations resulted in multiple bound species, which indicate multiple, likely up to three, binding events (Figure 4.2D, Supplementary Figure 6).

Among tunnel-fold proteins, QueD plays a role in the queuosine biosynthesis pathway in *E. coli* (KEGG pathway map00790). It is functionally related to PTPS, which participates in tetrahydrobiopterin and folate biosynthesis in other organisms. Both QueD and PTPS use H_2NTP as a substrate but catalyze distinct, pathway-specific reactions: QueD produces 6-carboxy-5,6,7,8-tetrahydropterin (CPH_4) during queuosine biosynthesis, while PTPS synthesizes 6-pyruvoyltetrahydropterin (PPH_4) in the biopterin biosynthesis pathway. Remarkably, *E. coli* QueD can also convert PPH_4 and sepiapterin to CPH_4[215].

In bacteria, two distinct pathways exist for tetrahydropterin biosynthesis: the canonical pathway involving the tetrahydrobiopterin synthesis enzyme PTPS-II, and an alternative pathway mediated by FolX and FolM[164].

FolX (dihydroneopterin triphosphate 2′-epimerase, EC 5.1.99.7) is also a tunnel-fold protein and required for the biosynthesis of tetrahydromonapterin, one of the major pterins in *E. coli*. It catalyzes the epimerization at carbon 2′ of the side chain of 7,8-dihydroneopterin triphosphate (H_2NTP) to form 7,8-dihydromonapterin triphosphate (H_2MTP)[164]. This modification creates a metabolic branch from folate biosynthesis and contributes to the formation of other pterins.

FolB (dihydroneopterin aldolase, EC:4.1.2.25), another tunnel-fold protein, catalyzes the conversion of 7,8-dihydroneopterin to 6-hydroxymethyl-7,8-dihydropterin, accepts both L-threo- and D-erythro-dihydroneopterin as substrates, and mediates 2′-carbon epimerization to produce dihydromonapterin[164].

The gene for 6-pyruvoyl tetrahydrobiopterin synthase, *pts*, was observed to be upregulated in different cyanobacteria (*Prochlorococcus* MIT9313, *Synechococcus* WH 8102 and *Synechococcus* 9311) under both iron and copper stress[156]. These findings suggest that pterin biosynthesis may contribute to cellular adaptation to metal stress. This potential coordination between CutA and the pterin biosynthesis pathway could be particularly relevant under metal

stress conditions, where shifts in the redox environment and enzyme cofactor requirements might necessitate tight regulation of both metal and pterin pools. Given that CutA has been found to bind pterin derivatives, it is conceivable that this protein is involved in modulating pterin availability, stability or function during metal stress.

5.4.4 Pteridines and Their Role in Redox-Reactions

Pterins exhibit multielectron redox reactivity, a property that mirrors the redox capabilities of transition metals[152]. They exist in three interconvertible oxidation states: the fully oxidized form, the semi-reduced (dihydro) form, and the fully reduced (tetrahydro) form. These redox states are interconvertible via two-electron, two-proton transfer steps, with each reduction adding hydrogen atoms to defined nitrogen positions within the bicyclic N-heterocyclic ring system[204]. Due to this redox-active structure, pterins are functionally comparable to cofactors like flavin (e.g. FAD). However, pterins possess greater redox versatility. While FAD typically undergoes 2-electron, 2-proton transfer, pterins can participate in sequential redox transformations involving up to 4 electrons and 4 protons[222].

The reversible redox cycling is central to the biological activity of pterins, enabling them to act as electron shuttles in enzymatic processes and redox regulation[223]. In particular, the tetrahydro- and dihydro- forms act as important biological reductants, participating in oxidative stress defense by scavenging ROS and protecting enzymes from inactivation[224]. The oxidized forms of pterins accumulate during oxidative stress, signaling redox imbalance and dysfunction in pterin cycling, which can be biomarkers of diseases[225,226].

The three canonical redox forms of biopterin and monapterin are shown in Figure 5.4.

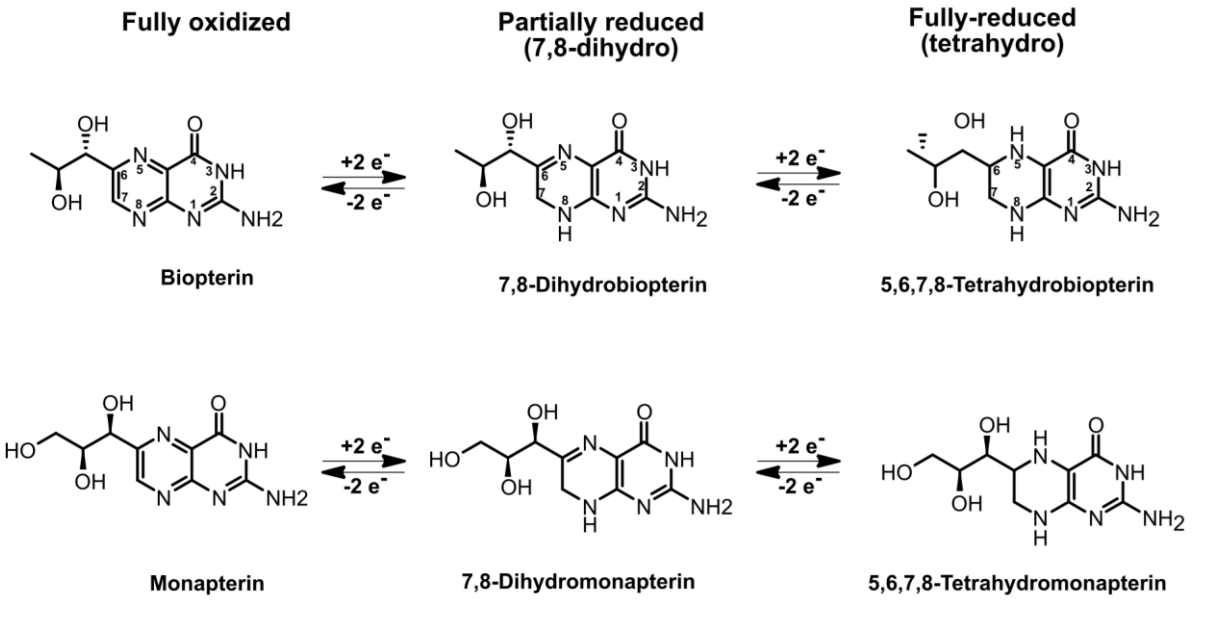

Figure 5.4: Redox states of biopterin and monapterin.
Both molecules exist in three redox forms: fully oxidized, partially reduced (7,8-dihydro-), and fully reduced (5,6,7,8-tetrahydro-). Each transition involves a reversible two-electron transfer. The tetrahydro-form acts as a biologically active cofactor in various enzymatic and redox-related processes.

5.4.5 Pterins: Established Examples and Their Biological Roles

This section provides background information on well-characterized pteridines and their roles in biological systems. Drawing on previous studies and literature, it aims to establish a basis for understanding the possible function of CutA, particularly in the context of pterin binding and redox-related processes.

5.4.5.1 Tetrahydrobiopterin

6R-L-erythro-5,6,7,8-tetrahydrobiopterin (BH4) is one of the most examined unconjugated pterins and is widely conserved across higher organisms[227] and certain bacterial lineages, including *S. elongatus*[228]. It occurs in different oxidation states, as shown in Figure 5.4. As an essential cofactor, BH4 serves as an electron donor for nitric oxide synthase (EC 1.14.13.39), it acts as a reducing agent for alkylglycerol monooxygenase (EC 1.14.16.5) and the aromatic amino acid hydroxylases phenylalanine 4-hydroxylase (EC 1.14.16.1), tyrosine hydroxylase (EC 1.14.16.2), and tryptophan hydroxylase (EC 1.14.16.4)[229]. Therefore, BH4 is crucial for the biosynthesis of monoamine neurotransmitters, such as dopamine, serotonin and norepinephrine, for the metabolism of phenylalanine and lipid-derived esters, and for the

generation of nitric oxide as signaling molecule[230,231]. In the absence of sepiapterin reductase, BH4 biosynthesis can be maintained via alternative pathways involving non-specific reductases such as aldolase reductase and carbonyl reductase[231].

BH4 deficiency in humans manifests in metabolic and neurological dysfunction, primarily through the disruption of phenylalanine metabolism and depletion of monoamine transmitters[232]. Furthermore, dysregulation of BH4 homeostasis has been linked to Alzheimer´s disease pathology, potentially via compromised nitric oxide signaling and increased oxidative stress[233].

As shown in Figure 5.2, BH4 is synthesized de novo from GTP through three enzymes: GTP cyclohydrolase I (GTPCH, EC 3.5.4.16) converts GTP to dihydroneopterin triphosphate (H_2NTP). Subsequently, 6-pyrovyltetrahydropterin synthase (PTPS, EC 4.2.3.12) catalyzes the transformation of H_2NTP into 6-pyruvoyltetrahydropterin (PPH4). Finally, sepiapterin reductase (SR, EC 1.1.1.153) reduces PPH4 to BH4[234].

This biosynthetic pathway of BH4 is conserved in eukaryotes and in some bacteria, including *S. elongatus*[228]. Additionally, in certain bacteria taxa, tetrahydrobiopterin occurs in glycosylated forms, such as 5,6,7,8 tetrahydrobiopterin glucoside, which has been identified in *S. elongatus* PCC 7942[218]. Beyond its cofactor roles, BH4 also contributes to cellular antioxidant defense. It protects enzymes such as tyrosine hydroxylase from inactivation by reactive nitrogen species (RNS), including peroxynitrite ($ONOO^-$) and nitrogen dioxide (NO_2) and therefore preserves enzymatic activity under oxidative and nitrosative stress conditions[235].

BH4 was observed to inhibit Cu^{2+} induced low density lipoprotein oxidation[236]. This antioxidant function underscores the critical importance of reduced pterins in maintaining cellular redox homeostasis and aligns with previous reports demonstrating the ability of BH4 and related pteridines to form stable cupric-pterin complexes[152,237]. In this reaction, the pterin donates electrons to copper ions, reducing Cu^{2+} (e.g. from $CuSO_4$) to Cu^+, while the pterin itself is oxidized[238] (in this case from BH4 to BH2, see also Figure 5.5).

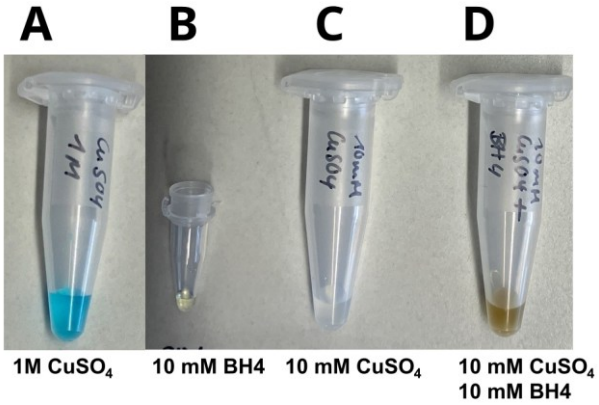

Figure 5.5: Formation of brown complex upon mixing $CuSO_4$ with tetrahydrobiopterin.
(A) 1M $CuSO_4$ displays characteristic blue color. **(B)** 10 mM BH4 is colorless. **(C)** 10 mM $CuSO_4$ appears nearly colorless. **(D)** A 1:1 mixture of 10 mM $CuSO_4$ and 10 mM BH4 rapidly develops a brown color, indicating a redox reaction and formation of a Cu^{2+}-BH4 complex. This figure appears also in the SI of Wagner et al., 2025[46].

Such pterin-mediated Cu^{2+} reduction is biologically relevant, as the resulting Cu^{+} species is more reactive and can participate in Fenton-like reactions with molecular oxygen, leading to the generation of ROS[239]. These ROS can cause oxidative damage and promote cell stress or death through various mechanisms, such as cuproptosis[240]. Interestingly, the key enzyme for many pteridine pathways, GTP cyclohydrolase I can be inhibited by copper ions[241]. Therefore, the interactions between BH4 and copper ions *in vivo* must be tightly regulated to prevent uncontrolled redox activity. It is plausible that CutA plays a role in orchestrating or buffering these interactions, potentially preventing deleterious outcomes by spatially or temporally coordinating the co-localization of BH4 and copper ions.

5.4.5.2 Monapterin and Neopterin

5,6,7,8-Tetrahydromonapterin (MH4) is a major pterin in *E. coli* and has been proposed as the physiological cofactor for phenylalanine hydroxylase (PhhA) in *Pseudomonas aeruginosa*, implicating its involvement in amino acid metabolism[164]. As illustrated in Figure 5.2 and Figure 5.3, tetrahydromonapterin is synthesized in *E. coli* via the sequential action of FolX (dihydroneopterin triphosphate epimerase) and FolM (a short-chain dehydrogenase/reductase)[164]. Like other pteridines such as BH4, MH4 exists in multiple interchangeable oxidation states[242], which are illustrated in Figure 5.4. Beyond bacteria, monapterin has also been detected in eukaryotic cells, where it localizes to actin-rich regions and has been associated with chemotactic signaling[243]. Structurally, monapterin closely resembles neopterin, a pterin derivative predominantly found in eukaryotic cells. Both compounds are diastereomers that are difficult to distinguish using standard metabolomic

methods. While monapterin derivatives in bacteria have been associated with metabolic functions[164], neopterin functions as a marker of immune activation in eukaryotic systems[205].

The formation of neopterin or monapterin is determined by an epimerization reaction that can occur at different points along the biosynthetic pathway. In *E. coli*, this reaction is catalyzed by the epimerase FolX, which converts dihydroneopterin triphosphate to dihydromonapterin triphosphate, thereby redirecting the pathway away from folate biosynthesis (see Figure 5.2). The resulting intermediate is subsequently reduced by the NADPH-dependent reductase FolM to produce tetrahydromonapterin[164].

The close structural and functional similarity between monapterin and tetrahydrobiopterin raises the question of whether MH4 can act as a functional analog of BH4 and vice versa.

This functional interchangeability has already been demonstrated for nitric oxide synthase (NOS). NOS synthesizes nitric oxide (NO) from L-arginine, utilizing NADPH, tetrahydrobiopterin and molecular oxygen (O). NOS is not naturally present in *E. coli*. However, Correa-Aragunde et al. (2022)[244] demonstrated that heterologous expression of NOS from the alga *Ostreococcus tauri* (OtNOS) and the cyanobacterium *Synechococcus* PCC 7335 (SyNOS) in *E. coli* promotes growth, enhances arginine utilization, reduces ROS levels, and protects the bacteria against nitrosative stress induced by sodium nitroprusside (SNP) or S-nitrosoglutathione (GSNO). Importantly, because *E. coli* does not produce BH4, which is the canonical NOS cofactor, the authors proposed that MH4 can act as an alternative cofactor to support NOS activity in the *E. coli* host. This provides experimental evidence that tetrahydromonapterin may fulfill a physiological role analogous to BH4 in enabling NOS function. In this context, our observation of BH4 binding to CutA could also reflect a physiologically relevant interaction with MH4 in *E. coli* or cyanobacteria. Given this functional substitution for tetrahydrobiopterin, it would be worthwhile to investigate whether tetrahydromonapterin can also bind to CutA. In the present study, tetrahydrobiopterin was used due to its commercial availability.

5.4.5.3 Molybdopterin

Molybdenum-dependent enzymes are integral to fundamental metabolic pathways and contribute significantly to agriculture, global biogeochemical cycling, and host-microbe interactions. These enzymes primarily catalyze oxo-transfer reactions central to the metabolism and degradation of nitrogen-, sulfur-, and carbon-containing substrates[245]. A key

metabolite of their catalytic capacity is a specialized metal-binding cofactor. This role can be fulfilled by molybdopterin, a pterin-derived cofactor essential for the catalytic activity of most molybdenum- and tungsten-dependent oxidoreductases[246]. Upon coordination with either metal, it forms the molybdenum cofactor (Moco) or tungsten cofactor, which is incorporated into the active site of the enzyme to enable redox catalysis[246].

The biosynthesis of Moco proceeds through four conserved steps mediated by at least six dedicated enzymes and requires iron, ATP, and copper[247]. Following its maturation, Moco is distributed intracellularly by Moco-binding proteins to target molybdoenzymes[248]. Given the central role of Moco-dependent oxidoreductases in core metabolic pathways, disruptions in Moco biosynthesis are frequently lethal[245]. One of the most well-characterized Moco-dependent enzymes is xanthine oxidase, which plays a central role in purine catabolism[249].

Moco depicts a biological system in which a transition metal is coordinated by a pterin scaffold (molybdopterin) to enable redox catalysis. CutA similarly binds both copper ions and pteridine-derived ligands. This parallel shows that pterins can act as flexible ligands that bind metals and influence their redox activity. In CutA, the combined binding of copper ions and pterin ligands may modulate redox chemistry by limiting uncontrolled electron transfer and $Cu^{2+/}Cu^{+}$ cycling, thereby contributing to the maintenance of cellular redox homeostasis under copper stress.

5.4.5.4 Isosepiapterin

In this work, isosepiapterin was co-purified alongside 2'-deoxyxanthopertin B2 from *S. elongatus* cell extracts and was also shown to bind to CutA in native metabolomics experiments (Figure 4.3, Supplementary Figure 13).

Isosepiapterin is a yellow-colored pteridine derivative and a structural isomer of sepiapterin[250]. It has been identified in various biological systems, in pro- and eukaryotes, for example as an eye-pigment of *Drosophila melanogaster*[251], in amphibians[252] or the mexican fruit fly *Anastrepha ludens,* where it is proposed as a potential age-determination marker[253]. Isosepiapterin was first described in different cyanobacteria in the 1950s, particularly in *Anacystis nidulans* (now *Synechococcus elongatus*), where it is released in response to cold shock, accompanied by a loss of photosynthetic activity and cell viability[147].

In the present study, we neither identified isosepiapterin in the supernatant of standard grown cells (28°, constant illumination) nor observed a growth difference between *S. elongatus* WT

and *ΔcutA* after cold shock. However, isosepiapterin was found in and purified from the cell extracts (Figure 4.3). This likely reflects intact membrane integrity of the harvested cells, in contrast to earlier cold shock experiments of the study cited above, where the cold shock and harsher treatment to obtain the supernatant might have caused disruption of the cell membrane integrity, which might have led to leakage of polar intracellular compounds such as pterins into the medium, as well as to reduced photosynthetic activity and viability of the cells. The gentle handling used in the current setup aimed to avoid cell lysis and preserve intracellular content.

The cellular biosynthesis of isosepiapterin is not well understood and may result from oxidative degradation of other pterins. Enzymes such as sepiapterin deaminase (EC3.5.4.24) and pterin deaminase (EC 3.5.4.11) can process isosepiapterin, albeit less efficiently than their primary substrates. In silkworms, sepiapterin deaminase catalyzes the hydrolysis of sepiapterin to form xanthopterin-B2 and ammonia, though it also accepts isosepiapterin[148]. In *Bacillus megaterium*, pterin deaminase can deaminate isosepiapterin to its corresponding lumazine[216], a process that might also have occurred in the *S. elongatus* samples analyzed and described in Chapter 4, as DXan-B2 might be the corresponding lumazine to isosepiapterin (Figure 4.3). In insects, isosepiapterin can be derived from 6-pyruvoyl-tetrahydropterin as a side product of the sepiapterin-branch of pteridine biosynthesis[254]. In *S. elongatus*, tetrahydrobiopterin (BH4)-glucoside is produced by the UDP-glucose:BH4 glucosyltransferase[218]. BH4 or its derivatives have been reported to be converted into sepiapterin in engineered *E. coli* expressing cyanobacterial and human pterin biosynthesis enzymes[255]. By analogy, BH4-glucoside produced in cyanobacteria could potentially serve as a precursor for isosepiapterin, although this has not been directly demonstrated.

An internal metabolome study in the Forchhammer group (Mahrholdt, 2015) detected sepiapterin and dihydrobiopterin in a P_{II}:I86N mutant of *Nostoc* sp. 7120, although genome analysis revealed no sepiapterin reductase gene[256], suggesting the presence of alternative metabolic pathways.

5.4.6 Lumazines

Natural occuring lumazines have been characterized as pigments in both animals and plants and appear to be more prevalent in marine-derived bacteria and fungi than the widely studied pterin family[207]. Lumazines are heterocyclic compounds derived from the riboflavin biosynthetic pathway (see Figure 5.2) but can also arise from the microbial degradation of folic acid or pterins, mediated by pterin deaminases[207,257]. These enzymes catalyze the deamination of pterins at the C-2 position, leading to the formation of stable lumazine tautomers[207,258]. In nature, lumazines are frequently found together with their corresponding pterin derivatives[207]. This was also observed in this study. Here, 6-propionyllumazine was co-purified with 6- propyonylpterin and 2'-deoxyxanthopterin B2 with isosepiapterin (as visualized in Figure 4.3, Chapter 4).

Lumazines have fluorescent properties and exhibit photochemical activity[259]. They have been used as biomarkers, as seen with lepteridine, a lumazine-derivative that is uniquely detectable in the authentic mānuka honey and has been proposed as a marker for its verification[260].

Several natural lumazines demonstrate biological activity. For example, 6-oxolumazine is an inhibitor of xanthine oxidase (which catalyzes the final steps of purine metabolism, where it is oxidizing hypoxanthine to xanthine and xanthine to uric acid)[261], and various ribityl-lumazines found in the supernatant of *Salmonella typhimurium* have been shown to activate human mucosal-associated invariant (MAIT) cells, indicating their role in microbial immune recognition[207,262]. Other lumazines could inhibit riboflavin synthase of *E. coli*[263], which underscores their potential as antimicrobial agents. Against this background, 2'- deoxyxanthopterin B2, the previously unrecognized lumazine identified in this study (Figure 4.3), would be an interesting candidate for antimicrobial activity. Since *S. elongatus* is easily maintained under laboratory conditions, this would allow for comparably straightforward production and purification of the compound. Moreover, as the genus *Synechococcus* is among the most prevalent cyanobacteria in aquatic environments and plays a central role in global oxygen production, insights into its specialized metabolites may also contribute to a better understanding of its ecological fitness and survival strategies.

Lumazines, like pterins, also possess redox activity and the ability to coordinate metal ions. They undergo pH-dependent redox reactions involving two-electron/ two-proton transfers. It was observed that oxidation is irreversible above pH 7, while reduction is quasi-reversible in acidic and reversible in basic conditions[264]. Additionally, lumazines derivates form stable bidentate complexes (in which the ligand coordinates to the metal through two donor atoms)

with transitions metals such as $Cu^{2+,}$ Co^{2+} and Cd^{2+} [265]. In natural ecosystems, the ability of lumazines and related pterins to coordinate transition metals may play a crucial role in metal availability, particularly in aquatic environments where factors such as ocean acidification can limit the bioavailability of essential metals like copper.

Given that CutA binds $CuSO_4$ and was observed to bind the lumazine derivative 2'- deoxyxanthopterin B2 and considering that lumazine derivatives form stable complexes with transition metals, it is conceivable that CutA also mediates or stabilizes metal-lumazine complexes, thereby linking its metal-binding capacity to lumazine-related redox chemistry.

5.4.7 Pterins and NOS

Nitrogen is a vital element for life, serving as an essential constituent of proteins and nucleic acids. In nature, it occurs in oxidation states ranging from N(V) to N(−III)[266] and its interconversion drives the global biogeochemical nitrogen cycle, in which bacteria play a central role[267]. Among the enzymes involved in nitrogen and redox metabolism, the nitric oxide synthases (NOS) catalyze the oxidation of L-arginine to L-citrulline with concomitant production of nitric oxide (NO)[244].

NOS enzymes function as homodimers, composed of an N-terminal oxygenase domain and a C-terminal reductase domain. The oxygenase domain contains a heme prosthetic group, the essential pterin cofactor tetrahydrobiopterin and a binding site for the substrate L-arginine. The reductase domain binds flavins (FAD and FMN) and transfers electrons from NADPH to the oxygenase domain to support catalysis[268]. Between these two domains lies a calmodulin-binding region, which is critical for both the structural integrity and enzymatic activity of NOS[269]. Unlike animal NOS, bacterial NOS proteins are flexible regarding their pterin cofactor, using either tetrahydrobiopterin, tetrahydrofolate or tetrahydromonapterin[244,270] (as described in section 5.4.5.2). In cyanobacteria, such as *Synechococcus* PCC 7335, the nitric oxide synthase SyNOS catalyzes the oxidation of L-arginine to NO and citrulline, with BH4 supplying electrons to the heme for oxygen activation[268,271].

Proteomics pulldown experiments support a role for CutA in nitrogen-and redox-related regulation. In *E. coli,* the NO-responsive transcription factor OxyR was co-purified with CutA in the *in vivo* pulldown after *cutA* induction (Figure 3.12).

In the *in vitro* pulldown of *S. elongatus*, there was significantly more P_{II}-nitrogen regulatory protein in the samples with CutA than without (Figure 3.9).

Furthermore, L-arginine was enriched in the *ΔcutA::kan* mutant compared to the WT in untargeted metabolomics. Conversely, ornithine was decreased in targeted metabolomics (Figure 4.1), suggesting a disturbed nitrogen metabolism.

The observed binding of tetrahydrobiopterin to CutA, a P_{II} nitrogen regulatory-like protein, raises the possibility that CutA may functionally interact with pterin-dependent enzymes such as NOS. In this context, CutA could potentially serve as a stabilizing or carrier protein for BH4, thereby influencing NO production and linking its biochemical role to both nitrogen metabolism and redox chemistry.

5.4.8 Pterins in Cyanobacteria

The first bacterial pteridines were identified in cyanobacterial species, including *Anacystis* (a former name for *Synechococcus*), *Anabaena*, and *Nostoc*[272,273]. Cyanobacteria are known to produce distinctive unconjugated pteridines, often in the form of glycosylated derivatives called pteridine glycosides, where various sugars are attached to the C6 side chain of the pterin ring[274,275]. These compounds are not unique to cyanobacteria, for example neopterinyl-3′-β-d-glucuronic acid has been described in *Bacillus subtilis*[276] and *Mycobacterium smegmatis* produces a glucuronide conjugate of a pentahydroxy-pentyl-substituted pterin[277].

In *S. elongatus*, tetrahydrobiopterin (BH4)-glucoside is synthesized from UDP-glucose and BH4 by UDP-glucose:BH4 glucosyltransferase, a monomeric enzyme of 39.2 kDa requiring Mg^{2+} as a cofactor[218]. In *Synechocystis* PCC 6803, another pterin glycoside, cyanopterin, has been implicated in phototaxis, enabling the cyanobacterium to sense and respond to UV-A/blue light[217]. Inactivating the pteridine glycosyltransferase gene (*pgtA*), which is essential for cyanopterin biosynthesis, caused abnormal photomovement, leading the mutant strain to move away from UV-A light, unlike the wild type. Inhibiting pterin biosynthesis with N-acetylseretonin, an inhibitor of sepiapterin reductase, also reduced positive phototaxis in the wild type under certain light conditions. This findings suggests that cyanopterin functions as a chromophore in a UV/blue light photoreceptor system that regulates phototaxis[278].

Cyanopterin is constitutively produced within cells at a high concentration, with a molar ratio to chlorophyll *a* of approximately 1:1. In *vivo*, it predominantly exists in its fully reduced 5,6,7,8-tetrahydro form[279]. Comparative analysis of chlorophyll content and pterine production in *Synechocystis* indicate that pteridine production correlates with growth rate[280].

This is consistent with the findings that more 2'-deoxyxanthopterin B2 was observed in the exponential growth phase than in the stationary growth phase (Supplementary Figure 7).

Pteridine glycosyltransferases are present in cyanobacteria, including *Synechococcus* species, where they play a role in the glycosylation of pterins. Homologs of these enzymes have been identified in various cyanobacteria, such as *Anabaena* sp. PCC 7120, *Nostoc punctiforme*, *Synechococcus* sp. WH8102, and *Prochlorococcus marinus* (MED4). However, the specific pteridine glycosyltransferase responsible for the first glycosylation step in *Synechocystis* sp. PCC 6803 remains unidentified, despite the apparent conservation of these enzymes across cyanobacteria[280].

Given that tetrahydrobiopterin (BH4) binds to CutA *in vitro*, it is conceivable that glycosylated derivatives of BH4, such as BH4-glucoside, could also interact with CutA. In cyanobacteria, also other pterin glycosides such as cyanopterin are abundant and play important physiological roles, suggesting that CutA might recognize a broader range of pterin-containing ligands. This possibility warrants experimental testing, particularly to determine whether CutA shows specificity for glycosylated versus non-glycosylated pterins.

While purification of BH4-glucoside directly from crude cell extracts would be challenging due to its likely low intracellular abundance, the compound could instead be generated in vitro by heterologous expression and purification of the corresponding UDP-glucose:BH4 glucosyltransferase followed by incubation with purchased BH4 (sapropterin) and UDP-glucose in the presence of Mg^{2+}. The resulting enzymatic reaction product could be used without full purification, after desalting or buffer exchange, in binding assays such as isothermal titration calorimetry, microscale thermophoresis, or pulldown followed by LC-MS analysis, to compare CutA's affinity for BH4 and its glycosylated form.

6 Conclusion

This study aimed to elucidate the functional role of CutA, a P_{II}-like protein conserved across all domains of life. To investigate its function, a combination of different experimental approaches, like physiological comparison of WT and knockout mutants, metabolome and proteome studies, investigation of ligand binding using native metabolomics as well as biophysical approaches were performed employing two model organisms: *Escherichia coli*, a well-characterized facultative anaerobic bacterium relevant to microbiome research, and *Synechococcus elongatus* PCC 7942, a photosynthetic cyanobacterium.

Physiological experiments comparing wild-type and *ΔcutA* strains revealed that the knockout strains exhibited delayed recovery under various stress conditions, including heat (both species), low pH and copper (in *E. coli*), and β-lactam antibiotics (*S. elongatus*). These phenotypes indicate that CutA contributes to maintenance and repair of the cell envelope likely by supporting repair mechanisms that are impaired and operate more slowly in its absence.

To explore potential molecular mechanisms, native metabolomics was employed to screen a broad range of metabolites for interactions with trimeric CutA. A previously unknown pteridine, 2'-deoxyxanthopterin B2, was identified in *S. elongatus* extracts, which interacted with CutA from both species. Subsequent purification of this fraction led to the discovery of three additional pteridines, two of which were found to bind to CutA. Pteridines are heterocyclic, nitrogen-containing compounds that often act as cofactors, pigments, or electron shuttles and can form redox-active complexes with metals. Subsequent testing of tetrahydrobiopterin and 7,8-dihydrobiopterin confirmed their binding to *Ec*CutA, using native metabolomics and nano differential scanning fluorimetry. Microscale thermophoresis confirmed that $CuSO_4$ binds to *Ec*CutA, with binding enhanced in the presence of tetrahydrobiopterin, which may point to cooperative interactions between metal and pterin ligands.

Given that pterins can form complexes with copper[152] and facilitate the reduction of Cu^{2+} to the more reactive Cu^{+} state, thereby promoting redox cycling and ROS generation, the simultaneous binding of copper and pteridines to CutA suggests a functional role in regulating redox-active copper species *in vivo.*

Complementary physiological assays reinforced these findings: *ΔcutA* mutants were significantly more sensitive to copper stress, and this phenotype was partly rescued by complementation with native *cutA*. Complementation with a CutA variant in which three conserved glutamate residues in the negatively charged binding pocket were substituted with alanine also improved stress recovery, but less effectively than complementation with the native *cutA*, indicating that pterin binding at this site contributes to CutA's protective function under copper stress.

Proteomic pulldown experiments further revealed that CutA associates with the fatty acid biosynthesis proteins FabZ and AcpP, suggesting that, in addition to redox and copper regulation, CutA participates in membrane-responsive stress adaptation.

These findings are consistent with reports that other genes originally annotated as *cut* genes also contribute to cell envelope stress responses beyond their roles in copper regulation[20].

This study points to a role for CutA as a coordinator of metal homeostasis, redox regulation, and stress adaptation. By binding pteridine metabolites and copper, CutA likely modulates redox-active copper species, mitigating oxidative damage under stress conditions such as heat, low pH, β-lactam antibiotics, and copper exposure. The physiological defects observed in *ΔcutA* mutants, along with identified pterin and copper binding and associations with fatty acid biosynthesis proteins, indicate that CutA supports cell envelope maintenance, redox balance, and membrane-responsive stress adaptation.

Overall, these findings position CutA as a mediator of cellular stress responses, linking metal and redox regulation to cellular integrity.

7 Materials and Methods

In this section, the methods applied in Chapter 3 are described. The methods corresponding to the manuscript in Chapter 4 are presented within the manuscript itself, and those related to the paper draft in the appendix are described in the respective draft.

7.1 Strains, Plasmids and Oligonucleotides

Details of the strains, plasmids and oligonucleotides employed and constructed in this work are provided in Table 7.1, Table 7.2 and Table 7.3, respectively.

Table 7.1: Bacterial strains used in this work.

Strain	Genotype	Purpose	Reference
Cyanobacterial strains			
Synechococcus elongatus PCC 7942	WT	Characterization, Pteridine Purification	Van den Hondel et al., 1980[281]
Synechococcus elongatus PCC 7942 Δ*cutA::kan*[13]	Δ*cutA::kan*	Characterizations	Selim et al., 2021
Nostoc sp. 7120	WT	Pulldown	Rippka et al., 1979
***E. coli* strains**			
E. coli BW25113	WT	Characterization	Baba T, et al., 2006 Keio collection Strain
E. coli BW25113 Δ*cutA* (seamless)	*E. coli* Δ*cutA*	Characterization	This work
E. coli Lemo21(DE3) Competent Cells	*fhuA2 [lon] ompT gal* (λ DE3) [*dcm*] Δ*hsdS*/ pLemo(Cam^R) λ DE3 = λ sBamHIo ΔEcoRI-B *int::(lacI::*PlacUV5::T7 gene1) *i21* Δ*nin5* pLemo = pACYC184-PrhaBAD-*lysY*	Protein expression (purchased)	New England Biolabs
E. coli Lemo21(DE3) pASK[*EccutA*]	*fhuA2 [lon] ompT gal* (λ DE3) [*dcm*] Δ*hsdS*/ pLemo(Cam^R) λ DE3 = λ sBamHIo ΔEcoRI-B *int::(lacI::*PlacUV5::T7 gene1) *i21* Δ*nin5* pLemo = pACYC184-PrhaBAD-*lysY*, Amp^r	Protein expression of *E. coli* CutA	This work
E. coli Lemo21(DE3) pASK[Se*cutA*]	*fhuA2 [lon] ompT gal* (λ DE3) [*dcm*] Δ*hsdS*/ pLemo(Cam^R)	Protein expression of *S. elongatus* CutA	This work

	λ DE3 = λ sBamHIo ΔEcoRI-B *int::(lacI::*PlacUV5::T7 gene1) *i21* Δ*nin5* pLemo = pACYC184-PrhaBAD-*lysY*, Amp^r		
E. coli Lemo21(DE3) pASK[*NscutA*]	*fhuA2 [lon] ompT gal* (λ DE3) [*dcm*] Δ*hsdS*/ pLemo(Cam^R) λ DE3 = λ sBamHIo ΔEcoRI-B *int::(lacI::*PlacUV5::T7 gene1) *i21* Δ*nin5* pLemo = pACYC184-PrhaBAD-*lysY*, Amp^r	Protein expression of *Nostoc* sp. PCC 7120 CutA	This work
NEB 10-beta Competent *E. coli*	Δ(*ara-leu*) 7697 *araD139 fhuA* Δ*lacX74 galK16 galE15* e14-Φ80d lacZΔM15 *recA1 relA1 endA1 nupG rpsL*(StrR) *rph spo*T1 Δ(*mrr-hsdRMS-mcrBC)*	Plasmid propagation for molecular cloning of larger plasmids or difficult constructs (purchased)	New England Biolabs
E. coli TOP10 Competent Cells	F$^-$ *mcrA* Δ(*mrr-hsdRMS-mcrBC*) φ80lacZΔM15 *lacX74 recA1 araD139* Δ(*ara-leu*)7697 *galU galK rpsL* (Str^r) *endA1 nupG*	Plasmid propagation for molecular cloning of smaller plasmids (purchased)	Thermo Fisher Scientific
E. coli Δ*cutA::kan*	F-, Δ(*araD-araB*)567, Δ*lacZ*4787(::rrnB-3), λ-, *rph-1,* Δ(*rhaD-rhaB*)568, Δ*cutA*763::kan, *hsdR*514	Characterization	Baba T, et al., 2006 Keio collection Strain JW4097-1
E. coli Δ*cutA::folX*	F-, Δ(*araD-araB*)567, Δ*lacZ*4787(::rrnB-3), λ-, Δ*folX*785::kan, *rph*-1, Δ(*rhaD-rhaB*)568, *hsdR*514	Characterization	Baba T, et al., 2006 Keio collection Strain JW2300-1
E. coli JW4097(Δ cutA::kan) -DE3+ pet15b-cutA1	F-, Δ(*araD-araB*)567, Δ*lacZ*4787(::rrnB-3), λ-, rph-1, Δ(*rhaD-rhaB*)568, Δ*cutA*763::kan, *hsdR*514, pET15b-*cutA*1, Amp^R	Complementation	Rubio, in Selim et a., 2021
E. coli JW4097(Δ cutA::kan) -DE3+ pet15b-cutA2	F-, Δ(*araD-araB*)567, ΔlacZ4787(::rrnB-3), λ-, rph-1, Δ(*rhaD-rhaB*)568, Δ*cutA*763::kan, *hsdR*514, pET15b-*cutA2*, Amp^R	Complementation	Rubio, in Selim et a., 2021
E. coli Δ*cutA::kan* pETblank-*cutA*	pETblank carrying cutA including native promoter and RBS	Characterization	This work
E. coli Δ*cutA::kan* pETblank-*cutA*-E59A/E61A/E90A	pETblank carrying *cutA* allele with substitutions E59A, E61A, E90A, including native promoter and RBS	Characterization	This work

Table 7.2: Plasmids used in this work.

Plasmid	Resistance	Purpose	Reference
pSLTS [175]	Amp (100µg/m), Cm (25µg/m)	Temperature-sensitive plasmid carrying λ Red recombinase genes (gam, bet, exo) under arabinose control and the I-SceI endonuclease for double-strand break induction during markerless mutagenesis.	Kim et al., 2014
pT2SK[175]	Amp (100µg/m) and Kan (50µg/m)	Cloning vector carrying a selection marker, I-SceI recognition site, and transcription terminator (TT) for generating deletion cassettes used in recombineering.	Kim et al., 2014
pASK[*E. coli*_cutA]	Ampicillin (100 µg/mL)	Protein purification	This work
pASK[*S. elongatus_cutA*]	Ampicillin (100 µg/mL)	Protein purification	Selim et al., 2021
pet15b-EccutA1	Ampicillin (100 µg/mL)	Complementation	Selim et al., 2021
pet15b-EccutA1	Ampicillin (100 µg/mL)	Complementation	Selim et al., 2021
pASK[*Nostoc7120 _cutA*]	Ampicillin (100 µg/mL)	Protein purification	Selim et al., 2021
pETblank[*E.c.cutA*]	Ampicillin (100 µg/mL)	Complementation	This work
pETblank[*E.c.cutA1* E59A, E61A, E90A]	Ampicillin (100 µg/mL)	Complementation	This work

Table 7.3: Oligonucleotides used in this work.

Oligo Name	Sequence (5′-3′)	Template	Product / Purpose
P1_cutA_fw	TAGCTTCATGCTGTAATGATCAATCGCG	*E. coli* genomic DNA	Amplify *E. coli cutA1*
P2_cutA_rev	TAGAGGTAGTAACCGTCTTTGATCTGCC		
Sel_cutA_fw	TGACCTCAGTTCCCTGATTG	*S. elongatus* genomic DNA	Amplify *S. elongatus cutA*
Sel_cutA_rev	AGGACTGAATCGGCGTAATG		
Asp7120_cutA_fw	AGAACACGGAGAACGGATTG	*Nostoc* sp. PCC 7120 genomic DNA	Amplify *Nostoc* sp. PCC 7120 *cutA*
Asp7120_cutA_rev	TGTCACTTCTGCCTCTGAAC		
pASK_IBA3_fw	GAGTTATTTTACCACTCCCT	pASK-IBA3 plasmid	Verification of insert in pASK plasmid MCS
pASK_IBA3_rev	ACGCAGTAGCGGTAAAC		
Ecoli_cutA_Gibson_fw	GTGAAATGAATAGTTCGACAAAAATCTAGATAACGAGGGCAAAAAATGCTTGATGAAAAAAG	*E. coli* genomic DNA	*E. coli cutA* with Gibson overlaps for pASK
Ecoli_cutA_Gibson_rev	CTTATTATTTTTCGAACTGCGGGTGGCTCCAAGCGCTGCGTAAAGATGCGTTGAGCCATG		*E. coli cutA* with Gibson overlaps for pASK
Ecoli_rnpB_qPCR_fw	TAAACTCCACCCGGAGCAAG	*E. coli* cDNA	Amplify *rnpB* (reference gene)
Ecoli_rnpB_qPCR_rev	TTCATCTAGGCCAGCAATCG	*E. coli* cDNA	Amplify *rnpB* (reference gene)
Ecoli_cutA_qPCR_fw	GCTATGTACGGCACCAGATG	*E. coli* cDNA	Amplify *cutA1* (target gene)
Ecoli_cutA_qPCR_rev	CTTGCTCCAGCTTACCTTCC	*E. coli* cDNA	Amplify *cutA1* (target gene)
Seamless PCR cloning after Kim, 2014			
pKDTS_fw	TAGGCGCAATCACTTTCGTCTACTC	pSLTS plasmid	Sequencing of pSLTS
pKDTS_rev	TTGAGTGACATGCAAAGTAAGTATGATCTC		
MF_fw	ATCTCAAGAGTGGCAGC	pT2SK plasmid	Amplify selection cassette
MF_rev	TTACGCCCCGCCCTGC		
pHA_fw	CGCAGGAAAGAACATGTG	pT2SK plasmid	Amplify plasmid backbone
pHA_rev	AAGGGCCTCGTGATACG		
pHA_seq_fw	TATCAGGGTTATTGTCTCATGAGCG	mutant construct	Verify mutation fragment
pHA_seq_rev	ACTTGAGCGTCGATTTTTGTGATGC		
5`mutCassette_fw	AGGCGTATCACGAGGCCCTTATGATCAATCGCGGGGCGTTCAC	Mutation template plasmid	5`-mutation fragment
5`mutCassette_rev	ACCGCTGCCACTCTTGAGATTGCAAAGTAGCAGGAAAACACCTCGCAAGAACAGATGGAACCG	Mutation template plasmid	5`-mutation fragment
3`mutCassette_fw	GCAGGGCGGGGCGTAATCTTGCGAGGTGTTTTCCTGCTACTTTGCAGCACTTCCGTTTTTG	Mutation template plasmid	3´-mutation fragment
3`mutCassette_rev	CTCACATGTTCTTTCCTGCGCATGTTGGTTTTGCTGAAAATC	Mutation template plasmid	3´-mutation fragment

7.2 Cultivation of Bacterial Strains

Media compositions and cultivation conditions used for bacterial strains are described below.

7.2.1 BG11 Medium

Cyanobacterial strains were cultivated under photoautotrophic conditions in BG11 medium (according to Rippka, 1979) supplemented with 5 mM $NaHCO_3$. Stock solutions of the individual components were prepared with Milli-Q water and autoclaved separately. The final medium was obtained by combining the autoclaved stock solutions, adding the trace element solution (Table 7.4), and filling up to the desired volume with Milli-Q water. Sodium hydrogen carbonate ($NaHCO_3$) was sterile-filtered and added after autoclaving. The final concentrations of all medium components are listed in Table 7.5.

Table 7.4: Composition of BG11-medium for cultivation of cyanobacterial strains.

Component	Final concentration [mM] in BG11
$NaNO_3$	17.65
K_2HPO_4	0.18
$MgSO_4$ x 7 H_2O	0.30
$CaCl_2$ x 2 H_2O	0.250
EDTA	0.003
Na_2CO_3	0.38
Fe-citrate	0.03
Citric acid	0.03
$NaHCO_3$	5.0

Table 7.5: Composition and final concentration of the trace element solution for BG11.

Component	Final concentration [µM] in BG11
H_3BO_4	46.26
$MnCl_2$ x 4 H_2O	9.15
$ZnSO_4$ x 7 H_2O	0.77
Na_2MoO_4	1.61
$CuSO_4$ x 5 H_2O	0.32
Co $(NO_3)_2$ x 6 H_2O	0.17

Cultures (50 mL) were grown in 100 mL shaking flasks under continuous light (30-60 µmol photons m^{-2} s^{-2}) and constant agitation (120 rpm) at 28 °C, unless stated otherwise. For solid cultures, BG11-agar plates were prepared by mixing 2x concentrated

BG11 medium with 10g/L Bacto agar (Becton, Dickinsons and Company) and poured after autoclaving.

7.2.2 LB Medium

Escherichia coli strains were cultivated in liquid lysogeny broth (LB) medium[282] (Table 7.6) at 37°C in the dark with constant shaking (250 rpm) to maintain aerobic growth, or on solid LB-Agar (Lennox, Roth).

Table 7.6: Composition of Lysogeny Broth.

Component	g/L
Tryptone	10
Yeast extract	5
NaCl	10

7.2.3 M9 Medium

For experiments under limited nutrient conditions or to limit the background noise for LC-MS experiments, *E. coli* was cultivated in minimal medium. M9 minimal medium was prepared according to the protocol of Klaus Hantke. A 10x M9 salt stock solution was prepared containing 60 g Na_2HPO_4, 30 g KH_2PO_4, 5 g NaCl and 10 g NH_4Cl per L of distilled water. For 1 L of M9 medium, 100 mL of 10x M9 salt solution was mixed with 10 mL of sterile 40% (w/v) glucose and 1 mL of sterile 1 M $MgSO_4$. The volume was adjusted to 1 L with ultra-pure water.

7.2.4 SOC (Super Optimal Broth with Catabolite Repression)

SOC medium was used for recovery of *E. coli* cells after transformation. The composition is shown in Table 7.7.

Table 7.7: Composition of SOC medium (500 mL).

Component	Amount
Tryptone	10 g
Yeast extract	2.5 g
$MgSO_4$	1.2 g
NaCl	0.25 g
KCl	0.093 g
ddH_2O	480 mL
Glucose 10 %	20 mL

7.2.5 TSS Medium and Preparation of Competent Cells

Competent *E. coli* BW25113 cells were prepared according to the Transformation and Storage Solution (TSS) method described by Chung et al. 1989[283]. Cells were grown to the exponential phase (OD_{600} = 0.3-0.4), harvested by centrifugation (10 min, 1,000 x g, 4 °C), and resuspended in one-tenth of the original culture volume in ice-cold TSS. The transformation was performed by mixing the cell suspension with plasmid DNA and incubating on ice for 30 min without heatshock. Transformed bacteria were recovered in SOC medium and plated on selective LB agar plates. Competent cells were either used immediately or frozen at -82 °C in TSS (without additional cryoprotectants).

Table 7.8: Composition of the Transformation and Storage Solution (TSS) for competent *E. coli* (100 mL).

Component	Amount
LB broth	85 mL (base)
PEG (3350 or 8000 MW)	10 % (w/v)
DMSO	5 % (v/v)
$MgCl_2$ or $MgSO_4$	50 mM, adjusted to pH 6.5

7.3 Preparation of Cryostocks

E. coli strains were cultivated overnight in LB medium at 37°C with constant shaking (250 rpm) and appropriate antibiotics. Subsequently, 700 µL of culture was mixed with 300 µL sterile glycerol and stored at -80°C. Revival was performed by spreading frozen cells onto agar plates.

Cyanobacterial strains were cultivated in 50 mL BG11 medium to an $OD_{750} \geq 0.8$. Cultures were centrifuged (3500 x g, 10 min) and resuspended in 4 mL fresh BG11. Aliquots of 1 mL were mixed with 80 µL sterile dimethyl sulfoxide (DMSO), frozen immediately in liquid nitrogen, and stored at -80°C. Frozen cells were revived in darkness and subsequently inoculated into fresh medium to minimize cytotoxic effects of DMSO at room temperature.

7.4 Molecular Cloning

DNA fragments for cloning or plasmid construction were amplified by polymerase chain reaction (PCR) using Q5 high fidelity polymerase (NEB). Colony PCR, performed to screen transformations or verify strain identity, was carried out using RedTaq Master Mix (Genaxxon). Both PCRs were conducted in a SensoQuest Labcycler according to the manufacturer´s protocols. DNA fragments were separated by agarose gel electrophoresis on 0.8% gels prepared in TAE buffer (50 mM Tris, pH8, 1 mM EDTA). Nucleic acids were visualized with Midori Green Advanced stain (Nippon Genetics) and 1x TAX as running buffer. If not dyed previously by polymerase mix, samples were mixed with Purple 6x loading dye (NEB) and separated at a constant voltage of 120 V for ~ 20 min. DNA fragment sizes were estimated using GenLadder 1 kb (Genaxxon).

PCR fragments were purified using the Monarch PCR & DNA Clean-up Kit (NEB), with ultrapure water used as elution buffer. DNA fragments were extracted from gels using Monarch DNA Gel Extraction Kit (NEB). Plasmid DNA was prepared using the Monarch Plasmid Miniprep Kit (NEB). DNA quality and concentration were assessed by measuring absorbance at 260 nm using a NanoPhotometer (Implen).

All plasmids generated in this study (Table 7.2) were assembled via Gibson Assembly[284]. For this, DNA fragments were combined and 5 µL of the mixture was added to 15 uL of pre-cooled Gibson Assembly master mix. The reaction was incubated at 50°C for 1 hour in a thermocycler. The assembly was introduced into electrocompetent *E. coli* NEB 10-β or

E. coli TOP10 cells by electroporation (1.8 kV, 25 µF, 200Ω) with an optimal time constant of ~5 ms using a gene pulser (Bio-Rad).

Plasmids and PCR products were sequenced using the "GATC LIGHTRUN" service of Eurofins Scientifics (Luxembourg). The resulting sequences were analyzed and compared to reference sequences.

7.5 Seamless PCR Cloning and Construction of *E. coli ΔcutA*

The *cutA* deletion mutant was generated using the λ-Red/ I-Sec-based recombineering system as described by Kim et al. (2014)[175]. This approach employed two plasmids: pSLTS, which carries λ-Red recombinase genes under an arabinose-inducible promoter and the I-ScI endonuclease under an anhydrotetracycline (AHT)-inducible promoter, and pT2SK, which was used to construct a mutation cassette for targeted insertion and subsequent knockout of the *cutA* locus. Primers 25_pKDTS-F and 25_pKDTS-R were used to verify pSLTS, pHA_seqF/pHA_seqR to verify pT2SK.

7.5.1 Strain Preparation

E. coli BW25113 cells were transformed with 100 ng of the helper plasmid pSLTS, which encodes λ-Red recombinase genes under an L-arabinose-inducible promoter and the I SecI endonuclease under an anhydrotetracycline-inducible promoter as well as carbenicillin resistance. Transformants were selected on LB agar plates containing carbenicillin (100 µg/mL) and incubated at 30 °C. Since pSLTS carries a temperature-sensitive origin of replication, growth above 37 °C was avoided.

A single colony was inoculated into 5 mL LB medium with carbenicillin and grown overnight at 30 °C, then used to inoculated 10 mL LB + carbenicillin. After 1h of growth, λ-Red expression was induced by addition of L-arabinose (2 mM), and cultures were incubated for an additional 2-3 h at 30 °C until an OD_{600} of 0.7-0.9 was reached. Cells were harvested by centrifugation (4500 x g, 10 min, 4 °C), washed twice with ice-cold 10% glycerol, resuspended in 50-100 µL 10% glycerol and used for electroporation.

7.5.2 Genome Editing

A mutation cassette containing a kanamycin resistance gene flanked by ~ 100 bp homology regions was constructed using Gibson assembly. The 5´and 3´homology fragments were PCR amplified from *E. coli* BW25113 genomic DNA, using primers 5`mut.frag_fw /5`mut.frag_rev and 3`mut.frag_fw/ 3`mut.frag.rev, respectively, to target sequences immediately upstream and downstream of *cutA*.

The selection cassette was amplified from pT2SK, which carries kanamycin resistance genes, using primers 27_MF/28_MR and the plasmid backbone of pT2SK was amplified using pHAFor/ pHARev.

The mutation cassette was assembled by combining 25 fmol of plasmid backbone, 75 fmol of selection cassette, 125 fmol 5´mutation cassette and 125 fmol 3´mutation cassette (sequence of the designed cassettes is listed in

Table 7.9) using Gibson assembly. After transformation, cells were outgrown for 45 min at 37°C and plated on LB crb kan plates. Correct construction of mutation cassette inside the created mutation template plasmid was verified using colony PCR with primers pHA_seqF/ pHA_seqR. The mutation fragment was purified using the Monarch PCR and DNA cleanup kit (NEB).

Subsequently, electrocompetent *E. coli* BG25113 cell harboring the λ-Red helper plasmid pSLTS were mixed with 50-100 ng of the purified mutation cassette on ice. Electroporation was performed and cells were recovered in 450 µL SOC medium for 3 h at 30°C while shaking. Cells were plated on LB agar supplemented with carbenicillin (100 µg/mL) to maintain pSLTS and kanamycin (50 µg/mL) to select for chromosomal integration of the mutation cassette carrying the selection marker.

After overnight incubation at 30 °C, colonies were restreaked on fresh LB + carbenicillin/kanamycin plates. Single colonies were resuspended in sterile phosphate-buffered saline (PBS) plated on LB agar with or without AHT (100 ng/mL) to induce I-SceI-mediated double-streak break formation. This facilitated a second recombination event between homology regions, resulting in excision of the selection cassette and kanamycin marker, generating a markerless and seamless deletion of *cutA*.

Colonies were screened for kanamycin sensitivity to confirm loss of the selection cassette. Deletion of *cutA* was confirmed by colony PCR using primers 5`mut.frag_fw/5´mut.frag_rev and 3´mut.frag_fw/3´mut.frag_rev as well as P1_fw and P2_rev followed by Sanger

sequencing ("GATC LIGHTRUN" service). The helper plasmid pSLTS was cured by growth at 37°C due to its temperature-sensitive origin of replication.

Table 7.9: Mutation fragments for seamless cloning.

Fragment	Sequence (5`→ 3`)
5´ -mutation fragment *cutA*.ec.del. up **Size: 171 bp**	AGGCGTATCACGAGGCCCTTATGATCAATCGCGGGGC GTTCACGCCCCGCTTTCTTTCCCGCCGACTAACATCCTTCC CCCGTCCGTTGTATAGTGACCTCTCTCTTGCGGTTCCATCT GTTCTTGCGAGGTGTTTTCCTGCTACTTTGCAATCTCAAG AGTGGCAGCGGT
3`-mutation fragment *cutA*.ec.del. down **Size: 165 bp**	GCAGGGCGGGGCGTAATCTTGCGAGGTGTTTTCCTGCTAC TTTGCAGCACTTCCGTTTTTGCCGGATTATTCGACGCGCCGG GACGTTCACAATTTGTCCCCGCGGATCAAGCCTTTGCTTTTG ATTTTCAGCAAAACCAACATGCGCAGGAAAGAACATGTGAG

7.6 Protein Expression and Purification

For expression and purification of *E. coli*, *S. elongatus* or *Nostoc* sp. PCC 7120 CutA, 2 L baffled flasks containing 500 mL 2x LB medium were inoculated to OD_{600} = 0.05 from an overnight culture. Cells were grown at 37°C with constant shaking and protein expression was induced at OD_{600} 0.4-0.6 by addition of 200 µg/L anhydrotetracycline or 0.3 mM IPTG. Cultures were further incubated at 20°C for 12-15 h with constant shaking.

Cells were harvested by centrifugation and resuspended in lysis buffer (100 mM Tris/HCL pH 8, 150 mM NaCl, 1 mM EDTA) supplemented with DNase I, RNase, lysozyme and a protease inhibitor tablet (cOmplete, Roche). Cells were disrupted by sonification (4x4 min at a duty cycle of 50% and output control 4 using Branson Sonifier 250 with 5 min breaks on ice between cycles. The lysate was clarified by centrifugation (39000 x g, 90 min, 4°C) and sterile filtration through 0.22 µm PVDF syringe filter (Carl Roth GmbH) and purified via affinity chromatography.

7.7 Affinity Chromatography

Affinity chromatography was performed using either Strep-Tactin XT (IBA Lifescience, Göttingen, Germany, for Strep-tagged proteins or HisTrap HP columns (Cytiva, Marlborough, USA) for His-tagged proteins), following the manufacturers protocols. The lysate containing the expressed protein was loaded onto 5 mL columns via a ÄKTApurifier system (GE Healthcare) with flowrates of 0.5 mL/min. The column was washed until the UV absorbance signal stabilized, indicating that unbound proteins and cell debris had been removed. Fractions of 1 mL were collected, analyzed by SDS-PAGE for purity, and pooled. Samples were either dialyzed or concentrated using Amicon Ultra-15 centrifugal filters (3 kDa cutoff, Merck KGaA). Aliquots of 200 µL were frozen in PCR tubes -80°C in 20% (v/v) glycerol.

7.8 *In vitro* Pulldown Assay

Pull-down assays were performed using heterologous expressed Strep-tagged CutA from *S. elongatus* or *Nostoc* 7120. Pull-downs were performed using Strep-Tactin magnetic beads (IBA Lifesciences). Three experimental setups were carried out: **Treatment A:** Strep-tagged CutA was first incubated with crude cell extract (3 mg/mL total protein) for 15 min at 28 °C, followed by addition of magnetic beads and an additional 15 min incubation with gentle mixing every 3-5 min. **Treatment B:** Strep-tagged CutA was pre-bound to magnetic beads for 15 min at 28 °C, after which crude extract was added and incubated for another 15 min under the same conditions. **Treatment C:** Identical to treatment A but performed at 58 °C to assess heat stability. After incubation, beads were washed 5 times with 1 mL wash buffer, and bound proteins were eluted with 30 µL elution buffer containing 0.5 M biotin. Strep-tagged SbtB or crude extract alone served as controls. Crude extracts were prepared from *S. elongatus ΔcutA::kan*, or *Nostoc* 7120 wild type. Cultures (25 mL) were harvested at mid-logarithmic phase (OD_{750} = 0.6-0.7), pelleted by centrifugation, and resuspended in 250 µL wash buffer (100 mM Tris-HCL, pH8, 150 mM NaCl, 1 mM EDTA). Cells were disrupted by bead beating (6.5 m/s, 30 s, 2 cycles, with a 5-min interval) in glass bead-filled tubes. Lysates were clarified by centrifugation, and total protein concentrations were determined using a BCA assay by measuring absorbance at 562 nm.

7.9 *In vivo* Pulldown Assay

E. coli BW25113 Δ*cutA* strains harboring the pASK[*cutA*_strep] plasmid were used. The experimental design included two main conditions: standard growth at 37°C and heat shock at 58°C for 30 minutes. Biological triplicates were conducted for each condition: three control samples (no CutA expression) and three samples with induced CutA expression under both standard and heat-stressed conditions. The cultures were initially grown in LB medium with ampicillin to secure presence of the complementation plasmid until they reached an OD_{600} of ~0.3. At this point, the cultures were divided, with one half being induced with anhydrotetracycline (AHT) to initiate CutA expression, while the other half served as the non-induced control. After further incubation, cells were either harvested directly or subjected to a heat shock at 58°C for 30 minutes. Following this treatment, the cells were harvested, and the pellets were rapidly frozen in liquid nitrogen for further analysis.

Crude cell extracts were prepared by resuspending the pellets in wash buffer (100 mM Tris-HCL, pH 8, 150 mM NaCl, 1 mM EDTA) and mechanically disrupting the cells using glass beads. The resulting lysates were centrifuged to remove cell debris, and the protein concentration of the supernatant was determined using a Bradford assay. For the pulldown experiments, magnetic Strep-Tactin®XT beads were incubated with the crude cell extract to capture CutA and its potential binding partners. After a series of washes to remove non-specific proteins, the bound proteins were eluted and prepared for downstream analysis.

7.10 Mass Spectrometry Analysis (Proteome-Data)

All pull-down samples were processed and pre-analyzed at the Proteomcenter (Tübingen) by Irina Droste-Borel. Eluted protein fractions were first subjected to a short SDS-polyacrylamide gel electrophoresis purification step, in which proteins were migrated ~1.5 cm into 12% gels and stained with Coomassie blue. Stained gel pieces were excised, followed by in-gel digestion with trypsin. Tryptic peptides were analyzed by liquid chromatography–tandem mass spectrometry (LC-MS/MS) using a Proxeon Easy-nLC system coupled to a Q Exactive HF mass spectrometer (Thermo Fisher Scientific) with a 60 min linear gradient.

Label-free quantification (LFQ) was used to calculate intensities and iBAQ values for semi-quantitative assessment of protein enrichment. Proteins were considered for further analysis

based on the number of unique identified peptides, sequence coverage, and identification score.

7.11 Mass Spectrometry Analysis (Untargeted Metabolome Data)

Experimental setup, measurement methods and data analysis are described in Chapters 3.8.

7.12 Multiple-Sequence Alignment

Amino-acid sequences of CutA and P_{II} (GlnB) from *Escherichia coli*, *Synechococcus elongatus*, and *Nostoc sp.* PCC 7120 were downloaded from UniProt (accession numbers P69488, Q31KX8, Q8YL42, P0A9Z1, P0A3F4, Q9L422). The sequences were aligned in MEGA X with the Clustal W algorithm (gap-opening penalty = 10; gap-extension penalty = 0.2; other parameters at default).

For the multiple-sequence alignment, the amino acid sequences of CutA were retrieved from UniProt for the following species and strains (accession numbers in parentheses): *Escherichia coli* (P69488), *Salmonella typhi* (Q8XGE0), *S. elongatus* (Q31KX8), *Nostoc* sp. PCC 7120 (Q8YL42), *Shewanella oneidensis* (Q8EIY0), *Pyrococcus horikoshii* (O58720), *Homo sapiens* (O60888), *Oryza sativa* (Q109R6).

The FASTA alignment was rendered in Python using pymsaviz 1.x (class MsaViz), applying Taylor residue coloring and displaying a consensus line that reports positional conservation (uppercase = fully conserved, lowercase = partially conserved).

7.13 Optical Density and Absorbance Measurements

Bacterial growth was monitored by measuring the optical density (OD) using a photometer (Specord 205, Analytik Jena). Absorbance spectra of cyanobacterial cultures were recorded from 350 to 750 nm, with growth specifically monitored at 750 nm. To ensure measurements were within the linear range of the photometer, cultures were diluted to an OD_{750} of 0.1-0.4 prior to the measurement.

7.14 Drop Dilution Assays

S. elongatus cultures (OD_{750} = 1) were serially diluted (10^0-10^{-6}) in BG11 medium. For each dilution, 5 µL was spotted in biological replicates onto BG11 agar plates, which were incubated at 28 °C under continuous illumination (30-60 µmol photons m^{-2} s^{-1}). For *E. coli*, cells were treated as indicated, then serially diluted 1:10 in LB medium. Subsequently, 4 µL of each dilution was spotted onto LB agar plates. Colony growth was visualized by scanning the plates on a black background after overnight incubation at 37 °C.

For β-lactam assays, liquid cultures of *S. elongatus* were inoculated at OD_{750} = 0.4 in BG11 and treated with 10 µg/mL ampicillin. Cultures were incubated with shaking at 28 °C under continuous illumination (30-60 µmol photons m^{-2} s^{-1}) and monitored for growth over 14 days. The Δ*cutA::kan* mutant was assessed both with and without ampicillin treatment to evaluate increased β-lactam sensitivity.

A drop dilution assay was performed on BG11 agar containing 2.5 µg/mL carbenicillin. Serial 1:10 dilutions were spotted from cultures at OD_{750} = 1. All assays were conducted at 28 °C under continuous light, and the experiments were performed by Amelie Stadelmann.

E. coli cultures were adjusted to OD_{600} = 0.2 and incubated in 24-well plates containing 500 µL LB and 20 µg/mL ampicillin. Growth was monitored at regular intervals using a plate reader.

7.15 Nanoscale Differential Scanning Fluorimetry

Nanoscale differential scanning fluorimetry (nanoDSF) was performed using a Prometheus NT.48 instrument (Nanotemper Technologies, Munich, Germany) with standard Prometheus capillaries (PR-C002). Protein and ligand samples, both prepared in HEPES buffer, were analyzed with a temperature ramp of 0.5 °C/min from 30 °C to 110 °C. Thermal stability was assessed by monitoring the fluorescence ratio of tryptophane residues (F_{350}/F_{330}), with the melting temperature (Tm) determined from the inflection point of the fluorescence ratio curve and verified using first-derivative analysis. Approximately 300 µM of the *E. coli* CutA trimer was used for these measurements

7.16 RNA Purification and Reverse-Transcriptase- PCR

7.16.1 Primer Design for RT-PCR

For RT-PCR, primers were designed to amplify products between 70-200 bp. The melting temperature of the primers was kept between 60°C and 63°C, with a maximum difference of 3°C between the forward and reverse primers. Each primer's 3' end contained a C or G residue, and the GC content was maintained between 40-60%. Self-complementarity was avoided, and primer lengths were kept between 18-30 nucleotides. The annealing temperature was not set more than 5°C below the melting temperature of the primers. Primers were designed to target the middle of the gene of interest, with a concentration of 0.05-1 µM to avoid primer-dimer formation.

7.16.2 RNA Isolation and cDNA Synthesis

For RNA extraction, 1 mL of *E. coli* culture (OD_{600} =0.6) was harvested by centrifugation both before and after heat treatment at 58°C for 30 or 60 min. The preculture was grown to an OD_{600} of approximately 0.6 and subsequently adjusted to the same density prior to treatment.

RNA isolation was performed using the RNeasy Mini Kit (Quiagen, Hilden, Germany) according to the manufacturer`s protocol with minor modifications.

For cell lysis, 20 mg/mL lysozyme solution was prepared in TE buffer (pH 8.0) and added in a ratio of 2 µL lysozyme to 100 µL TE buffer. β-mercaptoethanol was added to the RLT buffer. Samples were processed in sterile 1.5 mL microcentrifuge tubes using sterile filter tips. RNA was eluted with 30 µL diethylpyrocarbonate (DEPC)-treated water in sterile tubes.

Residual DNA was removed with DNase I (amplification grade, Sigma Aldrich).

Following isolation, RNA quality was assessed by agarose gel electrophoresis (1.5%) in TAE buffer. RNA samples (2 µL) were mixed with 2x RNA Loading Dye (Thermo Fisher) and heated to 70°C for 5 min, then cooled on ice. The RuboRuler High Range RNA Ladder (Thermo Fisher) was used as a reference. Gels were run at 90 V, and distinct 18S and 28S bands indicating RNA integrity.

Subsequently, cDNA was synthesized using the High-Capacity cDNA Reverse Transcription Kit (Applied Biosystems, Waltham, USA) following the manufacturer´s protocol.

Reverse-transcriptase PCR was performed using Q5 High Fidelity DNA-Polymerase (NEB, Ipswich, USA). Amplification cycles were optimized for clear, specific bands (here 30 cycles were used). PCR products were analyzed on 1.5% agarose gels using the NEB 1 kb Plus DNA Ladder and Purple Gel Loading Dye (NEB).

7.16.3 Statistical Analysis

Statistical Analyses were performed using GraphPad Prism version 10.1.2 (334), unless stated otherwise.

8 References

(1) Tetaz, T. J.; Luke, R. K. Plasmid-Controlled Resistance to Copper in Escherichia Coli. *J. Bacteriol.* **1983**, *154* (3), 1263–1268. https://doi.org/10.1128/jb.154.3.1263-1268.1983.

(2) Rouch, D.; Camakaris, J.; Lee, B. T. O.; Luke, R. K. J. Inducible Plasmid-Mediated Copper Resistance in Escherichia Coli. *Microbiology* **1985**, *131* (4), 939–943. https://doi.org/10.1099/00221287-131-4-939.

(3) Bacterial Response to Copper in the Environment: Copper Resistance in Escherichia Coli as a Model System. In *Metal Speciation in the Environment*; Springer Berlin Heidelberg: Berlin, Heidelberg, 1990; pp 625–632. https://doi.org/10.1007/978-3-642-74206-4_34.

(4) Brown, N. L.; Rouch, D. A.; Lee, B. T. O. Copper Resistance Determinants in Bacteria. *Plasmid* **1992**, *27* (1), 41–51. https://doi.org/10.1016/0147-619X(92)90005-U.

(5) Fong, S.; Camakaris, J.; Lee, B. T. O. Molecular Genetics of a Chromosomal Locus Involved in Copper Tolerance in *Escherichia Coli* K-12. *Mol. Microbiol.* **1995**, *15* (6), 1127–1137. https://doi.org/10.1111/j.1365-2958.1995.tb02286.x.

(6) Rogers, S. D.; Bhave, M. R.; Mercer, J. F.; Camakaris, J.; Lee, B. T. Cloning and Characterization of cutE, a Gene Involved in Copper Transport in Escherichia Coli. *J. Bacteriol.* **1991**, *173* (21), 6742–6748. https://doi.org/10.1128/jb.173.21.6742-6748.1991.

(7) Gupta, S. D.; Lee, B. T.; Camakaris, J.; Wu, H. C. Identification of cutC and cutF (nlpE) Genes Involved in Copper Tolerance in Escherichia Coli. *J. Bacteriol.* **1995**, *177* (15), 4207–4215. https://doi.org/10.1128/jb.177.15.4207-4215.1995.

(8) Brown, N. L.; Rouch, D. A.; Lee, B. T. O. Copper Resistance Determinants in Bacteria. *Plasmid* **1992**, *27* (1), 41–51. https://doi.org/10.1016/0147-619X(92)90005-U.

(9) Liang, D.; Nunes-Tavares, N.; Xie, H. Q.; Carvalho, S.; Bon, S.; Massoulié, J. Protein CutA Undergoes an Unusual Transfer into the Secretory Pathway and Affects the Folding, Oligomerization, and Secretion of Acetylcholinesterase. *J. Biol. Chem.* **2009**, *284* (8), 5195–5207. https://doi.org/10.1074/jbc.M806260200.

(10) Zhao, Y.; Wang, Y.; Hu, J.; Zhang, X.; Zhang, Y. CutA Divalent Cation Tolerance Homolog (Escherichia Coli) (CUTA) Regulates β-Cleavage of β-Amyloid Precursor Protein (APP) through Interacting with β-Site APP Cleaving Protein 1 (BACE1). *J. Biol. Chem.* **2012**, *287* (14), 11141–11150. https://doi.org/10.1074/jbc.M111.330209.

(11) Yang, J.; Li, Q.; Yang, H.; Yan, L.; Yang, L.; Yu, L. Overexpression of Human CUTA Isoform2 Enhances the Cytotoxicity of Copper to HeLa Cells. *Acta Biochim. Pol.* **2008**, *55* (2), 411–415. https://doi.org/10.18388/abp.2008_3089.

(12) Arnesano, F.; Banci, L.; Benvenuti, M.; Bertini, I.; Calderone, V.; Mangani, S.; Viezzoli, M. S. The Evolutionarily Conserved Trimeric Structure of CutA1 Proteins Suggests a Role in Signal Transduction. *J. Biol. Chem.* **2003**, *278* (46), 45999–46006. https://doi.org/10.1074/jbc.M304398200.

(13) Selim, K. A.; Tremiño, L.; Marco-Marín, C.; Alva, V.; Espinosa, J.; Contreras, A.; Hartmann, M. D.; Forchhammer, K.; Rubio, V. Functional and Structural Characterization of PII-like Protein CutA Does Not Support Involvement in Heavy Metal Tolerance and Hints at a Small-molecule Carrying/Signaling Role. *FEBS J.* **2021**, *288* (4), 1142–1162. https://doi.org/10.1111/febs.15464.

(14) Stirnimann, C. U.; Grütter, M. G.; Glockshuber, R.; Capitani, G. nDsbD: A Redox Interaction Hub in the Escherichia Coli Periplasm. *Cell. Mol. Life Sci. CMLS* **2006**, *63* (14), 1642–1648. https://doi.org/10.1007/s00018-006-6055-1.

(15) Crooke, H.; Cole, J. The Biogenesis of *c* -type Cytochromes in *Escherichia Coli* Requires a Membrane-bound Protein, DipZ, with a Protein Disulphide Isomerase-like Domain. *Mol. Microbiol.* **1995**, *15* (6), 1139–1150. https://doi.org/10.1111/j.1365-2958.1995.tb02287.x.

(16) Gagarinova, A.; Hosseinnia, A.; Rahmatbakhsh, M.; Istace, Z.; Phanse, S.; Moutaoufik, M. T.; Zilocchi, M.; Zhang, Q.; Aoki, H.; Jessulat, M.; Kim, S.; Aly, K. A.; Babu, M. Auxotrophic and Prototrophic Conditional Genetic Networks Reveal the Rewiring of Transcription Factors in Escherichia Coli. *Nat. Commun.* **2022**, *13* (1), 4085. https://doi.org/10.1038/s41467-022-31819-x.

(17) Guo, M. S.; Updegrove, T. B.; Gogol, E. B.; Shabalina, S. A.; Gross, C. A.; Storz, G. MicL, a New σE-Dependent sRNA, Combats Envelope Stress by Repressing Synthesis of Lpp, the Major Outer Membrane Lipoprotein. *Genes Dev.* **2014**, *28* (14), 1620–1634. https://doi.org/10.1101/gad.243485.114.

(18) Ge, Q.; Zhu, X.; Cobine, P. A.; De La Fuente, L. The Copper-Binding Protein CutC Is Involved in Copper Homeostasis and Affects Virulence in the Xylem-Limited Pathogen *Xylella Fastidiosa*. *Phytopathology®* **2022**, *112* (8), 1620–1629. https://doi.org/10.1094/PHYTO-11-21-0488-R.

(19) Miyadai, H.; Tanaka-Masuda, K.; Matsuyama, S.; Tokuda, H. Effects of Lipoprotein Overproduction on the Induction of DegP (HtrA) Involved in Quality Control in the Escherichia Coli Periplasm. *J. Biol. Chem.* **2004**, *279* (38), 39807–39813. https://doi.org/10.1074/jbc.M406390200.

(20) Giachino, A.; Waldron, K. J. Copper Tolerance in Bacteria Requires the Activation of Multiple Accessory Pathways. *Mol. Microbiol.* **2020**, *114* (3), 377–390. https://doi.org/10.1111/mmi.14522.

(21) Brown, N. L.; Barrett, S. R.; Camakaris, J.; Lee, B. T. O.; Rouch, D. A. Molecular Genetics and Transport Analysis of the Copper-resistance Determinant (*Pco*) from *Escherichia Coli* Plasmid pRJ1004. *Mol. Microbiol.* **1995**, *17* (6), 1153–1166. https://doi.org/10.1111/j.1365-2958.1995.mmi_17061153.x.

(22) Arnesano, F.; Banci, L.; Bertini, I.; Ciofi-Baffoni, S.; Molteni, E.; Huffman, D. L.; O'Halloran, T. V. Metallochaperones and Metal-Transporting ATPases: A Comparative Analysis of Sequences and Structures. *Genome Res.* **2002**, *12* (2), 255–271. https://doi.org/10.1101/gr.196802.

(23) Selim, K. A.; Haffner, M. Heavy Metal Stress Alters the Response of the Unicellular Cyanobacterium Synechococcus Elongatus PCC 7942 to Nitrogen Starvation. *Life* **2020**, *10* (11), 275. https://doi.org/10.3390/life10110275.

(24) Sant'Anna, F. H.; Trentini, D. B.; De Souto Weber, S.; Cecagno, R.; Da Silva, S. C.; Schrank, I. S. The PII Superfamily Revised: A Novel Group and Evolutionary Insights. *J. Mol. Evol.* **2009**, *68* (4), 322–336. https://doi.org/10.1007/s00239-009-9209-6.

(25) Huergo, L. F.; Chandra, G.; Merrick, M. P_{II} Signal Transduction Proteins: Nitrogen Regulation and Beyond. *FEMS Microbiol. Rev.* **2013**, *37* (2), 251–283. https://doi.org/10.1111/j.1574-6976.2012.00351.x.

(26) Forchhammer, K.; Selim, K. A.; Huergo, L. F. New Views on PII Signaling: From Nitrogen Sensing to Global Metabolic Control. *Trends Microbiol.* **2022**, *30* (8), 722–735. https://doi.org/10.1016/j.tim.2021.12.014.

(27) Forchhammer, K. PII Signal Transducers: Novel Functional and Structural Insights. *Trends Microbiol.* **2008**, *16* (2), 65–72. https://doi.org/10.1016/j.tim.2007.11.004.

(28) Arcondéguy, T.; Jack, R.; Merrick, M. P_{II} Signal Transduction Proteins, Pivotal Players in Microbial Nitrogen Control. *Microbiol. Mol. Biol. Rev.* **2001**, *65* (1), 80–105. https://doi.org/10.1128/MMBR.65.1.80-105.2001.

(29) Hsieh, M.-H.; Lam, H.-M.; Van De Loo, F. J.; Coruzzi, G. A PII-like Protein in *Arabidopsis* : Putative Role in Nitrogen Sensing. *Proc. Natl. Acad. Sci.* **1998**, *95* (23), 13965–13970. https://doi.org/10.1073/pnas.95.23.13965.

(30) Forchhammer, K.; Lüddecke, J. Sensory Properties of the P_{II} Signalling Protein Family. *FEBS J.* **2016**, *283* (3), 425–437. https://doi.org/10.1111/febs.13584.

(31) Selim, K. A.; Alva, V. PII-like Signaling Proteins: A New Paradigm in Orchestrating Cellular Homeostasis. *Curr. Opin. Microbiol.* **2024**, *79*, 102453. https://doi.org/10.1016/j.mib.2024.102453.

(32) Forchhammer, K. Global Carbon/Nitrogen Control by P_{II} Signal Transduction in Cyanobacteria: From Signals to Targets. *FEMS Microbiol. Rev.* **2004**, *28* (3), 319–333. https://doi.org/10.1016/j.femsre.2003.11.001.

(33) Jiang, P.; Ninfa, A. J. Sensation and Signaling of α-Ketoglutarate and Adenylylate Energy Charge by the *Escherichia Coli* PII Signal Transduction Protein Require Cooperation of the Three Ligand-Binding Sites within the PII Trimer. *Biochemistry* **2009**, *48* (48), 11522–11531. https://doi.org/10.1021/bi9011594.

(34) Atkinson, M. R.; Kamberov, E. S.; Weiss, R. L.; Ninfa, A. J. Reversible Uridylylation of the Escherichia Coli PII Signal Transduction Protein Regulates Its Ability to Stimulate the Dephosphorylation of the Transcription Factor Nitrogen Regulator I (NRI or NtrC). *J. Biol. Chem.* **1994**, *269* (45), 28288–28293. https://doi.org/10.1016/S0021-9258(18)46926-8.

(35) Jiang, P.; Peliska, J. A.; Ninfa, A. J. Enzymological Characterization of the Signal-Transducing Uridylyltransferase/Uridylyl-Removing Enzyme (EC 2.7.7.59) of *Escherichia Coli* and Its Interaction with the PII Protein. *Biochemistry* **1998**, *37* (37), 12782–12794. https://doi.org/10.1021/bi980667m.

(36) Hesketh, A.; Fink, D.; Gust, B.; Rexer, H. -U.; Scheel, B.; Chater, K.; Wohlleben, W.; Engels, A. The GlnD and GlnK Homologues of *Streptomyces Coelicolor* A3(2) Are Functionally Dissimilar to Their Nitrogen Regulatory System Counterparts from Enteric Bacteria. *Mol. Microbiol.* **2002**, *46* (2), 319–330. https://doi.org/10.1046/j.1365-2958.2002.03149.x.

(37) Forchhammer, K.; Tandeau De Marsac, N. The PII Protein in the Cyanobacterium Synechococcus Sp. Strain PCC 7942 Is Modified by Serine Phosphorylation and Signals the Cellular N-Status. *J. Bacteriol.* **1994**, *176* (1), 84–91. https://doi.org/10.1128/jb.176.1.84-91.1994.

(38) Jaggi, R.; Ybarlucea, W.; Cheah, E.; Carr, P. D.; Edwards, K. J.; Ollis, D. L.; Vasudevan, S. G. The Role of the T-loop of the Signal Transducing Protein P_{II} from *Escherichia Coli*. *FEBS Lett.* **1996**, *391* (1–2), 223–228. https://doi.org/10.1016/0014-5793(96)00737-5.

(39) Martínez-Argudo, I.; Contreras, A. PII T-Loop Mutations Affecting Signal Transduction to NtrB Also Abolish Yeast Two-Hybrid Interactions. *J. Bacteriol.* **2002**, *184* (13), 3746–3748. https://doi.org/10.1128/JB.184.13.3746-3748.2002.

(40) Sticht, H.; Rösch, P. The Structure of Iron–Sulfur Proteins. *Prog. Biophys. Mol. Biol.* **1998**, *70* (2), 95–136. https://doi.org/10.1016/S0079-6107(98)00027-3.

(41) Tagawa, K.; Arnon, D. I. Ferredoxins as Electron Carriers in Photosynthesis and in the Biological Production and Consumption of Hydrogen Gas. *Nature* **1962**, *195* (4841), 537–543. https://doi.org/10.1038/195537a0.

(42) Poudel, S.; Colman, D. R.; Fixen, K. R.; Ledbetter, R. N.; Zheng, Y.; Pence, N.; Seefeldt, L. C.; Peters, J. W.; Harwood, C. S.; Boyd, E. S. Electron Transfer to

Nitrogenase in Different Genomic and Metabolic Backgrounds. *J. Bacteriol.* **2018**, *200* (10). https://doi.org/10.1128/JB.00757-17.

(43) Lin, S. J.; Culotta, V. C. The ATX1 Gene of Saccharomyces Cerevisiae Encodes a Small Metal Homeostasis Factor That Protects Cells against Reactive Oxygen Toxicity. *Proc. Natl. Acad. Sci. U. S. A.* **1995**, *92* (9), 3784–3788. https://doi.org/10.1073/pnas.92.9.3784.

(44) Arnesano, F.; Banci, L.; Bertini, I.; Ciofi-Baffoni, S. Perspectives in Inorganic Structural Genomics: A Trafficking Route for Copper. *Eur. J. Inorg. Chem.* **2004**, *2004* (8), 1583–1593. https://doi.org/10.1002/ejic.200300841.

(45) Raanan, H.; Poudel, S.; Pike, D. H.; Nanda, V.; Falkowski, P. G. Small Protein Folds at the Root of an Ancient Metabolic Network. *Proc. Natl. Acad. Sci.* **2020**, *117* (13), 7193–7199. https://doi.org/10.1073/pnas.1914982117.

(46) Wagner, B. C.; Steuer-Lodd, K.; Geibel, C.; Stadelmann, A.; Rapp, J.; Link, H.; Schramm, T.; Boodaghian, N.; Hsiao, A.; Nussbaum, E.; Grenzendorfer, H.-P.; Albrecht, R.; Hartmann, M. D.; Forchhammer, K.; Selim, K. A.; Hughes, C. C.; Petras, D. Native Metabolomics Identifies Pteridines as CutA Ligands and Modulators of Copper Binding. *Proc. Natl. Acad. Sci.* **2025**, *122* (48), e2509468122. https://doi.org/10.1073/pnas.2509468122.

(47) Bagautdinov, B. The Structures of the CutA1 Proteins from Thermus Thermophilus and Pyrococcus Horikoshii: Characterization of Metal-Binding Sites and Metal-Induced Assembly. *Acta Crystallogr. Sect. F Struct. Biol. Commun.* **2014**, *70* (Pt 4), 404–413. https://doi.org/10.1107/S2053230X14003422.

(48) Hromada, S. E.; Hilbrands, A. M.; Wolf, E. M.; Ross, J. L.; Hegg, T. R.; Roth, A. G.; Hollowell, M. T.; Anderson, C. E.; Benson, D. E. Protein Oxidation Involved in Cys-Tyr Post-Translational Modification. *J. Inorg. Biochem.* **2017**, *176*, 168–174. https://doi.org/10.1016/j.jinorgbio.2017.08.028.

(49) Wensien, M.; Von Pappenheim, F. R.; Funk, L.-M.; Kloskowski, P.; Curth, U.; Diederichsen, U.; Uranga, J.; Ye, J.; Fang, P.; Pan, K.-T.; Urlaub, H.; Mata, R. A.; Sautner, V.; Tittmann, K. A Lysine–Cysteine Redox Switch with an NOS Bridge Regulates Enzyme Function. *Nature* **2021**, *593* (7859), 460–464. https://doi.org/10.1038/s41586-021-03513-3.

(50) Arcondéguy, T.; Jack, R.; Merrick, M. P(II) Signal Transduction Proteins, Pivotal Players in Microbial Nitrogen Control. *Microbiol. Mol. Biol. Rev. MMBR* **2001**, *65* (1), 80–105. https://doi.org/10.1128/MMBR.65.1.80-105.2001.

(51) Shapiro, B. M. Glutamine Synthetase Deadenylylating Enzyme System from Escherichia Coli. Resolution into Two Components, Specific Nucleotide Stimulation, and Cofactor Requirements. *Biochemistry* **1969**, *8* (2), 659–670. https://doi.org/10.1021/bi00830a030.

(52) Chellamuthu, V. R.; Alva, V.; Forchhammer, K. From Cyanobacteria to Plants: Conservation of PII Functions during Plastid Evolution. *Planta* **2013**, *237* (2), 451–462. https://doi.org/10.1007/s00425-012-1801-0.

(53) Kinch, L. N.; Grishin, N. V. Expanding the Nitrogen Regulatory Protein Superfamily: Homology Detection at below Random Sequence Identity. *Proteins Struct. Funct. Bioinforma.* **2002**, *48* (1), 75–84. https://doi.org/10.1002/prot.10110.

(54) Selim, K. A.; Alva, V. PII-like Signaling Proteins: A New Paradigm in Orchestrating Cellular Homeostasis. *Curr. Opin. Microbiol.* **2024**, *79*, 102453. https://doi.org/10.1016/j.mib.2024.102453.

(55) Mantovani, O.; Haffner, M.; Walke, P.; Elshereef, A. A.; Wagner, B.; Petras, D.; Forchhammer, K.; Selim, K. A.; Hagemann, M. The Redox-Sensitive R-Loop of the Carbon Control Protein SbtB Contributes to the Regulation of the Cyanobacterial CCM. *Sci. Rep.* **2024**, *14* (1), 7885. https://doi.org/10.1038/s41598-024-58354-7.

(56) Gerhardt, E. C. M.; Parize, E.; Gravina, F.; Pontes, F. L. D.; Santos, A. R. S.; Araújo, G. A. T.; Goedert, A. C.; Urbanski, A. H.; Steffens, M. B. R.; Chubatsu, L. S.; Pedrosa, F. O.; Souza, E. M.; Forchhammer, K.; Ganusova, E.; Alexandre, G.; De Souza, G. A.; Huergo, L. F. The Protein-Protein Interaction Network Reveals a Novel Role of the Signal Transduction Protein PII in the Control of c-Di-GMP Homeostasis in Azospirillum Brasilense. *mSystems* **2020**, *5* (6). https://doi.org/10.1128/msystems.00817-20.

(57) Van Heeswijk, W. C.; Rabenberg, M.; Westerhoff, H. V.; Kahn, D. The Genes of the Glutamine Synthetase Adenylylation Cascade Are Not Regulated by Nitrogen in *Escherichia Coli*. *Mol. Microbiol.* **1993**, *9* (3), 443–457. https://doi.org/10.1111/j.1365-2958.1993.tb01706.x.

(58) Jiang, P.; Ninfa, A. J. Regulation of Autophosphorylation of *Escherichia Coli* Nitrogen Regulator II by the PII Signal Transduction Protein. *J. Bacteriol.* **1999**, *181* (6), 1906–1911. https://doi.org/10.1128/jb.181.6.1906-1911.1999.

(59) Conroy, M. J.; Durand, A.; Lupo, D.; Li, X.-D.; Bullough, P. A.; Winkler, F. K.; Merrick, M. The Crystal Structure of the *Escherichia Coli* AmtB–GlnK Complex Reveals How GlnK Regulates the Ammonia Channel. *Proc. Natl. Acad. Sci.* **2007**, *104* (4), 1213–1218. https://doi.org/10.1073/pnas.0610348104.

(60) Feria Bourrellier, A. B.; Valot, B.; Guillot, A.; Ambard-Bretteville, F.; Vidal, J.; Hodges, M. Chloroplast Acetyl-CoA Carboxylase Activity Is 2-Oxoglutarate–Regulated by Interaction of PII with the Biotin Carboxyl Carrier Subunit. *Proc. Natl. Acad. Sci.* **2010**, *107* (1), 502–507. https://doi.org/10.1073/pnas.0910097107.

(61) Hou, P.; Liu, G.; Zhao, Y.; Shi, Z.; Zheng, Q.; Bu, G.; Xu, H.; Zhang, Y. The Role of Copper and the Copper-Related Protein CUTA in Mediating APP Processing and Aβ Generation. *Neurobiol. Aging* **2015**, *36* (3), 1310–1315. https://doi.org/10.1016/j.neurobiolaging.2014.12.005.

(62) Navaratnam, D. S.; Fernando, F. S.; Priddle, J. D.; Giles, K.; Clegg, S. M.; Pappin, D. J.; Craig, I.; Smith, A. D. Hydrophobic Protein That Copurifies with Human Brain Acetylcholinesterase: Amino Acid Sequence, Genomic Organization, and Chromosomal Localization. *J. Neurochem.* **2000**, *74* (5), 2146–2153. https://doi.org/10.1046/j.1471-4159.2000.0742146.x.

(63) Perrier, A. L.; Cousin, X.; Boschetti, N.; Haas, R.; Chatel, J.-M.; Bon, S.; Roberts, W. L.; Pickett, S. R.; Massoulié, J.; Rosenberry, T. L.; Krejci, E. Two Distinct Proteins Are Associated with Tetrameric Acetylcholinesterase on the Cell Surface. *J. Biol. Chem.* **2000**, *275* (44), 34260–34265. https://doi.org/10.1074/jbc.M004289200.

(64) Anbar, A. D.; Duan, Y.; Lyons, T. W.; Arnold, G. L.; Kendall, B.; Creaser, R. A.; Kaufman, A. J.; Gordon, G. W.; Scott, C.; Garvin, J.; Buick, R. A Whiff of Oxygen Before the Great Oxidation Event? *Science* **2007**, *317* (5846), 1903–1906. https://doi.org/10.1126/science.1140325.

(65) Ridge, P. G.; Zhang, Y.; Gladyshev, V. N. Comparative Genomic Analyses of Copper Transporters and Cuproproteomes Reveal Evolutionary Dynamics of Copper Utilization and Its Link to Oxygen. *PLoS ONE* **2008**, *3* (1), e1378. https://doi.org/10.1371/journal.pone.0001378.

(66) Imlay, J. A. Common Mechanisms of Bacterial Metal Homeostasis. In *Trace Metals and Infectious Diseases*; Nriagu, J. O., Skaar, E. P., Eds.; The MIT Press, 2015; pp 57–82. https://doi.org/10.7551/mitpress/9780262029193.003.0008.

(67) Linder, M. C. The Relationship of Copper to DNA Damage and Damage Prevention in Humans. *Mutat. Res. Mol. Mech. Mutagen.* **2012**, *733* (1–2), 83–91. https://doi.org/10.1016/j.mrfmmm.2012.03.010.

(68) Falcone, E.; Hureau, C. Redox Processes in Cu-Binding Proteins: The “in-between” States in Intrinsically Disordered Peptides. *Chem. Soc. Rev.* **2023**, *52* (19), 6595–6600. https://doi.org/10.1039/D3CS00443K.
(69) Ayala, A.; Muñoz, M. F.; Argüelles, S. Lipid Peroxidation: Production, Metabolism, and Signaling Mechanisms of Malondialdehyde and 4-Hydroxy-2-Nonenal. *Oxid. Med. Cell. Longev.* **2014**, *2014*, 360438. https://doi.org/10.1155/2014/360438.
(70) Michalska, P.; León, R. When It Comes to an End: Oxidative Stress Crosstalk with Protein Aggregation and Neuroinflammation Induce Neurodegeneration. *Antioxid. Basel Switz.* **2020**, *9* (8), 740. https://doi.org/10.3390/antiox9080740.
(71) Macomber, L.; Imlay, J. A. The Iron-Sulfur Clusters of Dehydratases Are Primary Intracellular Targets of Copper Toxicity. *Proc. Natl. Acad. Sci.* **2009**, *106* (20), 8344–8349. https://doi.org/10.1073/pnas.0812808106.
(72) Brancaccio, D.; Gallo, A.; Piccioli, M.; Novellino, E.; Ciofi-Baffoni, S.; Banci, L. [4Fe-4S] Cluster Assembly in Mitochondria and Its Impairment by Copper. *J. Am. Chem. Soc.* **2017**, *139* (2), 719–730. https://doi.org/10.1021/jacs.6b09567.
(73) Holmström, K. M.; Finkel, T. Cellular Mechanisms and Physiological Consequences of Redox-Dependent Signalling. *Nat. Rev. Mol. Cell Biol.* **2014**, *15* (6), 411–421. https://doi.org/10.1038/nrm3801.
(74) D’Autréaux, B.; Toledano, M. B. ROS as Signalling Molecules: Mechanisms That Generate Specificity in ROS Homeostasis. *Nat. Rev. Mol. Cell Biol.* **2007**, *8* (10), 813–824. https://doi.org/10.1038/nrm2256.
(75) Harrison, M.; Jones, C.; Solioz, M.; Dameron, C. Intracellular Copper Routing: The Role of Copper Chaperones. *Trends Biochem. Sci.* **2000**, *25* (1), 29–32. https://doi.org/10.1016/S0968-0004(99)01492-9.
(76) Stewart, L. J.; Ong, C. Y.; Zhang, M. M.; Brouwer, S.; McIntyre, L.; Davies, M. R.; Walker, M. J.; McEwan, A. G.; Waldron, K. J.; Djoko, K. Y. Role of Glutathione in Buffering Excess Intracellular Copper in *Streptococcus Pyogenes*. *mBio* **2020**, *11* (6), e02804-20. https://doi.org/10.1128/mBio.02804-20.
(77) Gomes, I. B.; Simões, M.; Simões, L. C. Copper Surfaces in Biofilm Control. *Nanomaterials* **2020**, *10* (12), 2491. https://doi.org/10.3390/nano10122491.
(78) Shih, H.-Y.; Lin, Y. E. Efficacy of Copper-Silver Ionization in Controlling Biofilm- and Plankton-Associated Waterborne Pathogens. *Appl. Environ. Microbiol.* **2010**, *76* (6), 2032–2035. https://doi.org/10.1128/AEM.02174-09.
(79) Forouzandeh, A.; Blavi, L.; Pérez, J. F.; D’Angelo, M.; González-Solé, F.; Monteiro, A.; Stein, H. H.; Solà-Oriol, D. How Copper Can Impact Pig Growth: Comparing the Effect of Copper Sulfate and Monovalent Copper Oxide on Oxidative Status, Inflammation, Gene Abundance, and Microbial Modulation as Potential Mechanisms of Action. *J. Anim. Sci.* **2022**, *100* (9), skac224. https://doi.org/10.1093/jas/skac224.
(80) Schaefer, M.; Gitlin, J. D. IV. Wilson’s Disease and Menkes Disease. *Am. J. Physiol.-Gastrointest. Liver Physiol.* **1999**, *276* (2), G311–G314. https://doi.org/10.1152/ajpgi.1999.276.2.G311.
(81) Członkowska, A.; Litwin, T.; Dusek, P.; Ferenci, P.; Lutsenko, S.; Medici, V.; Rybakowski, J. K.; Weiss, K. H.; Schilsky, M. L. Wilson Disease. *Nat. Rev. Dis. Primer* **2018**, *4* (1), 21. https://doi.org/10.1038/s41572-018-0018-3.
(82) Multhaup, G.; Schlicksupp, A.; Hesse, L.; Beher, D.; Ruppert, T.; Masters, C. L.; Beyreuther, K. The Amyloid Precursor Protein of Alzheimer’s Disease in the Reduction of Copper(II) to Copper(I). *Science* **1996**, *271* (5254), 1406–1409. https://doi.org/10.1126/science.271.5254.1406.
(83) White, A. R.; Multhaup, G.; Galatis, D.; McKinstry, W. J.; Parker, M. W.; Pipkorn, R.; Beyreuther, K.; Masters, C. L.; Cappai, R. Contrasting, Species-Dependent Modulation of Copper-Mediated Neurotoxicity by the Alzheimer’s Disease Amyloid Precursor

Protein. *J. Neurosci.* **2002**, *22* (2), 365–376. https://doi.org/10.1523/JNEUROSCI.22-02-00365.2002.

(84) Eskici, G.; Axelsen, P. H. Copper and Oxidative Stress in the Pathogenesis of Alzheimer's Disease. *Biochemistry* **2012**, *51* (32), 6289–6311. https://doi.org/10.1021/bi3006169.

(85) Tanaka, Y.; Tsumoto, K.; Nakanishi, T.; Yasutake, Y.; Sakai, N.; Yao, M.; Tanaka, I.; Kumagai, I. Structural Implications for Heavy Metal-induced Reversible Assembly and Aggregation of a Protein: The Case of *Pyrococcus Horikoshii* CutA[1]. *FEBS Lett.* **2004**, *556* (1–3), 167–174. https://doi.org/10.1016/S0014-5793(03)01402-9.

(86) Burkhead, J. L.; Abdel-Ghany, S. E.; Morrill, J. M.; Pilon-Smits, E. A. H.; Pilon, M. The *Arabidopsis Thaliana CUTA* Gene Encodes an Evolutionarily Conserved Copper Binding Chloroplast Protein. *Plant J.* **2003**, *34* (6), 856–867. https://doi.org/10.1046/j.1365-313X.2003.01769.x.

(87) Clerico, E. M.; Ditty, J. L.; Golden, S. S. Specialized Techniques for Site-Directed Mutagenesis in Cyanobacteria. In *Circadian Rhythms*; Rosato, E., Ed.; Walker, J. M., Series Ed.; Methods in Molecular Biology; Humana Press: Totowa, NJ, 2007; Vol. 362, pp 155–171. https://doi.org/10.1007/978-1-59745-257-1_11.

(88) Waterbury, J. B.; Watson, S. W.; Guillard, R. R. L.; Brand, L. E. Widespread Occurrence of a Unicellular, Marine, Planktonic, Cyanobacterium. *Nature* **1979**, *277* (5694), 293–294. https://doi.org/10.1038/277293a0.

(89) Revsbech, N. P.; Trampe, E.; Lichtenberg, M.; Ward, D. M.; Kühl, M. In Situ Hydrogen Dynamics in a Hot Spring Microbial Mat during a Diel Cycle. *Appl. Environ. Microbiol.* **2016**, *82* (14), 4209–4217. https://doi.org/10.1128/AEM.00710-16.

(90) Parnasa, R.; Nagar, E.; Sendersky, E.; Reich, Z.; Simkovsky, R.; Golden, S.; Schwarz, R. Small Secreted Proteins Enable Biofilm Development in the Cyanobacterium Synechococcus Elongatus. *Sci. Rep.* **2016**, *6* (1), 32209. https://doi.org/10.1038/srep32209.

(91) Yang, Y.; Lam, V.; Adomako, M.; Simkovsky, R.; Jakob, A.; Rockwell, N. C.; Cohen, S. E.; Taton, A.; Wang, J.; Lagarias, J. C.; Wilde, A.; Nobles, D. R.; Brand, J. J.; Golden, S. S. Phototaxis in a Wild Isolate of the Cyanobacterium *Synechococcus Elongatus*. *Proc. Natl. Acad. Sci.* **2018**, *115* (52). https://doi.org/10.1073/pnas.1812871115.

(92) Hallmann, C.; Stannek, L.; Fritzlar, D.; Hause-Reitner, D.; Friedl, T.; Hoppert, M. Molecular Diversity of Phototrophic Biofilms on Building Stone. *FEMS Microbiol. Ecol.* **2013**, *84* (2), 355–372. https://doi.org/10.1111/1574-6941.12065.

(93) Scanlan, D. J.; West, N. J. Molecular Ecology of the Marine Cyanobacterial Genera Prochlorococcus and Synechococcus. *FEMS Microbiol. Ecol.* **2002**, *40* (1), 1–12. https://doi.org/10.1111/j.1574-6941.2002.tb00930.x.

(94) Flombaum, P.; Gallegos, J. L.; Gordillo, R. A.; Rincón, J.; Zabala, L. L.; Jiao, N.; Karl, D. M.; Li, W. K. W.; Lomas, M. W.; Veneziano, D.; Vera, C. S.; Vrugt, J. A.; Martiny, A. C. Present and Future Global Distributions of the Marine Cyanobacteria *Prochlorococcus* and *Synechococcus*. *Proc. Natl. Acad. Sci.* **2013**, *110* (24), 9824–9829. https://doi.org/10.1073/pnas.1307701110.

(95) Golden, S. S. The International Journeys and Aliases of *Synechococcus Elongatus*. *N. Z. J. Bot.* **2019**, *57* (2), 70–75. https://doi.org/10.1080/0028825X.2018.1551805.

(96) Tenaillon, O.; Skurnik, D.; Picard, B.; Denamur, E. The Population Genetics of Commensal Escherichia Coli. *Nat. Rev. Microbiol.* **2010**, *8* (3), 207–217. https://doi.org/10.1038/nrmicro2298.

(97) Tanaka, T.; Sawano, M.; Ogasahara, K.; Sakaguchi, Y.; Bagautdinov, B.; Katoh, E.; Kuroishi, C.; Shinkai, A.; Yokoyama, S.; Yutani, K. Hyper-thermostability of CutA1

Protein, with a Denaturation Temperature of Nearly 150 °C. *FEBS Lett.* **2006**, *580* (17), 4224–4230. https://doi.org/10.1016/j.febslet.2006.06.084.

(98) Hirata, A.; Sato, A.; Tadokoro, T.; Koga, Y.; Kanaya, S.; Takano, K. A Stable Protein - CutA1. In *Protein Structure*; Faraggi, E., Ed.; InTech, 2012. https://doi.org/10.5772/37042.

(99) Tanaka, T.; Sawano, M.; Ogasahara, K.; Sakaguchi, Y.; Bagautdinov, B.; Katoh, E.; Kuroishi, C.; Shinkai, A.; Yokoyama, S.; Yutani, K. Hyper-thermostability of CutA1 Protein, with a Denaturation Temperature of Nearly 150 °C. *FEBS Lett.* **2006**, *580* (17), 4224–4230. https://doi.org/10.1016/j.febslet.2006.06.084.

(100) Sawano, M.; Yamamoto, H.; Ogasahara, K.; Kidokoro, S.; Katoh, S.; Ohnuma, T.; Katoh, E.; Yokoyama, S.; Yutani, K. Thermodynamic Basis for the Stabilities of Three CutA1s from *Pyrococcus Horikoshii, Thermus Thermophilus* , and *Oryza Sativa* , with Unusually High Denaturation Temperatures. *Biochemistry* **2008**, *47* (2), 721–730. https://doi.org/10.1021/bi701761m.

(101) Bagautdinov, B.; Matsuura, Y.; Yamamoto, H.; Sawano, M.; Ogasahara, K.; Takehira, M.; Kunishima, N.; Katoh, E.; Yutani, K. Thermodynamic Analysis of Unusually Thermostable CutA1 Protein from Human Brain and Its Protease Susceptibility. *J. Biochem. (Tokyo)* **2015**, *157* (3), 169–176. https://doi.org/10.1093/jb/mvu062.

(102) Matsuura, Y.; Ota, M.; Tanaka, T.; Takehira, M.; Ogasahara, K.; Bagautdinov, B.; Kunishima, N.; Yutani, K. Remarkable Improvement in the Heat Stability of CutA1 from Escherichia Coli by Rational Protein Design. *J. Biochem. (Tokyo)* **2010**, mvq079. https://doi.org/10.1093/jb/mvq079.

(103) Sato, A.; Yokotani, S.; Tadokoro, T.; Tanaka, S.; Angkawidjaja, C.; Koga, Y.; Takano, K.; Kanaya, S. Crystal Structure of Stable Protein CutA1 from Psychrotrophic Bacterium *Shewanella* Sp. SIB1. *J. Synchrotron Radiat.* **2011**, *18* (1), 6–10. https://doi.org/10.1107/S0909049510028669.

(104) Baba, T.; Ara, T.; Hasegawa, M.; Takai, Y.; Okumura, Y.; Baba, M.; Datsenko, K. A.; Tomita, M.; Wanner, B. L.; Mori, H. Construction of Escherichia Coli K-12 in-Frame, Single-Gene Knockout Mutants: The Keio Collection. *Mol. Syst. Biol.* **2006**, *2*, 2006.0008. https://doi.org/10.1038/msb4100050.

(105) Small, P.; Blankenhorn, D.; Welty, D.; Zinser, E.; Slonczewski, J. L. Acid and Base Resistance in Escherichia Coli and Shigella Flexneri: Role of rpoS and Growth pH. *J. Bacteriol.* **1994**, *176* (6), 1729–1737. https://doi.org/10.1128/jb.176.6.1729-1737.1994.

(106) Ducat, D. C.; Avelar-Rivas, J. A.; Way, J. C.; Silver, P. A. Rerouting Carbon Flux To Enhance Photosynthetic Productivity. *Appl. Environ. Microbiol.* **2012**, *78* (8), 2660–2668. https://doi.org/10.1128/AEM.07901-11.

(107) Zheng, Z.; Omairi-Nasser, A.; Li, X.; Dong, C.; Lin, Y.; Haselkorn, R.; Zhao, J. An Amidase Is Required for Proper Intercellular Communication in the Filamentous Cyanobacterium *Anabaena* Sp. PCC 7120. *Proc. Natl. Acad. Sci.* **2017**, *114* (8). https://doi.org/10.1073/pnas.1621424114.

(108) Clarke, A. K.; Schelin, J.; Porankiewicz, J. Inactivation of the clpP1 Gene for the Proteolytic Subunit of the ATP-Dependent Clp Protease in the Cyanobacterium Synechococcus Limits Growth and Light Acclimation. *Plant Mol. Biol.* **1998**, *37* (5), 791–801. https://doi.org/10.1023/A:1006016302074.

(109) Clarke, D. J.; Ortega, X. P.; Mackay, C. L.; Valvano, M. A.; Govan, J. R. W.; Campopiano, D. J.; Langridge-Smith, P.; Brown, A. R. Subdivision of the Bacterioferritin Comigratory Protein Family of Bacterial Peroxiredoxins Based on Catalytic Activity. *Biochemistry* **2010**, *49* (6), 1319–1330. https://doi.org/10.1021/bi901703m.

(110) Williams, R. E.; Bruce, N. C. 'New Uses for an Old Enzyme' – the Old Yellow Enzyme Family of Flavoenzymes. *Microbiology* **2002**, *148* (6), 1607–1614. https://doi.org/10.1099/00221287-148-6-1607.
(111) Brown, A. M.; Hoopes, S. L.; White, R. H.; Sarisky, C. A. Purine Biosynthesis in Archaea: Variations on a Theme. *Biol. Direct* **2011**, *6*, 63. https://doi.org/10.1186/1745-6150-6-63.
(112) Jo, I.; Chung, I.-Y.; Bae, H.-W.; Kim, J.-S.; Song, S.; Cho, Y.-H.; Ha, N.-C. Structural Details of the OxyR Peroxide-Sensing Mechanism. *Proc. Natl. Acad. Sci.* **2015**, *112* (20), 6443–6448. https://doi.org/10.1073/pnas.1424495112.
(113) Denise, R.; Babor, J.; Gerlt, J. A.; De Crécy-Lagard, V. Pyridoxal 5'-Phosphate Synthesis and Salvage in Bacteria and Archaea: Predicting Pathway Variant Distributions and Holes. *Microb. Genomics* **2023**, *9* (2). https://doi.org/10.1099/mgen.0.000926.
(114) Truglio, J. J.; Croteau, D. L.; Van Houten, B.; Kisker, C. Prokaryotic Nucleotide Excision Repair: The UvrABC System. *Chem. Rev.* **2006**, *106* (2), 233–252. https://doi.org/10.1021/cr040471u.
(115) Jakomin, M.; Chessa, D.; Bäumler, A. J.; Casadesús, J. Regulation of the *Salmonella Enterica Std* Fimbrial Operon by DNA Adenine Methylation, SeqA, and HdfR. *J. Bacteriol.* **2008**, *190* (22), 7406–7413. https://doi.org/10.1128/JB.01136-08.
(116) Petersen, C.; Møller, L. B. The RihA, RihB, and RihC Ribonucleoside Hydrolases of Escherichia Coli. *J. Biol. Chem.* **2001**, *276* (2), 884–894. https://doi.org/10.1074/jbc.M008300200.
(117) Freundlieb, S.; Boos, W. Maltose Transacetylase of Escherichia Coli: A Preliminary Report. *Ann. Microbiol. (Paris)* **1982**, *133A* (1), 181–189.
(118) Janßen, H.; Steinbüchel, A. Fatty Acid Synthesis in Escherichia Coli and Its Applications towards the Production of Fatty Acid Based Biofuels. *Biotechnol. Biofuels* **2014**, *7* (1), 7. https://doi.org/10.1186/1754-6834-7-7.
(119) Chambers, M. C.; Maclean, B.; Burke, R.; Amodei, D.; Ruderman, D. L.; Neumann, S.; Gatto, L.; Fischer, B.; Pratt, B.; Egertson, J.; Hoff, K.; Kessner, D.; Tasman, N.; Shulman, N.; Frewen, B.; Baker, T. A.; Brusniak, M.-Y.; Paulse, C.; Creasy, D.; Flashner, L.; Kani, K.; Moulding, C.; Seymour, S. L.; Nuwaysir, L. M.; Lefebvre, B.; Kuhlmann, F.; Roark, J.; Rainer, P.; Detlev, S.; Hemenway, T.; Huhmer, A.; Langridge, J.; Connolly, B.; Chadick, T.; Holly, K.; Eckels, J.; Deutsch, E. W.; Moritz, R. L.; Katz, J. E.; Agus, D. B.; MacCoss, M.; Tabb, D. L.; Mallick, P. A Cross-Platform Toolkit for Mass Spectrometry and Proteomics. *Nat. Biotechnol.* **2012**, *30* (10), 918–920. https://doi.org/10.1038/nbt.2377.
(120) Dührkop, K.; Fleischauer, M.; Ludwig, M.; Aksenov, A. A.; Melnik, A. V.; Meusel, M.; Dorrestein, P. C.; Rousu, J.; Böcker, S. SIRIUS 4: A Rapid Tool for Turning Tandem Mass Spectra into Metabolite Structure Information. *Nat. Methods* **2019**, *16* (4), 299–302. https://doi.org/10.1038/s41592-019-0344-8.
(121) Pakkir Shah, A. K.; Walter, A.; Ottosson, F.; Russo, F.; Navarro-Diaz, M.; Boldt, J.; Kalinski, J.-C. J.; Kontou, E. E.; Elofson, J.; Polyzois, A.; González-Marín, C.; Farrell, S.; Aggerbeck, M. R.; Pruksatrakul, T.; Chan, N.; Wang, Y.; Pöchhacker, M.; Brungs, C.; Cámara, B.; Caraballo-Rodríguez, A. M.; Cumsille, A.; De Oliveira, F.; Dührkop, K.; El Abiead, Y.; Geibel, C.; Graves, L. G.; Hansen, M.; Heuckeroth, S.; Knoblauch, S.; Kostenko, A.; Kuijpers, M. C. M.; Mildau, K.; Papadopoulos Lambidis, S.; Portal Gomes, P. W.; Schramm, T.; Steuer-Lodd, K.; Stincone, P.; Tayyab, S.; Vitale, G. A.; Wagner, B. C.; Xing, S.; Yazzie, M. T.; Zuffa, S.; De Kruijff, M.; Beemelmanns, C.; Link, H.; Mayer, C.; Van Der Hooft, J. J. J.; Damiani, T.; Pluskal, T.; Dorrestein, P.; Stanstrup, J.; Schmid, R.; Wang, M.; Aron, A.; Ernst, M.; Petras, D. Statistical Analysis

of Feature-Based Molecular Networking Results from Non-Targeted Metabolomics Data. *Nat. Protoc.* **2024**. https://doi.org/10.1038/s41596-024-01046-3.

(122) Huergo, L. F.; Chandra, G.; Merrick, M. P_{II} Signal Transduction Proteins: Nitrogen Regulation and Beyond. *FEMS Microbiol. Rev.* **2013**, *37* (2), 251–283. https://doi.org/10.1111/j.1574-6976.2012.00351.x.

(123) Forchhammer, K.; Tandeau De Marsac, N. The PII Protein in the Cyanobacterium Synechococcus Sp. Strain PCC 7942 Is Modified by Serine Phosphorylation and Signals the Cellular N-Status. *J. Bacteriol.* **1994**, *176* (1), 84–91. https://doi.org/10.1128/jb.176.1.84-91.1994.

(124) Zhao, Y.; Wang, Y.; Hu, J.; Zhang, X.; Zhang, Y. CutA Divalent Cation Tolerance Homolog (Escherichia Coli) (CUTA) Regulates β-Cleavage of β-Amyloid Precursor Protein (APP) through Interacting with β-Site APP Cleaving Protein 1 (BACE1). *J. Biol. Chem.* **2012**, *287* (14), 11141–11150. https://doi.org/10.1074/jbc.M111.330209.

(125) Hou, P.; Liu, G.; Zhao, Y.; Shi, Z.; Zheng, Q.; Bu, G.; Xu, H.; Zhang, Y. The Role of Copper and the Copper-Related Protein CUTA in Mediating APP Processing and Aβ Generation. *Neurobiol. Aging* **2015**, *36* (3), 1310–1315. https://doi.org/10.1016/j.neurobiolaging.2014.12.005.

(126) Navaratnam, D. S.; Fernando, F. S.; Priddle, J. D.; Giles, K.; Clegg, S. M.; Pappin, D. J.; Craig, I.; Smith, A. D. Hydrophobic Protein That Copurifies with Human Brain Acetylcholinesterase: Amino Acid Sequence, Genomic Organization, and Chromosomal Localization. *J. Neurochem.* **2000**, *74* (5), 2146–2153. https://doi.org/10.1046/j.1471-4159.2000.0742146.x.

(127) Perrier, A. L.; Cousin, X.; Boschetti, N.; Haas, R.; Chatel, J.-M.; Bon, S.; Roberts, W. L.; Pickett, S. R.; Massoulié, J.; Rosenberry, T. L.; Krejci, E. Two Distinct Proteins Are Associated with Tetrameric Acetylcholinesterase on the Cell Surface. *J. Biol. Chem.* **2000**, *275* (44), 34260–34265. https://doi.org/10.1074/jbc.M004289200.

(128) Katzen, F.; Beckwith, J. Transmembrane Electron Transfer by the Membrane Protein DsbD Occurs via a Disulfide Bond Cascade. *Cell* **2000**, *103* (5), 769–779. https://doi.org/10.1016/S0092-8674(00)00180-X.

(129) Xu, Y.; Carr, P. D.; Huber, T.; Vasudevan, S. G.; Ollis, D. L. The Structure of the P_{II} – ATP Complex. *Eur. J. Biochem.* **2001**, *268* (7), 2028–2037. https://doi.org/10.1046/j.1432-1327.2001.02074.x.

(130) Xu, Y.; Cheah, E.; Carr, P. D.; Van Heeswijk, W. C.; Westerhoff, H. V.; Vasudevan, S. G.; Ollis, D. L. GlnK, a PII-Homologue: Structure Reveals ATP Binding Site and Indicates How the T-Loops May Be Involved in Molecular Recognition. *J. Mol. Biol.* **1998**, *282* (1), 149–165. https://doi.org/10.1006/jmbi.1998.1979.

(131) Sawano, M.; Yamamoto, H.; Ogasahara, K.; Kidokoro, S.; Katoh, S.; Ohnuma, T.; Katoh, E.; Yokoyama, S.; Yutani, K. Thermodynamic Basis for the Stabilities of Three CutA1s from *Pyrococcus Horikoshii, Thermus Thermophilus* , and *Oryza Sativa* , with Unusually High Denaturation Temperatures. *Biochemistry* **2008**, *47* (2), 721–730. https://doi.org/10.1021/bi701761m.

(132) Sato, A.; Yokotani, S.; Tadokoro, T.; Tanaka, S.; Angkawidjaja, C.; Koga, Y.; Takano, K.; Kanaya, S. Crystal Structure of Stable Protein CutA1 from Psychrotrophic Bacterium *Shewanella* Sp. SIB1. *J. Synchrotron Radiat.* **2011**, *18* (1), 6–10. https://doi.org/10.1107/S0909049510028669.

(133) Reher, R.; Aron, A. T.; Fajtová, P.; Stincone, P.; Wagner, B.; Pérez-Lorente, A. I.; Liu, C.; Shalom, I. Y. B.; Bittremieux, W.; Wang, M.; Jeong, K.; Matos-Hernandez, M. L.; Alexander, K. L.; Caro-Diaz, E. J.; Naman, C. B.; Scanlan, J. H. W.; Hochban, P. M. M.; Diederich, W. E.; Molina-Santiago, C.; Romero, D.; Selim, K. A.; Sass, P.; Brötz-Oesterhelt, H.; Hughes, C. C.; Dorrestein, P. C.; O'Donoghue, A. J.; Gerwick, W. H.; Petras, D. Native Metabolomics Identifies the Rivulariapeptolide Family of Protease

Inhibitors. *Nat. Commun.* **2022**, *13* (1), 4619. https://doi.org/10.1038/s41467-022-32016-6.

(134) Aron, A. T.; Petras, D.; Schmid, R.; Gauglitz, J. M.; Büttel, I.; Antelo, L.; Zhi, H.; Nuccio, S.-P.; Saak, C. C.; Malarney, K. P.; Thines, E.; Dutton, R. J.; Aluwihare, L. I.; Raffatellu, M.; Dorrestein, P. C. Native Mass Spectrometry-Based Metabolomics Identifies Metal-Binding Compounds. *Nat. Chem.* **2022**, *14* (1), 100–109. https://doi.org/10.1038/s41557-021-00803-1.

(135) Matsuura, Y.; Ota, M.; Tanaka, T.; Takehira, M.; Ogasahara, K.; Bagautdinov, B.; Kunishima, N.; Yutani, K. Remarkable Improvement in the Heat Stability of CutA1 from Escherichia Coli by Rational Protein Design. *J. Biochem. (Tokyo)* **2010**, mvq079. https://doi.org/10.1093/jb/mvq079.

(136) Jiang, M.; Su, Y.; Ye, J.; Li, H.; Kuang, S.; Wu, J.; Li, S.; Peng, X.; Peng, B. Ampicillin-Controlled Glucose Metabolism Manipulates the Transition from Tolerance to Resistance in Bacteria. *Sci. Adv.* **2023**, *9* (10), eade8582. https://doi.org/10.1126/sciadv.ade8582.

(137) Zhang, R.; Hartline, C.; Zhang, F. The Ability in Managing Reactive Oxygen Species Affects *Escherichia Coli* Persistence to Ampicillin after Nutrient Shifts. *mSystems* **2024**, *9* (11), e01295-24. https://doi.org/10.1128/msystems.01295-24.

(138) Dwyer, D. J.; Belenky, P. A.; Yang, J. H.; MacDonald, I. C.; Martell, J. D.; Takahashi, N.; Chan, C. T. Y.; Lobritz, M. A.; Braff, D.; Schwarz, E. G.; Ye, J. D.; Pati, M.; Vercruysse, M.; Ralifo, P. S.; Allison, K. R.; Khalil, A. S.; Ting, A. Y.; Walker, G. C.; Collins, J. J. Antibiotics Induce Redox-Related Physiological Alterations as Part of Their Lethality. *Proc. Natl. Acad. Sci.* **2014**, *111* (20). https://doi.org/10.1073/pnas.1401876111.

(139) Tsuchiya, Y.; Zhyvoloup, A.; Baković, J.; Thomas, N.; Yu, B. Y. K.; Das, S.; Orengo, C.; Newell, C.; Ward, J.; Saladino, G.; Comitani, F.; Gervasio, F. L.; Malanchuk, O. M.; Khoruzhenko, A. I.; Filonenko, V.; Peak-Chew, S. Y.; Skehel, M.; Gout, I. Protein CoAlation and Antioxidant Function of Coenzyme A in Prokaryotic Cells. *Biochem. J.* **2018**, *475* (11), 1909–1937. https://doi.org/10.1042/BCJ20180043.

(140) Radyukina, N. L.; Mikheeva, L. E.; Karbysheva, E. A. Low Molecular Weight Antioxidants in Cyanobacteria and Plant Cells. *Biol. Bull. Rev.* **2019**, *9* (6), 520–531. https://doi.org/10.1134/S2079086419060045.

(141) Vo, K. C.; Sakamoto, J. J.; Furuta, M.; Tsuchido, T. The Impact of Heat Treatment on *E. Coli* Cell Physiology in Rich and Minimal Media Considering Oxidative Secondary Stress. *J. Appl. Microbiol.* **2024**, *135* (9), lxae216. https://doi.org/10.1093/jambio/lxae216.

(142) Marcén, M.; Ruiz, V.; Serrano, M. J.; Condón, S.; Mañas, P. Oxidative Stress in E. Coli Cells upon Exposure to Heat Treatments. *Int. J. Food Microbiol.* **2017**, *241*, 198–205. https://doi.org/10.1016/j.ijfoodmicro.2016.10.023.

(143) Fedyaeva, A. V.; Stepanov, A. V.; Lyubushkina, I. V.; Pobezhimova, T. P.; Rikhvanov, E. G. Heat Shock Induces Production of Reactive Oxygen Species and Increases Inner Mitochondrial Membrane Potential in Winter Wheat Cells. *Biochem. Mosc.* **2014**, *79* (11), 1202–1210. https://doi.org/10.1134/S0006297914110078.

(144) Baur, R.; Sugimoto, T.; Pfleiderer, W. Pteridines. Part LXXXV. Chemical Synthesis of Deoxysepiapterin and 6-acylpteridines by Acyl Radical Substitution Reactions. *Helv. Chim. Acta* **1988**, *71* (3), 531–543. https://doi.org/10.1002/hlca.19880710305.

(145) Ikawa, M. Pterins of the Cyanobacterium Aphanizomenon Flos-Aquae. *Phytochemistry* **1995**, *38* (5), 1229–1232. https://doi.org/10.1016/0031-9422(94)00775-O.

(146) Durairaju Nisshanthini, S.; Teresa Infanta S., A. K.; Raja, D. S.; Natarajan, K.; Palaniswamy, M.; Angayarkanni, J. Spectral Characterization of a Pteridine Derivative

from Cyanide-Utilizing Bacterium Bacillus Subtilis - JN989651. *J. Microbiol.* **2015**, *53* (4), 262–271. https://doi.org/10.1007/s12275-015-4138-0.

(147) Forrest, H. S.; Van Baalen, C.; Myers, J. Occurrence of Pteridines in a Blue-Green Alga. *Science* **1957**, *125* (3250), 699–700. https://doi.org/10.1126/science.125.3250.699.

(148) Tsusué, M. Studies on Sepiapterin Deaminase from the Silkworm, Bombyx Mori. *J. Biochem. (Tokyo)* **1971**, *69* (4), 781–788. https://doi.org/10.1093/oxfordjournals.jbchem.a129526.

(149) Green, C. L.; Mitchell, S. E.; Derous, D.; García-Flores, L. A.; Wang, Y.; Chen, L.; Han, J.-D. J.; Promislow, D. E. L.; Lusseau, D.; Douglas, A.; Speakman, J. R. The Effects of Graded Levels of Calorie Restriction: XVI. Metabolomic Changes in the Cerebellum Indicate Activation of Hypothalamocerebellar Connections Driven by Hunger Responses. *J. Gerontol. Ser. A* **2021**, *76* (4), 601–610. https://doi.org/10.1093/gerona/glaa261.

(150) Inoue, S.; Tanino, H.; Takakura, H.; Kakoi, H.; Okada, K. (S)-2-Methyl-1,5-Bis(1,3-Dimethyl-6-Lumazinyl)-1,5-Pentanedione from the Marine Polychaete, Odontosyllis Undecimdonta. *HETEROCYCLES* **1996**, *42* (1), 125. https://doi.org/10.3987/COM-95-S40.

(151) Feirer, N.; Fuqua, C. Pterin Function in Bacteria. *Pteridines* **2017**, *28* (1), 23–36. https://doi.org/10.1515/pterid-2016-0012.

(152) Nieter Burgmayer, S. J. Electron Transfer in Transition Metal-Pteridine Systems. In *Less Common Metals in Proteins and Nucleic Acid Probes*; Structure and Bonding; Springer Berlin Heidelberg, 1998; Vol. 92, pp 67–119. https://doi.org/10.1007/BFb0081078.

(153) Blau, N.; Hennermann, J. B.; Langenbeck, U.; Lichter-Konecki, U. Diagnosis, Classification, and Genetics of Phenylketonuria and Tetrahydrobiopterin (BH4) Deficiencies. *Mol. Genet. Metab.* **2011**, *104*, S2–S9. https://doi.org/10.1016/j.ymgme.2011.08.017.

(154) Hyland, K.; Surtees, R. A. H.; Heales, S. J. R.; Bowron, A.; Howells, D. W.; Smith, I. Cerebrospinal Fluid Concentrations of Pterins and Metabolites of Serotonin and Dopamine in a Pediatric Reference Population. *Pediatr. Res.* **1993**, *34* (1), 10–14. https://doi.org/10.1203/00006450-199307000-00003.

(155) Burkhead, J. L.; Abdel-Ghany, S. E.; Morrill, J. M.; Pilon-Smits, E. A. H.; Pilon, M. The *Arabidopsis Thaliana CUTA* Gene Encodes an Evolutionarily Conserved Copper Binding Chloroplast Protein. *Plant J.* **2003**, *34* (6), 856–867. https://doi.org/10.1046/j.1365-313X.2003.01769.x.

(156) Houston, M.; Estevez, A.; Chumley, P.; Aslan, M.; Marklund, S.; Parks, D. A.; Freeman, B. A. Binding of Xanthine Oxidase to Vascular Endothelium. *J. Biol. Chem.* **1999**, *274* (8), 4985–4994. https://doi.org/10.1074/jbc.274.8.4985.

(157) Enroth, C.; Eger, B. T.; Okamoto, K.; Nishino, T.; Nishino, T.; Pai, E. F. Crystal Structures of Bovine Milk Xanthine Dehydrogenase and Xanthine Oxidase: Structure-Based Mechanism of Conversion. *Proc. Natl. Acad. Sci.* **2000**, *97* (20), 10723–10728. https://doi.org/10.1073/pnas.97.20.10723.

(158) Filiz, E.; Vatansever, R.; Ozyigit, I. I. Insights into a Key Sulfite Scavenger Enzyme Sulfite Oxidase (SOX) Gene in Plants. *Physiol. Mol. Biol. Plants* **2017**, *23* (2), 385–395. https://doi.org/10.1007/s12298-017-0433-z.

(159) Teigen, K.; Frøystein, N. Å.; Martínez, A. The Structural Basis of the Recognition of Phenylalanine and Pterin Cofactors by Phenylalanine Hydroxylase: Implications for the Catalytic Mechanism 1 1Edited by D. C. Rees. *J. Mol. Biol.* **1999**, *294* (3), 807–823. https://doi.org/10.1006/jmbi.1999.3288.

(160) Haavik, J.; Andersson, K. K.; Petersson, L.; Flatmark, T. Soluble Tyrosine Hydroxylase (Tyrosine 3-Monooxygenase) from Bovine Adrenal Medulla: Large-Scale Purification and Physicochemical Properties. *Biochim. Biophys. Acta BBA - Protein Struct. Mol. Enzymol.* **1988**, *953*, 142–156. https://doi.org/10.1016/0167-4838(88)90019-2.

(161) Batinić-Haberle, I.; Spasojević, I.; Fridovich, I. Tetrahydrobiopterin Rapidly Reduces the SOD Mimic Mn(III) Ortho -Tetrakis(N -Ethylpyridinium-2-Yl)Porphyrin. *Free Radic. Biol. Med.* **2004**, *37* (3), 367–374. https://doi.org/10.1016/j.freeradbiomed.2004.04.041.

(162) Bürgisser, D. M.; Thöny, B.; Redweik, U.; Hess, D.; Heizmann, C. W.; Huber, R.; Nar, H. 6-Pyruvoyl Tetrahydropterin Synthase, An Enzyme With a Novel Type of Active Site Involving Both Zinc Binding and an Intersubunit Catalytic Triad Motif; Site-Directed Mutagenesis of the Proposed Active Center, Characterization of the Metal Binding Site and Modelling of Substrate Binding. *J. Mol. Biol.* **1995**, *253* (2), 358–369. https://doi.org/10.1006/jmbi.1995.0558.

(163) Chung, H. J.; Kim, Y.-A.; Kim, Y. J.; Choi, Y. K.; Hwang, Y. K.; Park, Y. S. Purification and Characterization of UDP-Glucose:Tetrahydrobiopterin Glucosyltransferase from Synechococcus Sp. PCC 7942. *Biochim. Biophys. Acta BBA - Gen. Subj.* **2000**, *1524* (2–3), 183–188. https://doi.org/10.1016/S0304-4165(00)00156-2.

(164) Pribat, A.; Blaby, I. K.; Lara-Núñez, A.; Gregory, J. F.; De Crécy-Lagard, V.; Hanson, A. D. FolX and FolM Are Essential for Tetrahydromonapterin Synthesis in *Escherichia Coli* and *Pseudomonas Aeruginosa*. *J. Bacteriol.* **2010**, *192* (2), 475–482. https://doi.org/10.1128/jb.01198-09.

(165) Rippka, R.; Stanier, R. Y.; Deruelles, J.; Herdman, M.; Waterbury, J. B. Generic Assignments, Strain Histories and Properties of Pure Cultures of Cyanobacteria. *Microbiology* **1979**, *111* (1), 1–61. https://doi.org/10.1099/00221287-111-1-1.

(166) Guder, J. C.; Schramm, T.; Sander, T.; Link, H. Time-Optimized Isotope Ratio LC–MS/MS for High-Throughput Quantification of Primary Metabolites. *Anal. Chem.* **2017**, *89* (3), 1624–1631. https://doi.org/10.1021/acs.analchem.6b03731.

(167) Marty, M. T.; Baldwin, A. J.; Marklund, E. G.; Hochberg, G. K. A.; Benesch, J. L. P.; Robinson, C. V. Bayesian Deconvolution of Mass and Ion Mobility Spectra: From Binary Interactions to Polydisperse Ensembles. *Anal. Chem.* **2015**, *87* (8), 4370–4376. https://doi.org/10.1021/acs.analchem.5b00140.

(168) Chambers, M. C.; Maclean, B.; Burke, R.; Amodei, D.; Ruderman, D. L.; Neumann, S.; Gatto, L.; Fischer, B.; Pratt, B.; Egertson, J.; Hoff, K.; Kessner, D.; Tasman, N.; Shulman, N.; Frewen, B.; Baker, T. A.; Brusniak, M.-Y.; Paulse, C.; Creasy, D.; Flashner, L.; Kani, K.; Moulding, C.; Seymour, S. L.; Nuwaysir, L. M.; Lefebvre, B.; Kuhlmann, F.; Roark, J.; Rainer, P.; Detlev, S.; Hemenway, T.; Huhmer, A.; Langridge, J.; Connolly, B.; Chadick, T.; Holly, K.; Eckels, J.; Deutsch, E. W.; Moritz, R. L.; Katz, J. E.; Agus, D. B.; MacCoss, M.; Tabb, D. L.; Mallick, P. A Cross-Platform Toolkit for Mass Spectrometry and Proteomics. *Nat. Biotechnol.* **2012**, *30* (10), 918–920. https://doi.org/10.1038/nbt.2377.

(169) Schmid, R.; Heuckeroth, S.; Korf, A.; Smirnov, A.; Myers, O.; Dyrlund, T. S.; Bushuiev, R.; Murray, K. J.; Hoffmann, N.; Lu, M.; Sarvepalli, A.; Zhang, Z.; Fleischauer, M.; Dührkop, K.; Wesner, M.; Hoogstra, S. J.; Rudt, E.; Mokshyna, O.; Brungs, C.; Ponomarov, K.; Mutabdžija, L.; Damiani, T.; Pudney, C. J.; Earll, M.; Helmer, P. O.; Fallon, T. R.; Schulze, T.; Rivas-Ubach, A.; Bilbao, A.; Richter, H.; Nothias, L.-F.; Wang, M.; Orešič, M.; Weng, J.-K.; Böcker, S.; Jeibmann, A.; Hayen, H.; Karst, U.; Dorrestein, P. C.; Petras, D.; Du, X.; Pluskal, T. Integrative Analysis of

Multimodal Mass Spectrometry Data in MZmine 3. *Nat. Biotechnol.* **2023**, *41* (4), 447–449. https://doi.org/10.1038/s41587-023-01690-2.

(170) Nothias, L.-F.; Petras, D.; Schmid, R.; Dührkop, K.; Rainer, J.; Sarvepalli, A.; Protsyuk, I.; Ernst, M.; Tsugawa, H.; Fleischauer, M.; Aicheler, F.; Aksenov, A. A.; Alka, O.; Allard, P.-M.; Barsch, A.; Cachet, X.; Caraballo-Rodriguez, A. M.; Da Silva, R. R.; Dang, T.; Garg, N.; Gauglitz, J. M.; Gurevich, A.; Isaac, G.; Jarmusch, A. K.; Kameník, Z.; Kang, K. B.; Kessler, N.; Koester, I.; Korf, A.; Le Gouellec, A.; Ludwig, M.; Martin H., C.; McCall, L.-I.; McSayles, J.; Meyer, S. W.; Mohimani, H.; Morsy, M.; Moyne, O.; Neumann, S.; Neuweger, H.; Nguyen, N. H.; Nothias-Esposito, M.; Paolini, J.; Phelan, V. V.; Pluskal, T.; Quinn, R. A.; Rogers, S.; Shrestha, B.; Tripathi, A.; Van Der Hooft, J. J. J.; Vargas, F.; Weldon, K. C.; Witting, M.; Yang, H.; Zhang, Z.; Zubeil, F.; Kohlbacher, O.; Böcker, S.; Alexandrov, T.; Bandeira, N.; Wang, M.; Dorrestein, P. C. Feature-Based Molecular Networking in the GNPS Analysis Environment. *Nat. Methods* **2020**, *17* (9), 905–908. https://doi.org/10.1038/s41592-020-0933-6.

(171) Wang, M.; Carver, J. J.; Phelan, V. V.; Sanchez, L. M.; Garg, N.; Peng, Y.; Nguyen, D. D.; Watrous, J.; Kapono, C. A.; Luzzatto-Knaan, T.; Porto, C.; Bouslimani, A.; Melnik, A. V.; Meehan, M. J.; Liu, W.-T.; Crüsemann, M.; Boudreau, P. D.; Esquenazi, E.; Sandoval-Calderón, M.; Kersten, R. D.; Pace, L. A.; Quinn, R. A.; Duncan, K. R.; Hsu, C.-C.; Floros, D. J.; Gavilan, R. G.; Kleigrewe, K.; Northen, T.; Dutton, R. J.; Parrot, D.; Carlson, E. E.; Aigle, B.; Michelsen, C. F.; Jelsbak, L.; Sohlenkamp, C.; Pevzner, P.; Edlund, A.; McLean, J.; Piel, J.; Murphy, B. T.; Gerwick, L.; Liaw, C.-C.; Yang, Y.-L.; Humpf, H.-U.; Maansson, M.; Keyzers, R. A.; Sims, A. C.; Johnson, A. R.; Sidebottom, A. M.; Sedio, B. E.; Klitgaard, A.; Larson, C. B.; Boya P, C. A.; Torres-Mendoza, D.; Gonzalez, D. J.; Silva, D. B.; Marques, L. M.; Demarque, D. P.; Pociute, E.; O'Neill, E. C.; Briand, E.; Helfrich, E. J. N.; Granatosky, E. A.; Glukhov, E.; Ryffel, F.; Houson, H.; Mohimani, H.; Kharbush, J. J.; Zeng, Y.; Vorholt, J. A.; Kurita, K. L.; Charusanti, P.; McPhail, K. L.; Nielsen, K. F.; Vuong, L.; Elfeki, M.; Traxler, M. F.; Engene, N.; Koyama, N.; Vining, O. B.; Baric, R.; Silva, R. R.; Mascuch, S. J.; Tomasi, S.; Jenkins, S.; Macherla, V.; Hoffman, T.; Agarwal, V.; Williams, P. G.; Dai, J.; Neupane, R.; Gurr, J.; Rodríguez, A. M. C.; Lamsa, A.; Zhang, C.; Dorrestein, K.; Duggan, B. M.; Almaliti, J.; Allard, P.-M.; Phapale, P.; Nothias, L.-F.; Alexandrov, T.; Litaudon, M.; Wolfender, J.-L.; Kyle, J. E.; Metz, T. O.; Peryea, T.; Nguyen, D.-T.; VanLeer, D.; Shinn, P.; Jadhav, A.; Müller, R.; Waters, K. M.; Shi, W.; Liu, X.; Zhang, L.; Knight, R.; Jensen, P. R.; Palsson, B. Ø.; Pogliano, K.; Linington, R. G.; Gutiérrez, M.; Lopes, N. P.; Gerwick, W. H.; Moore, B. S.; Dorrestein, P. C.; Bandeira, N. Sharing and Community Curation of Mass Spectrometry Data with Global Natural Products Social Molecular Networking. *Nat. Biotechnol.* **2016**, *34* (8), 828–837. https://doi.org/10.1038/nbt.3597.

(172) Shannon, P.; Markiel, A.; Ozier, O.; Baliga, N. S.; Wang, J. T.; Ramage, D.; Amin, N.; Schwikowski, B.; Ideker, T. Cytoscape: A Software Environment for Integrated Models of Biomolecular Interaction Networks. *Genome Res.* **2003**, *13* (11), 2498–2504. https://doi.org/10.1101/gr.1239303.

(173) Pettersen, E. F.; Goddard, T. D.; Huang, C. C.; Meng, E. C.; Couch, G. S.; Croll, T. I.; Morris, J. H.; Ferrin, T. E. UCSF ChimeraX: Structure Visualization for Researchers, Educators, and Developers. *Protein Sci. Publ. Protein Soc.* **2021**, *30* (1), 70–82. https://doi.org/10.1002/pro.3943.

(174) Passaro, S.; Corso, G.; Wohlwend, J.; Reveiz, M.; Thaler, S.; Somnath, V. R.; Getz, N.; Portnoi, T.; Roy, J.; Stark, H.; Kwabi-Addo, D.; Beaini, D.; Jaakkola, T.; Barzilay, R. Boltz-2: Towards Accurate and Efficient Binding Affinity Prediction. *BioRxiv*

Prepr. Serv. Biol. **2025**, 2025.06.14.659707. https://doi.org/10.1101/2025.06.14.659707.

(175) Kim, J.; Webb, A. M.; Kershner, J. P.; Blaskowski, S.; Copley, S. D. A Versatile and Highly Efficient Method for Scarless Genome Editing in Escherichia Coli and Salmonella Enterica. *BMC Biotechnol.* **2014**, *14* (1), 84. https://doi.org/10.1186/1472-6750-14-84.

(176) Okuda, S.; Tokuda, H. Lipoprotein Sorting in Bacteria. *Annu. Rev. Microbiol.* **2011**, *65* (1), 239–259. https://doi.org/10.1146/annurev-micro-090110-102859.

(177) May, K. L.; Lehman, K. M.; Mitchell, A. M.; Grabowicz, M. A Stress Response Monitoring Lipoprotein Trafficking to the Outer Membrane. *mBio* **2019**, *10* (3), e00618-19. https://doi.org/10.1128/mBio.00618-19.

(178) Yakushi, T.; Tajima, T.; Matsuyama, S.; Tokuda, H. Lethality of the Covalent Linkage between Mislocalized Major Outer Membrane Lipoprotein and the Peptidoglycan of Escherichia Coli. *J. Bacteriol.* **1997**, *179* (9), 2857–2862. https://doi.org/10.1128/jb.179.9.2857-2862.1997.

(179) Raivio, T. L. Everything Old Is New Again: An Update on Current Research on the Cpx Envelope Stress Response. *Biochim. Biophys. Acta BBA - Mol. Cell Res.* **2014**, *1843* (8), 1529–1541. https://doi.org/10.1016/j.bbamcr.2013.10.018.

(180) Kadokura, H.; Katzen, F.; Beckwith, J. Protein Disulfide Bond Formation in Prokaryotes. *Annu. Rev. Biochem.* **2003**, *72* (1), 111–135. https://doi.org/10.1146/annurev.biochem.72.121801.161459.

(181) Ito, K.; Inaba, K. The Disulfide Bond Formation (Dsb) System. *Curr. Opin. Struct. Biol.* **2008**, *18* (4), 450–458. https://doi.org/10.1016/j.sbi.2008.02.002.

(182) Collet, J.-F.; Cho, S.-H.; Iorga, B. I.; Goemans, C. V. How the Assembly and Protection of the Bacterial Cell Envelope Depend on Cysteine Residues. *J. Biol. Chem.* **2020**, *295* (34), 11984–11994. https://doi.org/10.1074/jbc.REV120.011201.

(183) Mainardi, J.-L.; Fourgeaud, M.; Hugonnet, J.-E.; Dubost, L.; Brouard, J.-P.; Ouazzani, J.; Rice, L. B.; Gutmann, L.; Arthur, M. A Novel Peptidoglycan Cross-Linking Enzyme for a β-Lactam-Resistant Transpeptidation Pathway. *J. Biol. Chem.* **2005**, *280* (46), 38146–38152. https://doi.org/10.1074/jbc.M507384200.

(184) Peters, K.; Pazos, M.; Edoo, Z.; Hugonnet, J.-E.; Martorana, A. M.; Polissi, A.; VanNieuwenhze, M. S.; Arthur, M.; Vollmer, W. Copper Inhibits Peptidoglycan LD-Transpeptidases Suppressing β-Lactam Resistance Due to Bypass of Penicillin-Binding Proteins. *Proc. Natl. Acad. Sci.* **2018**, *115* (42), 10786–10791. https://doi.org/10.1073/pnas.1809285115.

(185) Nakajima, Y.; Umena, Y.; Nagao, R.; Endo, K.; Kobayashi, K.; Akita, F.; Suga, M.; Wada, H.; Noguchi, T.; Shen, J.-R. Thylakoid Membrane Lipid Sulfoquinovosyl-Diacylglycerol (SQDG) Is Required for Full Functioning of Photosystem II in Thermosynechococcus Elongatus. *J. Biol. Chem.* **2018**, *293* (38), 14786–14797. https://doi.org/10.1074/jbc.RA118.004304.

(186) Woong Lee, S.; Woo Lee, H.; Jae Chung, H.; Kim, Y.-A.; Jeong Kim, Y.; Hahn, Y.; Hoon Chung, J.; Shik Park, Y. Identification of the Genes Encoding Enzymes Involved in the Early Biosynthetic Pathway of Pteridines in *Synechocystis* Sp. PCC 6803. *FEMS Microbiol. Lett.* **1999**, *176* (1), 169–176. https://doi.org/10.1111/j.1574-6968.1999.tb13658.x.

(187) Wang, J.; Wu, G.; Chen, L.; Zhang, W. Cross-Species Transcriptional Network Analysis Reveals Conservation and Variation in Response to Metal Stress in Cyanobacteria. *BMC Genomics* **2013**, *14*, 112. https://doi.org/10.1186/1471-2164-14-112.

(188) Huergo, L. F.; Dixon, R. The Emergence of 2-Oxoglutarate as a Master Regulator Metabolite. *Microbiol. Mol. Biol. Rev. MMBR* **2015**, *79* (4), 419–435. https://doi.org/10.1128/MMBR.00038-15.
(189) Liu, S.; He, L.; Yao, K. The Antioxidative Function of Alpha-Ketoglutarate and Its Applications. *BioMed Res. Int.* **2018**, *2018*, 3408467. https://doi.org/10.1155/2018/3408467.
(190) Mailloux, R. J.; Singh, R.; Brewer, G.; Auger, C.; Lemire, J.; Appanna, V. D. α-Ketoglutarate Dehydrogenase and Glutamate Dehydrogenase Work in Tandem To Modulate the Antioxidant α-Ketoglutarate during Oxidative Stress in *Pseudomonas Fluorescens*. *J. Bacteriol.* **2009**, *191* (12), 3804–3810. https://doi.org/10.1128/JB.00046-09.
(191) Rehman, A. U.; Bashir, F.; Ayaydin, F.; Kóta, Z.; Páli, T.; Vass, I. Proline Is a Quencher of Singlet Oxygen and Superoxide Both in in Vitro Systems and Isolated Thylakoids. *Physiol. Plant.* **2021**, *172* (1), 7–18. https://doi.org/10.1111/ppl.13265.
(192) Ramis, R.; Ortega-Castro, J.; Caballero, C.; Casasnovas, R.; Cerrillo, A.; Vilanova, B.; Adrover, M.; Frau, J. How Does Pyridoxamine Inhibit the Formation of Advanced Glycation End Products? The Role of Its Primary Antioxidant Activity. *Antioxid. Basel Switz.* **2019**, *8* (9), 344. https://doi.org/10.3390/antiox8090344.
(193) Cheng, C.-H.; Huang, S.-C.; Chiang, T.-Y.; Wong, Y.; Huang, Y.-C. Higher Plasma Pyridoxal Phosphate Is Associated with Increased Antioxidant Enzyme Activities in Critically Ill Surgical Patients. *BioMed Res. Int.* **2013**, *2013*, 1–7. https://doi.org/10.1155/2013/572081.
(194) Raghavan, R.; Dryhurst, G. Redox Chemistry of Reduced Pterin Species. *J. Electroanal. Chem. Interfacial Electrochem.* **1981**, *129* (1–2), 189–212. https://doi.org/10.1016/S0022-0728(81)80014-9.
(195) Zhang, L.; Alfano, J. R.; Becker, D. F. Proline Metabolism Increases *katG* Expression and Oxidative Stress Resistance in Escherichia Coli. *J. Bacteriol.* **2015**, *197* (3), 431–440. https://doi.org/10.1128/JB.02282-14.
(196) Hopkins, F. G. III. The Pigments of the Pieridæ. A Contribution to the Study of Excretory Substances Which Function in Ornament. *Proc. R. Soc. Lond.* **1895**, *57* (340–346), 5–6. https://doi.org/10.1098/rspl.1894.0127.
(197) Hopkins, F. G. Pigment in Yellow Butterflies. *Nature* **1891**, *45* (1157), 197–198. https://doi.org/10.1038/045197c0.
(198) Schöpf, C.; Reichert, R. Zur Kenntnis Des Leukopterins. *Justus Liebigs Ann. Chem.* **1941**, *548* (1), 82–94. https://doi.org/10.1002/jlac.19415480108.
(199) Harmsen, R. The Excretory Role of Pteridines in Insects. *J. Exp. Biol.* **1966**, *45* (1), 1–13. https://doi.org/10.1242/jeb.45.1.1.
(200) Rüchardt, C. Die Farben Der Schmetterlingsflügel Und Anderer Insekten:: Die Entdeckung Der Pterine in Der Wieland-Schule. **2007**.
(201) Ziegler, I. [Quantitative determination of yellow pterin and riboflavin in the skin of the fire salamander (Salamandra salamandra)]. *Biochem. Z.* **1961**, *334*, 425–430.
(202) Andrade, P.; Carneiro, M. Pterin-Based Pigmentation in Animals. *Biol. Lett.* **2021**, *17* (8), 20210221. https://doi.org/10.1098/rsbl.2021.0221.
(203) Ducker, G. S.; Rabinowitz, J. D. One-Carbon Metabolism in Health and Disease. *Cell Metab.* **2017**, *25* (1), 27–42. https://doi.org/10.1016/j.cmet.2016.08.009.
(204) Basu, P.; Burgmayer, S. J. N. Pterin Chemistry and Its Relationship to the Molybdenum Cofactor. *Coord. Chem. Rev.* **2011**, *255* (9–10), 1016–1038. https://doi.org/10.1016/j.ccr.2011.02.010.
(205) Murr, C.; Widner, B.; Wirleitner, B.; Fuchs, D. Neopterin as a Marker for Immune System Activation. *Curr. Drug Metab.* **2002**, *3* (2), 175–187. https://doi.org/10.2174/1389200024605082.

(206) Zheng, Y.; Cantley, L. C. Toward a Better Understanding of Folate Metabolism in Health and Disease. *J. Exp. Med.* **2019**, *216* (2), 253–266. https://doi.org/10.1084/jem.20181965.
(207) Daniels, B. J.; Li, F. F.; Furkert, D. P.; Brimble, M. A. Naturally Occurring Lumazines. *J. Nat. Prod.* **2019**, *82* (7), 2054–2065. https://doi.org/10.1021/acs.jnatprod.9b00351.
(208) Fischer, M.; Bacher, A. Biosynthesis of Riboflavin. *EcoSal Plus* **2010**, *4* (1), 10.1128/ecosalplus.3.6.3.2. https://doi.org/10.1128/ecosalplus.3.6.3.2.
(209) Fraaije, M. W.; Mattevi, A. Flavoenzymes: Diverse Catalysts with Recurrent Features. *Trends Biochem. Sci.* **2000**, *25* (3), 126–132. https://doi.org/10.1016/S0968-0004(99)01533-9.
(210) Dalal, F. R.; Gots, J. S. Requirement of GTP for Pteridine Synthesis in Salmonellatyphimurium and Its Inhibition by AMP. *Biochem. Biophys. Res. Commun.* **1965**, *20* (4), 509–514. https://doi.org/10.1016/0006-291x(65)90609-1.
(211) Kis, K.; Volk, R.; Bacher, A. Biosynthesis of Riboflavin. Studies on the Reaction Mechanism of 6,7-Dimethyl-8-Ribityllumazine Synthase. *Biochemistry* **1995**, *34* (9), 2883–2892. https://doi.org/10.1021/bi00009a019.
(212) Rudolph, M. J.; Schindelin, H.; Wuebbens, M. M.; Rajagopalan, K. V. Crystal Structure of Molybdopterin Synthase and Its Evolutionary Relationship to Ubiquitin Activation. *Nat. Struct. Biol.* **2001**, *8* (1), 42–46. https://doi.org/10.1038/83034.
(213) de Crécy-Lagard, V.; Hutinet, G.; Cediel-Becerra, J. D. D.; Yuan, Y.; Zallot, R.; Chevrette, M. G.; Ratnayake, R. M. M. N.; Jaroch, M.; Quaiyum, S.; Bruner, S. Biosynthesis and Function of 7-Deazaguanine Derivatives in Bacteria and Phages. *Microbiol. Mol. Biol. Rev. MMBR* **2024**, *88* (1), e0019923. https://doi.org/10.1128/mmbr.00199-23.
(214) Miles, Z. D.; Roberts, S. A.; McCarty, R. M.; Bandarian, V. Biochemical and Structural Studies of 6-Carboxy-5,6,7,8-Tetrahydropterin Synthase Reveal the Molecular Basis of Catalytic Promiscuity within the Tunnel-Fold Superfamily. *J. Biol. Chem.* **2014**, *289* (34), 23641–23652. https://doi.org/10.1074/jbc.M114.555680.
(215) McCarty, R. M.; Somogyi, Á.; Bandarian, V. *Escherichia Coli* QueD Is a 6-Carboxy-5,6,7,8-Tetrahydropterin Synthase. *Biochemistry* **2009**, *48* (11), 2301–2303. https://doi.org/10.1021/bi9001437.
(216) Takikawa, S.; Kitayama-Yokokawa, C.; Tsusue, M. Pterin Deaminase from Bacillus Megaterium. Purification and Properties. *J. Biochem. (Tokyo)* **1979**, *85* (3), 785–790.
(217) Moon, Y.-J.; Lee, E.-M.; Park, Y. M.; Park, Y. S.; Chung, W.-I.; Chung, Y.-H. The Role of Cyanopterin in UV/Blue Light Signal Transduction of Cyanobacterium Synechocystis Sp. PCC 6803 Phototaxis. *Plant Cell Physiol.* **2010**, *51* (6), 969–980. https://doi.org/10.1093/pcp/pcq059.
(218) Chung, H. J.; Kim, Y.-A.; Kim, Y. J.; Choi, Y. K.; Hwang, Y. K.; Park, Y. S. Purification and Characterization of UDP-Glucose:Tetrahydrobiopterin Glucosyltransferase from Synechococcus Sp. PCC 7942. *Biochim. Biophys. Acta BBA - Gen. Subj.* **2000**, *1524* (2–3), 183–188. https://doi.org/10.1016/s0304-4165(00)00156-2.
(219) Phillips, G.; Grochowski, L. L.; Bonnett, S.; Xu, H.; Bailly, M.; Blaby-Haas, C.; El Yacoubi, B.; Iwata-Reuyl, D.; White, R. H.; de Crécy-Lagard, V. Functional Promiscuity of the COG0720 Family. *ACS Chem. Biol.* **2012**, *7* (1), 197–209. https://doi.org/10.1021/cb200329f.
(220) Ploom, T.; Haußmann, C.; Hof, P.; Steinbacher, S.; Bacher, A.; Richardson, J.; Huber, R. Crystal Structure of 7,8-Dihydroneopterin Triphosphate Epimerase. *Structure* **1999**, *7* (5), 509–516. https://doi.org/10.1016/S0969-2126(99)80067-7.
(221) Colloc'h, N.; Poupon, A.; Mornon, J.-P. Sequence and Structural Features of the T-Fold, an Original Tunnelling Building Unit. *Proteins Struct. Funct. Genet.* **2000**, *39*

(2), 142–154. https://doi.org/10.1002/(SICI)1097-0134(20000501)39:2%253C142::AID-PROT4%253E3.0.CO;2-X.

(222) Basu, P.; Burgmayer, S. J. N. Pterin Chemistry and Its Relationship to the Molybdenum Cofactor. *Coord. Chem. Rev.* **2011**, *255* (9–10), 1016–1038. https://doi.org/10.1016/j.ccr.2011.02.010.

(223) Wei, C.-C.; Wang, Z.-Q.; Tejero, J.; Yang, Y.-P.; Hemann, C.; Hille, R.; Stuehr, D. J. Catalytic Reduction of a Tetrahydrobiopterin Radical within Nitric-Oxide Synthase. *J. Biol. Chem.* **2008**, *283* (17), 11734–11742. https://doi.org/10.1074/jbc.M709250200.

(224) Shen, R.; Zhang, Y. Reduced Pterins as Scavengers for Reactive Oxygen Species. In *Chemistry and Biology of Pteridines and Folates*; Ayling, J. E., Nair, M. G., Baugh, C. M., Eds.; Advances in Experimental Medicine and Biology; Springer US: Boston, MA, 1993; Vol. 338, pp 351–354. https://doi.org/10.1007/978-1-4615-2960-6_73.

(225) Buglak, A. A.; Kapitonova, M. A.; Vechtomova, Y. L.; Telegina, T. A. Insights into Molecular Structure of Pterins Suitable for Biomedical Applications. *Int. J. Mol. Sci.* **2022**, *23* (23), 15222. https://doi.org/10.3390/ijms232315222.

(226) Wakabayashi, I.; Nakanishi, M.; Ohki, M.; Suehiro, A.; Uchida, K. A Simple and Useful Method for Evaluation of Oxidative Stress in Vivo by Spectrofluorometric Estimation of Urinary Pteridines. *Sci. Rep.* **2020**, *10* (1), 11223. https://doi.org/10.1038/s41598-020-67681-4.

(227) Kaufman, S. New Tetrahydrobiopterin-Dependent Systems. *Annu. Rev. Nutr.* **1993**, *13* (1), 261–286. https://doi.org/10.1146/annurev.nu.13.070193.001401.

(228) Kong, J. S.; Kang, J.-Y.; Kim, H. L.; Kwon, O.-S.; Lee, K. H.; Park, Y. S. 6-Pyruvoyltetrahydropterin Synthase Orthologs of Either a Single or Dual Domain Structure Are Responsible for Tetrahydrobiopterin Synthesis in Bacteria. *FEBS Lett.* **2006**, *580* (20), 4900–4904. https://doi.org/10.1016/j.febslet.2006.08.006.

(229) Fitzpatrick, P. F. Mechanism of Aromatic Amino Acid Hydroxylation. *Biochemistry* **2003**, *42* (48), 14083–14091. https://doi.org/10.1021/bi035656u.

(230) Eichwald, T.; da Silva, L. de B.; Staats Pires, A. C.; Niero, L.; Schnorrenberger, E.; Filho, C. C.; Espíndola, G.; Huang, W.-L.; Guillemin, G. J.; Abdenur, J. E.; Latini, A. Tetrahydrobiopterin: Beyond Its Traditional Role as a Cofactor. *Antioxid. Basel Switz.* **2023**, *12* (5), 1037. https://doi.org/10.3390/antiox12051037.

(231) Werner, E. R.; Blau, N.; Thöny, B. Tetrahydrobiopterin: Biochemistry and Pathophysiology. *Biochem. J.* **2011**, *438* (3), 397–414. https://doi.org/10.1042/BJ20110293.

(232) Himmelreich, N.; Blau, N.; Thöny, B. Molecular and Metabolic Bases of Tetrahydrobiopterin (BH4) Deficiencies. *Mol. Genet. Metab.* **2021**, *133* (2), 123–136. https://doi.org/10.1016/j.ymgme.2021.04.003.

(233) Foxton, R. H.; Land, J. M.; Heales, S. J. R. Tetrahydrobiopterin Availability in Parkinson's and Alzheimer's Disease; Potential Pathogenic Mechanisms. *Neurochem. Res.* **2007**, *32* (4–5), 751–756. https://doi.org/10.1007/s11064-006-9201-0.

(234) Thöny, B.; Auerbach, G.; Blau, N. Tetrahydrobiopterin Biosynthesis, Regeneration and Functions. *Biochem. J.* **2000**, *347 Pt 1* (Pt 1), 1–16.

(235) Kuhn, D. M.; Geddes, T. J. Tetrahydrobiopterin Prevents Nitration of Tyrosine Hydroxylase by Peroxynitrite and Nitrogen Dioxide. *Mol. Pharmacol.* **2003**, *64* (4), 946–953. https://doi.org/10.1124/mol.64.4.946.

(236) Sakuma, S.; Fujimoto, Y.; Gohda, Y.; Fujita, T. Tetrahydrobiopterin Inhibits Copper-Induced Oxidation of Low Density Lipoprotein. *Res. Commun. Mol. Pathol. Pharmacol.* **2000**, *107* (5–6), 397–406.

(237) Vonderschmitt, D. J.; Scrimgeour, K. G. Reaction of Cu2+ and Fe3+ with Tetrahydropteridines. *Biochem. Biophys. Res. Commun.* **1967**, *28* (3), 302–308. https://doi.org/10.1016/0006-291X(67)90309-9.

(238) Funahashi, Y.; Kohzuma, T.; Odani, A.; Yamauchi, O. Spectroscopic Evidence for the Redox Reaction between Copper(II) and a Pterin Cofactor Model, 6,7-Dimethyl-5,6,7,8-Tetrahydropterin. *Chem. Lett.* **1994**, *23* (2), 385–388. https://doi.org/10.1246/cl.1994.385.

(239) Vo, T. T. T.; Peng, T.-Y.; Nguyen, T. H.; Bui, T. N. H.; Wang, C.-S.; Lee, W.-J.; Chen, Y.-L.; Wu, Y.-C.; Lee, I.-T. The Crosstalk between Copper-Induced Oxidative Stress and Cuproptosis: A Novel Potential Anticancer Paradigm. *Cell Commun. Signal. CCS* **2024**, *22* (1), 353. https://doi.org/10.1186/s12964-024-01726-3.

(240) Tsvetkov, P.; Coy, S.; Petrova, B.; Dreishpoon, M.; Verma, A.; Abdusamad, M.; Rossen, J.; Joesch-Cohen, L.; Humeidi, R.; Spangler, R. D.; Eaton, J. K.; Frenkel, E.; Kocak, M.; Corsello, S. M.; Lutsenko, S.; Kanarek, N.; Santagata, S.; Golub, T. R. Copper Induces Cell Death by Targeting Lipoylated TCA Cycle Proteins. *Science* **2022**, *375* (6586), 1254–1261. https://doi.org/10.1126/science.abf0529.

(241) Wang, H.; Yang, B.; Hao, G.; Feng, Y.; Chen, H.; Feng, L.; Zhao, J.; Zhang, H.; Chen, Y. Q.; Wang, L.; Chen, W. Biochemical Characterization of the Tetrahydrobiopterin Synthesis Pathway in the Oleaginous Fungus Mortierella Alpina. *Microbiol. Read. Engl.* **2011**, *157* (Pt 11), 3059–3070. https://doi.org/10.1099/mic.0.051847-0.

(242) Ghosh, A. K.; Sharma, A.; Nagam, S.; Fuqua, C. Syntheses of Optically Active Monapterin, 7,8-Dihydromonapterin, and 5,6,7,8-Tetrahydromonapterin from L -Xylose. *RSC Adv.* **2024**, *14* (48), 35644–35649. https://doi.org/10.1039/D4RA07179D.

(243) Tillinghast, H. S.; Newell, P. C. Chemotaxis towards Pteridines during Development of *Dictyostelium*. *J. Cell Sci.* **1987**, *87* (1), 45–53. https://doi.org/10.1242/jcs.87.1.45.

(244) Correa-Aragunde, N.; Nejamkin, A.; Del Castello, F.; Foresi, N.; Lamattina, L. Nitric Oxide Synthases from Photosynthetic Organisms Improve Growth and Confer Nitrosative Stress Tolerance in E. Coli. Insights on the Pterin Cofactor. *Nitric Oxide* **2022**, *119*, 41–49. https://doi.org/10.1016/j.niox.2021.12.005.

(245) Magalon, A.; Fedor, J. G.; Walburger, A.; Weiner, J. H. Molybdenum Enzymes in Bacteria and Their Maturation. *Coord. Chem. Rev.* **2011**, *255* (9–10), 1159–1178. https://doi.org/10.1016/j.ccr.2010.12.031.

(246) Hille, R. Molybdenum and Tungsten in Biology. *Trends Biochem. Sci.* **2002**, *27* (7), 360–367. https://doi.org/10.1016/S0968-0004(02)02107-2.

(247) Morrison, M. S.; Cobine, P. A.; Hegg, E. L. Probing the Role of Copper in the Biosynthesis of the Molybdenum Cofactor in Escherichia Coli and Rhodobacter Sphaeroides. *JBIC J. Biol. Inorg. Chem.* **2007**, *12* (8), 1129–1139. https://doi.org/10.1007/s00775-007-0279-x.

(248) Kruse, T. Moco Carrier and Binding Proteins. *Mol. Basel Switz.* **2022**, *27* (19), 6571. https://doi.org/10.3390/molecules27196571.

(249) Okamoto, K.; Kusano, T.; Nishino, T. Chemical Nature and Reaction Mechanisms of the Molybdenum Cofactor of Xanthine Oxidoreductase. *Curr. Pharm. Des.* **2013**, *19* (14), 2606–2614. https://doi.org/10.2174/1381612811319140010.

(250) Forrest, H. S.; Nawa, S. Structures of Sepiapterin and Isosepiapterin. *Nature* **1962**, *196* (4852), 372–373. https://doi.org/10.1038/196372b0.

(251) Viscontini, M.; Möhlmann, E. Fluoreszierende Stoffe Aus *Drosophila Melanogaster*. 12. Mitteilung. Die Gelb Fluoreszierenden Pterine: Sepiapterin Und Isosepiapterin. *Helv. Chim. Acta* **1959**, *42* (3), 836–841. https://doi.org/10.1002/hlca.19590420325.

(252) Kokolis, N.; Zafiratos, C. Organ-Specific Patterns of Pteridines in Bufo Viridis. *Comp. Biochem. Physiol.* **1967**, *21* (2), 373–382. https://doi.org/10.1016/0010-406x(67)90799-2.

(253) Tomic-carruthers, N.; Mangan, R.; Carruthers, R. Age Estimation of Mexican Fruit Fly (Diptera: Tephritidae) Based on Accumulation of Pterins. *J. Econ. Entomol.* **2002**, *95* (6), 1319–1325. https://doi.org/10.1603/0022-0493-95.6.1319.

(254) Ferré, J. Biosynthesis of Pteridines in Insects: A Review. *Insects* **2024**, *15* (5), 370. https://doi.org/10.3390/insects15050370.
(255) Lee, Y. G.; Kim, A. H.; Park, M. B.; Kim, H.-L.; Lee, K. H.; Park, Y. S. Molecular Cloning of Cyanobacterial Pteridine Glycosyltransferases That Catalyze the Transfer of Either Glucose or Xylose to Tetrahydrobiopterin. *Appl. Environ. Microbiol.* **2010**, *76* (22), 7658–7661. https://doi.org/10.1128/AEM.01083-10.
(256) Mahrholdt, V. Charakterisierung der PII:(I86N) Mutante in Anabaena sp. PCC 7120. Unpublished 2015. https://doi.org/10.13140/RG.2.1.4789.3844.
(257) Bacher, A.; Rappold, H. [91] Bacterial Degradation of Folic Acid. In *Methods in Enzymology*; Elsevier, 1980; Vol. 66, pp 652–656. https://doi.org/10.1016/0076-6879(80)66521-5.
(258) Jayaraman, A.; Thandeeswaran, M.; Priyadarsini, U.; Sabarathinam, S.; Nawaz, K. A. A.; Palaniswamy, M. Characterization of Unexplored Amidohydrolase Enzyme—Pterin Deaminase. *Appl. Microbiol. Biotechnol.* **2016**, *100* (11), 4779–4789. https://doi.org/10.1007/s00253-016-7513-9.
(259) Denofrio, M. P.; Dántola, M. L.; Vicendo, P.; Oliveros, E.; Thomas, A. H.; Lorente, C. Mechanism of Electron Transfer Processes Photoinduced by Lumazine. *Photochem. Photobiol. Sci.* **2012**, *11* (2), 409–417. https://doi.org/10.1039/c1pp05315a.
(260) Lin, B.; Loomes, K. M.; Prijic, G.; Schlothauer, R.; Stephens, J. M. Lepteridine as a Unique Fluorescent Marker for the Authentication of Manuka Honey. *Food Chem.* **2017**, *225*, 175–180. https://doi.org/10.1016/j.foodchem.2016.12.099.
(261) Oettl, K.; Reibnegger, G. Pteridines as Inhibitors of Xanthine Oxidase: Structural Requirements. *Biochim. Biophys. Acta BBA - Protein Struct. Mol. Enzymol.* **1999**, *1430* (2), 387–395. https://doi.org/10.1016/S0167-4838(99)00023-0.
(262) Kjer-Nielsen, L.; Patel, O.; Corbett, A. J.; Le Nours, J.; Meehan, B.; Liu, L.; Bhati, M.; Chen, Z.; Kostenko, L.; Reantragoon, R.; Williamson, N. A.; Purcell, A. W.; Dudek, N. L.; McConville, M. J.; O'Hair, R. A. J.; Khairallah, G. N.; Godfrey, D. I.; Fairlie, D. P.; Rossjohn, J.; McCluskey, J. MR1 Presents Microbial Vitamin B Metabolites to MAIT Cells. *Nature* **2012**, *491* (7426), 717–723. https://doi.org/10.1038/nature11605.
(263) Cushman, M.; Yang, D.; Gerhardt, S.; Huber, R.; Fischer, M.; Kis, K.; Bacher, A. Design, Synthesis, and Evaluation of 6-Carboxyalkyl and 6-Phosphonoxyalkyl Derivatives of 7-Oxo-8-Ribitylaminolumazines as Inhibitors of Riboflavin Synthase and Lumazine Synthase. *J. Org. Chem.* **2002**, *67* (16), 5807–5816. https://doi.org/10.1021/jo0201631.
(264) Diculescu, V. C.; Militaru, A.; Shah, A.; Qureshi, R.; Tugulea, L.; Brett, A. M. O. Redox Mechanism of Lumazine at a Glassy Carbon Electrode. *J. Electroanal. Chem.* **2010**, *647* (1), 1–7. https://doi.org/10.1016/j.jelechem.2010.05.020.
(265) Acuña-Cueva, E. R.; Faure, R.; Illán-Cabeza, N. A.; Jiménez-Pulido, S. B.; Moreno-Carretero, M. N.; Quirós-Olozábal, M. Synthesis and Characterization of New Complexes Formed between 1-Methyllumazine and 1,6,7-Trimethyllumazine Ligand with Transition Metal(II) Nitrate. Crystal Structure of Cobalt(II), Copper(II) and Cadmium(II) Complexes. *Inorganica Chim. Acta* **2003**, *342*, 209–218. https://doi.org/10.1016/S0020-1693(02)01165-9.
(266) Moreno-Vivián, C.; Cabello, P.; Martínez-Luque, M.; Blasco, R.; Castillo, F. Prokaryotic Nitrate Reduction: Molecular Properties and Functional Distinction among Bacterial Nitrate Reductases. *J. Bacteriol.* **1999**, *181* (21), 6573–6584. https://doi.org/10.1128/JB.181.21.6573-6584.1999.
(267) Richardson, D. J.; Watmough, N. J. Inorganic Nitrogen Metabolism in Bacteria. *Curr. Opin. Chem. Biol.* **1999**, *3* (2), 207–219. https://doi.org/10.1016/S1367-5931(99)80034-9.

(268) Picciano, A. L.; Crane, B. R. A Nitric Oxide Synthase-like Protein from Synechococcus Produces NO/NO3- from l-Arginine and NADPH in a Tetrahydrobiopterin- and Ca2+-Dependent Manner. *J. Biol. Chem.* **2019**, *294* (27), 10708–10719. https://doi.org/10.1074/jbc.RA119.008399.
(269) Andrew, P. Enzymatic Function of Nitric Oxide Synthases. *Cardiovasc. Res.* **1999**, *43* (3), 521–531. https://doi.org/10.1016/S0008-6363(99)00115-7.
(270) Picciano, A. L.; Crane, B. R. A Nitric Oxide Synthase–like Protein from Synechococcus Produces NO/NO3− from l-Arginine and NAPDH in a Tetrahydrobiopterin- and Ca2+-Dependent Manner. *J. Biol. Chem.* **2019**, *294* (27), 10708–10719. https://doi.org/10.1074/jbc.RA119.008399.
(271) Correa-Aragunde, N.; Foresi, N.; Del Castello, F.; Lamattina, L. A Singular Nitric Oxide Synthase with a Globin Domain Found in Synechococcus PCC 7335 Mobilizes N from Arginine to Nitrate. *Sci. Rep.* **2018**, *8* (1), 12505. https://doi.org/10.1038/s41598-018-30889-6.
(272) Forrest, H. S.; Van Baalen, C.; Myers, J. Occurrence of Pteridines in a Blue-Green Alga. *Science* **1957**, *125* (3250), 699–700. https://doi.org/10.1126/science.125.3250.699.
(273) Forrest, H. S.; Van Baalen, C.; Myers, J. Isolation and Identification of a New Pteridine from a Blue-Green Alga. *Arch. Biochem. Biophys.* **1958**, *78* (1), 95–99. https://doi.org/10.1016/0003-9861(58)90317-5.
(274) Lee, H. W.; Oh, C. H.; Geyer, A.; Pfleiderer, W.; Park, Y. S. Characterization of a Novel Unconjugated Pteridine Glycoside, Cyanopterin, in Synechocystis Sp. PCC 6803. *Biochim. Biophys. Acta BBA - Bioenerg.* **1999**, *1410* (1), 61–70. https://doi.org/10.1016/S0005-2728(98)00175-3.
(275) Forrest, H. S.; Baalen, C. V. Microbiology of Unconjugated Pteridines. *Annu. Rev. Microbiol.* **1970**, *24* (1), 91–108. https://doi.org/10.1146/annurev.mi.24.100170.000515.
(276) Kobayashi, K.; Forrest, H. S. Isolation and Identification of a New Pteridine, Neopterinyl-3′-β-d-Glucuronic Acid from Bacillus Subtilis. *Comp. Biochem. Physiol.* **1970**, *33* (1), 201–207. https://doi.org/10.1016/0010-406X(70)90495-0.
(277) Goto, M.; Kobayashi, K.; Sato, H.; Korte, F. Ein Neues Pteridin Aus Mycobacterium Smegmatis. *Justus Liebigs Ann. Chem.* **1965**, *689* (1), 221–228. https://doi.org/10.1002/jlac.19656890126.
(278) Moon, Y.-J.; Lee, E.-M.; Park, Y. M.; Park, Y. S.; Chung, W.-I.; Chung, Y.-H. The Role of Cyanopterin in UV/Blue Light Signal Transduction of Cyanobacterium Synechocystis Sp. PCC 6803 Phototaxis. *Plant Cell Physiol.* **2010**, *51* (6), 969–980. https://doi.org/10.1093/pcp/pcq059.
(279) Lee, H. W.; Oh, C. H.; Geyer, A.; Pfleiderer, W.; Park, Y. S. Characterization of a Novel Unconjugated Pteridine Glycoside, Cyanopterin, in Synechocystis Sp. PCC 6803. *Biochim. Biophys. Acta BBA - Bioenerg.* **1999**, *1410* (1), 61–70. https://doi.org/10.1016/S0005-2728(98)00175-3.
(280) Hwang, Y. K.; Kang, J. Y.; Woo, H. J.; Choi, Y. K.; Park, Y. S. Functional Investigation of a Gene Encoding Pteridine Glycosyltransferase for Cyanopterin Synthesis in Synechocystis Sp. PCC 6803. *Biochim. Biophys. Acta BBA - Gen. Subj.* **2002**, *1570* (2), 141–144. https://doi.org/10.1016/S0304-4165(02)00156-3.
(281) Van Den Hondel, C. A.; Verbeek, S.; Van Der Ende, A.; Weisbeek, P. J.; Borrias, W. E.; Van Arkel, G. A. Introduction of Transposon Tn901 into a Plasmid of Anacystis Nidulans: Preparation for Cloning in Cyanobacteria. *Proc. Natl. Acad. Sci.* **1980**, *77* (3), 1570–1574. https://doi.org/10.1073/pnas.77.3.1570.

(282) Bertani, G. STUDIES ON LYSOGENESIS I: The Mode of Phage Liberation by Lysogenic Escherichia Coli. *J. Bacteriol.* **1951**, *62* (3), 293–300. https://doi.org/10.1128/jb.62.3.293-300.1951.

(283) Chung, C. T.; Niemela, S. L.; Miller, R. H. One-Step Preparation of Competent Escherichia Coli: Transformation and Storage of Bacterial Cells in the Same Solution. *Proc. Natl. Acad. Sci.* **1989**, *86* (7), 2172–2175. https://doi.org/10.1073/pnas.86.7.2172.

(284) Gibson, D. G.; Young, L.; Chuang, R.-Y.; Venter, J. C.; Hutchison, C. A.; Smith, H. O. Enzymatic Assembly of DNA Molecules up to Several Hundred Kilobases. *Nat. Methods* **2009**, *6* (5), 343–345. https://doi.org/10.1038/nmeth.1318.

(285) Reher, R.; Aron, A. T.; Fajtová, P.; Stincone, P.; Wagner, B.; Pérez-Lorente, A. I.; Liu, C.; Shalom, I. Y. B.; Bittremieux, W.; Wang, M.; Jeong, K.; Matos-Hernandez, M. L.; Alexander, K. L.; Caro-Diaz, E. J.; Naman, C. B.; Scanlan, J. H. W.; Hochban, P. M. M.; Diederich, W. E.; Molina-Santiago, C.; Romero, D.; Selim, K. A.; Sass, P.; Brötz-Oesterhelt, H.; Hughes, C. C.; Dorrestein, P. C.; O'Donoghue, A. J.; Gerwick, W. H.; Petras, D. Native Metabolomics Identifies the Rivulariapeptolide Family of Protease Inhibitors. *Nat. Commun.* **2022**, *13* (1), 4619. https://doi.org/10.1038/s41467-022-32016-6.

(286) Zuffa, S.; Schmid, R.; Bauermeister, A.; P. Gomes, P. W.; Caraballo-Rodriguez, A. M.; El Abiead, Y.; Aron, A. T.; Gentry, E. C.; Zemlin, J.; Meehan, M. J.; Avalon, N. E.; Cichewicz, R. H.; Buzun, E.; Terrazas, M. C.; Hsu, C.-Y.; Oles, R.; Ayala, A. V.; Zhao, J.; Chu, H.; Kuijpers, M. C. M.; Jackrel, S. L.; Tugizimana, F.; Nephali, L. P.; Dubery, I. A.; Madala, N. E.; Moreira, E. A.; Costa-Lotufo, L. V.; Lopes, N. P.; Rezende-Teixeira, P.; Jimenez, P. C.; Rimal, B.; Patterson, A. D.; Traxler, M. F.; Pessotti, R. D. C.; Alvarado-Villalobos, D.; Tamayo-Castillo, G.; Chaverri, P.; Escudero-Leyva, E.; Quiros-Guerrero, L.-M.; Bory, A. J.; Joubert, J.; Rutz, A.; Wolfender, J.-L.; Allard, P.-M.; Sichert, A.; Pontrelli, S.; Pullman, B. S.; Bandeira, N.; Gerwick, W. H.; Gindro, K.; Massana-Codina, J.; Wagner, B. C.; Forchhammer, K.; Petras, D.; Aiosa, N.; Garg, N.; Liebeke, M.; Bourceau, P.; Kang, K. B.; Gadhavi, H.; De Carvalho, L. P. S.; Silva Dos Santos, M.; Pérez-Lorente, A. I.; Molina-Santiago, C.; Romero, D.; Franke, R.; Brönstrup, M.; Vera Ponce De León, A.; Pope, P. B.; La Rosa, S. L.; La Barbera, G.; Roager, H. M.; Laursen, M. F.; Hammerle, F.; Siewert, B.; Peintner, U.; Licona-Cassani, C.; Rodriguez-Orduña, L.; Rampler, E.; Hildebrand, F.; Koellensperger, G.; Schoeny, H.; Hohenwallner, K.; Panzenboeck, L.; Gregor, R.; O'Neill, E. C.; Roxborough, E. T.; Odoi, J.; Bale, N. J.; Ding, S.; Sinninghe Damsté, J. S.; Guan, X. L.; Cui, J. J.; Ju, K.-S.; Silva, D. B.; Silva, F. M. R.; Da Silva, G. F.; Koolen, H. H. F.; Grundmann, C.; Clement, J. A.; Mohimani, H.; Broders, K.; McPhail, K. L.; Ober-Singleton, S. E.; Rath, C. M.; McDonald, D.; Knight, R.; Wang, M.; Dorrestein, P. C. microbeMASST: A Taxonomically Informed Mass Spectrometry Search Tool for Microbial Metabolomics Data. *Nat. Microbiol.* **2024**, *9* (2), 336–345. https://doi.org/10.1038/s41564-023-01575-9.

(287) Sánchez-Baracaldo, P.; Bianchini, G.; Wilson, J. D.; Knoll, A. H. Cyanobacteria and Biogeochemical Cycles through Earth History. *Trends Microbiol.* **2022**, *30* (2), 143–157. https://doi.org/10.1016/j.tim.2021.05.008.

(288) Dittmann, E.; Gugger, M.; Sivonen, K.; Fewer, D. P. Natural Product Biosynthetic Diversity and Comparative Genomics of the Cyanobacteria. *Trends Microbiol.* **2015**, *23* (10), 642–652. https://doi.org/10.1016/j.tim.2015.07.008.

(289) Nawaz, T.; Gu, L.; Fahad, S.; Saud, S.; Jiang, Z.; Hassan, S.; Harrison, M. T.; Liu, K.; Khan, M. A.; Liu, H.; El-Kahtany, K.; Wu, C.; Zhu, M.; Zhou, R. A Comprehensive Review of the Therapeutic Potential of Cyanobacterial Marine Bioactives: Unveiling

the Hidden Treasures of the Sea. *Food Energy Secur.* **2023**, *12* (5), e495. https://doi.org/10.1002/fes3.495.

(290) Sánchez, K. F.; von Elert, E.; Monell, K.; Calhoun, S.; Maisha, A.; McCreadie, P.; Duffy, M. A. Inhibition of Gut Digestive Proteases by Cyanobacterial Diets Decreases Infection in a Daphnia Host-Parasite System. *Ecol. Evol.* **2024**, *14* (4), e11340. https://doi.org/10.1002/ece3.11340.

(291) Rohrlack, T.; Christoffersen, K.; Kaebernick, M.; Neilan, B. A. Cyanobacterial Protease Inhibitor Microviridin J Causes a Lethal Molting Disruption in Daphnia Pulicaria. *Appl. Environ. Microbiol.* **2004**, *70* (8), 5047–5050. https://doi.org/10.1128/AEM.70.8.5047-5050.2004.

(292) Tan, L. T.; Phyo, M. Y. Marine Cyanobacteria: A Source of Lead Compounds and Their Clinically-Relevant Molecular Targets. *Mol. Basel Switz.* **2020**, *25* (9), 2197. https://doi.org/10.3390/molecules25092197.

(293) Gallegos, D. A.; Saurí, J.; Cohen, R. D.; Wan, X.; Videau, P.; Vallota-Eastman, A. O.; Shaala, L. A.; Youssef, D. T. A.; Williamson, R. T.; Martin, G. E.; Philmus, B.; Sikora, A. E.; Ishmael, J. E.; McPhail, K. L. Jizanpeptins, Cyanobacterial Protease Inhibitors from a Symploca Sp. Cyanobacterium Collected in the Red Sea. *J. Nat. Prod.* **2018**, *81* (6), 1417–1425. https://doi.org/10.1021/acs.jnatprod.8b00117.

(294) Klein, T.; Eckhard, U.; Dufour, A.; Solis, N.; Overall, C. M. Proteolytic Cleavage—Mechanisms, Function, and "Omic" Approaches for a Near-Ubiquitous Posttranslational Modification. *Chem. Rev.* **2018**, *118* (3), 1137–1168. https://doi.org/10.1021/acs.chemrev.7b00120.

(295) Cottrell, G. S. Roles of Proteolysis in Regulation of GPCR Function. *Br. J. Pharmacol.* **2013**, *168* (3), 576–590. https://doi.org/10.1111/j.1476-5381.2012.02234.x.

(296) Papadopoulou, A. A.; Fluhrer, R. Signaling Functions of Intramembrane Aspartyl-Proteases. *Front. Cardiovasc. Med.* **2020**, *7*, 591787. https://doi.org/10.3389/fcvm.2020.591787.

(297) Fortelny, N.; Cox, J. H.; Kappelhoff, R.; Starr, A. E.; Lange, P. F.; Pavlidis, P.; Overall, C. M. Network Analyses Reveal Pervasive Functional Regulation Between Proteases in the Human Protease Web. *PLoS Biol.* **2014**, *12* (5), e1001869. https://doi.org/10.1371/journal.pbio.1001869.

(298) Wolf, D. H.; Menssen, R. Mechanisms of Cell Regulation – Proteolysis, the Big Surprise. *FEBS Lett.* **2018**, *592* (15), 2515–2524. https://doi.org/10.1002/1873-3468.13109.

(299) Boon, L.; Ugarte-Berzal, E.; Vandooren, J.; Opdenakker, G. Protease Propeptide Structures, Mechanisms of Activation, and Functions. *Crit. Rev. Biochem. Mol. Biol.* **2020**, *55* (2), 111–165. https://doi.org/10.1080/10409238.2020.1742090.

(300) Heutinck, K. M.; Ten Berge, I. J. M.; Hack, C. E.; Hamann, J.; Rowshani, A. T. Serine Proteases of the Human Immune System in Health and Disease. *Mol. Immunol.* **2010**, *47* (11–12), 1943–1955. https://doi.org/10.1016/j.molimm.2010.04.020.

(301) Solary, E.; Eymin, B.; Droin, N.; Haugg, M. [No Title Found]. *Cell Biol. Toxicol.* **1998**, *14* (2), 121–132. https://doi.org/10.1023/A:1007481921502.

(302) Goldberg, A. L. Protein Degradation and Protection against Misfolded or Damaged Proteins. *Nature* **2003**, *426* (6968), 895–899. https://doi.org/10.1038/nature02263.

(303) Turk, B. Targeting Proteases: Successes, Failures and Future Prospects. *Nat. Rev. Drug Discov.* **2006**, *5* (9), 785–799. https://doi.org/10.1038/nrd2092.

(304) Apoorva, O. S.; Shukla, K.; Khurana, A.; Chaudhary, N. Proteases: Role in Various Human Diseases. *Curr. Pharm. Biotechnol.* **2024**, *26*. https://doi.org/10.2174/0113892010316162240910103659.

(305) Abbenante, G.; Fairlie, D. Protease Inhibitors in the Clinic. *Med. Chem.* **2005**, *1* (1), 71–104. https://doi.org/10.2174/1573406053402569.

(306) Neurath, H. Evolution of Proteolytic Enzymes. *Science* **1984**, *224* (4647), 350–357. https://doi.org/10.1126/science.6369538.
(307) Cotten, S. W. Evaluation of Exocrine Pancreatic Function. In *Contemporary Practice in Clinical Chemistry*; Elsevier, 2020; pp 573–585. https://doi.org/10.1016/B978-0-12-815499-1.00033-8.
(308) Morrison, H. Chymotrypsin. In *Enzyme Active Sites and their Reaction Mechanisms*; Elsevier, 2021; pp 41–44. https://doi.org/10.1016/B978-0-12-821067-3.00009-X.
(309) Al-Moraissi, E. A.; Al-Zendani, E. A.; Al-Selwi, A. M. Efficacy of Submucosal Injection of Chymotrypsin, Oral Serratiopeptidase or Oral Dexamethasone in Reducing Postoperative Complications Following Impacted Lower Third Molar Surgery: A Prospective, Randomized, Double-Blind, Controlled Clinical Trial. *Front. Oral Health* **2020**, *1*, 575176. https://doi.org/10.3389/froh.2020.575176.
(310) Szmola, R.; Sahin-Toth, M. Pancreatitis-Associated Chymotrypsinogen C (CTRC) Mutant Elicits Endoplasmic Reticulum Stress in Pancreatic Acinar Cells. *Gut* **2010**, *59* (3), 365–372. https://doi.org/10.1136/gut.2009.198903.
(311) Zhou, J.; Sahin-Tóth, M. Chymotrypsin C Mutations in Chronic Pancreatitis. *J. Gastroenterol. Hepatol.* **2011**, *26* (8), 1238–1246. https://doi.org/10.1111/j.1440-1746.2011.06791.x.
(312) Jura, N.; Archer, H.; Bar-Sagi, D. Chronic Pancreatitis, Pancreatic Adenocarcinoma and the Black Box in-Between. *Cell Res.* **2005**, *15* (1), 72–77. https://doi.org/10.1038/sj.cr.7290269.
(313) Radisky, E. S. Extracellular Proteolysis in Cancer: Proteases, Substrates, and Mechanisms in Tumor Progression and Metastasis. *J. Biol. Chem.* **2024**, *300* (6), 107347. https://doi.org/10.1016/j.jbc.2024.107347.
(314) Koivunen, E.; Ristimäki, A.; Itkonen, O.; Osman, S.; Vuento, M.; Stenman, U. H. Tumor-Associated Trypsin Participates in Cancer Cell-Mediated Degradation of Extracellular Matrix. *Cancer Res.* **1991**, *51* (8), 2107–2112.
(315) Wessler, S.; Schneider, G.; Backert, S. Bacterial Serine Protease HtrA as a Promising New Target for Antimicrobial Therapy? *Cell Commun. Signal.* **2017**, *15* (1), 4, s12964-017-0162–0165. https://doi.org/10.1186/s12964-017-0162-5.
(316) Rosendal, E.; Mihai, I. S.; Becker, M.; Das, D.; Frängsmyr, L.; Persson, B. D.; Rankin, G. D.; Gröning, R.; Trygg, J.; Forsell, M.; Ankarklev, J.; Blomberg, A.; Henriksson, J.; Överby, A. K.; Lenman, A. Serine Protease Inhibitors Restrict Host Susceptibility to SARS-CoV-2 Infections. *mBio* **2022**, *13* (3), e0089222. https://doi.org/10.1128/mbio.00892-22.
(317) Al Adem, K.; Ferreira, J. C.; Villanueva, A. J.; Fadl, S.; El-Sadaany, F.; Masmoudi, I.; Gidiya, Y.; Gurudza, T.; Cardoso, T. H. S.; Saksena, N. K.; Rabeh, W. M. 3-Chymotrypsin-like Protease in SARS-CoV-2. *Biosci. Rep.* **2024**, *44* (8), BSR20231395. https://doi.org/10.1042/BSR20231395.
(318) Kim, Y.; Lovell, S.; Tiew, K.-C.; Mandadapu, S. R.; Alliston, K. R.; Battaile, K. P.; Groutas, W. C.; Chang, K.-O. Broad-Spectrum Antivirals against 3C or 3C-like Proteases of Picornaviruses, Noroviruses, and Coronaviruses. *J. Virol.* **2012**, *86* (21), 11754–11762. https://doi.org/10.1128/JVI.01348-12.
(319) Jin, Z.; Du, X.; Xu, Y.; Deng, Y.; Liu, M.; Zhao, Y.; Zhang, B.; Li, X.; Zhang, L.; Peng, C.; Duan, Y.; Yu, J.; Wang, L.; Yang, K.; Liu, F.; Jiang, R.; Yang, X.; You, T.; Liu, X.; Yang, X.; Bai, F.; Liu, H.; Liu, X.; Guddat, L. W.; Xu, W.; Xiao, G.; Qin, C.; Shi, Z.; Jiang, H.; Rao, Z.; Yang, H. Structure of Mpro from SARS-CoV-2 and Discovery of Its Inhibitors. *Nature* **2020**, *582* (7811), 289–293. https://doi.org/10.1038/s41586-020-2223-y.
(320) Okino, T.; Murakami, M.; Haraguchi, R.; Munekata, H.; Matsuda, H.; Yamaguchi, K. Micropeptins A and B, Plasmin and Trypsin Inhibitors from the Blue-Green Alga

Microcystis Aeruginosa. *Tetrahedron Lett.* **1993**, *34* (50), 8131–8134. https://doi.org/10.1016/S0040-4039(00)61471-5.

(321) Ishida, K.; Murakami, M.; Matsuda, H.; Yamaguchi, K. Micropeptin 90, a Plasmin and Trypsin Inhibitor from the Blue-Green Alga Microcystis Aeruginosa (NIES-90). *Tetrahedron Lett.* **1995**, *36* (20), 3535–3538. https://doi.org/10.1016/0040-4039(95)00547-P.

(322) Monteiro, P. R.; do Amaral, S. C.; Siqueira, A. S.; Xavier, L. P.; Santos, A. V. Anabaenopeptins: What We Know So Far. *Toxins* **2021**, *13* (8), 522. https://doi.org/10.3390/toxins13080522.

(323) Harada, K.; Fujii, K.; Shimada, T.; Suzuki, M.; Sano, H.; Adachi, K.; Carmichael, W. W. Two Cyclic Peptides, Anabaenopeptins, a Third Group of Bioactive Compounds from the cyanobacteriumAnabaena Flos-Aquae NRC 525-17. *Tetrahedron Lett.* **1995**, *36* (9), 1511–1514. https://doi.org/10.1016/0040-4039(95)00073-L.

(324) Murakami, M.; Okita, Y.; Matsuda, H.; Okino, T.; Yamaguchi, K. Aeruginosin 298-A, a Thrombin and Trypsin Inhibitor from the Blue-Green Alga Microcystis Aeruginosa (NIES-298). *Tetrahedron Lett.* **1994**, *35* (19), 3129–3132. https://doi.org/10.1016/S0040-4039(00)76848-1.

(325) Adiv, S.; Carmeli, S. Protease Inhibitors from *Microcystis Aeruginosa* Bloom Material Collected from the Dalton Reservoir, Israel. *J. Nat. Prod.* **2013**, *76* (12), 2307–2315. https://doi.org/10.1021/np4006844.

(326) Liu, J.; Zhang, M.; Huang, Z.; Fang, J.; Wang, Z.; Zhou, C.; Qiu, X. Diversity, Biosynthesis and Bioactivity of Aeruginosins, a Family of Cyanobacteria-Derived Nonribosomal Linear Tetrapeptides. *Mar. Drugs* **2023**, *21* (4), 217. https://doi.org/10.3390/md21040217.

(327) Ishida, K.; Kato, T.; Murakami, M.; Watanabe, M.; Watanabe, M. F. Microginins, Zinc Metalloproteases Inhibitors from the Cyanobacterium Microcystis Aeruginosa. *Tetrahedron* **2000**, *56* (44), 8643–8656. https://doi.org/10.1016/S0040-4020(00)00770-5.

(328) Reshef, V.; Carmeli, S. New Microviridins from a Water Bloom of the Cyanobacterium Microcystis Aeruginosa. *Tetrahedron* **2006**, *62* (31), 7361–7369. https://doi.org/10.1016/j.tet.2006.05.028.

(329) do Amaral, S. C.; Monteiro, P. R.; Neto, J. da S. P.; Serra, G. M.; Gonçalves, E. C.; Xavier, L. P.; Santos, A. V. Current Knowledge on Microviridin from Cyanobacteria. *Mar. Drugs* **2021**, *19* (1), 17. https://doi.org/10.3390/md19010017.

(330) Rippka, R.; Herdman, M.; Waterbury, J. B. Generic Assignments, Strain Histories and Properties of Pure Cultures of Cyanobacteria. *Microbiology* **1979**, *111* (1), 1–61. https://doi.org/10.1099/00221287-111-1-1.

(331) Marty, M. T.; Baldwin, A. J.; Marklund, E. G.; Hochberg, G. K. A.; Benesch, J. L. P.; Robinson, C. V. Bayesian Deconvolution of Mass and Ion Mobility Spectra: From Binary Interactions to Polydisperse Ensembles. *Anal. Chem.* **2015**, *87* (8), 4370–4376. https://doi.org/10.1021/acs.analchem.5b00140.

9 Appendix: Proteaseinhibitors in Cyanobacteria

This chapter is based on an additional project and a manuscript in preparation which presents a follow-up study building on the knowledge gained from previous projects detailed in the manuscripts "Native Metabolomics Identifies the Rivulariapeptolide Family of Protease Inhibitors"[285] and "microbeMASST: A Taxonomically Informed Mass Spectrometry Search Tool for Microbial Metabolomics Data"[286]. The references cited in the manuscript have been incorporated into the main reference list of this thesis and adjusted to follow the sequential numbering of the thesis-wide bibliography (section 8, p.131ff).

Native Metabolomics-Based Profiling of Serine Protease Inhibitors Across 20 Cyanobacterial Strains

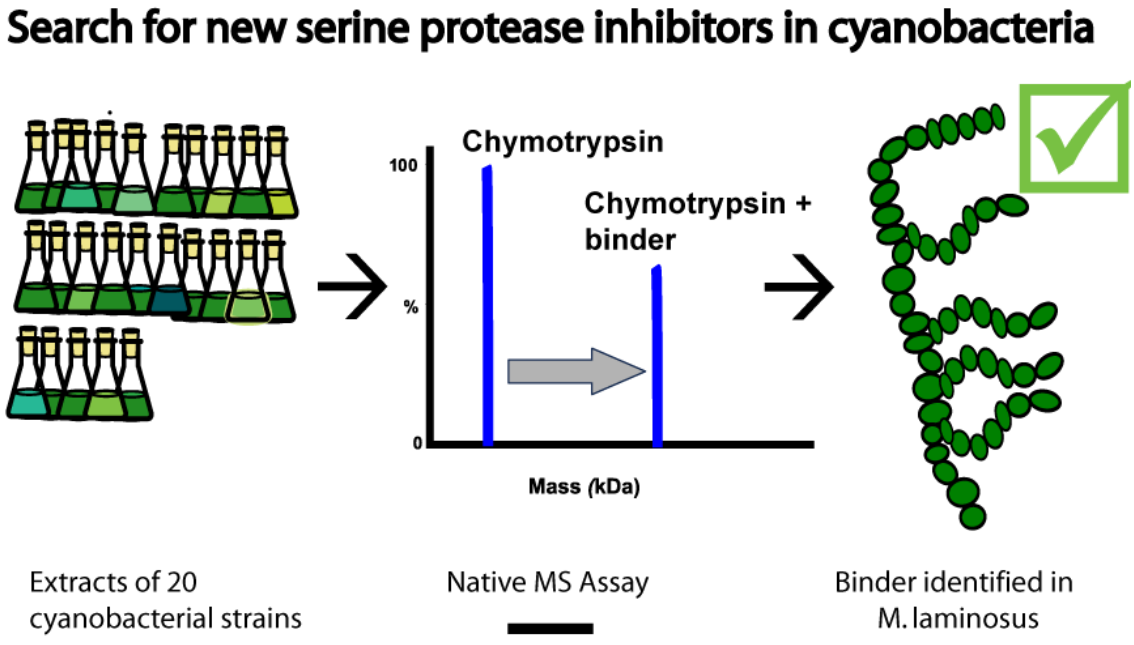

9.1 Abstract

In our previous study (*Native metabolomics identifies the rivulariapeptolide family of protease inhibitors*, *Nature Communications*, 2022), we employed a native metabolomics

approach combining native mass spectrometry (MS) with untargeted metabolomics to identify chymotrypsin-binding metabolites directly from complex cyanobacterial extracts. This high-throughput method enabled the detection of non-covalent protein-ligand interactions, leading to the discovery of the rivulariapeptolide family of protease inhibitors from an environmental cyanobacterial community.

Building on these findings, we conducted a follow-up study where we systematically screened intracellular and extracellular metabolites of 20 different laboratory cyanobacterial strains, representing marine, terrestrial, and freshwater environments, and covering the five orders of cyanobacteria: *Chroococcales*, *Pleurocapsales*, *Oscillatoriales*, *Nostocales*, and *Stigonematales*, for unknown chymotrypsin-binding metabolites using the same workflow. By extracting metabolites from supernatants and cell pellets on axenic cultures and analyzing the samples via native metabolomics, we aimed to detect species-specific, intact protein-ligand complexes and expand the known repertoire of cyanobacterial protease inhibitors.

This study provides further insights into the diversity and distribution of bioactive metabolites in cyanobacteria and their potential as a source of protease inhibitors. Due to their minimal growth requirements, needing only light, water, and basic salts, cyanobacteria represent a cost-effective and sustainable platform to produce protease inhibitors.

9.2 Introduction: Cyanobacteria and Proteinase Inhibitors

Cyanobacteria are photosynthetic prokaryotes that play a central role in global biogeochemical cycles, particularly through their contributions to oxygenic photosynthesis and biological carbon and nitrogen fixation[287]. Beyond their ecological significance, they are prolific producers of structurally diverse bioactive secondary metabolites, including cyanotoxins, antimicrobial peptides, antitumor compounds, herbicidal agents, and other molecules with pharmaceutical and biotechnological potential[288,289]. Among these metabolites, cyanobacterial protease inhibitors have attracted considerable attention due to their contribution to cellular survival and ecological competitiveness[290–293].

Protases catalyze the hydrolytic cleavage of peptide bonds within polypeptides, generating smaller peptide fragments. Far from being merely degradative enzymes, they are indispensable across all domains of life, orchestrating a wide array of physiological processes[294]. They regulate protein localization and function by generating bioactive peptides, modulating signal transduction pathways, and governing protein-protein interactions[295–297].

Proteases play pivotal roles in protein turnover[298], the maturation and activation of precursor proteins[299], immune responses[300], apoptosis[301], and the degradation of damaged or misfolded proteins[302].

Dysregulated protease activity is implicated in the pathogenesis of various human diseases, including cancer, inflammatory disorders, and neurodegenerative conditions[303,304]. Protease inhibitors mitigate these effects by binding to the active sites of proteases, thereby blocking their catalytic functions[305]. Based on their mechanisms of inhibition, protease inhibitors are categorized into several classes, including serine, cysteine, and metalloprotease inhibitors.

In this study, we investigated the inhibitory potential of cyanobacterial extracts against chymotrypsin, a well-characterized serine protease[306]. Chymotrypsin is synthesized in the pancreas as the inactive precursor chymotrypsinogen and is activated by trypsin-mediated cleavage. It plays a central role in protein digestion by hydrolyzing peptide bonds adjacent to aromatic amino acids[307]. Catalysis is mediated by a conserved catalytic triad composed of Ser195, His57, and Asp102, which facilitates a nucleophilic attack on the peptide backbone[308]. Clinically, chymotrypsin is used in enzyme replacement therapies for pancreatic insufficiency and in reducing postoperative inflammation[309]. Dysregulated chymotrypsin activity can contribute to chronic pancreatitis, a condition marked by inflammation and tissue damage[310,311], increasing the risk of pancreatic cancer[312]. As such, its inhibitors are of considerable therapeutic interest. Like other known protease inhibitors[313,314], these inhibitors may attenuate inflammation by reducing protease-mediated tissue damage and can potentially limit tumor invasion and metastasis. Furthermore, serin protease inhibitors are also being explored as antimicrobial agents, capable of neutralizing proteases secreted by pathogenic bacteria and viruses[315,316].

Chymotrypsin-like proteases (CLPs) extend beyond digestive physiology and are also found in viral systems. Notably, the SARS-CoV-2 main protease (M^{pro}), although a cysteine protease, exhibits a chymotrypsin-like fold and is essential for processing viral polyproteins during replication[317–319].

Cyanobacteria are recognized as a rich source of protease inhibitors with both ecological and biotechnological implications[288,292]. Several taxa, particularly those within the orders *Oscillatoriales* and *Nostocales*, are known for producing structurally diverse inhibitors. In their natural habitats, these compounds act as chemical defenses against grazers, microbial competitors, and pathogens, thereby enhancing the survival and ecological competitiveness

of the producing organisms. Some cyanobacterial protease inhibitors also exhibit pharmacological activities, such as antimicrobial, antiviral, and anticancer effects, making them attractive candidates for drug discovery. Based on their structural features and biosynthetic origins, cyanobacterial protease inhibitors are classified into five major families: micropeptins (cyclic depsipeptides primarily targeting chymotrypsin-like serine proteases)[320,321], anabaenopeptins (cyclic hexapeptides known to inhibit proteases, phosphatases, and carboxypeptidases)[322,323], aeruginosins (linear tetrapeptides with thrombin- and trypsin-inhibitory activity) [324–326] , microginins (linear peptides a characteristic decanoic acid-derived amino acid residue)[327], and microviridins (highly modified cyclic peptides that selectively inhibit serin-protreases like chymotrypsin, elastase, trypsin, thrombin and the oxidoreductase tyrosinase)[328,329]. These compounds frequently target serine proteases and are commonly detected in cyanobacterial blooms, where they contribute to bloom toxicity.

The diverse array of protease inhibitors produced by cyanobacteria holds promise for applications in both biotechnology and pharmaceuticals. These inhibitors could serve as lead compounds for drugs targeting proteases involved in diseases like HIV/AIDS and cancer. Additionally, the antimicrobial properties of cyanobacterial protease inhibitors suggest potential uses in natural pest control and food preservation.

9.3 Results

We cultivated 20 laboratory cyanobacterial strains under standardized growth conditions. An overview of the strains and their classification into taxonomic sections, as defined by Rippka et. al[330]. is provided in Table 9.1.

Table 9.1: Overview of used strains and cyanobacterial sections.

Section Morphology & Key Features	Used Strains	NCBI Taxa
I (Chroococcales) Unicellular, non-colonial: spherical or ovoid cells, divide by binary fission in one plane, no filaments	*Synechococcus elongatus* PCC 7942	1140
	Synechococcus elongatus PCC 6301	269084
	Synechococcus sp. PCC 7502	1173263
	Synechocystis sp. PCC 6803	2930568
II (Pleurocapsales) Unicellular, colonial: multiple planes of division, reproduce via baeocytes (small daughter cells)	*Pleurocapsa* sp. PCC 7327	118163
	Stanieria cyanosphaera SAG 33.87	1519461
III (Oscillatoriales) Filamentous, non-Heterocystous: unbranched trichomes, no heterocysts, divide in one plane	*Oscillatoria acuminata* PCC 6304	56110
	Phormidesmis molle SAG 26.99	2578135
	Leptolyngbya boryana PCC 6306	272134
IV (Nostocales) Filamentous, heterocystous: unbranched trichomes with heterocysts for nitrogen fixation, may form akinetes	*Nostoc* sp. PCC 7120	103690
	Nostoc punctiforme PCC 73102 (also *Nostoc punctiforme* ATCC 29133)	63737
	Desmonostoc sp. PCC 7906 (also Nostoc muscorum)	1181
	Tolypothrix tenuis SAG 94.79	1521527
	Trichormus variabilis ATCC 29413/ also *Anabaena variabilis*	240292
	Calothrix sp. PCC 6303	1170562
	Nodularia sphaerocarpa PCC 7804	88830
	Scytonema hofmannii PCC 7110	128403
V (Stigonematales) Filamentous, heterocystous, branched: true branching, heterocysts for nitrogen fixation, most complex structure	*Fischerella muscicola* PCC 7414	306281
	Mastigocladus laminosus SAG 4.840	447715
	Chlorogloeopsis fritschii PCC 6912	2111

To investigate the distribution of metabolites across cellular and extracellular fractions, we performed solid phase extraction (SPE) on culture supernatants of 20 cyanobacterial strains spanning five taxonomic sections, and separately extracted metabolites from the corresponding cell pellets. All features (defined as distinct mass-retention time pairs representing putative metabolites) detected in the medium control were removed to ensure that only strain-derived metabolites were included. The resulting stacked bar plot (Figure 9.1) shows the number of detected features in each fraction. Notably, the majority of features were exclusive to either the supernatant or the pellet, with minimal overlap between the two, indicating a clear separation of metabolite pools and suggesting low levels of cell lysis during harvesting. More features were detected in the supernatant than in the cell pellet for most strains, pointing to a diverse and potentially strain-specific exo-metabolome among cyanobacteria.

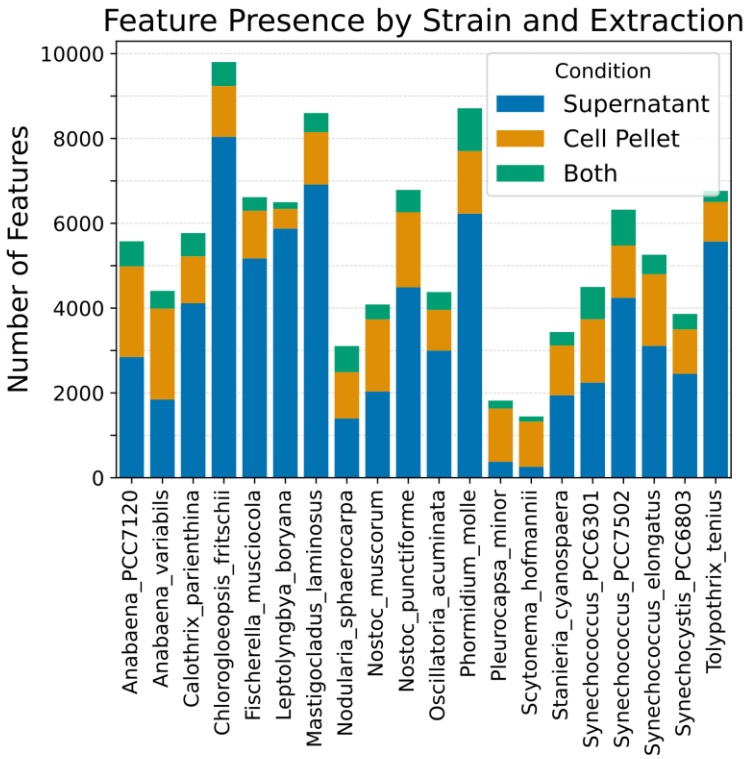

Figure 9.1: Distribution of detected metabolites in cell pellets and supernatants across cyanobacterial strains. Stacked bar plot showing the number of unique metabolite features detected in the supernatant (blue), the cell pellet (orange), or both (green) fractions for each of the 20 cyanobacterial strains analyzed. Metabolite features were defined as distinct mass-retention time pairs detected by LC-MS and filtered to exclude any features present in medium-only controls.

To rapidly screen for putative chymotrypsin inhibitors, we applied the native metabolomics workflow adapted from Reher *et al.* (2022)[285]. This method preserves the protein in its native state, maintaining its functional binding sites. Metabolite extracts from both cell pellets and

F

supernatants of 20 cyanobacterial strains, representing all five morphological sections, were analyzed individually. Each extract was separated by reversed-phase chromatography (C18), and chymotrypsin was continuously infused and mixed post-column with the eluting metabolites. Native mass spectra were deconvoluted, revealing the apo form of chymotrypsin at 25,449 ± 5 Da across all samples. Additional signals at higher molecular weights correspond to putative non-covalent chymotrypsin-ligand complexes. Mass shifts relative to the apo enzyme indicated the molecular weights of candidate ligands, while the retention times (RTs) of binding events provided additional information on their polarity and physicochemical properties. Figure 9.2 - Figure 9.5 summarize all observed mass shifts corresponding to putative chymotrypsin-binding metabolites, grouped by cyanobacterial section. We did not observe any binding events in strains of section III, Oscillatoriales. Therefore, they are not represented in the data.

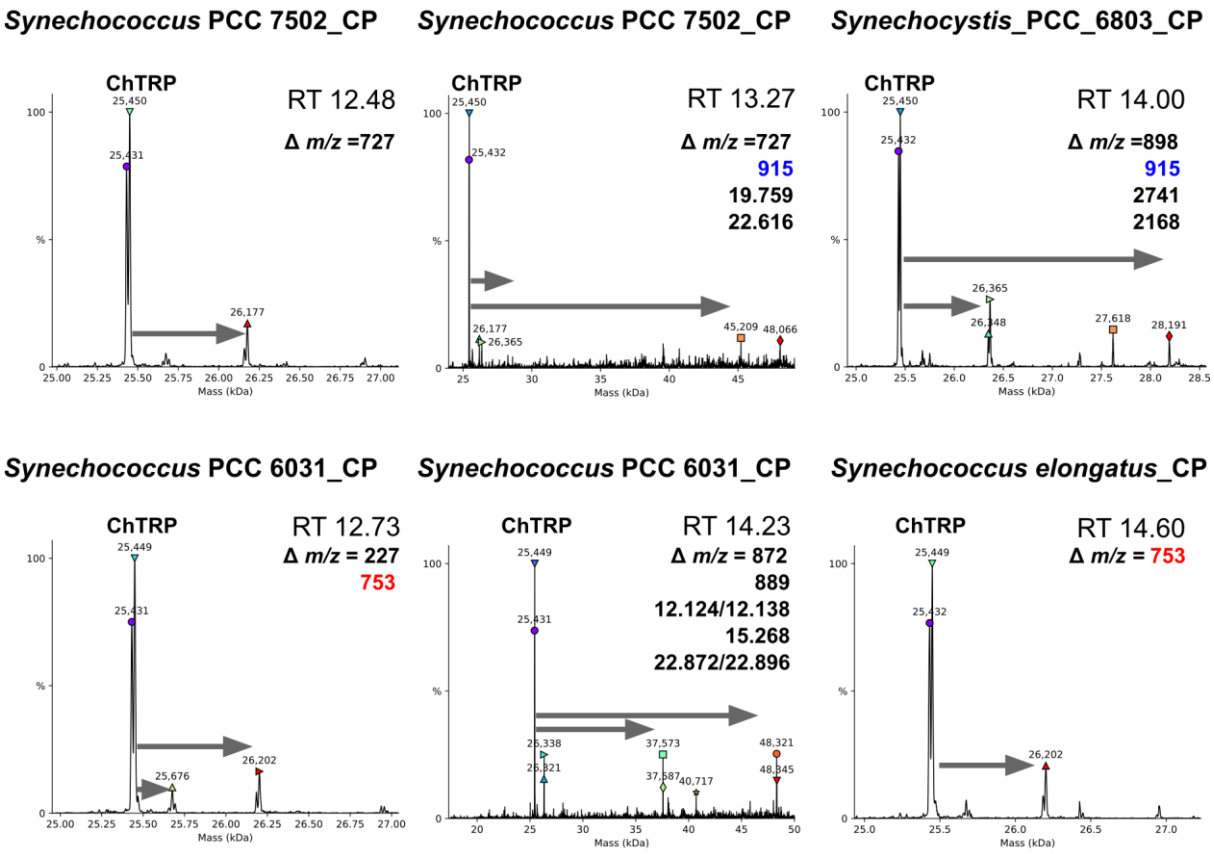

Figure 9.2: Deconvoluted native mass spectrometry spectra of chymotrypsin with extracts from strains of section I (Chroococcales). Strain names are indicated in the figure headers. The spectra show the apo-form of chymotrypsin (ChTRP, 25,449 ± 5 Da) and putative chymotrypsin-ligand complexes, which exhibit a shift to higher molecular weights. The mass differences, corresponding to the putative ligand *m/z* values, are indicated, alongside the retention times (RTs) of the binding events. Extracts from cell pellets (CP) and supernatants (SPE) were analyzed.

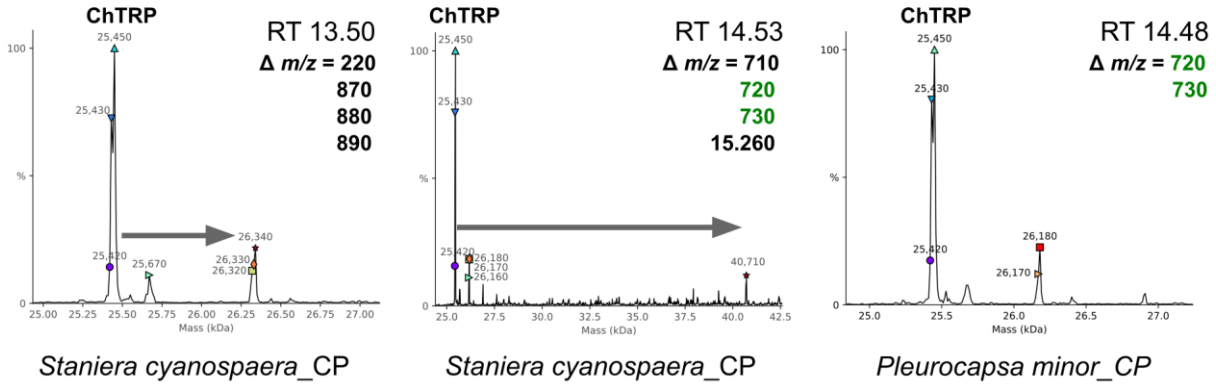

Figure 9.3: Deconvoluted native mass spectrometry spectra of chymotrypsin with extracts from strains of section II (Pleurocapsales). Strain names are indicated in the figure headers. The spectra show the apo-form of chymotrypsin (ChTRP, 25,449 ± 5 Da) and putative chymotrypsin-ligand complexes, which exhibit a shift to higher molecular weights. The mass differences, corresponding to the putative ligand *m/z* values, are indicated, (Δ*m/z*), alongside the retention times (RTs) of the binding events. Extracts from cell pellets (CP) and supernatants (SPE) were analyzed.

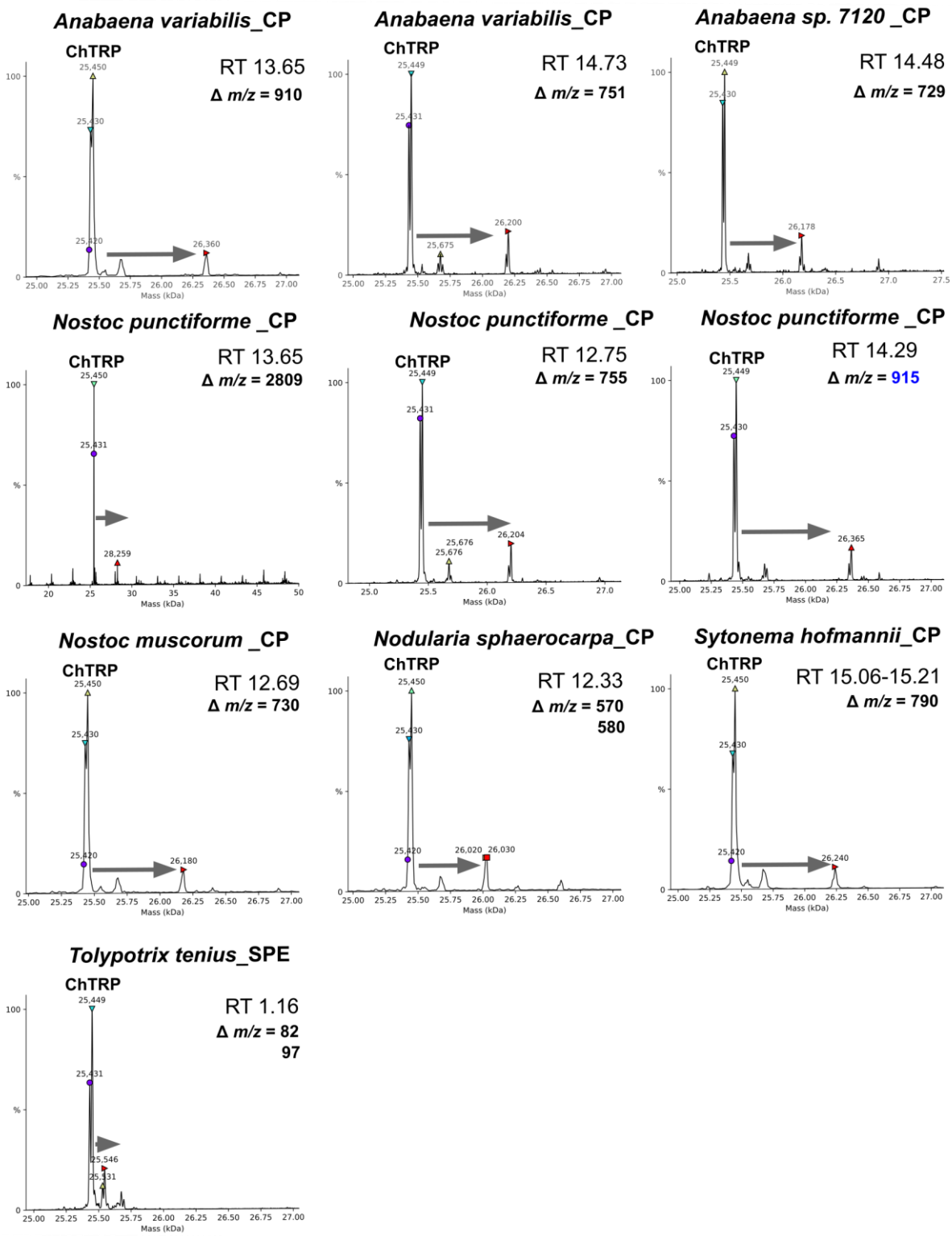

Figure 9.4: Deconvoluted native mass spectrometry spectra of chymotrypsin with extracts from strains of section IV (Nostocales). The strain names are indicated in the figure headers. The spectra show the apo-form of chymotrypsin (ChTRP, 25,449 ± 5 Da) and putative chymotrypsin-ligand complexes, which exhibit a shift to higher molecular weights. The mass differences, corresponding to the putative ligand *m/z* values, are indicated, *(Δm/z),* alongside the retention times (RTs) of the binding events. Extracts from cell pellets (CP) and supernatants (SPE) were analyzed.

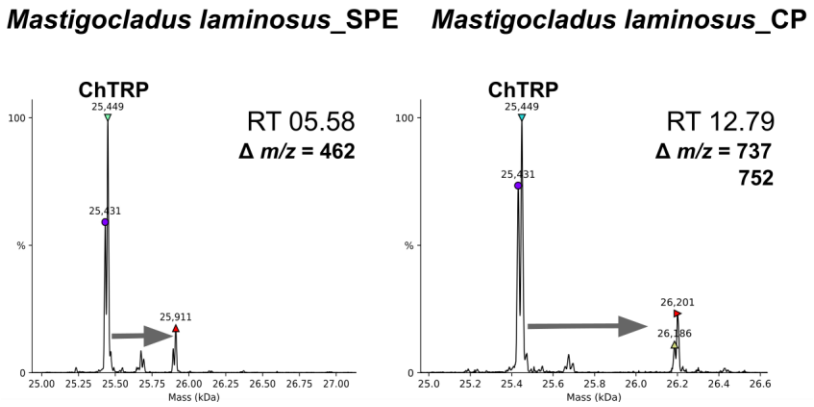

Figure 9.5: Deconvoluted native mass spectrometry spectra of chymotrypsin with extracts from strains of section V (Stigonematales). The strain names are indicated in the figure headers. The spectra show the apo-form of chymotrypsin (ChTRP, 25,449 ± 5 Da) and putative chymotrypsin-ligand complexes, which exhibit a shift to higher molecular weights. The mass differences, corresponding to the putative ligand *m/z* values, are indicated, (Δ*m/z*), alongside the retention times (RTs) of the binding events. Extracts from cell pellets (CP) and supernatants (SPE) were analyzed.

While many of the putative chymotrypsin binders were detected in the cell pellet, we were particularly interested in one compound found in the supernatant of *Mastigocladus laminosus*. This compound had not been previously annotated in common spectral libraries and appeared to be more suitable for purification. Furthermore, we hypothesize that it could function as an extracellular defense molecule, potentially produced by the strain to protect itself against other microbes or predators. Figure 9.6 shows the extracted ion chromatogram (XIC) of chymotrypsin, with a decrease in the chymotrypsin signal at the same retention time (RT) as the appearance of a peak at *m/z* 462.2 $[M+H]^+$ in the LC-MS/MS run without protein infusion. This shift in mass suggests binding of the compound to chymotrypsin, as the binding likely forms a protein-ligand complex, which alters the molecular mass of chymotrypsin. The disappearance of the original chymotrypsin signal and the emergence of the new peak at *m/z* 462.2 $[M+H]^+$ indicate that the compound has interacted with chymotrypsin, resulting in a change in the mass-to-charge ratio, thus providing strong evidence for binding. An MS/MS similarity network (Figure 9.6C) that was constructed with data from all strains investigated, revealed that the compound was present exclusively in the supernatant of *Mastigocladus laminosus* and *Fischerella muscicola*, though it was less abundant in the latter. Although traditionally assigned to *Stigonematales* based on morphology, both strains are currently classified within the family *Hapalosiphonaceae* of the order *Nostocales* based on 16S rRNA phylogeny (Figure 9.7).

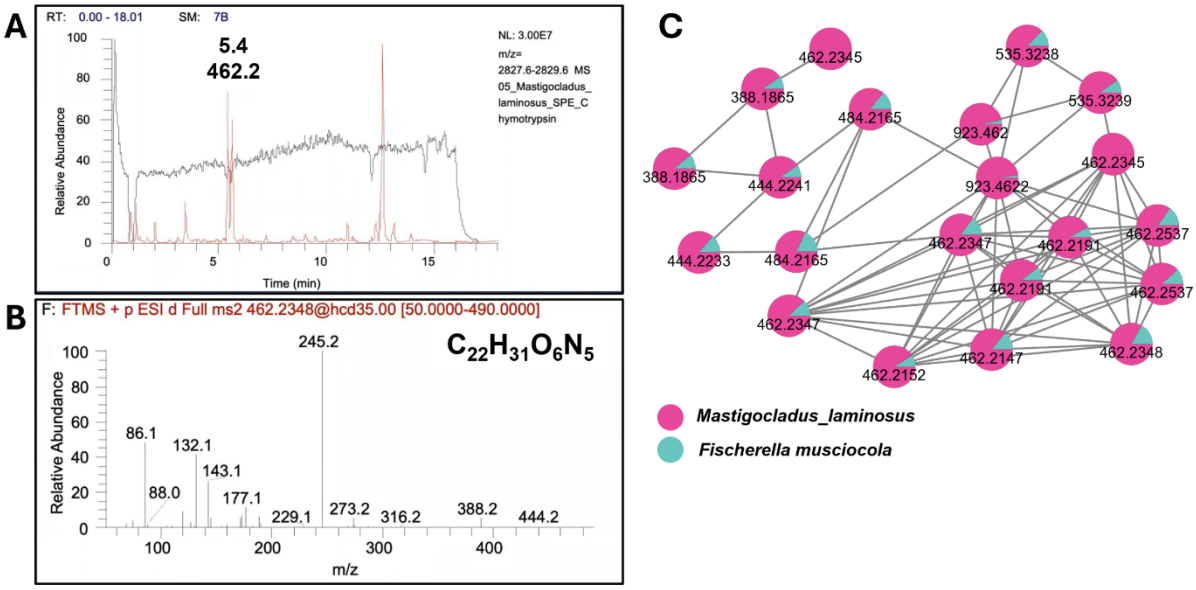

Figure 9.6: Characterization of putative chymotrypsin-binding ligands from *Mastigocladus laminosus* and *Fischerella muscicola* supernatants using native mass spectrometry and molecular network analysis.(A) Extracted ion chromatogram (XIC) of apo-chymotrypsin (black trace) and a signal corresponding to a putative ligand (462.2 *m/z)* at the same retention time (RT = 5.4 min) in the metabolomics run of *Mastigocladus laminosus* supernatant extracts. The decrease in the apo-chymotrypsin signal at this RT indicates a binding event, as the protein mass shifts to a higher value due to complex formation with the ligand**. (B)** MS/MS fragmentation spectrum of the putative binder. **(C)** Molecular network based on MS/MS spectral similarity of the putative binder. Nodes in pink represent features enriched in the supernatant of *Mastigocladus* laminosus, while nodes in cyan indicate features present in the supernatant of *Fischerella muscicola*.

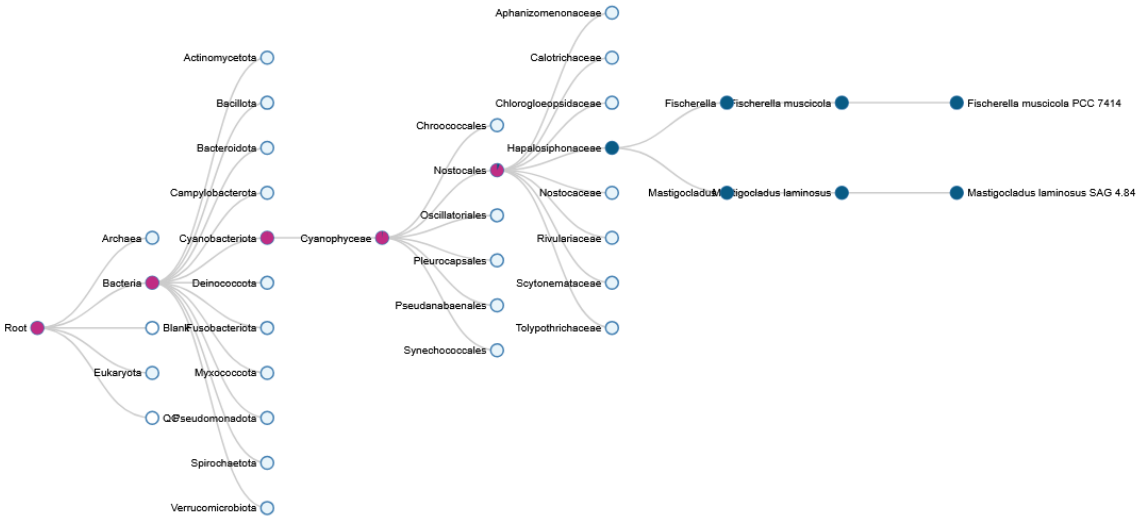

Figure 9.7: Phylogenetic tree of bacterial strains based on MicrobeMASST analysis, showing the producers of the putative chymotrypsin-binding compound. The tree is color-coded to highlight the strains that produce the compound of interest (pink and blue).

9.4 Discussion

In this study, we screened 40 cyanobacterial extracts, comprising both cell pellet and supernatant fractions, from 20 different strains for chymotrypsin-binding compounds using native mass spectrometry. Our goal was to identify natural inhibitors of the serine protease chymotrypsin, a key enzyme involved in numerous physiological processes and a well-established target in drug development.

Multiple putative binders were detected, with the majority localized in cell pellet extracts. However, a particularly compelling chymotrypsin-binding compound (*m/z* 462.23 $[M+H]^+$, RT 5.2 min) was identified in the supernatant of *Mastigocladus laminosus*. This metabolite, absent from common spectral libraries, likely represents a previously uncharacterized natural product. Interestingly, the same compound was also detected in extracts of *Fischerella* spp., a genus known for the production of fischerellin A. Both strains were not known so far to produce protease inhibitors.

Given its ability to bind chymotrypsin and its apparent peptide nature, the compound may belong to one of the known families of cyanobacterial serine protease inhibitors, such as the micropeptins or microviridins. Both families are characterized by cyclic peptides that selectively inhibit chymotrypsin-like proteases. However, the relatively low molecular weight of the compound (462 Da) suggests it may represent a truncated derivative or a structurally distinct member of these classes, or even a novel scaffold altogether.

A comparative analysis of all detected compounds revealed that supernatant extracts contained a greater number and wider diversity of features than cell pellets. While this may be attributed to extraction conditions, it emphasizes the untapped potential of cyanobacterial exo-metabolomes, which remain underexplored, as rich sources of bioactive natural products, including protease inhibitors. These extracellular metabolites may also serve ecological functions, such as mediating microbial interactions or deterring predation.

Importantly, the metabolomic data set generated in this study provides a valuable resource for the broader research community. It enables strain-level comparisons of metabolite production (e.g. as already possible via MicrobeMASST) and offers a foundation for exploring the chemical space of cyanobacterial taxa that are not routinely studied in laboratory settings. For several strains included in our screen, publicly available data remain scarce. Thus, this work contributes not only candidate bioactive compounds, but also contextual information that may

guide future efforts in compound isolation, ecological studies, and strain prioritization for bioprospecting.

The presence of a chymotrypsin inhibitor in *Mastigocladus* and *Fischerella* not only sheds light on their pharmacological potential but also raises ecotoxicological concerns. While these genera are not classical bloom-forming cyanobacteria, both are commonly found in thermal springs (*Mastigocladus*) or soil and freshwater habitats (*Fischerella*) across tropical and temperate regions. The release of protease inhibitors into aquatic ecosystems, even at low concentrations, could adversely affect the digestive physiology of exposed organisms, including fish and aquatic invertebrates. Additionally, the accidental consumption of these inhibitors by humans through contaminated water or food could pose a health risk, potentially affecting human digestive processes and overall health.

9.5 Methods

Cultivation of Cyanobacterial Strains

All cyanobacterial strains were cultivated under photoautotrophic conditions in 50 mL BG11 medium (Rippka et al.[330]) supplemented with 5 mM $NaHCO_3$, in 100 mL shaking flasks, unless stated otherwise. Cultures were maintained under continuous light (30-60 µmol photons m^{-2} s^{-1}) at constant shaking (120 rpm).

The following strains were cultivated at 28 °C: *Synechocystis sp.* PCC 6803 substr. GT-T, *Synechococcus elongatus* PCC 7942, *Synechococcus elongatus* PCC 6301, *Synechococcus sp.* PCC 7502, *Nostoc sp.* PCC 7120, *Nostoc punctiforme* PCC 73102, *Desmonostoc sp.* PCC 7906, *Fischerella muscicola* PCC 7414, *Chlorogloeopsis fritschii* PCC 6912, *Pleurocapsa sp.* PCC 7327, *Calothrix sp.* PCC 6303, *Stanieria cyanosphaera* SAG 33.87, *Phormidesmis molle* SAG 26.99, *Mastigocladus laminosus* SAG 4.840, and *Trichormus variabilis* ATCC 29413.

Scytonema hofmannii PCC 7110, *Oscillatoria acuminata* PCC 6304, and *Leptolyngbya boryana* PCC 6306 were cultivated at 22 °C.

Nitrogen-fixing strains (*Nostoc sp.* PCC 7120, *Nostoc punctiforme* PCC 73102, *Tolypothrix tenuis* SAG 94.79, and *Nodularia sphaerocarpa* PCC 7804) were grown in nitrogen-free BG11 medium (BG11-0).

Extraction of Metabolites

Harvest and Supernatant Preparation

Cells were harvested by gentle centrifugation (3,200 × *g*, 4 °C, 20 min, swing-bucket rotor) to minimize mechanical disruption and prevent contamination of the supernatant with intracellular contents.

Solid-Phase Extraction (SPE)

Aliquots of 40-50 mL supernatant were subjected to solid-phase extraction using C18 cartridges mounted in a vacuum manifold. Cartridges were activated with three column volumes of 100% methanol, followed by conditioning with one column volume of 3% methanol (v/v in LC-MS-grade water), ensuring the columns remained continuously wetted. Samples were loaded dropwise using PEG-free syringe extenders. After loading, cartridges were washed with one column volume of 3% methanol, and metabolites were eluted with 2-4 mL of 100% methanol into fresh collection tubes under gentle vacuum. Eluates were transferred to pre-weighed glass vials or Eppendorf tubes, dried in a vacuum concentrator, and reweighed. Dried extracts were reconstituted in 50% methanol (v/v) to a final concentration of 0.1 mg mL^{-1}.

Cell Pellet Extraction

Cell pellets were extracted with 10 mL of 80% methanol (v/v) per gram of biomass. Samples were sonicated in an ultrasonic bath to disrupt cells and centrifuged to remove debris. The supernatant was collected, dried under vacuum, and reconstituted in 50% methanol (v/v) to a final concentration of 0.1 mg mL^{-1}.

Micro-Flow LC-MS/MS and Native MS Data Acquisition

The experiment was performed as described in detail by Reher et al.[285]. Micro-flow UHPLC-MS/MS analysis was conducted by injecting 2 µL into a Vanquish UHPLC system coupled to a Q-Exactive HF quadrupole Orbitrap spectrometer (Thermo Fisher Scientific, Bremen, Germany). A fully integrated Vanquish quaternary UHPLC pump (Thermo Fisher Scientific, Bremen, Germany) provided the make-up pump support. For reversed-phase chromatographic separation, a Kinetex C18 core-shell microflow column (150 x 1 mm, 1.8 µm particle size, 100 Å pore size; Phenomenex, Torrance, USA) was used. The mobile

phase consisted of solvent A (H_2O + 0.1% formic acid) and solvent B (acetonitrile + 0.1% formic acid). The flow rate was set to 100 µL/min, with a gradient from 5-50% B between 0-8 min, 50-99% B between 8-10 min, followed by a washout phase at 99% B for 3 min and re-equilibration at 5% B for 5 min.

Metabolomics data-dependent acquisition (DDA, TOP5) of MS/MS spectra was performed in positive mode. Electrospray ionization (ESI) parameters were set to a sheath gas flow of 40 arbitrary units (AU), auxiliary gas flow of 10 AU, and sweep gas flow of 0 AU. The spray voltage was set to 3.5 kV, and the inlet capillary was heated to 320 °C. MS scan range for native MS was set to 2000-5000 *m/z* with a resolution at *m/z* 200 of 120,000, using one micro-scan. The maximum ion injection time was set to 100 ms.

For native metabolomics experiments, the same chromatographic parameters were used. The spray voltage was set to 3 kV. Additionally, ammonium acetate buffer was infused post-column at a flow rate of 150 µL/min through a make-up pump and a PEEK-splitter, while chymotrypsin solution was infused at 2 µL/min via an integrated syringe pump.

α-Chymotrypsin from bovine pancreas (Sigma Aldrich) was used for native metabolomics at a concentration of 2 mg/mL, dissolved in 10 mM ammonium acetate buffer.

Data Analysis

Native MS data were deconvoluted using UniDec[331]. Native MS spectra were deconvoluted using UniDec (Charge range 6-20, mass range 10000-50000, mass sampling every 1.0 Da, peak detection range 5.0 ppm, peak detection threshold 0.1). Shifted mass peak intensities were expressed as percentages relative to the apo protein. LCMS-MS Data were analyzed using GNPS1, GNPS2, Cytoscape and MicrobeMASST. PCoA analysis was performed using downstream analysis from GNPS2 with Hitchhiker Statistics Guide.

Cultivation Optimization and Extraction of *Mastigocladus laminosus*

Different cultivation conditions were tested to optimize the production of the putative chymotrypsin binder. The most favorable condition was growth at 37 °C under high light and constant shaking, where *M. laminosus* formed dense, ball-like aggregates and the culture supernatant appeared clear. This “bubble-rich” morphology contrasted with other conditions, under which the culture remained more dispersed. Additionally, cultures were grown in 10 L

flasks aerated with 2% CO_2 at 28 °C. Cells were harvested by filtration through 0.2 µm pore size filters, and the cell-free supernatant was used for solid-phase extraction.

Solid-Phase Fractionation of Putative Chymotrypsin Binders

Crude extracts were fractionated using a manually packed glass column containing 100 g of C18 reverse-phase silica. To prevent disturbance of the resin bed during loading, a thin layer of inert sand was applied on top of the C18 material. The column was preconditioned by settling the silica with 100% methanol, followed by washing with additional methanol and equilibration with ultrapure water. The aqueous supernatant containing the target metabolites was then applied to the column. Elution was performed stepwise with three column volumes (CV) each of 0%, 20%, 40%, 60%, and 100% methanol (v/v in water), all supplemented with 0.1% trifluoroacetic acid (TFA). The compound of interest was detected in the 40% and 60% methanol fractions. All fractions were dried under reduced pressure and stored at −20 °C until further analysis.

Information for strains and extraction: see ReDO-Metadata: https://tinyurl.com/2zrvu6f9

Source Data:

Native metabolomics cyanobacteria protease screen: MSV000088697

Non-targeted metabolomics with extracts of 20 cyanobacterial strains - contribution to microbeMASST: MSV000089884

MicrobeMASST Taxa matches:

file:///C:/Users/beren/Desktop/Proteaseinhibitors/Microbe_MASST_462/fastMASST_microbe.html

Author contributions

D.P. conceptualized and initiated the study. K.F. provided cyanobacterial strains and advice on cultivation and scale-up. B.C.W. cultivated the strains, performed SPE and cell pellet extraction under the supervision of D.P. D.P. and B.C.W. performed native MS and untargeted MS/MS experiments, and B.C.W. analyzed the data with advice from DP. B.C.W.

conducted growth experiments and scaled up cultivation of *Mastigocladus laminosus*. G.A.V. performed chemical metabolomics. G.A.V. and B.C.W. purified the inhibitor with advice from C.C.H. B.C.W. wrote the manuscript

9.6 References

The references cited in the manuscript have been incorporated into the main reference list of this thesis and adjusted to follow the sequential numbering of the thesis-wide bibliography (section 8, p.131ff).

10 List of Figures

R

11 Acknowledgements

This work was made possible thanks to the mentorship, guidance, collaboration, and friendship of many people, both inside and outside the lab, who supported me throughout my Ph.D. I sincerely thank everyone who accompanied me and positively influenced this time.

First, I would like to sincerely thank **Prof. Dr. Karl Forchhammer,** my supervisor, for his guidance and mentorship. I am grateful for the opportunity you gave me to explore the projects with room to develop my own ideas while always having your support. You also enabled me to establish collaborations with different research groups and supported me in pursuing many interesting side projects, providing the guidance and environment that made these experiences scientifically rewarding and helped me shape a direction I wish to continue following in the future. I not only learned a lot from your scientific enthusiasm, but also from your diplomatic skills and leadership style, and received proof that music and science can complement each other perfectly.

I am grateful to my second supervisor, **Prof. Dr**. **Christiane Wolz**, for listening to my research during our TAC meetings, critically questioning the process, and providing valuable ideas to improve it, as well as for always checking in on how I was doing when we met.

I would also like to thank my collaboration partner, **Prof. Dr. Daniel Petras**, for being the beaming lighthouse in the stormy sea of cyanobacterial metabolites and for persistently guiding the development of the CutA manuscript. Thank you for welcoming me into your lab. Thanks for your drive, support, curiosity, and belief in positive outcomes, as well as your encouragement.

I would also like to thank my other collaboration partner, **Dr. Chambers C. Hughes**, for welcoming me in his lab and for the efficient and insightful approach to compound purification. I am grateful for your guidance, advice, and enthusiasm for chemical metabolomics, as well as for taking the time to answer all my questions.

As member of my TAC committee, I am also grateful to **Prof. Dr. Gary Sawers** for his constructive input and insightful feedback throughout these discussions.

My sincere thanks go to **apl. Prof. Dr. Klaus Hantke** for sharing his vast knowledge of *E. coli*. Thank you for always keeping an open ear, sharing new scientific insights, and inspiring the drive to figure things out. Your example of hands-on dedication (including the

memorable “pipetting with mouth” demonstration) has been truly motivating. I also hope to continue receiving updates on your ongoing research.

I would like to thank my former bachelor student, **Amelie Stadelmann**, who worked with me on this project, for her dedication, kindness, and for being a great scientist. **Janette Alford** and **Nelli Deobald** for amazing, flowing teamwork, especially in the practical courses or on the ELISA project. **Johanna Rapp**, **Klaus Brilisauer** and **Nathan von Manteuffel** for great companionship while working together in 9P07. **Tim Orthwein** for introducing me to our band. The rest of my working colleagues for the great atmosphere inside and outside the lab: **Teresa Müller, Nathalie Becker, Markus Burkhard, Arianna Zini, Philipp Fink, Soumila Mondal, Sofia Doello, Rokhsareh Rozbeh, Sherihan Samir, Dimitris Bekiari, Heinz Grenzendorfer, Claudia Menzel, Eva Nußbaum, Iris Maldener, Michaela Kopp, Jörg Scholl, Björn Watzer, Philipp Spät, Eva Bok, Moritz Koch, Gulliver Black, Mulugeta Nega, Filipp Oesterhelt, Christoph** and **Marina Mayer, Martina Bianchi, Axel Walter, Simon Friz, Abzer Kelminal Pakkir Mohamed Shah, Stilianos Papadupoulos Lambidis, Sibgha Tayyab, Paolo Stincone and Giovanni Vitale.** Also, **Lana Graves**, for the best, most fun, and productive co-writing sessions, even when we are on opposite sides of the ocean. **Christian Geibel** for insights about columns and Van Deemter curves during long measurements and for always offering help when needed. Thank you, **Dr. Libera Lo Presti,** for correcting our manuscript and this thesis.

I would like to express my sincere thanks again to all co-authors of our CutA publication for their invaluable contributions and for being part of the long yet ultimately rewarding journey of this manuscript: **Christian Geibel, Amelie Stadelmann, Karoline Steuer-Lodd, Johanna Rapp, Hannes Link, Tilman Schramm, Nouneh Boodaghian, Ansel Hsiao, Eva Nussbaum, Heinz-Paul Grenzendorfer, Reinhard Albrecht, Marcus D. Hartmann, Karl Forchhammer, Khaled A. Selim, Chambers C. Hughes,** and **Daniel Petras**.

I would also like to thank AK Meixner and AK Scheele, especially **Jakob Keck** and **Martin Eberle**, for enjoyable late-day coffee breaks, advice with Python and for planting a forest together.

Finally, I want to thank my friends and family for their unwavering support. Especially **Jonas Hiller**, for your scientific drive, understanding, and encouragement, for your openness to new ideas and for being a truly wonderful partner overall.